Alma Mater Studiorum - Università di Bologna

DOTTORATO DI RICERCA IN

MECCANICA E SCIENZE AVANZATE DELL'INGEGNERIA (DIMSAI)

Ciclo 33

Settore Concorsuale: 09/C1 – MACCHINE E SISTEMI PER L'ENERGIA E L'AMBIENTE

Settore Scientifico Disciplinare: ING-IND/08 – MACCHINE A FLUIDO

TEST BENCH DEVELOPMENT, EXPERIMENTAL ANALYSIS AND MODELLING OF MICRO-ORGANIC RANKINE CYCLE FOR LOW-GRADE HEAT RECOVERY

Presentata da: Saverio Ottaviano

Coordinatore Dottorato

Marco Carricato

Supervisore

Andrea De Pascale

Co-supervisore

Antonio Peretto

Esame finale anno 2021

Abstract

This thesis presents the detailed experimental and numerical analysis conducted on a prototype of micro-scale organic Rankine cycle (ORC) power system. The system is conceived for stationary co-generative applications in the residential sector, since it is characterized by a power output in the kW-scale. Suitable heat sources are low-enthalpy geothermal energy, biomass combustion, solar thermal collectors or low-temperature waste heat recovery. The system is driven by a reciprocating piston expander prototype, and uses HFC-134a as working fluid. The other components are a brazed plate heat exchanger as evaporator, a shell and tube water condenser, a prototypal external gear pump and a brazed plate recuperator. The suitable temperature of heat source is in the range 60-90 °C.

The common aspects related to the development of the micro-ORC test bench are depicted. These aspects involve the implementation of the acquisition and control systems, including the installation and calibration of the sensors of temperature, pressure, flow rate and electric power, and the development of the acquisition software in LabVIEW platform. The issue of the assessment of the working fluid charge inside the circuit is addressed by means of an empirical approach, based on the measurement of pressure and temperature and on the observation of the liquid level with the system shut off.

The experimental campaign was conducted in steady state and dynamic regimes, acquiring a large number of operating points to assess the system behavior in off-design conditions. A methodology for the on-line detection of the steady-state condition, named R-test, is adapted and described for the system under investigation. The experimental results are presented in the form of operating maps, highlighting the influence of the controlled variables to the operating conditions and to the cycle performance. The main controlled variables are the hot water temperature and flow rate at the evaporator inlet, the ORC feed pump rotating speed and the external load connected to the expander, which consists of five pure resistive loads that can be activated individually, modifying the load impedance seen by the expander generator. The cold-water flow rate can be adjusted too within a limited range, while the cooling temperature depends on the ambient conditions. Main results show the dependence of the organic fluid evaporation pressure from the mass flow rate and, to a lesser extent, from the load impedance. Condensation pressure is mainly influenced by the cooling water temperature, with a smaller effect given by the mass flow rate. The maximum achieved value of the evaporation pressure is close to 23 bar, corresponding to a maximum pressure difference across the expander close to 15 bar and a pressure ratio of 2.9. The value of superheating degree at the expander inlet increases with the increment of heat source temperature and decreases with the rise of the pump speed. The relations between the load impedance and the expander performance is depicted over a wide range of working conditions. As main outcome it was observed that, with constant pump speed, the expander performs better at low rotating speed, corresponding to lower value of the load impedance. Indeed, increasing the rotational speed, both the expander filling factor and total efficiency decrease. The maximum gross power output results close to 1700 W, while the expander efficiency ranges between 38% and 43%. The feed pump behavior is deeply analyzed, revealing a relatively low performance of this component, with total efficiency lower than 25%. In fact, the pump consumption corresponds to a large fraction of the expander power output, between 50% and 90%. Phenomena of pump cavitation that have been experienced during the ORC system operation are described. The increment of the fluid charge inside the circuit have been applied, demonstrating to be able to solve cavitation issues for this system. An extensive analysis is dedicated to the heat exchangers performance. For the evaporator, the analysis based on the single zones (liquid, vapor, mixture) effectiveness allows to identify the effect of each zone on the global heat transfer performance.

A further experimental campaign has been conducted with the specific purpose of evaluating the response of the micro-ORC system to transient conditions. The response time of the key variables is calculated and compared among the key output variables, for different cases of increasing and decreasing variations of the hot water

temperature, pump speed and external load. In terms of control design, the superheating degree is selected as system output and control parameter, hence its response time is taken as reference index for the comparison between the different cases. As expected, the system output is more sensitive (i.e. shows lower response time) to the variation of the pump speed than to that of the hot water temperature.
A thermodynamic model has been developed using the Simscape library included in MATLAB Simulink, for both steady-state and dynamic simulations of the micro-ORC system. The model is of charge-sensitive type, meaning that no assumptions are made on the fluid states, and the operating conditions depend only on the boundary conditions (hot and cold-water temperature and flow rate) and on working fluid flow rate. The model is first calibrated and validated with steady-state experimental data, showing maximum error lower than 5% for the cycle pressure and expander inlet temperature, while higher inaccuracy is observed in the prediction of the expander outlet temperature, power output and rotational speed. At last, the model is applied to dynamic input conditions in two cases: increment of mass flow rate and increment of hot water temperature. The simulated evaporation pressure reveals a slower response to the variation of mass flow rate with respect to the experiments, still predicting accurately the steady-state values before and after the perturbation. The opposite is observed for the water temperature increment, for which the evaporator outlet temperature shows a much faster response than the measured one.

To summarize, the main objectives of this thesis are:

- providing accurate information about the issues related to the implementation of an organic Rankine cycle test bench;
- presenting the performance of a prototypal micro-ORC system, working with a piston expander and designed for low-temperature heat sources
- assessing the dependences of the micro-ORC system steady-state performance from the off-design operating conditions, by analyzing the behavior of each component;
- estimating experimentally the system response to transient variations of the operating conditions, in order to deduce guidelines for the control system design;
- developing and validating a charge-sensitive thermodynamic model to simulate the ORC system in stationary and dynamic conditions.

The analysis here presented aims at providing a contribution to the research field of micro-scale and low-temperature organic Rankine cycles, especially from the experimental point of view. The improvement of micro-ORC performance and reliability is one of the key factor for the market spread of this technology, helping to enhance the global electricity generation efficiency, save primary resources and greenhouse gases emissions, and increase the exploitation of renewable thermal sources.

The thesis is organized with the following structure:

Chapter 1 presents the context in which this research operates. General information on thermo-electric conversion are provided, with a special focus on the available low-temperature and micro-scale technologies. The working principle of the Organic Rankine Cycle is depicted, and an overview of the various components of the system, together with the working fluid analysis, are reported. The literature review of micro-ORC technology is presented and discussed, with particular attention to steady-state and dynamic analyses, both from experimental and modelling point of view.

Chapter 2 reports a detailed description of the experimental setup, implemented for testing the micro-ORC system under investigation. The characteristics of the plant components are depicted, together with the external circuits for the supply of hot and cold water. The acquisition and control systems, including all the measurement sensors, the actuators and the acquisition devices, are deeply described. A special focus is made on the development of the

acquisition and control software, which was one of the subject matters of the Ph.D. project presented in this thesis. The issue of the fluid charge assessment is also addressed by means of an experimental approach.

Chapter 3 presents the experimental campaign conducted on the micro-ORC system. Steady-state analysis is presented first, with the description of the test setup, the boundary conditions, the ranges of the controlled variables and the constant parameters set for the tests. The experimental results, averaged over the stationary intervals, are showed and discussed looking at each component of the cycle. An analytical-empirical model of the system is presented, based on the parameters derived experimentally, and has the purpose of estimating the operating conditions and the performance in case a specific application of this plant needs to be preliminary evaluated.

Chapter 4 presents the results of the experimental analysis focused on the dynamic response to transient operation. The analyzed cases are related to the system start-up, the variation of the pump frequency, of hot water temperature and of the external load. The response time and settling time of the main variables are presented and compared for each case.

In **Chapter 5,** the model developed in Simulink Simscape for simulating the micro-ORC system under investigation is presented. All the blocks that reproduce the system components are deeply described, with the analysis of the parameters that influence the model performance. The calibration procedure that allowed optimizing the components geometry is introduced. First, the results were validated with steady-state experimental data, to verify the good match between simulated and tested performance; then, the comparison with experiments is showed for dynamic conditions, in the cases of variation of the working fluid flow rate and hot water temperature.

Contents

List of figures

List of tables

Nomenclature

Symbols and acronyms

A	Surface area [m^2]
AI	Analog input
BWR	Back Work Ratio [%]
CHP	Combined Heat and Power
D	Diameter [m]
E	Error
FF	Filling Factor [-]
FPGA	Field Programmable Gate Array
FS	Full Scale
h	Enthalpy [kJ/kg]
H	Height [m]
I/O	Input/output
ICE	Internal Combustion Engine
L	Length [m]
m, M	Mass [kg]
$\dot{m}$	Mass flow rate [kg/s]
N	Rotational speed [rpm]
NA	Not available
Nu	Nusselt number [-]
ORC	Organic Rankine Cycle
p	Pressure [bar]
PCB	Printed Circuit Board
$\dot{Q}$	Thermal power [kW]
R	Steady state index [-]
Re	Reynolds number [-]
RV	Reading value
S	Cross sectional area [m^2]
T	Temperature [°C]
t_{ss}	Minimum duration for steady-state interval [s]
U	Uncertainty / Global heat transfer coefficient [W/m^2 K]
v	Specific volume [m^3/kg]
V	Volume
$\dot{V}$	Volumetric flow rate [l/s]
$\dot{W}$	Power [W]
WHR	*Waste Heat Recovery*
x	Vapor quality in two phase mixture [-]
Z_{load}	Load impedance [Ω]

Greek letters

α	Convective heat transfer coefficient [W/m^2 K]
η	Efficiency [%]
λ	Conductive heat transfer coefficient [W/m K]
ρ	Density [kg/m^3]
σ	Standard deviation (referred to uncertainty)
τ	Response/settling time [s]

Subscripts

C	Cold water
cond	Condensation
el	Electric
ev	Evaporation
exp	Expander
F	Furnace
gross	Gross
H	Hot water
in	Inlet
is	Isentropic
L	Liquid phase (saturation)
net	Net
out	Outlet
p	Referred to pressure
PLS	Primary Laboratory Standard
p, pump	Pump
r	Response
R	Residual (referred to uncertainty)
rec	Recuperator
ss	Steady state / settling time (referred to transient analysis)
suc	Suction
sc	Sub-cooling
sh	Superheating
T	Referred to temperature
th	Thermodynamic (referred to power)
V	Vapor phase (saturation)
w	Wall

CHAPTER 1

1 Introduction: context and state of the art

1.1 Energy context and scenario

Nowadays, the society must face the complex issues of energy shortage and environmental impact, which dictate the adoption of effective solutions to achieve a sustainable development. Even if a slow transition to a low-carbon economy has been in progress for the last twenty years, the current electricity generation is still dominated by fossil fuels, which account for almost 65% of the electric production share, followed by the renewables (25%) and nuclear plants (10%) (Figure 1.1) [1]. The electricity demand will most likely increase in the long term, due to the increase of the world population and to the rapid economic growth that is expected for some developing countries. The International Energy Agency (IEA) formulated the *Sustainable Development Scenario (SDS)*, the most ambitious energy outlook in terms of goals to achieve and efforts to implement for a more sustainable future. Following the *SDS*, the global energy production is expected to increase from almost 27000 TWh in 2018 to 37000 TWh in 2040 (≈ 37% increment) [2]. The share of renewable primary sources is likely to increase up to 66% in 2040, nearly tripling with respect to 2010. On the other hand, the coal-fired power plants would rapidly be dismissed, accounting for only 5% of energy generation in 2040. The carbon intensity of the electricity is expected to keep on reducing from about 400 g CO_2/kWh to about 70 g CO_2/kWh.

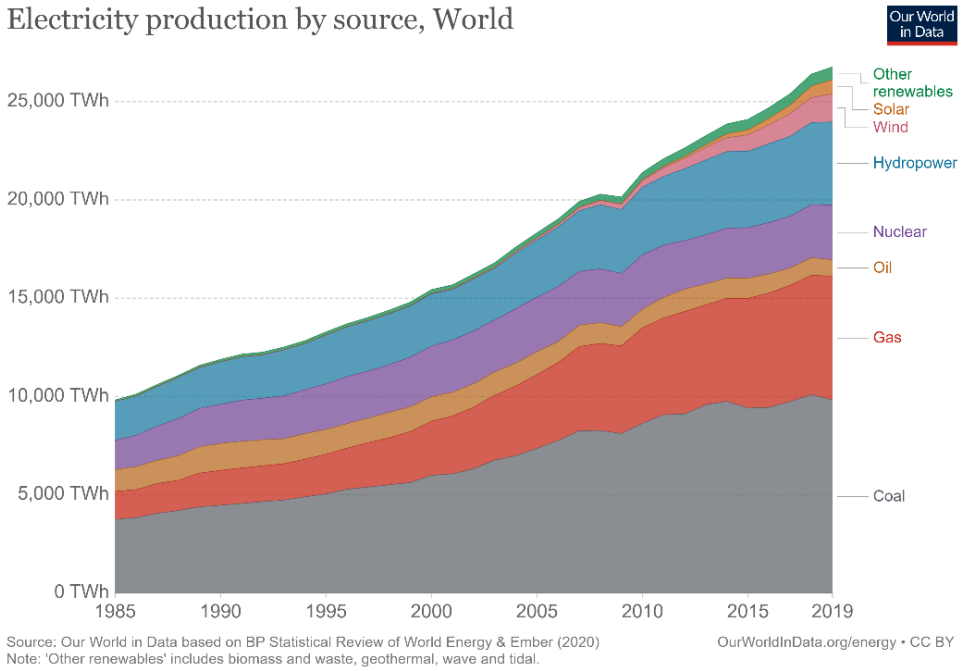

Figure 1.1 – Electric power generation by energy source over last decades [1].

According to the IEA *SDS*, which takes as reference the main outcomes of the Paris Agreement of 2015 (signed by 193 nations), the main goals to pursue for a sustainable global development are:

- **Holding the increase of global average temperature below 2 °C**. As shown in Figure 1.2, the CO_2 emissions, that are the main responsible of the global warming, have more than doubled in the past 40 years, mostly due to the economic growth of developing countries [3]. To this aim, the amount of carbon-based energy conversion technology should be substantially reduced, allowing lower emissions of

greenhouse gases. This can be accomplished by increasing the share of renewable sources in the energy production sector and by reducing the energy consumption per capita.

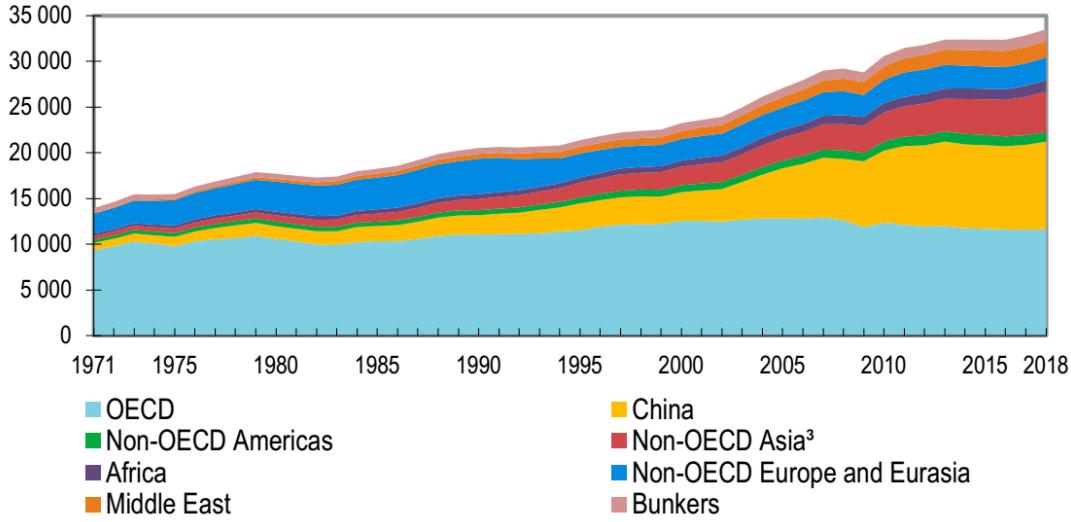

Figure 1.2 – World CO_2 emissions from fuel combustion in Mt of CO_2 [3].

- **Ensuring universal access to electricity**. Today indeed, the access to electricity is denied to almost one billion people, most of which living in Africa and South Asia (see Figure 1.3), that are regions with high growth rate of population [4]. The access to modern energy is an essential requisite for reducing poverty and inequalities. Some of the factors that can help to achieve this goal are the enhancement of international cooperation, the share of the new and most efficient technologies, but also the better use of local primary resources.

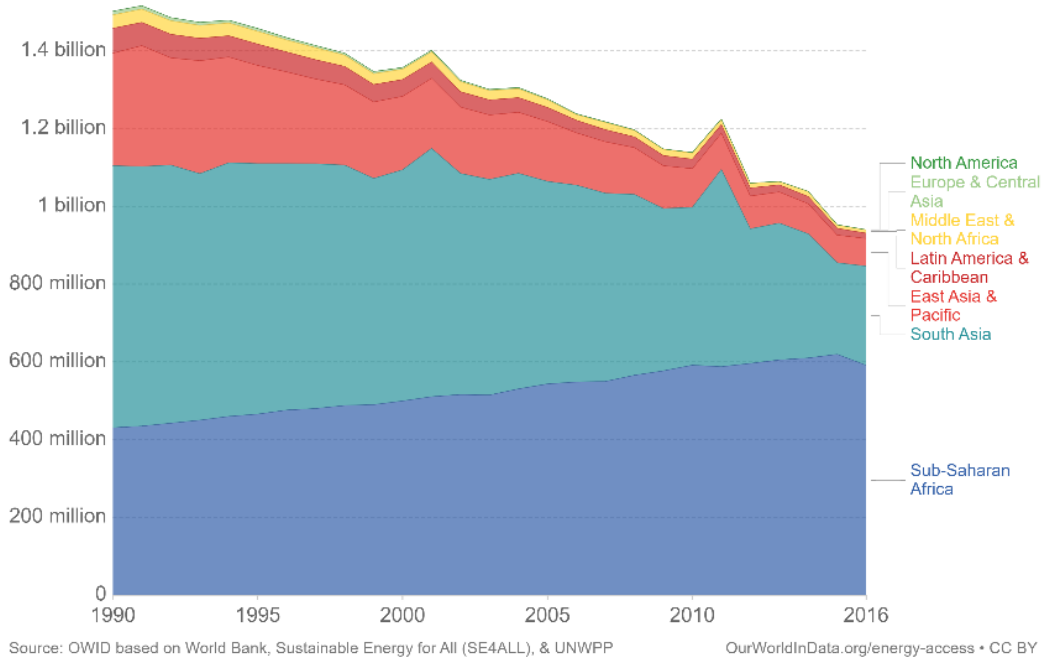

Figure 1.3 – Number of people without access to electricity [4].

- **Reducing significantly the air pollution**, that is the cause of many premature deaths, mostly due to respiratory system disease. The major pollutants are the sulfur dioxide (SO_2), the nitrogen oxides (NO_x) and the particulate matter. According to the Health Effect Institute, air pollution is the fourth largest threat to human health, being related to more than 5.5 million premature deaths each year [5]. The aim is to reduce pollution-linked deaths to around 3 million by 2040. This goal can be helped by cutting the coal-fired share in the electricity and heat generation.

To summarize, in order to meet the recommendation of the IEA, the global electricity generation is required to be **more efficient, renewable-oriented and more distributed**. The conversion efficiency of thermal energy systems has been continuously improved over the last decades, and even though there is still margin for further advancements, they come up against the limits fixed by the laws of thermodynamics. Indeed, a thermodynamic cycle has a maximum efficiency that is theoretically achievable, given by the Carnot cycle efficiency, which is function of the heat source and cold sink absolute temperatures. In Figure 1.4a) the Carnot efficiency is plotted versus the heat source temperature, at constant cold sink temperature corresponding to ISO conditions (15 °C). Figure 1.4b) reports the trend of growth over the last century for the maximum efficiency using any power cycle [6]. Today, the maximum efficiency of the state-of-the-art conversion technologies exceeds 60% and is achieved by natural gas and coal combined cycle. The actual efficiency of a cycle is influenced by a scale effect, as it is related to the size of the power plant: generally speaking, the higher is the size, the higher will be the investment on new and effective technologies and materials. An example is given by the gas turbine, whose performance depends on the maximum temperature of the cycle (turbine inlet temperature), which can be achieved by building the turbine with advanced materials, and with more sophisticated systems for coating and cooling of the turbine blades.

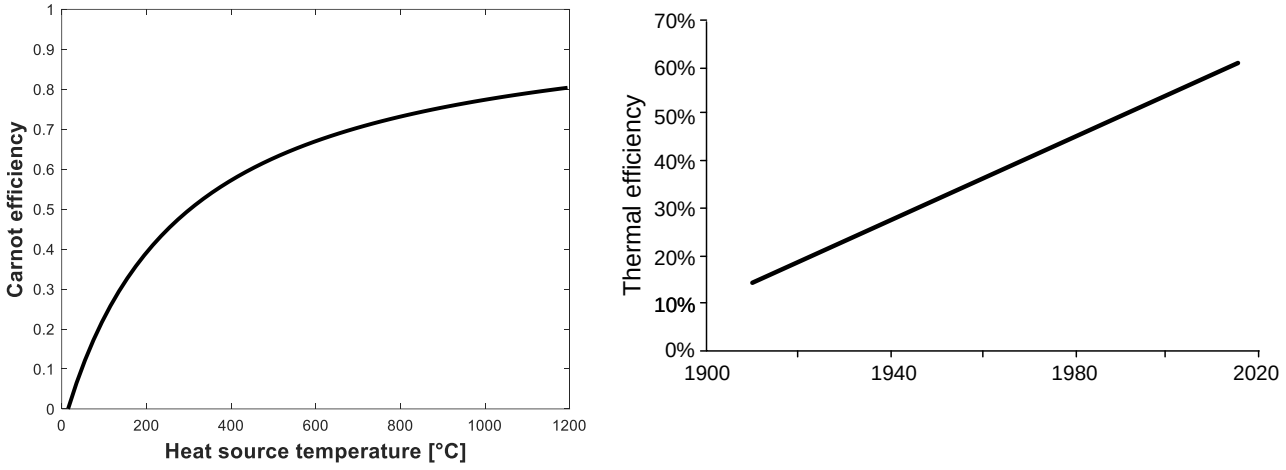

a) b)

Figure 1.4 – a) Carnot efficiency vs. heat source temperature @ 15 °C of cold sink temperature; b) Increasing trend of maximum thermal efficiency for electric power generation over the last century [6].

Large scale plants are proper of a **centralized power generation** (CPG) structure, which has been the dominant paradigm so far. Under the CPG model, the electricity is produced in a small number of large facilities, and then distributed to the end consumers through a network of high and medium voltage transmission lines [7]. The disadvantages of CPG are several: the transmission losses can reach up to 12% of the power generated, and up to 30% of the delivered cost of electricity; in case of fossil-fired system, there are high emission rates (also local pollutant emissions); the electrification of rural areas is not convenient due to the large investment capital to realize the infrastructures; some plants require considerable use of land for the facility; finally, traditional fossil-fired systems involve the production of high amount of waste and the utilization and discharge of much water. The alternative to the CPG is the **distributed power generation** (DPG), which is characterized by a large number of small plants located near the users, connected to low voltage transmission lines or directly to the end consumers.

The main advantages of DPG are the reduced transmission losses, better management of black-outs, lower investment costs, the possibility to serve the remote areas, and the suitability to the employment of low or zero-carbon primary sources. The main disadvantages are technical (redesign of distribution network, energy management system), economical (electricity price competitiveness) and regulatory (distributed operators have low incentives for the access to the network).
In addition to the technological progress and energy distribution mode, the enhancement of the global efficiency can be aided by the valorization of the low-grade heat sources. It was estimated that about 50% of the world energy generation is wasted as heat, due to the inevitable thermodynamic losses of the conversion processes. There is a large variety of waste heat sources, such as industrial heat, gas and steam turbines exhaust heat, internal combustion engines exhaust heat, solar thermal power, low-enthalpy geothermal power, biomass heat etc. The quality of a waste thermal source mainly depends on the usability of the source (i.e. from the form of the heat, location etc.), the available amount of thermal power (i.e. the mass flow rate of the heat source), and the heat source temperature. The term "waste heat" refers to the fact that until few years ago these sources of energy were considered useless and wasted to the ambient. A part of this thermal energy can be converted into electricity by means of heat recovery engines, like organic Rankine cycles.
The exploitation of the renewable energy sources has been increased worldwide, especially in developed countries, where advanced energy policies and larger investments on low-carbon technologies have been applied [8]. Figure 1.5 shows the global trend of electricity generation from low-carbon sources, including renewables, over the last 45 years. Currently, among the renewable power plants, the most adopted is the hydropower with almost 16% of total electricity generation share, followed by wind power (5.3%) and solar energy (2.7%), while other renewables (geothermal, biomass, wave and tide) cover about the 2.5% of the global share. Besides the reduction of pollutant and greenhouse gases emissions, renewable energy presents the unique advantage of being globally distributed, allowing for a solution to the problem of energy supply of the rural areas and developing countries.

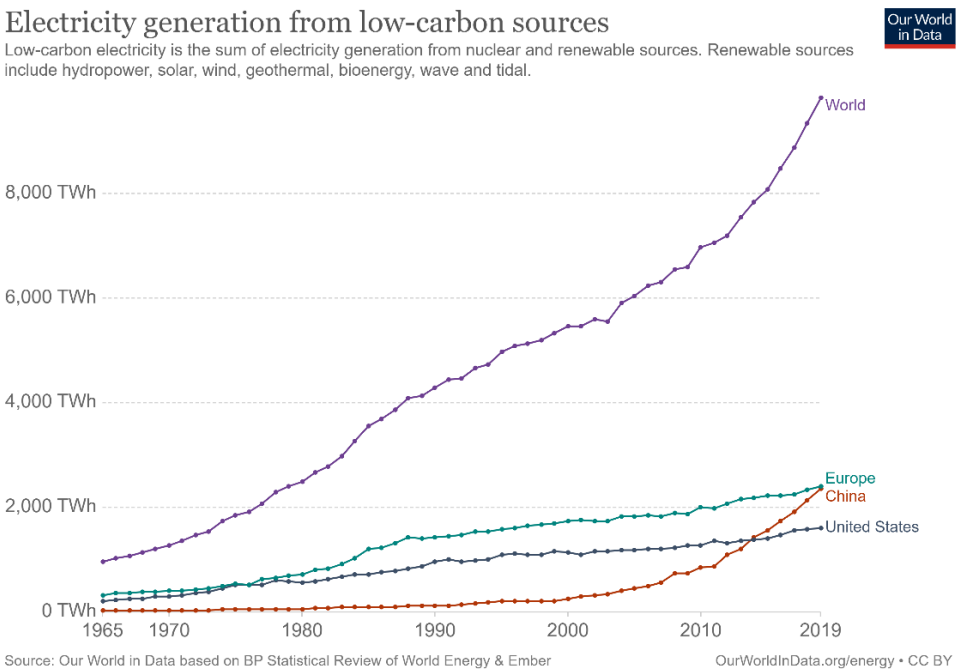

Figure 1.5 – Electricity generation from low carbon sources [1]

It appears clear that there is a big potential of development for thermal renewable energy sources, which include a multitude of applications characterized by a large variety of working temperature and conversion technologies. Figure 1.6 summarizes the currently most used renewable energy sources of thermal type (solar, geothermal, biomass), with the main technologies adopted for their conversion into electricity. The applications of organic Rankine cycles (ORC) to these heat sources are depicted in the next paragraph.

It can be concluded that the combined adoption of waste heat recovery, together with higher share of renewable sources and distributed generation solutions, may have a great impact on the achievements for a sustainable future, improving the system global efficiency, reducing the fossil-fuel exploitation and the related emissions of pollutant and greenhouse gases, and also helping the development of weak economies, by creating jobs and redistributing wealth between local population.

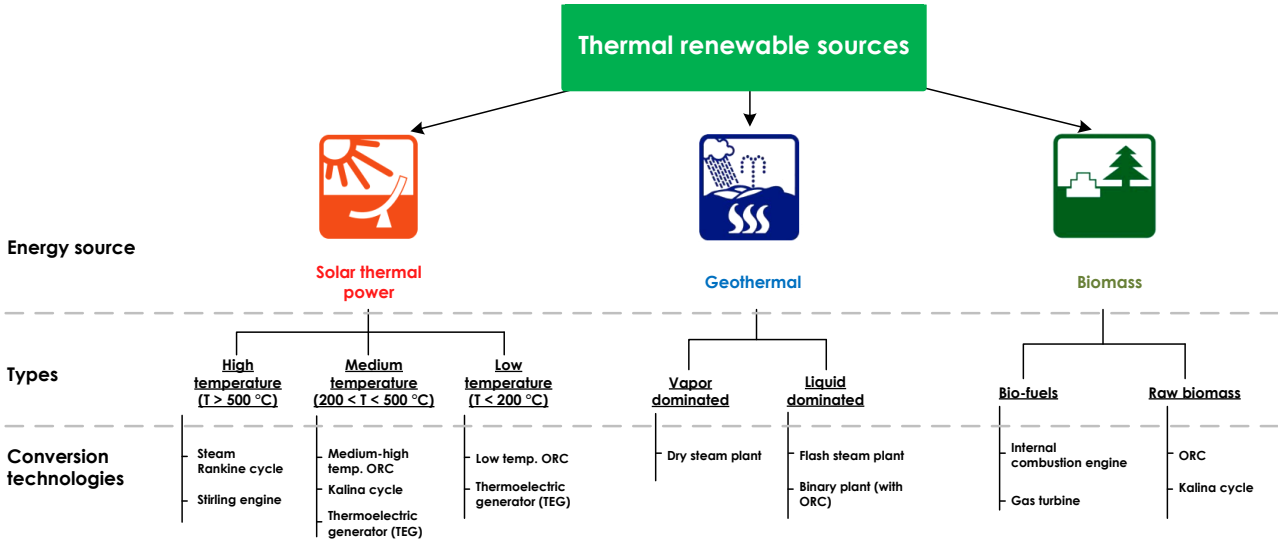

Figure 1.6 – Conceptual map of thermal renewable energy sources, with typologies and conversion technologies

1.2 Organic Rankine Cycle power systems

1.2.1 Operating principle and general features of ORC

The organic Rankine cycle is considered the best technology for the conversion of low-grade heat sources, being suitable for a wide range of plant size, from the micro-scale (less than 10 kW) to the medium power (up to 20 MW). The temperature level at which ORC results more performant than other energy conversion technologies ranges between 70-150 °C (low temperature ORC) and 300-400 °C (high temperature ORC). The main difference regards the employment of organic working fluids, which are characterized by lower vaporization temperature and pressure and by higher molecular mass. ORC systems operate with the same principle of the traditional water steam Rankine cycle plants. In the simple configuration shown in Figure 1.7 a), the main components are the evaporator, the expander, the condenser and the fee-pump. The working fluid, in liquid state, is pumped by the feed-pump to the high pressure of the cycle (1-2), then enters the evaporator to be preheated, vaporized and superheated by the thermal power transferred from the heat source (2-3), then is expanded in the expander generating mechanical work (3-4), and is finally returned to the liquid state in the condenser (4-1), where the fluid discharges the thermal power to the cold sink [9].

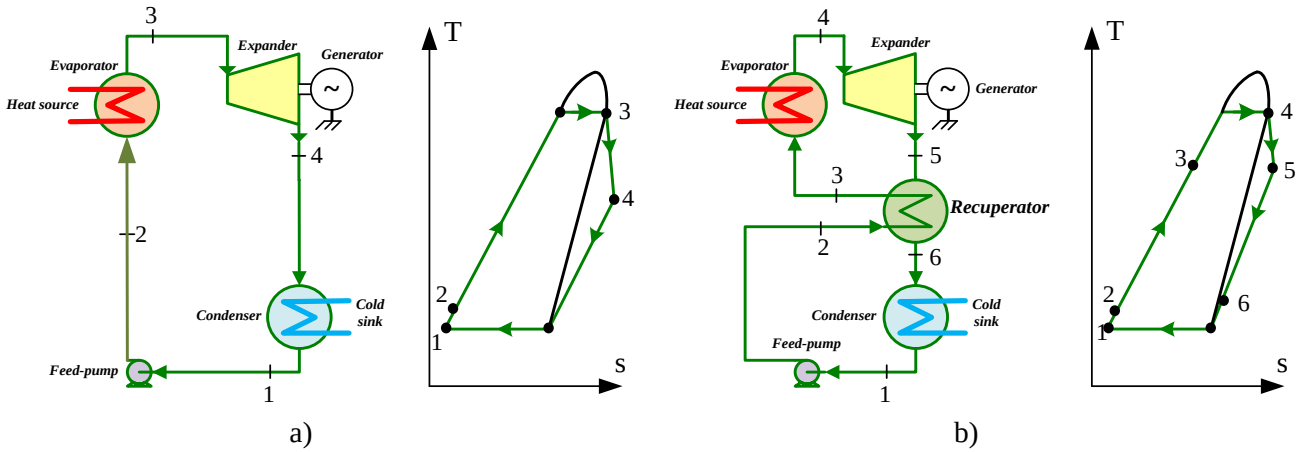

Figure 1.7 – Schematic layout of Organic Rankine Cycle: a) simple cycle, b) regenerative cycle.

Some peculiar features that reflect on the system design can be highlighted at this point: first, the higher molecular complexity, characteristic of the organic fluids, is related to a larger heat capacity, which determines the inclination of the saturated vapor curve in the temperature-entropy diagram. A complex molecule is related to a positive slope of the saturated vapor curve as depicted in Figure 1.8, where the cases of water, benzene, and MDM, that are called, respectively wet (negative slope), isentropic (infinite slope) and dry fluids (positive slope). Considering the thermodynamic cycles traced in the T-s diagrams, at equal heat source and cold sink temperature and with no superheating at the expander inlet, it can be seen that the expander outlet point is in the two-phase region for water (wet expansion), while for benzene and MDM the expansion occurs in the superheated zone, in dry conditions. One consequence of dry fluid's behavior is that the fluid does not need to be superheated in the evaporator in order to avoid liquid drops inside the expander. Moreover, the de-superheating phase counts for a large fraction of the heat rejection, differently from the case of water, where all the heat is rejected as latent heat of condensation. This aspect suggests the convenience in adopting a configuration such as that shown in Figure 1.7 b), referred as regenerative (or recuperated) ORC system. A heat exchanger (recuperator) is installed at the expander outlet, to recover the residual latent heat after the expansion, which is used for preheating the liquid fluid before entering the evaporator. This solution allows to reduce the thermal input for the vaporization of the working fluid. Also, the vaporization heat is substantially reduced, while the preheating (economizing) process increases its share of the total heat input [9], confirming the advantage of using a recuperator. Another peculiarity of dry fluids like MDM is the low difference between the liquid and vapor density at vaporization pressure, which allows to adopt a simpler design of the evaporator with respect to the steam cycle. Indeed, a typical water boiler for steam production is composed of the economizer, the vaporizer connected to the water-steam drum, and a super-heater as separated components, while in ORC generally a once-through boiler is employed. Moreover, some solutions that are normally adopted in steam plants, such as the reheating of the vapor after a first stage of expansion, or the regeneration by means of turbine bleeding, are not suitable for the ORC systems, which makes the ORC plant configuration generally simpler than that of a steam Rankine cycle [10]. This is reflected on a lower complexity and investment costs, low maintenance and high reliability. Another important difference with water steam cycles regards the possible employment of an intermediate circuit between the heat source and the ORC evaporator, where an intermediate heat transfer fluid (IHTF) absorbs the thermal power from the heat source to transfer it to the organic fluid. This solution is generally adopted in case of high temperature peaks of the heat source, that can cause problems of thermal stability of the working fluid. It is also employed in case of high temperature fluctuating thermal source, to smooth the temperature oscillation.

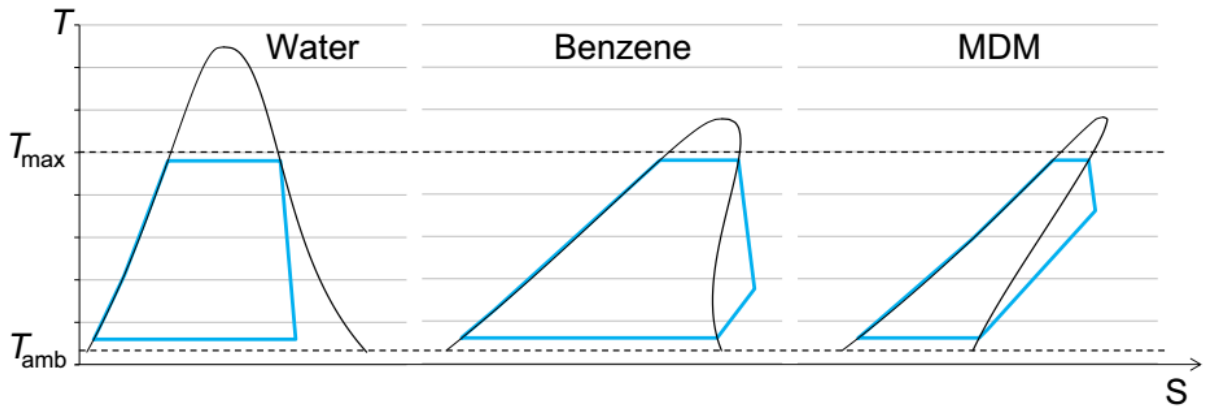

Figure 1.8 – Qualitative T-s diagram of wet (Water), isentropic (benzene) and dry (MDM) fluids.

1.2.2 Working fluid analysis

The working fluid selection has been the subject of many scientific studies on the design of ORC systems. The common approach provides for the analysis of the thermodynamic performance of different fluids, by means of thermodynamic models. The specific properties that influence the performance of a fluid operating in ORC are:

- Molecular complexity, expressed by the number of atoms
- Critical point, in terms of critical temperature and pressure
- Molecular mass

As already mentioned, the molecular complexity determines the shape of the saturation curves, affecting the weight of heat rates corresponding to vaporization, de-superheating and preheating, and also the possible need of a minimum superheating degree to avoid wet expansion. Regarding the critical point, it can be demonstrated that, at given fluid, the thermodynamic performance is higher if the evaporation temperature achieves values close to the critical temperature. Fluids with heavy molecules have the advantage of a lower ideal expansion enthalpy drop, which suggests the use of lower number of turbine stages, allowing for a simpler design of the expansion machine. On the contrary, high molecular mass affects negatively the heat transfer coefficients [11].

The other factors that should influence the selection of the working fluid in a specific application are briefly discussed in the following.

- Vapor density: a higher vapor density is associated to higher volume flow rates in the low pressure side of the ORC cycle, that require larger sizes of the heat exchangers to limit the pressure drop. This obviously has an impact on the system costs.
- Low viscosity and high conductivity, that are related to high heat transfer and low pressure losses in the heat exchangers.
- Evaporation and condensing pressure: increasing the maximum pressure of the cycle increases the system complexity and costs. Keeping the condensation pressure above the atmospheric pressure allows to avoid the air infiltration into the circuit.
- Safety class: some of the fluids employed in ORC applications have levels of toxicity and/or flammability not negligible. If a toxic or flammable fluid is selected, a higher capital cost related to additional safety systems must be considered. The safety classification is given by the ASHRAE Standard 34, which provides for a designation of each fluid made by a letter (A or B, for non-toxic and toxic substance respectively) and a number (1, 2 or 3, depending if the fluid is not flammable, has low flammability or high flammability, respectively).
- Null Ozone Depletion Potential (ODP) and low Global Warming Potential (GWP): non-null ODP fluids have been banned under the Montreal Protocol. Working fluids with high GWP (higher than 750) are progressively being phased-out in the European Union.

- Availability and costs: differently from the case of water, the availability and cost of organic fluids needs to be evaluated. For some fluids, the total cost of the fluid charge is not negligible in the capital cost of the plant.

Table 1-1 collects the different families of fluids employed in ORC systems, with a non-comprehensive list of commonly used fluids and their main properties, extracted from REFPROP library. The non-null ODP fluids (CFC and HCFC) have been omitted. The hydrocarbons (HC) are distinguished in alkanes, aliene and alkynes, alcohols. They cover a large range of critical temperatures, even if they are more suitable for medium to high temperature ORC. Their GWP is very low or null, but generally they are flammable. Among the refrigerant family, the hydro-fluoro-carbons (HFC) have dominated the refrigeration market during the last two decades. They are characterized by good performance in the medium-low temperature ORC and good safety class, but also by high values of the environmental index GWP. The hydro-fluoro-olefines (HFO) are a new type of fluids that entered the market during last years, in order to replace the currently widespread HFC. The HFO presents very low GWP, but some of them involves flammability issues. To help the transition to substitute fluids, several mixtures of HFC and HFO have been proposed, in order to reduce the typical high GWP of HFC and the non-null flammability associated to HFO. The refrigerant mixtures are distinguished in a-zeotropic (with constant vaporization temperature) or zeotropic (with a glide non-null glide) mixtures. Finally, the siloxane are most suitable for high temperature ORC plants. They have the advantages of being clean (GWP = 0) and of low evaporation pressure. On the contrary, they are subject to air infiltration issues due to low condensing pressure (below the atmospheric pressure), and also they are in general flammable.
Several studies have been published on the comparison of different working fluids. Nearly comprehensive reviews of working fluid for organic Rankine cycle are reported in [12], focused on solar thermal applications, and in [13]. Eyerer et al. performed an experimental investigation of a micro-scale ORC system working with HFO-1224yd(Z) and HFO-1233zd(E) as low GWP replacement for HFC-245fa They observed the highest thermal efficiency with HFC-1233zd, but the maximum power output was obtained with HFC-245fa [14]. Feng et al. conducted a thermo-economic optimization of low grade ORC using HFC-245, toluene and their mixtures as working fluid. They found that the thermodynamic performance is reduced with mixtures with respect to the pure fluids. The net power output and the total required heat transfer area first decrease with the HFC-245fa mass fraction, to a minimum corresponding to about 40% of HFC, to increase up to the maximum corresponding to the use pure HFC-245fa [15]. Bamorovat Abadi and Kim investigated the performance of binary zeotropic mixtures for ORC applications. They concluded that zeotropic mixtures can perform better in terms of first and second law efficiencies, due to the potential match with the heat source temperature profile. However, they deduced that each application should be evaluated, since no general rules can be provided for the selection of a mixture instead of a pure fluid [16]. Bianchi et al. simulated the behavior of a reciprocating expander in case of replacement of HFC-134a with HFO-1234yf and HFO-1234ze(E). The model results were validated only in the case of HFC-134a. The comparison highlighted that the best performance is obtained with HFC-134a, while between the two olefins, HFO-1234yf performs better in case of same superheating degree [17].

Table 1-1 – Main thermodynamic characteristics of organic fluids [18].

Family		***Fluid***	***Critical temp. [°C]***	***Critical press. [bar]***	***GWP***	***Safety class***
Hydrocarbons (HC)	Alkanes	Propane	96.7	42.5	4-6	A3
		butane	152	38		A3
		pentane	197	33.7		A3
		Octane	296	25		NA
		Dodecane	385	18.2		NA
		Cyclo-pentane	239	45.7		NA
	Aliene and alkynes	1-butene	145	40.1	0	NA
		benzene	289	49.1		NA
		Methyl-benzene	319	41.3		NA
	Alcohols	Dimethyl ether	127	53.4	4-6	NA
		Methanol	240	82.2		NA
		Ethanol	242	62.7		NA
Refrigerants	Hydro-fluoro-carbons (HFC)	HFC-125	66	36.2	3500	A1
		HFC-32	78.1	57.8	675	A2L
		HFC-134a	101	40.6	1430	A1
		HFC-152a	113	45.2	124	A2
		HFC-245fa	154	36.5	1030	B1
	Hydro-fluoro-olefines	HFO-1234yf	94.7	33.8	4	A2L
		HFO-1234ze	109	36.3	6	A2L
		HFO-1233zd	166.5	36.2	1	A1
	Mixtures	R452A (30% HFO-1234yf – 59% HFC-125 – 11% HFC-32)	74.9	40	2140	A1
		R513A (56% HFO-1234yf – 44% HFC-134a)	96.5	37.7	631	A1
Siloxanes		MM	245.5	19.4	0	NA
		MDM	291	14.2		NA
		MD2M	326	12.3		NA
		MD4M	380	8.8		NA

1.3 Micro-Organic Rankine Cycle

Micro-scale organic Rankine cycles are characterized by a power output lower than 50 kW. It was assessed that, in Europe, the market potential of the application of ORC-based micro-cogeneration systems to the residential sector is considerable [19]. They find their field of application in the residential or small commercial sector, present some peculiarities that distinguish them from large scale applications.

1.3.1 Micro-ORC applications

ORC systems with low power output are suitable for a multitude of application, both under stationary and dynamic conditions of the heat source. As mentioned, micro-cogeneration or micro-trigeneration systems (CHP – Combined Heating and Power and CCHP – Combined Cooling, Heating and power, respectively) may be viable solutions for resolving the issue of the electrification of rural areas. A CHP equipped with an ORC system has the possibility to supply, for example, an isolated house by using renewable energy sources (like solar thermal, low temperature geothermal, biomass, or a combination), providing both thermal and electrical energy continuously. In the following, the main applications of micro-ORC systems are briefly described.

Biomass-fired ORC systems

The valorization of biomass as energy source can occur in two ways: 1) transforming the biomass into a fuel, liquid or gaseous, and then burning the bio-fuel in internal combustion engines or in gas turbines; 2) burning directly the crude or densified solid biomass in a boiler, that works as the vapor generator of a Rankine cycle (see Figure 1.9). The combustion of biomass, regardless of the type of biomass and the mode of cultivation, provides for a power system able to work continuously in a controlled way [19]. Currently, the major part of biomass-fired energy systems are in the medium-scale field, with size ranging between 500 kW and 2 MW, and mostly work with binary organic Rankine cycle using intermediate heat transfer (IHT) fluid. Indeed, the implementation of direct heat transfer (DHT) in small size power plants is also under development. It was demonstrated that the most efficient way to exploit biomass sources is the combined production of heat and electric power (CHP), with overall efficiency (thermal + electric) higher than 80% and ORC electric efficiency between 15-18% [20]. The most applied working fluids are silicon oils, but in some cases with high power output hydrocarbons are employed, due to the lower volumetric flow rate at low pressure.

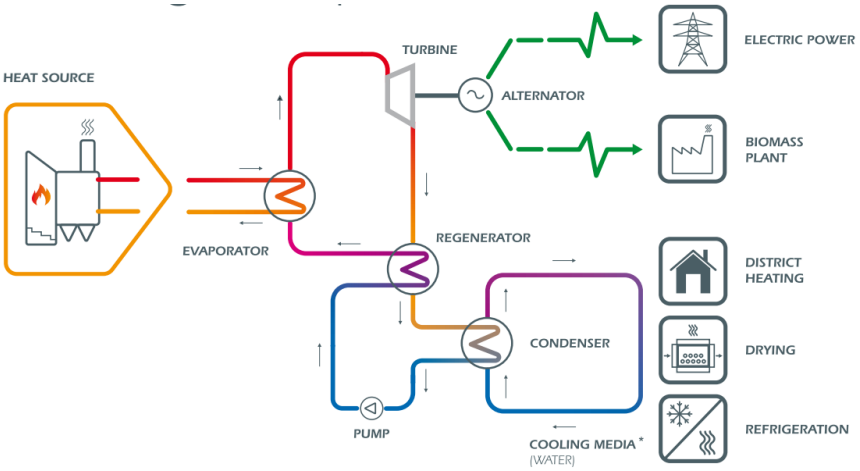

Figure 1.9 - Biomass fired power plant [21]

Biomass micro-CHP system based on organic Rankine cycle are a viable solution for electricity and heat supply in rural areas. Moreover, biomass burner can also be used as back-up system for renewable intermittent energy sources, such as solar thermal power, to supply the energy demand during nighttime and cloudy days, or to boost the power output during peaks of demand.

Solar thermal cycle

In solar thermal cycles, the sun radiations are used as thermal source for the vaporization of the ORC working fluid, which is then expanded in a turbine to produce electrical power. The main components of a solar thermal system are:

- solar receiver;
- reflector;
- intermediate heat transfer circuit;
- thermal storage;
- additional heat source;
- power cycle (Rankine cycle, ORC, Stirling).

The reflector may not be present in some installations with low capital costs. As in other applications, both the direct heat transfer (DHT) and the intermediate heat transfer (IHT) circuit are possible configurations for the heat supply loop. Using simple flat collectors with evacuated tubes, the maximum temperature achievable in the receiver is around 150 °C. By using particular systems for concentrating the solar radiation into a focus line (or point), temperatures up to 1000 °C may be achieved. In this case we talk of concentrating solar power (CSP) system. However, the cost of the reflector increases substantially with the target temperature, being in most cases convenient only for large solar fields. The types of reflectors can be distinguished between line focus and point focus (Figure 1.10). Line focus systems, such as parabolic trough collectors (PTC) and linear Fresnel reflector (LFR), are able to achieve maximum temperatures up to 800 °C and 300 °C for PTC and LFR respectively [22]. Usually a solar tracking system changes the angle of the mirrors on one axis depending on the inclination of sunrays. Point focus reflectors, like parabolic dishes and solar tower, work with maximum temperatures up to 1000 °C, but require more complex tracking systems, moving on two axis. Among the above-mentioned solar technologies, flat collectors, Fresnel reflectors and parabolic trough are the most appropriate for small solar fields coupled with small-scale ORC systems. The solar receiver of line focus solar collectors consists of a pipe, or series of pipes, in which the heat transfer fluid (or the ORC working fluid, in case of DHE) flows, absorbing the heat from the solar radiations that are concentrated on the receiver. The day-night intermittency of the solar radiation, as well as its dependency from the weather conditions, make the CSP plant suffer of low capacity factor. To partially overcome this limit, generally a thermal energy storage (TES) is installed, allowing to accumulate the surplus of thermal energy collected during sunny periods, to be used when the sun is not shining. The most employed solution for TES in low temperature solar system is based on two thermally isolated tanks ("hot" and "cold" tank), which are installed in line with the heat transfer fluid supply pipes. The IHT fluid can be pressurized water, thermal oil or molten salts. However, the current size of the state-of-the-art technologies for TES systems is much lower than that required to use the power plant as standalone facility for continuous electricity supply. To overcome this limit, besides the implementation of the thermal energy storage, the integration of a backup combustor is an option to increase the capacity factor of the facility, improving its dispatchability and potentially making the plant suitable for operating as a base load or as standalone facility. The combustor, which can be fed with biomass or with natural gas, is placed downstream the solar receiver to provide, in case of scarce solar radiation, the needed thermal input for the vaporization of the working fluid of the Rankine cycle. In case of high electric and/or thermal demand during sunny days, the additional combustor can be activated to boost the power output [23].

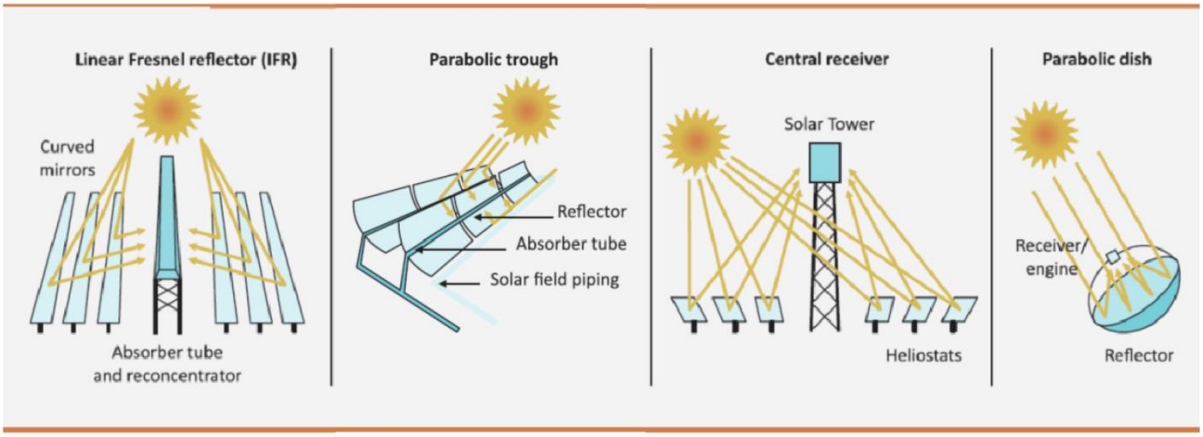

Figure 1.10 – The types of reflectors: line focus and point focus.

ORC-based solar thermal systems, with or without complex concentrating technologies, has not entered the market of the micro-scale generators yet. Indeed, in order to achieve comparable performance with photovoltaic (PV) panels, the CSP system should work at high hot source temperatures that require the installation of sophisticated reflectors, which are characterized by high cost [12]. This makes CSP not competitive with PV within the smallest scale. Nonetheless, solar thermal technology presents some advantages versus photovoltaic, first of all the possibility to employ the solar ORC in a CHP or CCHP arrangement, using the solar energy to supply heating, cooling and electric demand. To realize a stand-alone plant, able to operate in non-electrified areas, a thermal storage and a backup system should be included. A general representative layout is shown in Figure 1.11, including an intermediate heat transfer with two tanks for thermal storage and a backup combustor.

Garcia-Saez et al. investigated the techno-economic performance of a solar ORC CHP system for residential sector. They considered pressurized water as heat source medium, with temperature up to 140 °C, achieved thanks to the solar radiation. As working fluid, they tested three HFC (R-245fa, R-134a, R152a) and one hydrocarbon (isobutane). The payback values they calculated in case of installation in the north and in the south of Spain resulted, respectively, 4.4 and 3.8 years [24]. Another example of study conducted on micro-scale applications of solar ORC is reported in [25], and regards the integration of solar collectors, a micro-ORC system and an adsorption chiller, as main components of a trigeneration system for a single house within the near zero energy building (NZEB) concept. The existing prototypes of the ORC system and adsorption chiller were integrated only at model level, to assess how they perform in CCHP arrangement.

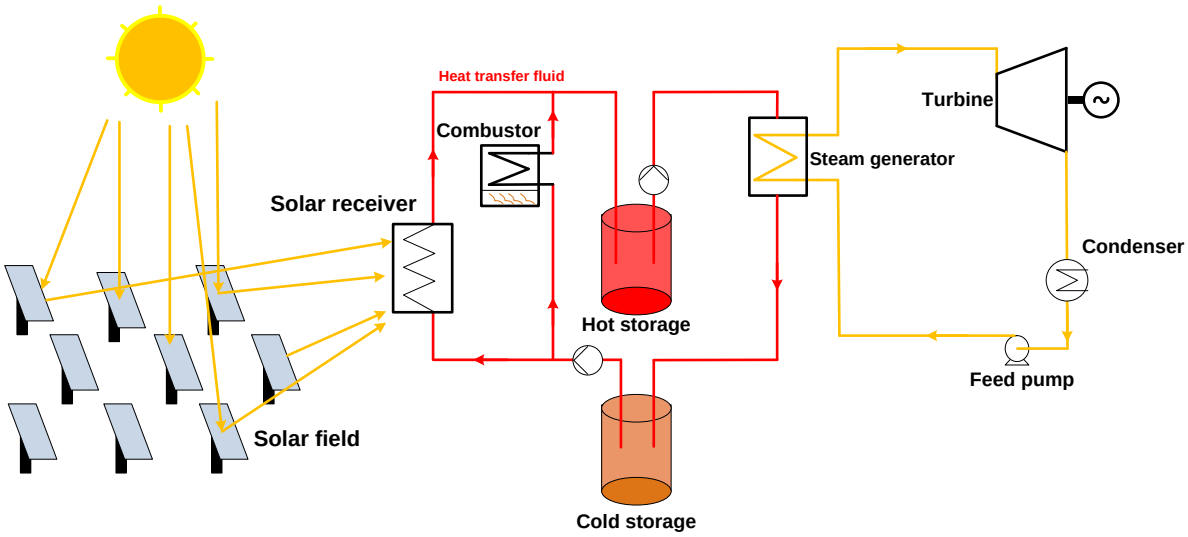

Figure 1.11 - Schematic layout of a Solar driven ORC cycle.

Low temperature geothermal binary cycle

Geothermal energy has the characteristic of being stable continually, regardless of the weather conditions, with no need of additional storage system. Geothermal resources are uniformly distributed on the planet, although different areas have different characteristics of the geothermal well. Based on the temperature level of the geothermal source, three categories have been identified: shallow geothermal energy (low temperature), hydro-geothermal energy (low-medium temperature), and hot dry rock (high temperature). Another classification regards the nature of the geothermal fluid: in vapor-dominated systems, the steam exits from the geothermal well and is sent directly to a turbine to produce electricity. In water-dominated systems, the mineral laden hot water, also referred as "brine", can be used directly to produce electricity in flash cycles, or is circulated into heat exchangers to transfer thermal power to a secondary fluid (binary cycle). The majority of the geothermal sources available worldwide are low-enthalpy water dominated wells with brine temperature lower than 150 °C. Most of these sources are employed for direct use of the thermal energy for heating purpose. The conversion into electricity of this kind of energy source, generally, occurs in binary cycles by means of organic Rankine cycles (ORC) [26]. The thermal efficiencies obtainable through geothermal ORC systems are generally lower than 15%, due to the limited temperature level of the heat source, that results in a low value of the equivalent Carnot cycle efficiency.
The layout (see Figure 1.12) and working principle of geothermal ORC are substantially similar to those of the other applications: the geothermal fluid (pressurized water) supplies the evaporator of the ORC, directly or with intermediate heat transfer fluid. Suitable working fluids are either HFC (R-134a, R-245fa) and hydrocarbons (isobutane, butane, isopentane, pentane), characterized by critical temperature ranging between 100 °C and 200 °C. The regeneration is not always present in low temperature application, as its installation has to be evaluated for each case, considering a balance between the benefit of the thermal recovery and the drawbacks, which are the increase of pressure losses and pump consumption, the decrease of turbine specific work and the increment of cost and plant complexity [27]. Just like the other micro-scale systems, the geothermal micro-ORC suffers from the scale effect on the costs of installation, especially the cost related to the drilling of the well and to the realization of the supply and discharge pipelines. The latter increases when high distances have to be covered with the geothermal heat source.

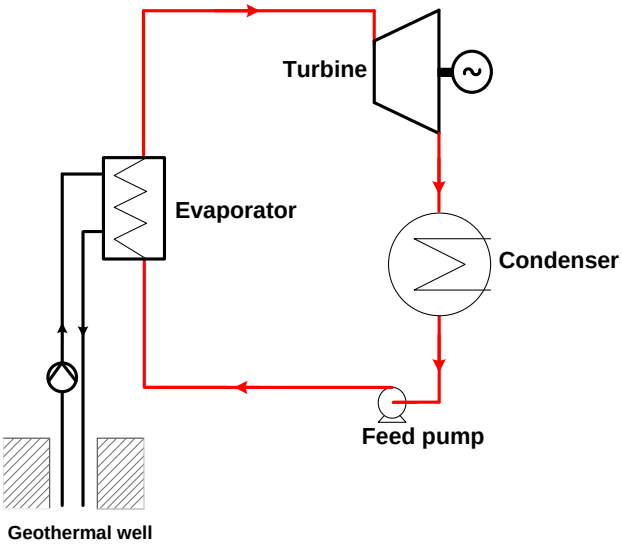

Figure 1.12 – Schematic layout of a geothermal binary cycle.

Waste heat recovery (ICE, MGT, steam cycle)

The last category is the waste heat recovery (WHR), which refers to a large number of applications that cover a wide range of small sizes and of heat source temperatures. It was estimated that currently about 50% of the world's energy generation is wasted as heat, despite in many cases the systems discharge a significant amount of good-quality energy (i.e. at high power and temperature) [7]. A typical example of potential for waste heat recovery regards the internal combustion engines employed in transport sector. On average, of the energy introduced with the fuel, about one third is wasted to the exhaust gases (EG) and one third to the cooling system. The exhaust gases provides for a high-quality energy flow, being characterized by high mass flow rate and high temperature (250-500 °C). With temperatures higher than 400 °C, water steam can be used with direct heat transfer, otherwise intermediate thermal oil circuit is required, to avoid exceeding the limits of thermal stability of the organic fluids, and to prevent risks of fire due to the flammability of most working fluids suitable for high temperature, such as hydrocarbons. The heat recovered from the engine cooling water can be considered a medium-quality energy source, since it is characterized by high mass flow rate and low temperature (80-90 °C).
The configurations conceived so far present substantial differences between them. If the heat is recovered only from exhaust gas, a simple configuration can be implemented, with an evaporator, an expander, a condenser, a fee-pump and, possibly, a recuperator. For the condenser, different solutions can be implemented, such as an air condenser with a fan, or the engine cooling water circuit with a heat exchanger. The latter option has the disadvantage of increasing the condensation pressure of the ORC cycle. If the heat is recovered both from exhaust gases and cooling water, the ORC layout assumes more complex architectures, such as the one shown in Figure 1.13, developed as WHR system from a diesel engine used in light-duty trucks application [28]. It is built in two circuit: one at low temperature, consisting in an evaporator (Evaporator2 in the figure), supplied by the engine cooling water, an expander, an air condenser, a pump and two stages of preheating: one is in the Intercooler, the other in the Preheater. The Preheater works also as condenser for the high temperature loop, whose other components are a pump, an evaporator supplied by the exhaust gases and the expander (Expander1). As working fluids, HFC-134a and HFC-245fa are used in the low temperature and in the high temperature loop, respectively.

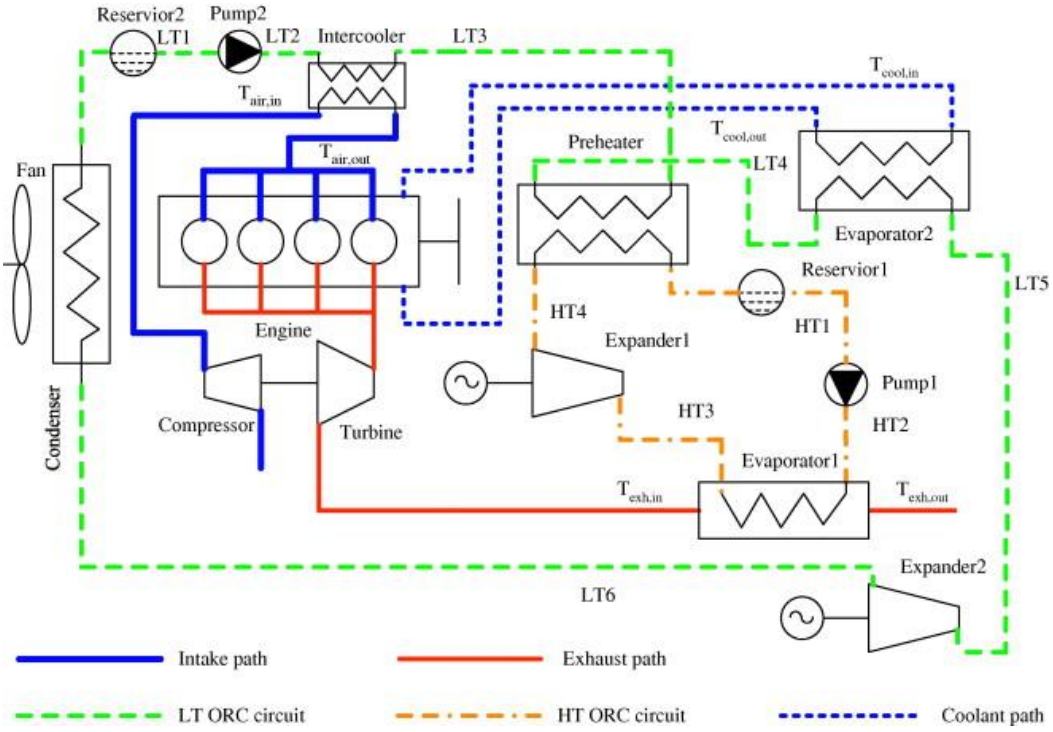

Figure 1.13 – Novel layout of ORC-WHR for diesel engine [28]

Another field of application of exhaust gas heat recovery is the micro-gas turbine (MGT). Indeed, with small to large scale gas turbines (1-300 MW), the heat recovery by water steam Rankine cycle is generally preferred, due to the high value of the GT exhaust temperature (up to 600 °C), forming the combined cycle gas-steam. Micro-gas turbines, on the contrary, due to the lower turbine inlet temperature and the use of a recuperator, are characterized by lower temperature of the exhaust gases (200-350 °C), more appropriate for the employment of organic Rankine cycles.

1.3.2 Micro-ORC components

The description of the main components of the ORC system is here focused on the micro-scale, for which some peculiarities, regarding the selection of the appropriate equipment, can be worth of some mention. In the following sub-sections, basic information are provided regarding the expander, the feed-pump and the heat exchangers, usually employed in micro-ORCs.

Expander

The expansion machine is probably the most important element of the ORC systems. Its performance strongly affects that of the whole cycle, and it is a fundamental component for the control of the system. The expansion machines are generally distinguished in two categories:

- Turbines
  The working principle of dynamic expanders (the turbines) is based on a first acceleration of the working fluid that enters the turbine stator at high pressure, transforming the pressure energy in kinetic energy. Then, the kinetic speed is transferred to the rotor, transforming the kinetic energy in shaft power. Turbines can have multiple stages, each consisting in one stator and one rotor. There are two types of turbine, axial (with high capacity) and radial turbines.

- Positive displacement (or volumetric) expander
  The energy conversion in displacement expanders is based on the decrease of the working fluid pressure due to the increase its volume. In volumetric expanders, the rotors (whatever their geometry is) defines a series of chambers where the fluid is confined. The high pressure fluid forces the rotors to move, transferring mechanical power to the shaft, to which the rotors are connected. The increase of the chambers volume makes decrease the pressure, and the fluid that has transferred its energy to the shaft flows through the discharge port.

Positive displacement type is generally the preferred solution for the expansion machine of ORC system with power output lower than 150 kW. They differ from turbines for lower flow rates and rotating speed. The technological maturity of displacement expander is largely lower than that achieved for compressors used in refrigeration or compressed air industries. For this reason, many applications adopts displacement compressors opportunely modified to work in reverse mode. In other cases, prototypes have been developed specifically for the applications. The geometry that have been used for volumetric expanders are several, but the most applied are the scroll, the screw, the piston and the vane expanders. They differs by their mechanical working principle, the presence of valves, the need of lubrication, and the available built-in volume ratio. The latter is a parameter defined for the machines in which an internal expansion occurs, as the ratio between maximum to minimum values of the volume of fluid in the expander chambers. The maximum volume corresponds to the total displacement of the machine, while the minimum is usually referred as the clearance volume. In the following, the most adopted models of volumetric expanders are briefly described. Comprehensive reviews of volumetric expanders used in small scale ORC systems have been published in [29], [30], [31].

The **scroll expanders** is in general the most adopted expansion machines in ORC with size lower than 5 kW. The main elements of scroll expanders are the two spirals, namely the orbiting and the fixed scrolls. Their relative position defines the fluid working chambers, their built-in volume ratio ranges between 1.5 and 5, with maximum pressure ratio up to 15. There are basically two types of scroll expanders: compliant and kinematically rigid. Compliant expanders provide for a degree of freedom in a given direction, to let the expander adapt to the operating conditions, improving its performance; kinematically rigid machines do not allow for any movement of the scrolls, and its efficiency results lower. The main advantage of the scroll expander is its simplicity, as it is composed by a low number of moving parts. Therefore, its cost is relatively low and it does not require maintenance. Moreover, scroll expander are often derived from compressors, which are very established and widespread in the HVAC & R market. Finally, compliant version are able to work in conditions of wet expansion. On the contrary, the maximum fluid temperature at the scroll expander inlet is limited to about 200 °C, due to the increase of internal leakage with higher temperatures. Also, high pressure ratios lead to a detriment of the performance, due to under-compression losses [30].

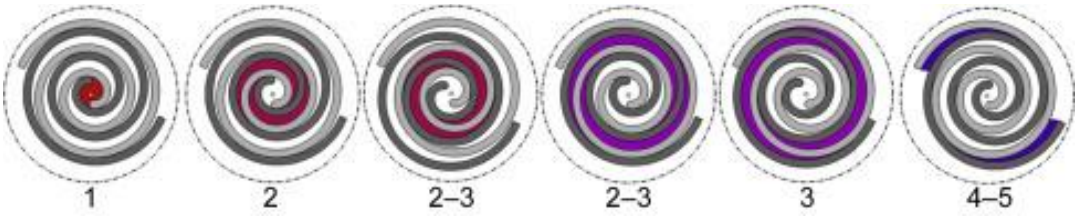

Figure 1.14 - Scroll expander operating phases.

The **screw expanders** are distinguished in single and twin screw machines (see Figure 1.15). The latter is the most adopted configuration in literature studies, even if some analyses have regarded single screw expanders (see for example [32] and [33]). They are suitable for micro-scale ORC systems larger than 10 kW, and cases of screw machines employed in power plant with size up to 1 MW. The smallest size (0-10 kW) is not suitable for screw expanders, due to the need of high machining precision and higher leakage losses. Twin screw expanders consist of two helical rotors (male and female) placed in a case. The space between the rotors and the case defines a series of chambers in which the fluid is trapped. As the male rotor moves, the chambers' volumes first increase to a maximum and then decreases to zero. Supply and discharge ports are located at the two extremities of the rotors.

Twin screw expanders can gain benefit from wet expansions, since the liquid helps to limit fluid leakages through clearances.

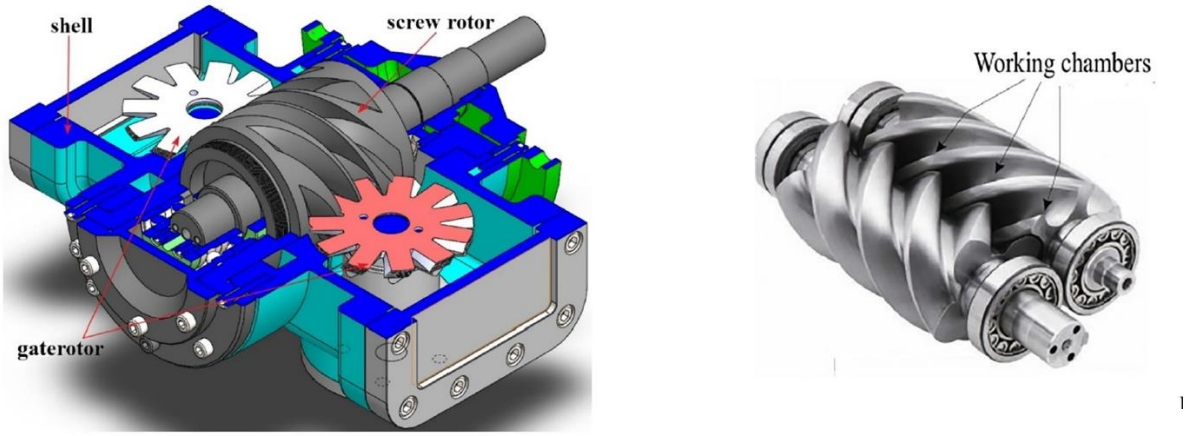

a) b)

Figure 1.15 - a) single screw expander prototype presented in [33]; b) twin screw expander.

The **vane expander** is characterized by being simple, economic, able to deliver high torque with high volumetric efficiency, and to operate at relatively high pressure [29]. It consists of a housing, a rotor and several vanes connected to the rotor as shown in Figure 1.16. The edge of the vanes is pushed against the housing surface, defining the working chambers. The pushing mechanism can be either made by springs or by the working fluid pressure [34]. There is an offset between rotor axis and housing axis, which determines a variation of the chambers volume as the rotor rotates. The actual expansion occurs as soon as the chamber leaves the communication with the suction ports, and ends when the chamber sees the discharge port. The main drawback of vane expanders is the maximum temperature, which is limited to about 150 °C. Pressure ratio can vary from 3 to 7, while the volume ratio is adjustable by changing the time of contact of the chambers with the inlet and outlet ports [30].

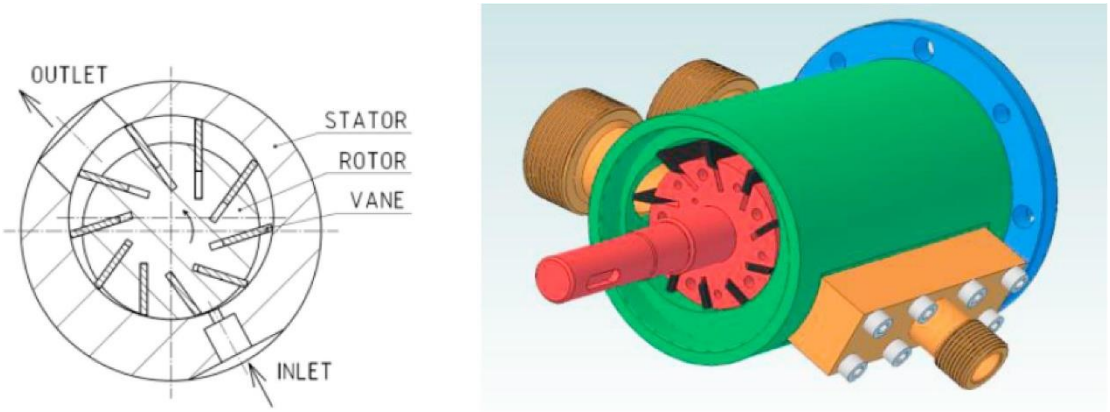

Figure 1.16 – Vane expander details [58].

Piston expanders can have several architectures, which results in slightly different working principles among the different models. First, piston machines are classified by their movement mechanisms: rolling piston and reciprocating piston expanders. The working principle of the rolling piston machine is depicted in Figure 1.17 a): a piston rotates inside a cylinder with an eccentric rotor. A sliding vane separates the high pressure from the low pressure chambers, which are connected to the inlet and outlet port, respectively. This type of expanders have a

simple structure mainly made of cylindrical elements, requiring simple manufacturing and low cost. Moreover, they can work without any lubrication, since the rotating speed is relatively low, and can tolerate high inlet pressures and temperature [35]. Reciprocating piston expanders can also present different architectures, having in common the expansion mechanism: the high-pressure fluid enters the cylinder and expands pushing against a piston that moves from the top dead center (TDC) to the bottom dead center (BDC). After the expansion, the fluid is discharged as the piston moves back from the BDC to the TDC. The inlet and outlet fluid ports are equipped with valves that regulate the admission and discharge of the fluid. The most common configuration consists of one or more single-effect pistons connected to the same crankshaft, moving inside as many cylinders with valves on the top. In other cases, free linear expanders are employed ([36], [37]), in which the reciprocating movement is not converted in rotation but is transformed in electrical energy by means of linear generators. In the application described in [36], the mechanical power produced by the linear piston expander is used directly to supply a water piston pump.

Piston expanders are characterized by high reliability, low maintenance, high built-in volume ratio, and low rotational speed. In most cases, piston expanders are employed with medium-to-high temperature heat sources, since they are able to exploit high pressure ratio and to tolerate high temperature of the working fluid. However, an example of piston machine applied to a pilot plant for low-grade geothermal well was reported in [38], where relatively good performance of the system were reported with geothermal brine temperature lower than 60 °C.

Currently, there are only few manufacturers that provide expansion devices specific for micro-scale organic Rankine cycle, most of which are original equipment manufacturers (OEM). Often, the expanders are designed for working with specific fluids and conditions, that may not be optimal for each application. The lack of many alternatives for these devices in the current market is caused by the non-maturity of the technology for the lowest scale.

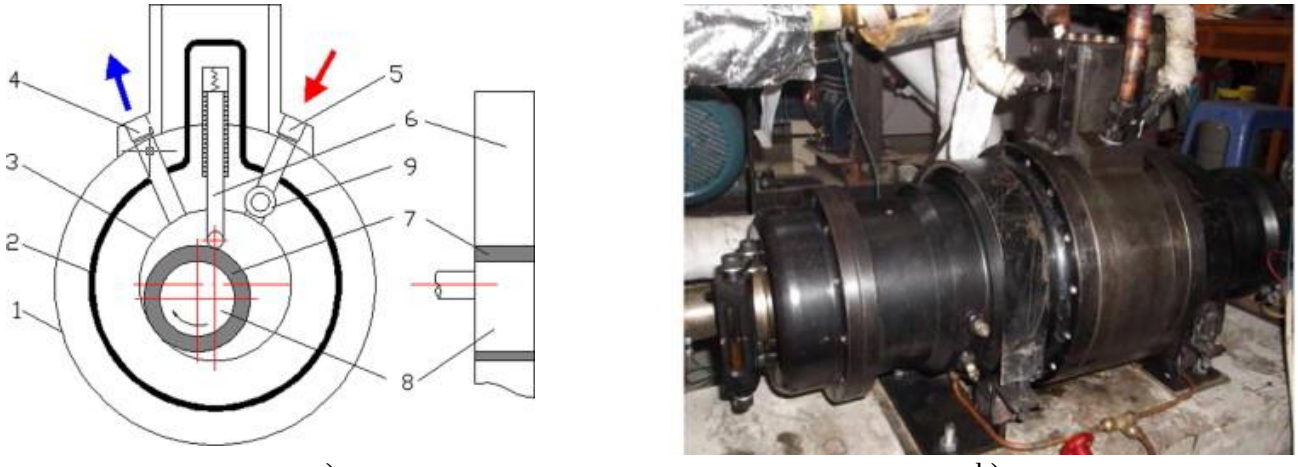

a) b)

Figure 1.17 – a) Rolling piston expander architecture; b) Photo of rolling piston expander (both images from [35]).

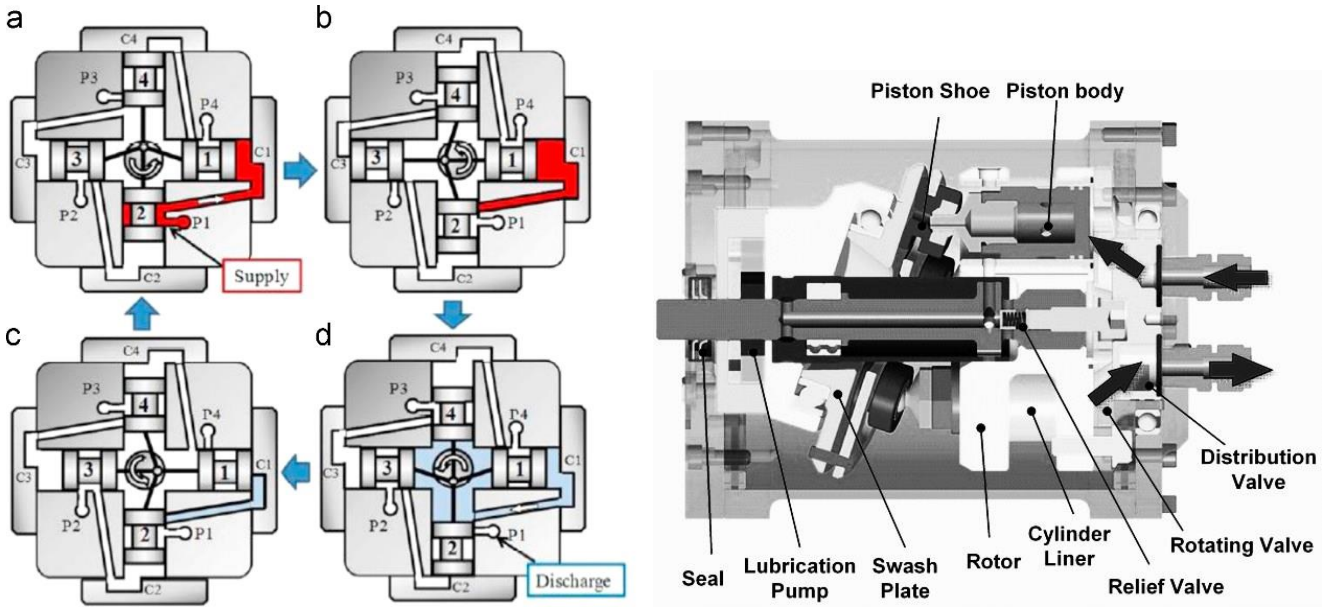

a) *b)*

Figure 1.18 – Typical architectures of radial piston expander (a), and swash plate piston expander (b).

Feed-pump

The role of the feed-pump in organic Rankine cycle systems is to pump the working fluid from the ambient at low pressure (condensation pressure) to another at high pressure (evaporation pressure). The pump is generally used for controlling the mass flow rate of the working fluid. In many cases, the pump selected for micro-ORC are of displacement type, meaning that the flow rate is proportional to the pump speed, otherwise centrifugal pumps are used. Among volumetric pumps, the most used models are the piston, gear, diaphragm and vane pump. Figure 1.19 shows the schematic of the architectures and working principle of the volumetric pumps for ORC systems. Differently from the large-size water steam Rankine cycles, where the pump consumption is considered nearly negligible with respect to the system power output (around 0.5-2%), and from large scale ORC system (1-10%) the feed-pump in small scale ORC is a critical component, as its operation can consume significant fraction of the system power output. Therefore, it requires a careful selection and sizing process during the design of the plant. The impact of the pump on the overall cycle is depicted by the Back Work Ratio (*BWR*), defined as the ratio of the pump power to the expander power output. It can be demonstrated that the *BWR* is influenced by the critical temperature of the working fluid (the higher T_{cr}, the lower *BWR*), and by the evaporation temperature, increasing with T_{ev} especially if there is a low difference between critical and evaporation temperatures [10]. Another factor of losses in the micro-ORC pump operation is the electric motor, whose efficiency can be low in case the motor is oversized. Therefore, the pump efficiency becomes a crucial parameter to optimize in order to reduce the penalization on the net power output of micro-ORC systems. An additional issue in the feed-pump operation is the phenomenon of cavitation, which should be always avoided in order to maintain good performance and to guarantee longer operating life of the machine.

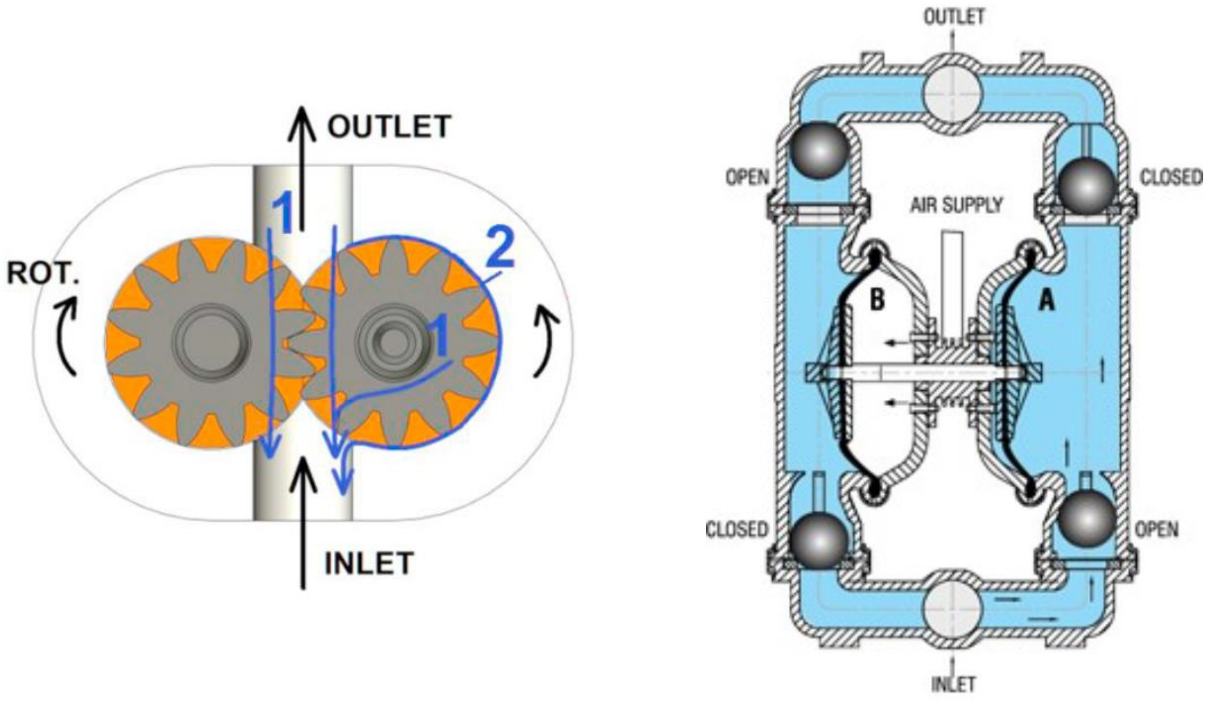

a) *b)*

Figure 1.19 – Operating schemes of volumetric pumps for ORC systems: a) external gear pump [39]; b) multi-diaphragm pump.

Different studies have reported the performance of the feed-pump implemented in experimental micro-ORC units. For example, Quoilin et al. [40] achieved a pump total efficiency of 25 %, while Reid et al. [41] report a value of 7 %, both in kW-scale ORC units. In [42], Landelle et al. collected from literature several ORC pump efficiency data as function of the hydraulic power. They observed that the average efficiency is around 35 % for small ORC power plants, but it is not specified if the electric losses are always included into the efficiency calculation.

Heat exchangers

The heat exchangers of micro-scale ORC systems are, as in large plants, the evaporator, the condenser and the recuperator. Even though they are well-known components, their selection and design deserve particular attention since they represent a significant share of the cost of installation. Among the heat exchangers, the evaporator is the most critical to implement, as it must work with high temperature, and so can be subject to fouling and corrosion. As mentioned in working fluid section, differently from water, organic fluid allows for the employment of once-through evaporator, avoiding the use of more complex heat recovery steam generator (HRSG), in which the two-phase mixture is separated in a boiling drum, as that required by water Rankine cycles. Therefore, the evaporator in micro-ORC system consist only of a heat exchanger, which should comply with dimensions constraints and still work with high heat transfer effectiveness. Most adopted type of heat exchangers for small applications is the brazed plate (Figure 1.20), which shows good advantages in terms of compactness, weight and performance. The shell-and-tube configuration, very common in the medium-to-large size plants, can also be found in micro-scale field. It works with one fluid flowing inside the pipes and the other filling the shell of the heat exchangers. Shell and tube HE is often used as condenser, with the water flowing into the tubes and the working fluid condensing in the shell. To increase the heat transfer surface on volume ratio, the shell and tube can be provided with more than one passage (2 or 4 mostly). Other types of heat exchangers that have reported in the literature are the fin and tube heat exchanger, mostly used as evaporators for heat recovery from flue gases [43], and the shell and plate configuration [44], represented schematically in Figure 1.22 a) and b), respectively.

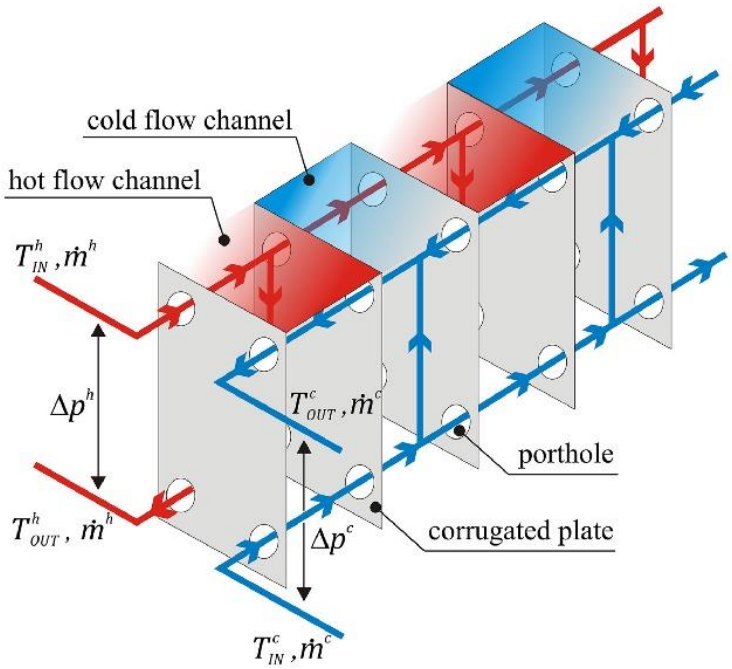

Figure 1.20 – Working principle of brazed plate heat exchangers.

Figure 1.21 – Brazed plate with different channel shape: a) conventional chevron type; b) microplate type.

Figure 1. 1-

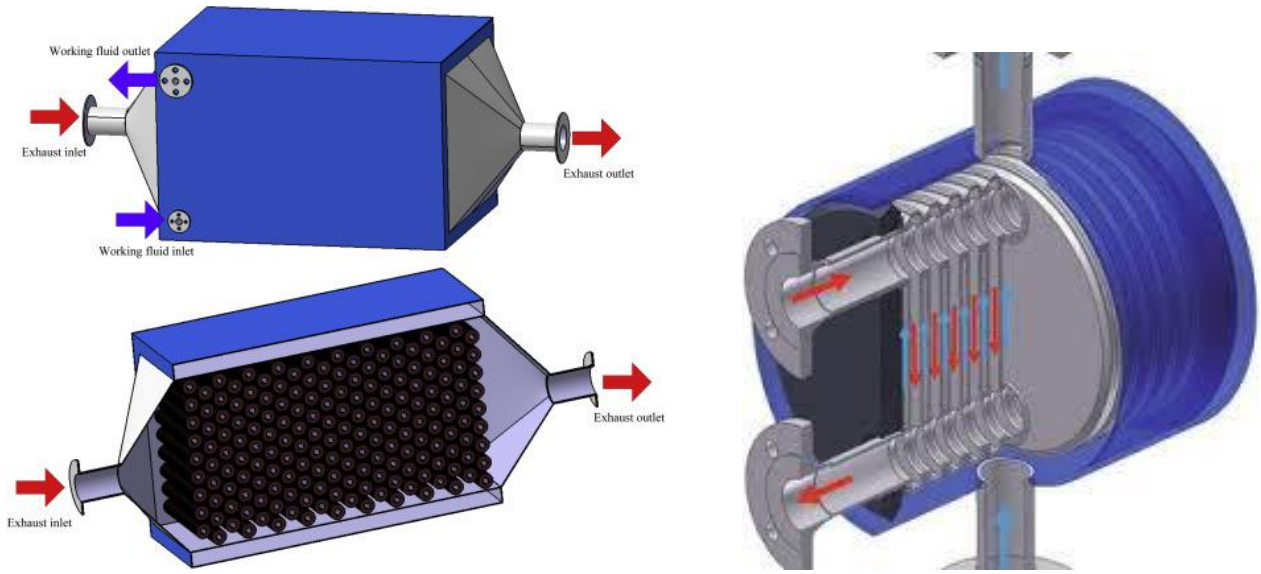

a) *b)*

Figure 1.22 – a) Fin and tube heat exchanger; b) plate and shell heat exchanger.

1.3.3 Market overview

The total installed capacity of ORC technology is close to 3 GW, distributed over almost 1800 units. The leader among the ORC manufacturers is ORMAT, with 62.9% of total installed capacity, followed by Turboden (13.4%) an Exergy (11.1%). Other companies active in the field are Triogen, TAS, General Electric, Adoratec / Maxxtec, GMK. In terms of capacity, the most adopted application is the geothermal binary plant (75%), mainly related to large scale ORC units (tens of MW). Waste heat recovery and biomass follow with a share around 14% and 11%, respectively, mostly distributed in a large number of small-medium plants [45]. Figure 1.23 shows, for geothermal, biomass and WHR applications, the number of installed ORC plants versus the size of the unit.
The solar share in the ORC market is still very small, mainly due to the high investment costs associated to the concentration technologies, that make the employment of photovoltaic panels more convenient. Nevertheless, Turboden has currently under operation two medium solar ORC plants in Italy and Morocco, with size of the power units equal to 600 kW and 2 MW, respectively, while other projects are under construction [46]. Within the niche of micro-scale ORC system, some examples of manufacturer active in the market are: Air Squared (US), which provides for a plug and play 1-kW unit (Figure 1.24a) working with R245fa and scroll expander [47]; Rank (ES) commercializes micro-ORC units with power from 1 kW to 80 kW, suitable for different heat source temperature, using a self-developed low-speed turbine [48]; the smallest ORC system produced by the French company Enogia has a power output of 10 kW, and works with olefin R1233zd and high-speed micro turbine [49]; Visorc (FI) produces ORC systems based on high-speed turbo-generators with power output ranging between 10 kW ad 50 kW [50]; the American ElectraTherm provides for low temperature (70 °C – 150 °C) ORC facilities with power output from 20 kW to 80 kW [51]; the Italian Zuccato Energia develops its smallest unit with a power output of 30 kW (Figure 1.24b), suitable for a minimum heat source temperature of 95 °C [52].

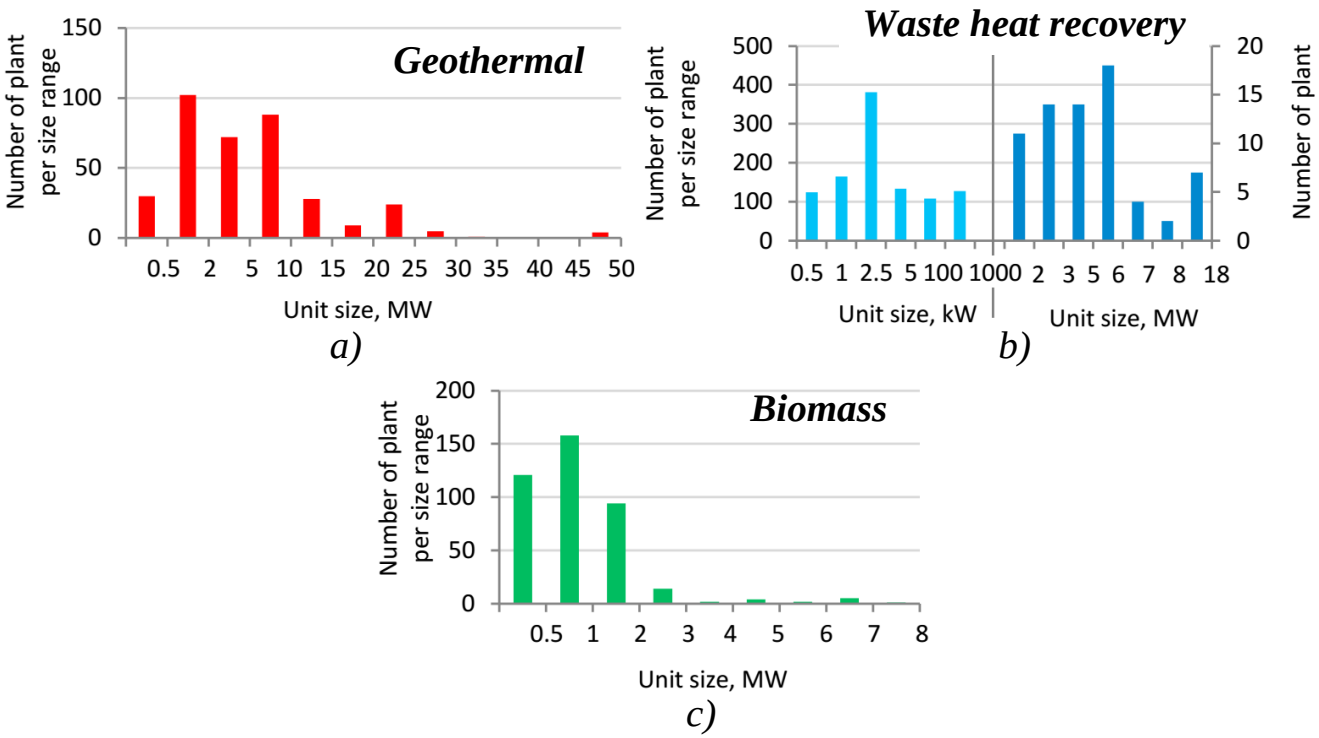

Figure 1.23 – Distribution of the installed ORC capacity per application [45].

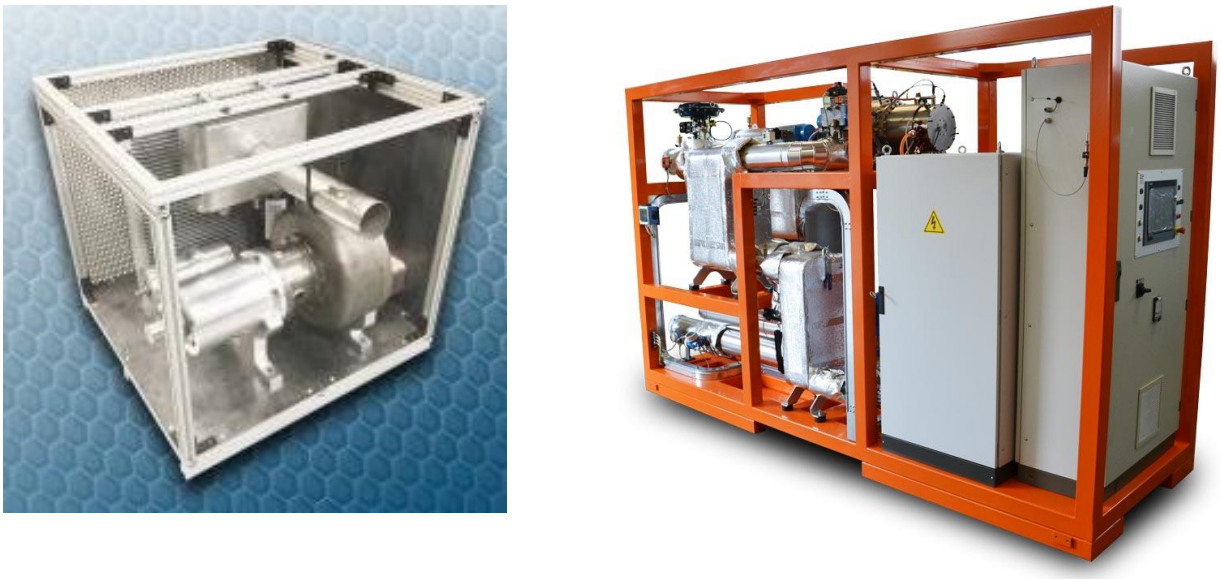

a) *b)*

Figure 1.24 – Micro-ORC units commercialized by Air Squared (a) and Zuccato (b).

1.4 Literature review

1.4.1 Micro-ORC test bench development

When conducting a literature analysis on experimental studies, it is very useful for researchers to have as much details as possible regarding the test equipment. Indeed, since there are no standards regarding either the system layout or the test equipment and procedure, different works are characterized by profound disparities between the apparatus implemented. A basic knowledge of the conditions at which the tests have been carried out is fundamental to compare results obtained with different test benches. In addition, it helps to provide an overview of the most adopted components in state-of-the-art test rigs, such as expander and pump. Moreover, sharing the information on the adopted techniques for developing a test rig can provide helpful guidelines for researchers to upgrade their systems or to develop new ones. The aim of this section is to collect the common features related to this topic, based on the information reported in experimental studies found in the literature.
Usually, when presenting an experimental system, the studies are provided at least with a basic description of the equipment and of test and data processing approaches. In general, these information regard:

- The layout of the tested ORC system, the working fluid, the nominal performance (if available)
- Information on the ORC components, such as expander, pump, heat exchangers etc. (commercial models, description of prototypes)
- The characteristics of the heat source and cold sink
- The main specifics of the acquisition and control system (sensors and actuators)
- The conditions at which the tests are conducted (controlled variables, ambient conditions)
- An estimation of the uncertainty related to the measurements

To provide a general overview on the information provided in the literature on the test rig development, Table 1-2 collects the main details of the test benches selected for this review. In general, the layouts of micro-ORC system have a form similar to that reported in Figure 1.25 (taken from Li et al. [53]). Some remarks on the possible solutions implemented for ORC test rigs are reported below.

- Heat source and cold sink

  Heat source and cold sink supply systems to be used in micro-ORC testing equipment should be characterized by high flexibility and easy regulation of temperatures and flow rates. In case of liquid hot medium (water or thermal oil), many times an electric heater is preferred as source of thermal power for the tests – like for example in [54], [55], [56] – as it is simple, flexible and does not require a fuel supply system. Natural gas and biomass (wood pellet) boilers are also used (see [57], [58]), also with direct heat transfer in a case with water as working fluid [59]. In waste heat recovery installations, often internal combustion engines are employed (see for example [60], [44], [61]), allowing for testing the ORC system at similar condition to its real application. Direct and intermediate heat transfer configurations are used. The heat sink solutions generally require a lower level of controllability, as also in real plants the cooling conditions are subjected to less variability with respect to the hot source. The ideal system for the heat rejection of the ORC cooling water is probably the compression chiller, since it is able to regulate and maintain the water temperature to the imposed values over a wide range of cooling temperatures (5 °C - 30 °C). Another advantage is the water saved with respect to open loop cold sink (such as tap water). The disadvantages are the high cost and electric consumption, and the space requirement. Another type of heat sink is the tap water, which has the advantages of constant and low temperature and of being always available in a laboratory, with no cost of installation. The drawbacks are the high water consumption, increasing with the power of the system, and the absence of temperature regulation options (see for example [54], [44]). Cooling tower is also a good compromise in terms of capital cost and energy consumption (see [62]), but it does not allow for a regulation of the water temperature at the condenser inlet, which depends on the ambient temperature. Some cases ([55], [57]), reports the use dry cooler, whose characteristics are similar to the cooling tower, but is characterized by lower performance (higher value of cooling water temperature at equal ambient temperature), and lower space and cost of installation.

- ORC circuit

  The hot source fluid is connected to the evaporator through one or more inlet and outlet ports, providing the heat for preheating, vaporizing and superheating the working fluid in compact once-through heat exchanger (evaporator); next to the evaporator outlet is located the expander, which in most cases (such as in [53], [54], [59]) is provided with a by-pass line to be used during warmups; the recuperator is placed at the expander outlet, and generally is of lower size than the evaporator; the components mentioned so far can be located at any part of the circuit, at its top or at its bottom. The condenser outlet is usually connected to a tank, or liquid receiver, that works as buffer for the organic fluid in case of temporary increment of the liquid density. Finally, the feed-pump should be always located underneath the liquid tank, at the lowest point of the circuit, with the highest possible height difference with the condenser. In case the expander needs an external lubrication, the relative circuit and equipment (oil pump, separator) are also present.

- External load

  Different solutions have been provided for the connection of the expander to the electric generator. In the case of [54], the generator is hermetically sealed within the expander case, not allowing to measure the expander torque directly. In other cases, the expander is connected to the generator externally by pulleys and belts or gearbox. The type of external load implemented is very relevant for the control of the ORC system, since it determines whether or not the expander rotating speed or torque can be controlled. When possible, researchers should select an external load that allows to regulate the expander within a large range of conditions. Loads with these specifics can be either mechanical, such as magnetic or eddy current brake, and electrical (electric grid, variable load with inverter, variable transformer, electronic load). In other cases [54], the electric load consists of a pure resistive load with discrete control option, and in this case the resistive load cannot be considered a fully controllable quantity.

- Other components

  Other components that should be installed in the circuit for safer operation are: a filter, to retain impurities and humidity from the working fluid; three-way valves, useful in order to be able to by-pass specific components of the circuit, such as the recuperator (for example for testing the performance of the ORC with and without its contribution), or the expander for startup operation, or any component of which two or more models have to be tested alternatively; shut-off valves, very helpful to isolate a circuit segment in case of needed maintenance for a component, since they allows to avoid the emptying and recovery of the organic fluid in the whole circuit, which is a time-consuming operation even for small facilities. In some layouts, additional components are installed in the ORC circuit, such as sub-cooler [60] and pre-feed pump [44], in order to prevent cavitation, or preheater.

- Instrumentation

  The basic instrumentation is substantially similar among the different works. Thermocouples of K-type or T-type and thermo-resistances (RTD) Pt100 or Pt1000 are employed for temperature measurements. Ceramic piezo resistive pressure transducers are generally used for pressure acquisition. The most adopted meter for mass flow rate is the Coriolis sensor, due to its good measuring performance with organic fluids, but also thermal and ultrasonic flow meters have been implemented. The evaluation of the performance requires a method to acquire the expander power output and the pump consumption. The easiest way is to measure the electric current and voltage at the external load terminals. However, when the expander actual performance needs to be distinguished from the electric conversion performance, the shaft torque and velocity can be acquired by a torque meter and an encoder, respectively, to calculate the expander mechanical power. This requires an external mechanical junction between expander and generator shafts [40]. The estimation of the power output only in the thermodynamic form (as enthalpy difference) is considered the least accurate method, since the enthalpy values are generally affected by higher error than directly measured quantities.

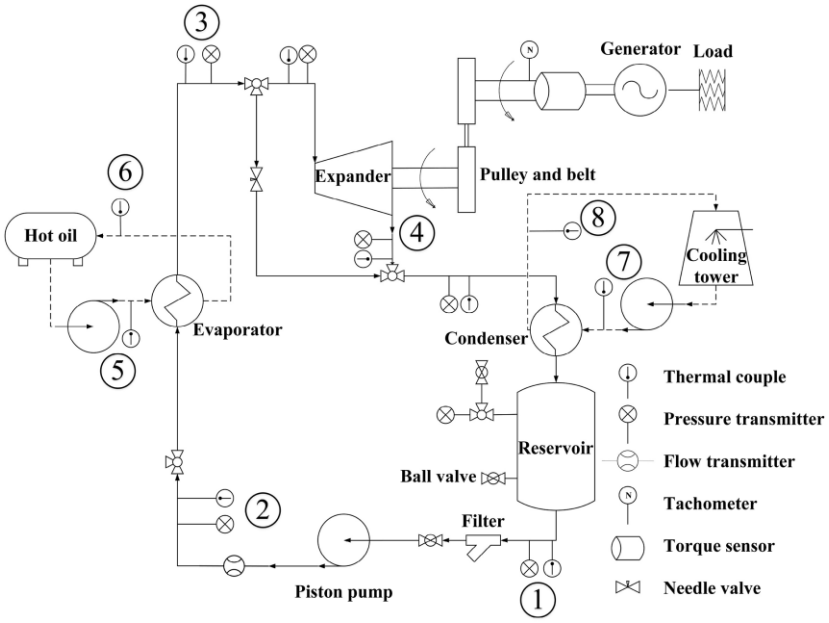

Figure 1.25 – Typical layout of experimental bench for micro-ORC testing [53].

Table 1-2 - Literature examples of information provided on ORC experimental benches.

Article [ref.]	Working fluid	Configuration	Expander and pump	Other components	Heat source and cold sink	Measurements Other information
Bianchi et al. [54]	HFC-134a	Recuperated	– Radial piston prototype – Gear pump prototype	– Brazed plate evaporator and recuperator – Shell and tube condenser – Permanent magnet generator – Array of light bulbs as external load	– Electric water heater – Tap water	– Pressure sensors, thermocouples, Coriolis, Electric power transducers – Uncertainty analysis
Bouvier et al. [59]	Water	Non-recuperated Direct vaporization (Figure 1.26b)	– Exoès single cylinder piston (Figure 1.26a)	– Vacuum pump – Expander cooling circuit	– Wood pellet boiler direct heat transfer	– Acquisition system – Uncertainty values
Carraro et al. [57]	HFC-245fa	Recuperated	– Scroll expander derived from compressor – Volumetric pump	– Brazed plate heat exchangers – Directly coupled electric generator	– Thermal oil circuit with gas burner – Water circuit with dry cooler	– Only monitoring sensors – Low-cost plant (cost of components provided)
Desideri et al. [56]	SES36	Recuperated	– Single screw expander derived from compressor	– Brazed plate heat exchangers – Asynchronous generator – External lubrication of expander	– Thermal oil circuit with electric heater	– Pressure sensors, RTD, Coriolis, electrical power by inverter
Feng et al. [62]	HFC-245fa	Recuperated	– Scroll expander derived from oil-free compressor – Centrifugal pump	– Preheater	– Cooling tower	– Stand-alone and grid connected operation (Figure 1.27a)
Jung et al. [61]	HFC-245fa and HFC-365mfc	Non recuperated Intermediate heat transfer	– Air Squared™ scroll expander – Plunger pump	– Finned tube intermediate heat exchanger – Brazed plate evaporator and condenser	– Diesel fueled gas turbine (Capstone) exhaust gas	– Commercial models of components – Acquisition system – Sensors accuracy

Table 1-2 cont.

Article [ref.]	Working fluid	Configuration	Expander and pump	Other components	Heat source and cold sink	Measurements Other information
Gusev et al. [63]	Air or nitrogen	Only expander and generator test rig	– Free piston expander prototype (architecture and dimensions provided)	– Servo-motor with gearbox for admission control – Linear generator	-	– Acquisition system
Mascuch et al. [58]	Isopropylbenzene	Recuperated	– Vane expander – Gear pump	– Brazed plate heat exchangers – Permanent magnet generator	– Thermal oil circuit with wood pellets heater	– Not specified
Quoilin et al. [40]	HCFC-123	Non-recuperated	– Scroll expander derived from oil-free compressor – Diaphragm piston-type pump	– Three-stages hot air boiler – Water condenser – Asynchronous generator with 2 belt-pulleys – Array of light bulbs as external load	– Hot air – Water	– Acquisition system
Taccani et al. [55]	HFC-245fa	Recuperated	– Scroll expander derived from compressor – Gear pump	– Brazed plate heat exchangers	– Vegetable oil circuit with electric heater – Water circuit with dry cooler	– Pressure sensors, thermocouples, Coriolis, electric power meters
Torregrosa et al. [60]	Ethanol	Non recuperated Direct heat transfer	– Swash plate expander (Exoès)	– Subcooler	– Turbocharged gasoline engine	– Pressure sensors, thermocouples, Coriolis, TDC sensor and angle encoder – Sensors accuracy
Turunen-Saaresti et al. [44]	MDM	Recuperated Direct heat transfer	– Turbo-generator prototype (turbo-pump, radial inflow turbine, generator) (Figure 1.27b)	– Plate and shell evaporator, recuperator and condenser – Pre-feed pump and vacuum pump	– Diesel engine exhaust gas – Tap water	– Acquisition system – Uncertainty values

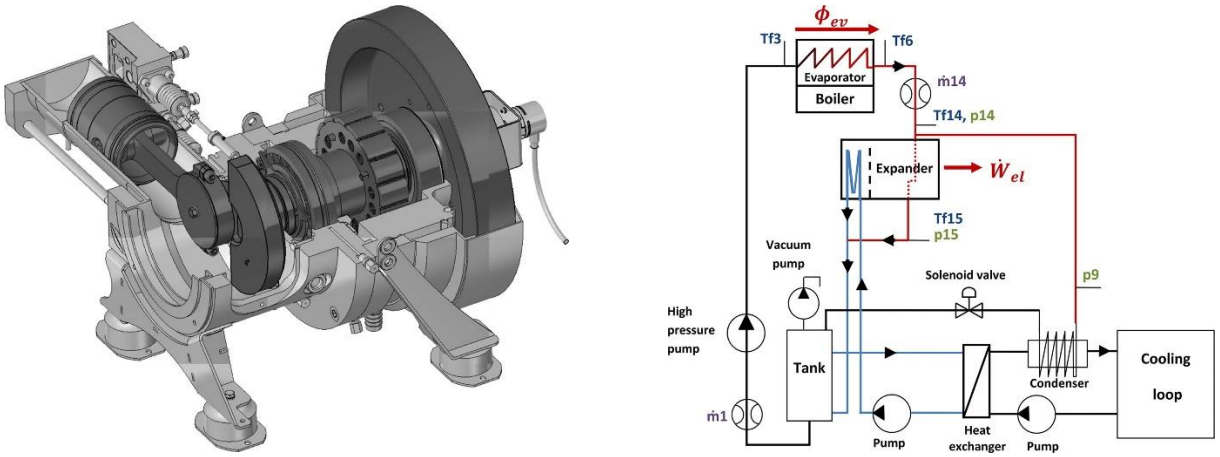

a) b)

Figure 1.26 – Piston expander (a) and test bench layout (b) studied in [59].

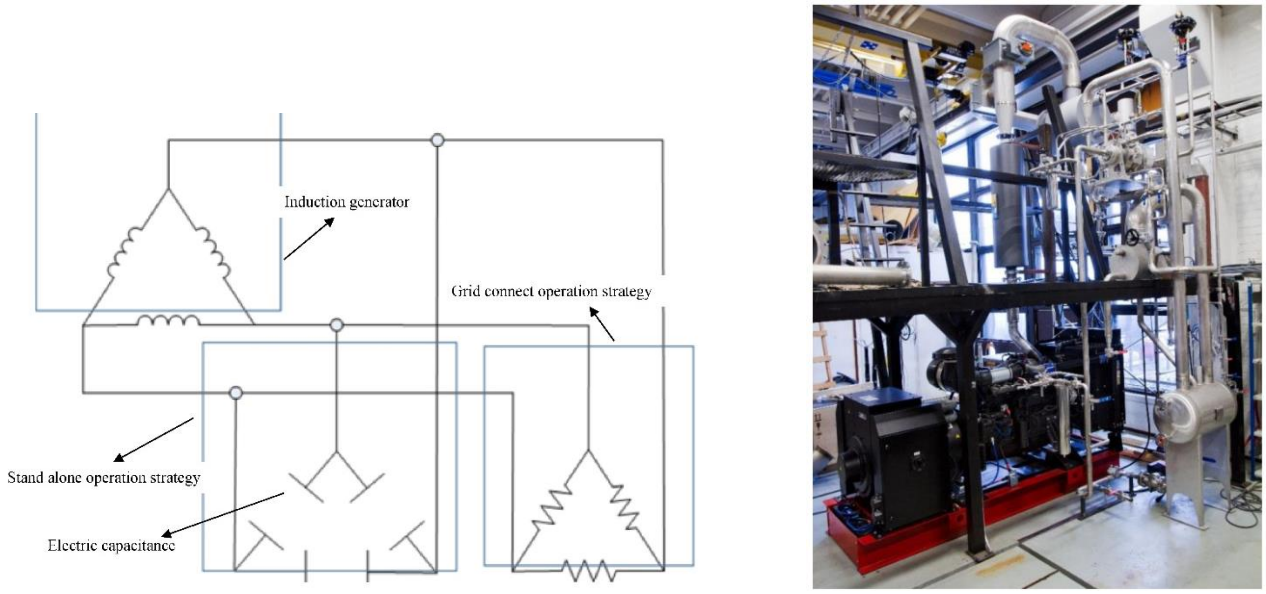

a) b)

Figure 1.27 – Scheme of electric connection of the system presented in [62] (a), and photo of the LUT test bench [44].

1.4.2 Micro-ORC experimental performance

Even though the number of experimental study in the literature on the micro-ORC topic is considerable, it is not comparable to the amount of modelling researches. Publications of experimental analysis have increased for the last decade, and now represent about 10% of total publications on ORC [64]. Detailed reviews of published experimental data trends are reported in [64] and [65]. The most part of the studies regard micro-scale ORC system, with size lower than 20 kW and temperature of the heat source lower than 150 °C, due to obvious reasons related to the costs and the space required by larger scale installations. The results of the survey presented in [65] show that, in the power range between 0.1 kW up to 10 kW, the most diffused applications are solar and waste heat recovery, while the coupling with biomass is less common. Moreover, their analysis confirms that the ORC achievable performances are strictly related to the operating conditions (hot and cold temperature levels), the

selection of the most appropriate working fluid, the choice and sizing of the expansion machine. Regarding the latter, the most adopted is the scroll expander, with power output between 0.5 kW and 10 kW, followed by screw machines that are more suitable in the range 10-50 kW, and turbines that better adapt to larger power. Naturally, there are some exceptions, such as turbines employed in micro-scale high temperature applications [44], or large size piston expander used in small scale (50-150 kW) ORC systems.
For example, Dumont et al. conducted an experimental investigation on a kW-size ORC system working alternatively with four volumetric expanders (scroll, screw, root and axial piston). They obtained the highest isentropic efficiency with the scroll expander (76%), followed by piston and screw (53%) and then by the roots expander (47%). It must be pointed out that their analysis was performed at the same conditions for all the machines, in terms of working fluid (HFC-245fa), size of the other components of the cycle, that were not the nominal conditions for all the expanders [66]. The study of Li et al. regards the experimental analysis of non-recuperated ORC system with nominal power output of 3 kW, using HFC-245fa and a scroll expander (Figure 1.28). They tested the system with thermal oil up to 100 °C as heat source, obtaining that the net electrical power increases from 600 W to 1.3 kW as the evaporation temperature rises from 75 °C to 92 °C. They found also that the system power output is less influenced by the mass flow rate of the working fluid [53]. In [67], the authors conducted an experimental study of a 3 kW ORC working with HFC-245fa and open-drive scroll expander, which was converted from a commercial oil-free scroll air compressor. The maximum performance they obtained are 1.9 kW and 5.9% of electric power output and thermal efficiency, respectively.

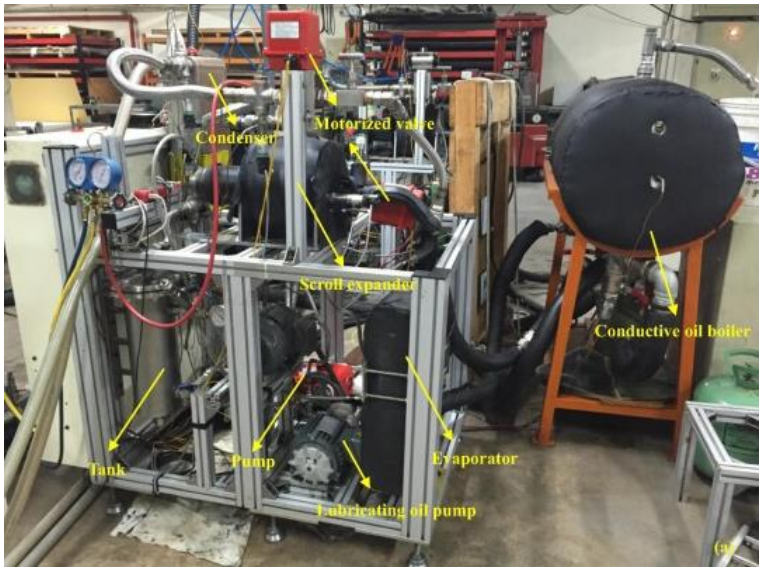

Figure 1.28 – Test bench used in Li et al. [53], taken from Yang et al [67].

Kosmadakis et al. investigated a micro-scale solar ORC plant, working with heat source temperature lower than 100 °C. The working fluid was the refrigerant R404A, while a reverted scroll compressor was used as expansion machine [68]. Collings et al. performed their tests on a kW-scale ORC working with HFC-245fa, with and without the recuperator. The expansion machine was a commercial semi-hermetic scroll model by Air Squared. The peak cycle efficiency they tested is 8.6%, at heat source temperature of 95 °C and regenerative configuration. The expander isentropic efficiency increases from 45% to 75% as the heat source temperature rises from 70 °C to 95 °C [69]. Desideri et al. analyzed a 11 kW regenerative ORC working with single-screw expander derived from a standard air compressor. They tested the system with two working fluids, namely HFC-245fa and SES36. Their results demonstrated that the maximum isentropic efficiency of 60% is achieved with SES36 at 3000 rpm. However, they also found that, at given pressure ratio, the expander power output is higher for HFC-245fa. Pump isentropic efficiency is rather low for both fluids, between increasing from 10% to 20% with the working fluid mass flow rate [56].

1.4.3 Piston expander experimental studies

What can be noted from the literature review is a lack of studies on reciprocating piston expanders. This scarcity is even more dramatic for piston machines working in low temperature ORCs.
Oudkerk et al. performed an experimental investigation on a swash-plate piston expander with total displacement of 195 cm^3, working with HFC-245fa. They tested the expander over a range of pressure ratio between 6 and 11, obtaining maximum isentropic efficiency around 53% with an expansion ratio close to 8.2 and a rotating speed of 2000 rpm [70]. Wronski et al. developed and tested a single-cylinder, single-effect expander prototype (Figure 1.29), which uses a novel system for the variable timing of the rotating admission valve, allowing to adjust the expansion volume ratio during the machine operation. Tanks to the valve timing system, the expander was able to achieve an isentropic efficiency of 70% with pressure ratio ranging between 10 and 16.5 [71]. Gusev et al. developed a test rig for validating a dynamic model of a novel free-piston expander linear generator (see Figure 1.30) [63]. In [72] and [73] the authors presented an experimental study on a prototype of free piston expander-linear generator, conceived for waste heat recovery applications. The test rig they developed is shown in Figure 1.31. The experiments were conducted using compressed air as working fluid, obtaining a peak power output around 110 W with an intake pressure of 3 bar. The conversion efficiency varied with the intake pressure and with the electric load resistance, achieving the maximum close to 73% with a pressure of 2.8 bar and a load resistance of 30 ohms.

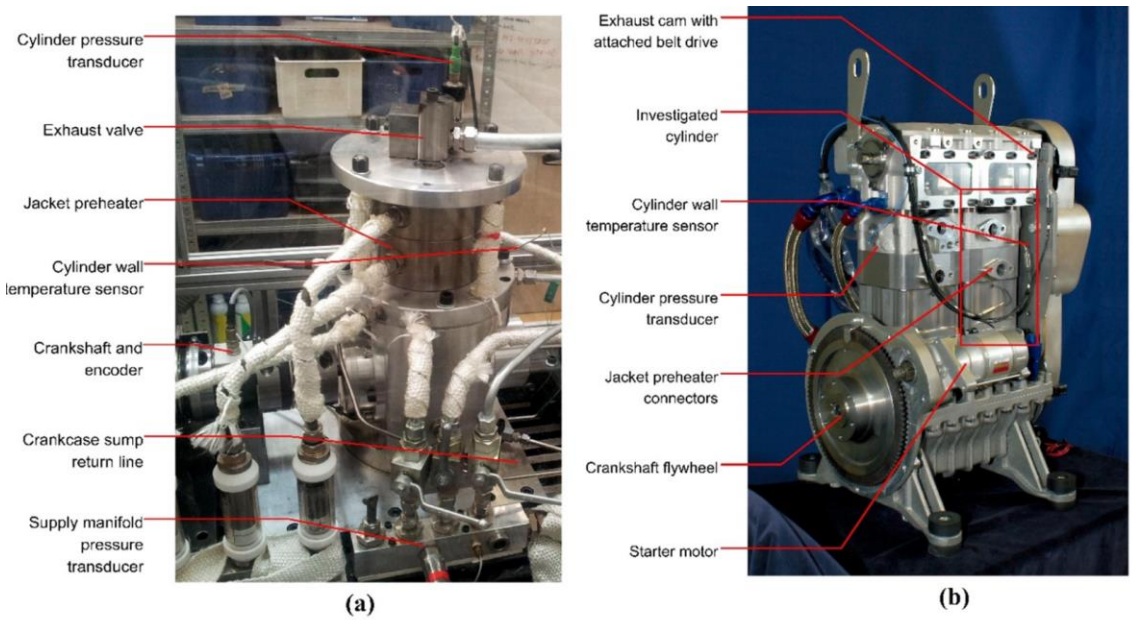

Figure 1.29 – Reciprocating piston expander: a) proof-of-concept design, b) second expander prototype [71].

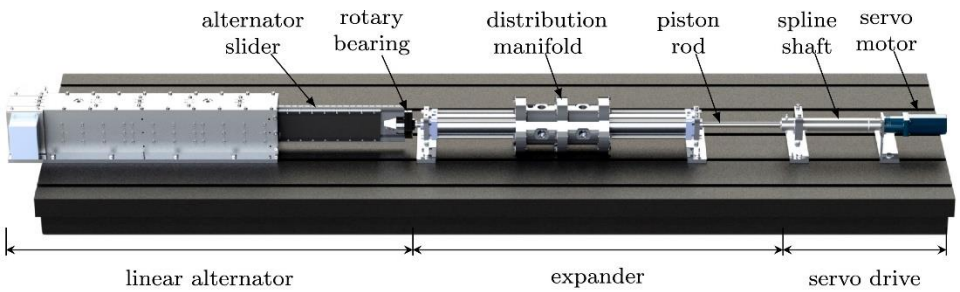

Figure 1.30 – Test rig for free piston expander developed by Gusev el al. [63].

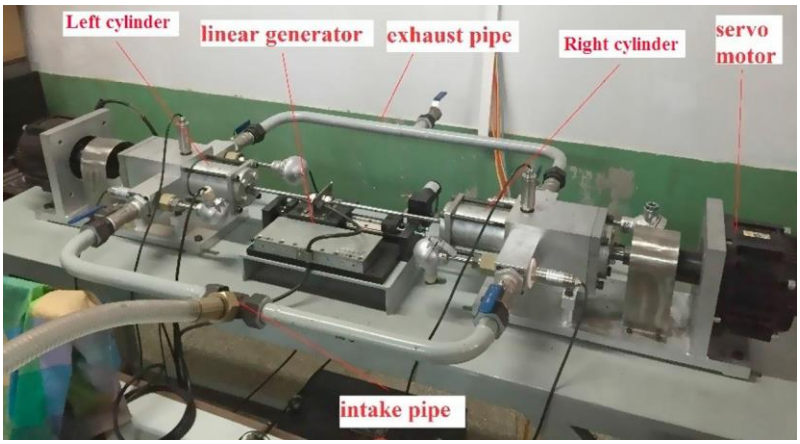

Figure 1.31 – Picture of the test rig developed in [72] and [73].

A final mention is deserved to a prototype of non-recuperated micro-ORC used to supply a water piston pump, developed by the Italian company Nova Somor. This system was installed and tested at the Laboratory of the University of Bologna (Figure 1.32a), and presented in [36]. Its operating principle is similar to that of the free piston expander-linear generator, but in this case three double-effect pistons move with reciprocating motion inside as many cylinders (Figure 1.32b). The three pistons are connected rigidly to the same reciprocating rod. Two cylinders hold the organic working fluid (R-134a): the smallest cylinder is used as organic fluid feed-pump, while the largest works as expander. The third piston is the water pump, which represents the mechanical load to the ORC prime mover. The prototype was tested with hot water between 50 °C and 80 °C, and the pump was able to deliver a water flow rate up to 0.5 l/s and a pressure head close to 18 m.

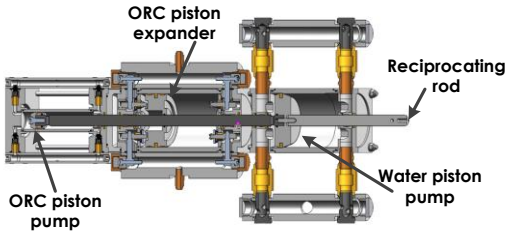

a) b)

Figure 1.32 – Photo of the test bench a) and detail b) of the piston pump supplied by micro-ORC system presented in [36].

1.4.4 Dynamic analyses

Within the variability of heat sources and applications suitable for micro-scale organic Rankine cycles, in several cases the system is forced to work in non-stationary conditions. This is more frequent when dealing with waste heat recovery as heat source. The most representative example of strongly dynamic heat source is the heat recovery from internal combustion engines (ICE) (see section 1.3.1). The majority of modelling and experimental works on ORC dynamic behavior is focused on the field of ICE waste heat recovery. The dynamic simulation of ORCs can be performed with two main objectives:

- design purpose, in order to orientate the selection and size of the different components to the real behavior of the ORC plant, already in the system design phase. The geometry, volumes and surface areas of the heat exchangers, together with the fluid properties, strongly affect the response of the operating variables to fast and frequent changes of the heat source conditions;
- control purpose, providing an effective tool for the development and tuning of the control system. This modelling approach allows to design and verify the control strategy at a simulation level, limiting the need of experimental tests that can be long and expensive to perform.

The common approach in dynamic modelling of ORC systems is to consider the machines of the plant (expander and pump) as stationary components, since their mass and thermal inertia is not comparable to those of the heat exchangers. In other words, pump and expander contribution to the response time is neglected, and they are generally modelled using empirical correlations, performance maps, or semi-empirical steady-state models [74]. The analysis is therefore focused on the heat exchangers dynamic behavior, and especially on the evaporator response to variating heat source. The two main techniques for heat exchanger models are the finite volume and the moving boundary methods. The finite volume (FM) method provides for a spatial discretization of the heat exchanger along the fluid flow direction. The number of finite volumes remains constant during the simulation. In the moving boundary (MB) approach, the volume of fluid is divided into as much zones as the number of the aggregate states of the fluid. For evaporators, three zones are identified, corresponding to liquid, vapor and two-phase. For a condenser in which the fluid enters in saturated state, only the zones corresponding to two-phase and saturated liquid can be considered. Differently from the FM method, in the MB the extensions of the zones separated by the moving boundaries vary over time. The finite volume is between the two methods the most accurate, but requires considerable computational costs, that increases with the increment of the number of discretized volumes. On the contrary, the moving boundary technique is simpler and less heavy to run, but it experiences singularities in the resolution of the equations when the extension of one of the zones becomes zero. A solution to this problem can be the switching moving boundary (SMB) approach, that provides for the switch between the possible configurations (all the three zones, two zones and one zone) to avoid solver issues [75]. Regardless of the discretization method applied, the models are typically based on mass, energy and momentum balances, computed in each control volume. The heat transfer coefficients and the pressure losses are usually provided by semi-empirical correlations. In general, the complexity of the model depends whether or not the all effects of the real process are considered, and under which simplifying assumptions. Some of the most common hypotheses assumed for heat exchangers dynamic modelling are listed below ([57], [75], [76]):

i. uniform thermodynamic state variables in each control volume, equal to the average values;
ii. omission of momentum balance equation (pressure losses neglected);
iii. cross sectional area constant throughout the whole heat exchanger length;
iv. no axial heat conduction;
v. radial thermal flow in the heat exchanger is neglected (one-dimensional tubes);
vi. no heat losses to the ambient
vii. neglect of conductive heat transfer through and/or along the heat exchanger walls.

Among the several available modelling tools suitable for dynamic analysis, the most used are the Modelica language (used either in commercial and open source software), Dymola, Matlab Simulink, AMESim, GT-Suite, Aspen HYSYS.

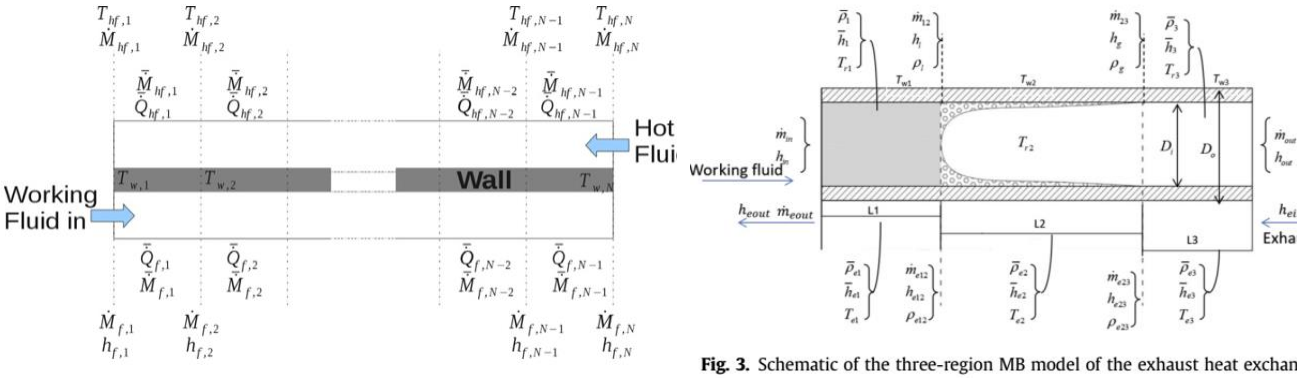

Fig. 3. Modeling paradigm of the evaporator.

Fig. 3. Schematic of the three-region MB model of the exhaust heat exchan

Figure 1.33 – a) Finite volume [76] and b) moving boundary [79] modelling logics.

For example, Jimènez-Arreola et al. investigated the dynamic behavior of a fin and tube heat exchanger used for direct evaporation in ORC. They developed a thermo-dynamic model using the commercial TIL library in the software Dymola, to evaluate the characteristic response of the evaporator key variables under fluctuating heat source, for control and design purposes. The model was based on a one-dimensional finite volume approach, with the fluid in the heat exchanger discretized in 20 cells. In order to compare the different evaporator response to heat source fluctuations, they defined a *dynamic regime number* as the ratio of the characteristic response time to the period of fluctuation of the thermal load. They compared two configurations, namely louver fin multi-port flat tubes and fin-and-tube heat exchangers, finding the former as the solution with faster response [77]. Carraro et al. modelled the dynamic operation of a micro-scale ORC with HFC-245fa as working fluid, using the Differential Algebraic systems of Equations (DAE) implemented in Matlab Simulink environment. They selected a moving boundary approach to model the evaporator and condenser, while the ε-NTU method was applied to the recuperator. The model parameters – such as heat transfer coefficients, geometry parameters and empirical coefficients for performance maps – have been calibrated with experimental data. Their model predicts the cycle pressures and temperatures and the expander power output with maximum error lower than 7%, with also acceptable synchronization of the transient response [57]. Desideri et al. presented a model developed with the open-source library ThermoCycle in Modelica language. They validated the model results with experimental data collected on their 11 kW test bench, using Solkatherm (SES36) as working fluid. The heat exchangers models are based on the finite volume-object oriented approach, whose paradigm is explained in Figure 1.33a. The also conducted a sensitivity analysis on the number of volumes (between 10 and 90), concluding that above twenty elements the improvement of accuracy becomes negligible [32]. A similar study was presented before in [78], with the condenser modelled with constant pinch point and sub-cooling, and an expander semi-empirical model. Wang et al. implemented a moving boundary model in Simulink for assessing the dynamic behavior of an ORC system coupled with natural gas engine, validating the results with data obtained in another study. They conducted the simulations to evaluate the influence of evaporating pressure, condensing pressure and exhaust outlet temperature. The analysis regarded eight different fluids (R114, R245fa, R123, R141b, hexane, heptane, cyclohexane and toluene). They concluded that the same PID controller can be employed if fluids have similar critical temperature [79]. In [80], the authors presented a dynamic model of ORC for heavy duty diesel engine applications. The ORC model was built in Simulink environment and coupled to a GT-power model of the diesel engine. A non-recuperative configuration with two parallel evaporators is developed, to recover the exhaust gas thermal power from both tail pipe and EGR. The heat exchangers have been modelled with finite volume method, taking into account the calculation of pressure losses. The models of control valves and of the liquid tank have been included. They validated the results with experimental data, proving that the model is able to predict evaporation temperature and pressure with a mean error of 2% and 3%, respectively.

CHAPTER 2

2 Test bench implementation

2.1 Micro-ORC description

2.1.1 Overview

The micro-Organic Rankine Cycle (ORC) test bench is installed at the Laboratory of Micro-cogeneration Technologies of the Department of Industrial Engineering of the University of Bologna (Figure 2.1). The installation works started in the late 2015, and the first start-up was performed at the beginning of 2016. The power plant was designed and assembled by the company StarEngine [81], and it was conceived for the application in the residential sector, being suitable to work also as off-grid supply system. The development of the test bench, including the external circuits of heat supply and cold sink and the acquisition and control system, have been accomplished by the UNIBO laboratory personnel. During the last years, the test bench has been continuously upgraded thanks to the addition of new devices for the data acquisition and control. The version developed and described in this Ph.D. thesis is the most updated.

The layout of the micro-ORC system under investigation is reported in Figure 2.2. It consists of a typical recuperated configuration that employs, as main components, a brazed plate evaporator, a piston expander, a brazed plate recuperator, a shell-and-tube condenser and a gear feed-pump. The evaporator is supplied by hot water heated by an electrical heater, while the condenser is fed with cold water at ambient conditions. The heat source can be either a biomass boiler, solar thermal collectors, low-enthalpy geothermal energy or any kind of low-grade industrial waste heat. The working fluid is HFC-134a (R134a), whose characteristics are reported in Table 2-1 and in the thermodynamic diagram of Figure 2.3. Since this is a high-GWP fluid, its phase-out in the European Union is already planned for the next years, and its more suitable replacement are the olefins R1234yf and R1233zd, that present similar value of critical temperature and pressure. Expander and feed-pump are prototypes manufactured by the system supplier, while the other components are commercial. The different components are connected by rigid copper pipes, with diameter equal to 42 mm and 35 mm, respectively for low and high pressure lines. Figure 2.2 also shows the presence of several manual valves (VM) installed for inspection and in case of breakage. A normally closed valve (VNC1) and two normally open valves (VNO2, VNO2') are also installed for the ORC startup operation, when the fluid flows through the external casing of the expander (branch 1'-1bp), bypassing the expander cylinders (branch 1'-1). This procedure allows, on one hand, to achieve the desired condition of superheating, avoiding potential liquid drops in the expander, on the other to increase the temperature of the expander surfaces, preventing thermal stresses on the machine. When the set point temperature is reached at the expander inlet (1bp), the VNC1 valve can be opened, admitting the fluid inside the cylinders and activating the expander. Finally, a safety valve is installed at the outlet of the evaporator to interrupt the operation in case of unexpected overpressure (max pressure is set at 26 bar). The system was designed in order to comply with constraints of compactness, with overall dimensions equal to 80 x 85 x 300 cm (width x width x height).

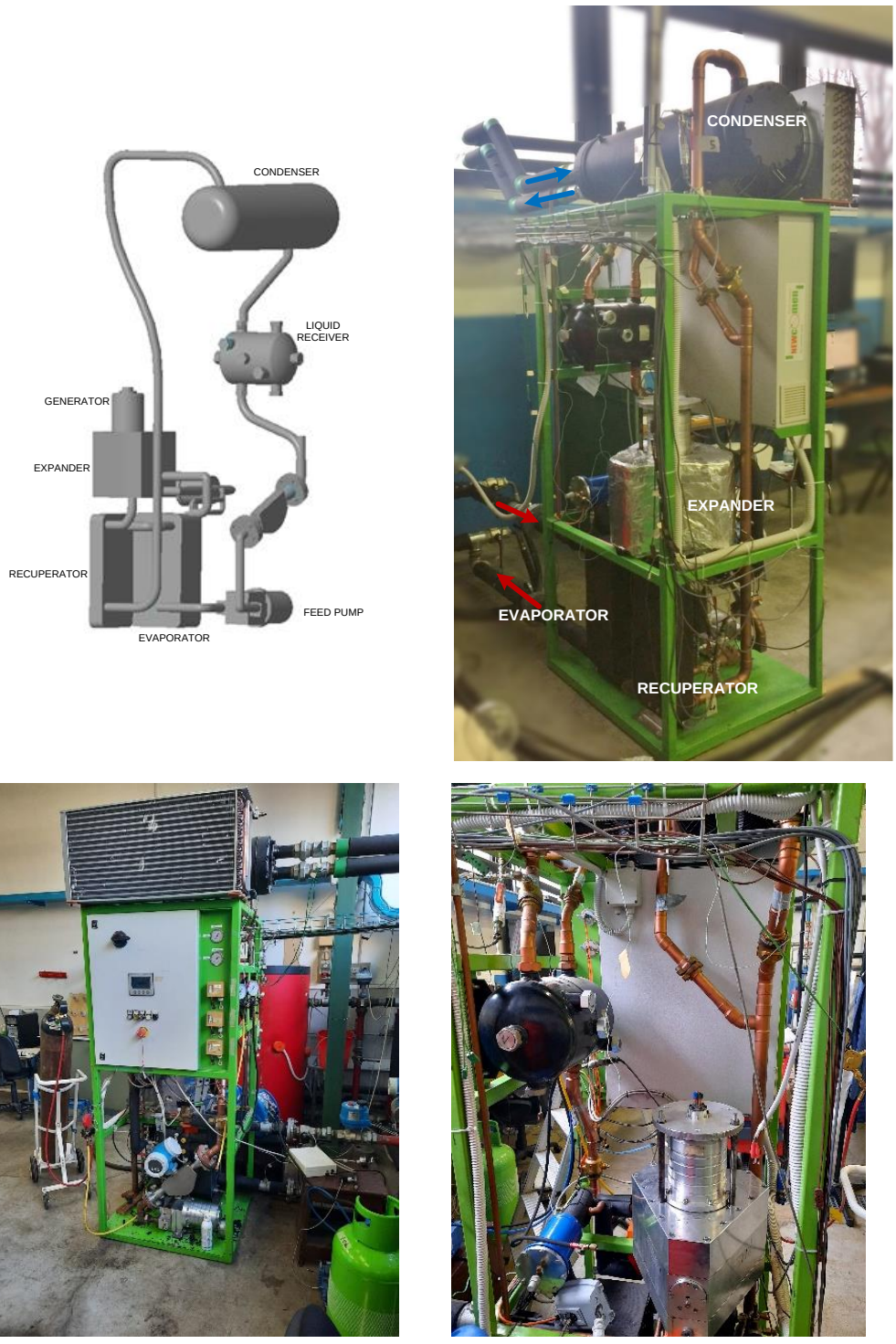

Figure 2.1 – 3D CAD model and different views of the micro-ORC test bench

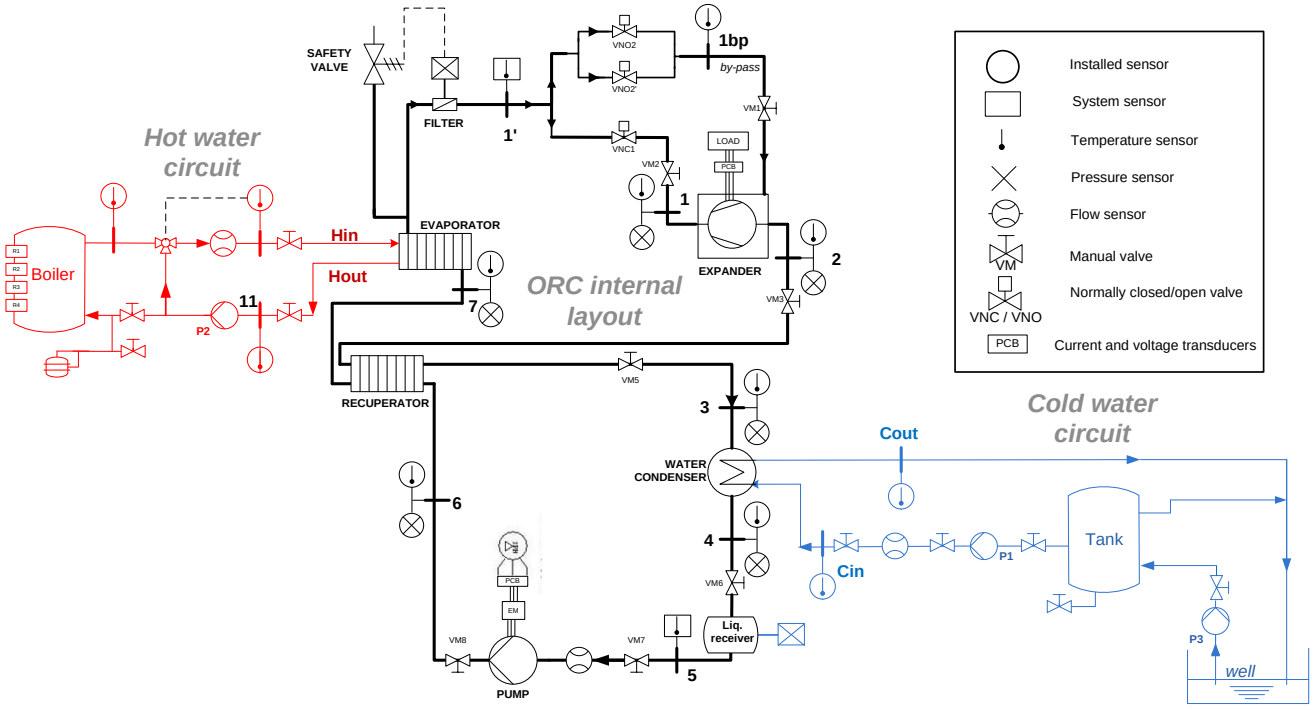

Figure 2.2 – General layout of the micro-ORC test bench

Table 2-1 – Main properties of working fluid HFC-134a

Property	Unit	Value
Critical temperature	°C	101.1
Critical pressure	bar	40.67
Density at 0 °C, 1 bar	kg/m^3	4.25
ODP	-	0
GWP	-	1430
Safety Classification	-	A1

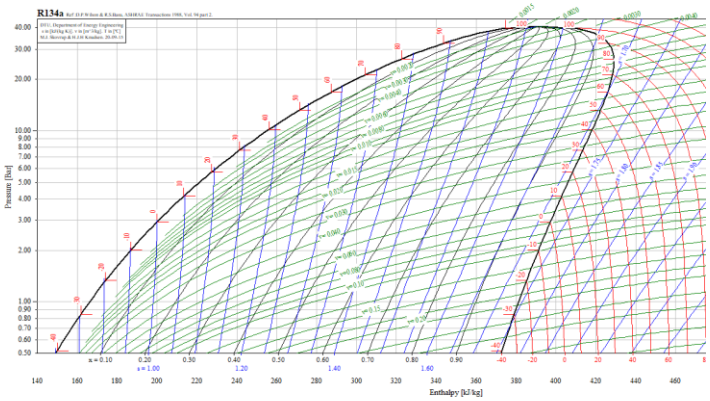

Figure 2.3 – Pressure enthalpy diagram for working fluid HFC-134a

2.1.2 Expander

The expander installed in the micro-ORC under investigation is a reciprocating piston prototype (Figure 2.4). It consists of three cylinder placed radially at 120° and moving the same crankshaft. Each cylinder has a volume of 76.5 cm^3, hence the total displacement is 230 cm^3/rev. The fluid admission and discharge is operated through rotating valves, which are moved by the shaft rotation by means of gears. The admission valve starts to open at the upper dead center (no advance timing is provided), and the valve remains open for about the 70% of the piston stroke. It has to be noticed that, while the valve is open, its flow passage area is not constant, but increases up to its maximum corresponding to the half of the opening stroke (hence to the 35% of the piston stroke), to decrease

back until the valve is closed again. The expander is provided with two inlet ports: one leads the fluid to the admission valves, the other leads directly to the discharge port without entering the cylinders. The latter path works when the external by-pass circuit is activated, i.e. during startup operations in order to let the fluid achieve the desired conditions of temperature and also to warm up the expander case. The expander external surface has been thermally insulated with sheets of mineral wool, to reduce the heat losses that have been demonstrated to be not negligible in similar applications [82]. The expander shaft is coupled with a permanent magnet generator without any speed reducer, so the two machines run at the same rotating speed. The generator is placed inside the expander sealed case and is cooled by the same working fluid. Table 2-2 collects the main features of the prototype expander under investigation.

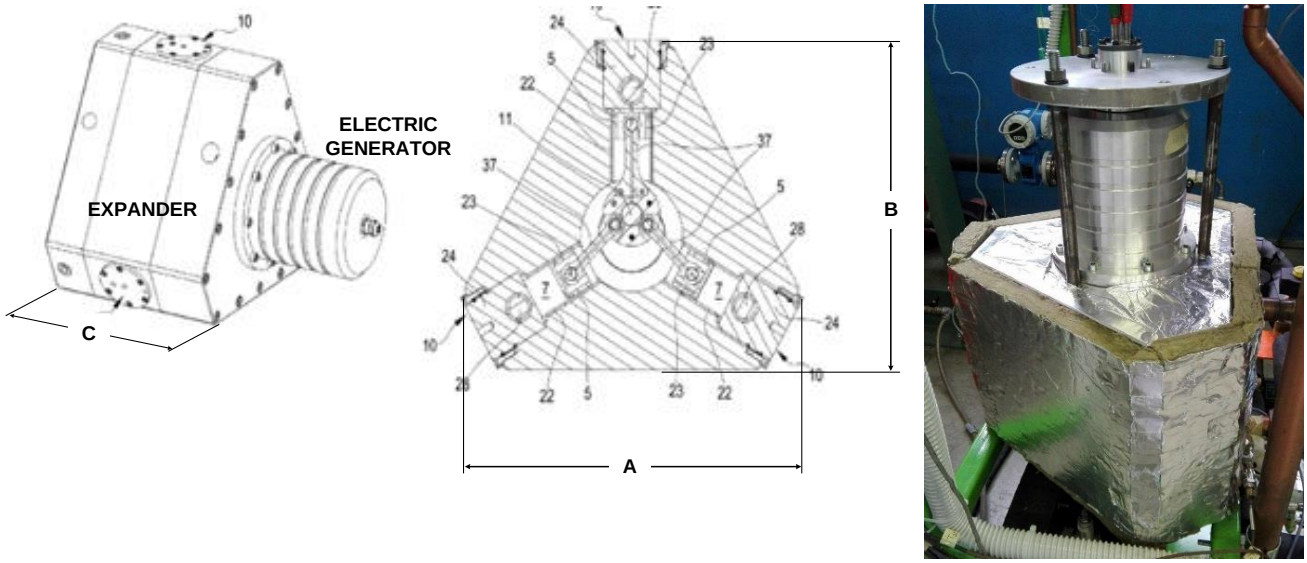

Figure 2.4 – Expander draw [81] and photo

Table 2-2 – Expander main specifics

Property	Unit	Value
Model	-	Reciprocating piston
Configuration	-	Three radial pistons at 120°
Total Displacement	cm^3	230
Cylinder bore	mm	46
Piston stroke	mm	46
External dimensions (A x B x C)	mm	350 x 410 x 320

2.1.3 Feed-pump

The organic fluid feed-pump is a prototype designed and realized by the micro-ORC provider (Star Engine). It is an external gear pump with displacement around 50 cm^3/rev, and coupled with a 1.5 kW asynchronous motor. Between the motor shaft and the pump shaft, a speed reducer is placed with a speed ratio equal to 3:1. The speed of the pump motor is controlled by a variable frequency drive, able to adjust the supply frequency between up to 60 Hz, corresponding to a motor frequency between equal to 15 Hz, since the motor has four pole pairs. The actual maximum mechanical frequency of the pump wheels is then 5 Hz, corresponding to 300 rpm. The choice to design the pump with relatively high displacement and low rotating speed was meant to reduce the risk of cavitation at the suction side of the pump, which increases with the wheels speed. Conversely, the low rotating speed has a

negative effect on the pump volumetric efficiency, since it increases the fluid leakages from the supply to the suction side of the pump.
Pump architecture can be observed in Figure 2.5. The pump body is composed by 5 elements: looking at Figure 2.5b and Figure 2.5d, from left to right, one can see the first flange in steel, that contains the bearings of the two shafts; then the left fixed side in bronze; in the middle there is the case of the pump wheels, in aluminum, where there are the inlet and outlet channels. The latter consists of two circular ports that separate the flow . Element 4 is the right fixed side in bronze, identical to the left one; the right flange is similar to the left one and contains the two bearings, but it has a hole for the drive wheel shaft transmission. The element 6 is the case of the wheels of the speed reducer, one of which (the smaller) is directly connected to the motor shaft. All the elements are packed to the central wheels case by means of screws, and the seal is provided by several O-rings in NBR placed between the elements. The drive shaft is hollow for two purposes: first, it allows the passage of the lubricant oil into the reducer case; second, it let the fluid pass into the motor case, so the same organic fluid provides the cooling for the electric motor. This solution implicate that the sealing must be assured in all the components of the pump, including the electric motor. The main specifics of the feed-pump are reported in Table 2-3. The 3D CAD model has been obtained from a process of reverse engineering, that allowed the assessment of the actual gear pump displacement, estimated around 50 cm^3, and the characteristic gear dimensions.

Table 2-3 – Feed-pump specifics

Property	Unit	Value
Model	-	External gear pump
Displacement	cm^3	50
Nominal speed	rpm	300
Number of teeth	-	10
Gear root diameter	mm	57
Gear inside diameter	mm	37
Gear face width	mm	33
Motor power	kW	1.5

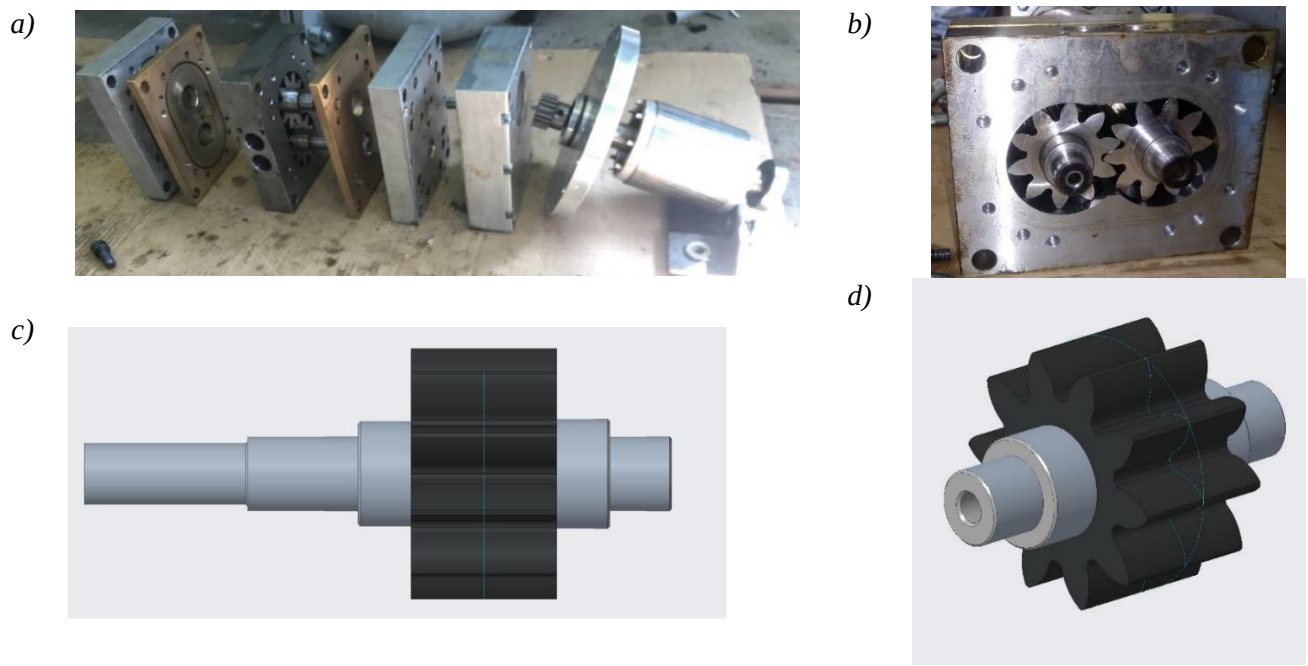

Figure 2.5 – Feed-pump photos and 3D CAD model: a) phot of pump disassemlbed elements; b) front view of pump gears; c) CAD model of drive wheel (side view); d) CAD model of driven wheel.

2.1.4 *Heat exchangers*

The heat exchangers of the system are the evaporator, the water condenser, the air condenser and the recuperator. The evaporator is a brazed plate heat exchanger model ONDA S202 (Figure 2.6), with 64 plates and a volume equal to 8.53 liters on organic fluid side and 8.80 liters on water side. The heat transfer surface is not indicated in the component data sheet, but it can be estimated from the dimensions and number of the plates, considering an enlargement factor that takes into account the passages where the fluid flows in each plate. The recuperator is the same model of the evaporator but with 19 plates, and a volume of 2.06 liters and 2.33 liters respectively on working fluid and water side. The water condenser is a shell and tube type with four passages, a volume on organic fluid side equal to 34.5 liters and on water side equal to 12.5 liters (Figure 2.7). The water condenser is the component that holds the highest volume of working fluid in the circuit. Since the condenser surface is not provided either, it was estimated as equal to the external surface of the tubes where the water flows, which have been field measured. The plant is equipped with an air condenser too, placed in parallel with the water one to enhance the cooling capacity in case high cooling load required. The air condenser is a finned tube heat exchanger equipped with two fans, and has a nominal cooling capacity around 9 kW. Hence, during the normal operation of the power plant, the air condenser would not be able to provide the whole working fluid cooling demand, but can only be used in combination with the water condenser, to boost the cooling capacity. However, the air condenser has been rarely employed during the tests, and no results have been reported in this thesis; indeed, the water condenser is generally able to satisfy the cooling demand, and also the split of the fluid flow rate would make the cooling power more difficult to evaluate. Table 2-4 collects the main specifics of the heat exchangers.

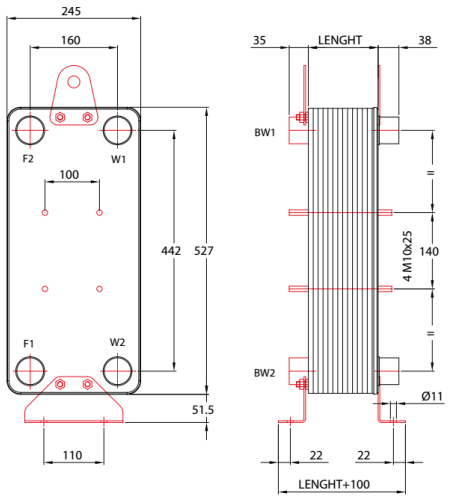

Figure 2.6 – Brazed plate evaporator draw with main dimensions

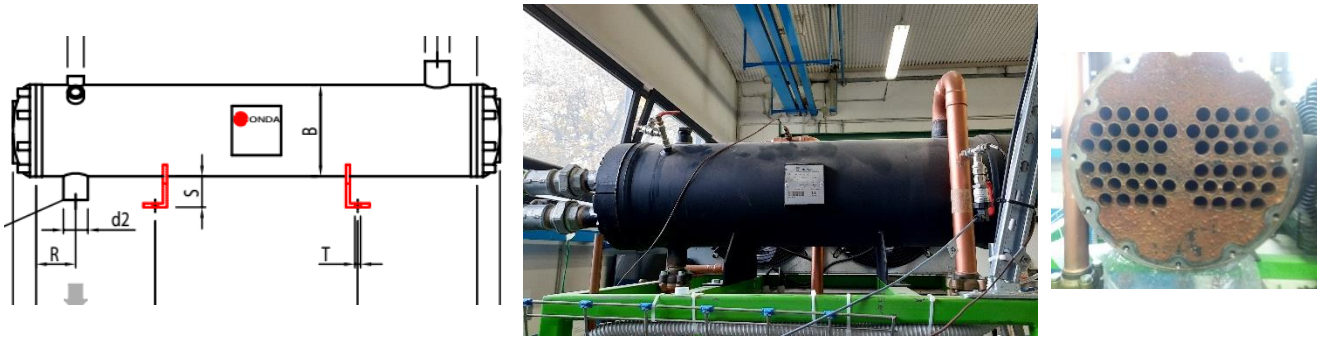

Figure 2.7 – Shell and tube condenser draw and photo

Table 2-4 – Main specifics of the heat exchangers

Property	Unit	Evaporator	Recuperator	Water condenser	Air condenser
Model	-	Onda S202	Onda S202	Onda CT292	NA
Hot side volume	l	8.796 (water)	2.330 (vapor)	34.5 (working fluid)	6
Cold side volume	l	8.526 (working fluid)	2.061 (liquid)	12.5 (water)	-
Number of plates	-	64	19	-	-
Number of passages / tubes per passage	-	-	-	4 / 14	-
Heat transfer surface (estimated)	m^2	6.2	1.8	3.5	NA
Rated power	kW	50	10	100	9

2.1.5 Other components

Liquid receiver

The liquid receiver is a tank placed downstream the condenser before the pump inlet (Figure 2.8). With an internal volume equal to 19 l, after the condenser is the component the holds the maximum volume of fluid. It is provided with liquid level indicators, so the user can be sure that the pump is sucking liquid fluid, avoiding cavitation. Its purpose is to provide a buffer volume to compensate the change of working fluid specific volume in the circuit, for example after the increase of liquid fraction at the condenser outlet. It is provided with two inlet ports, one connected to the water condenser outlet and the other to the air condenser, and one outlet port, directed to the pump suction. The receiver inlet and outlet pipes are provided with ball valves, so the tank is also used to store the organic fluid during maintenance of other components, generally together with the water condenser.

Figure 2.8 – Liquid receiver

Electrical generator and load

The electric generator is directly connected to the expander in a hermetic case. It is a three-phase permanent magnet synchronous generator with 4 pole pairs. The same working fluid is used for cooling the generator. The three-phase output is connected to a separate electrical cabinet that supplies the electric load, which consists of five pure

resistive loads, connected in parallel between them and in *delta* with the generator output three-phase line. Each load is composed by three light bulbs with a nominal power of 200 W each. Every load is provided with a separate switch, thus the nominal power absorbable by the resistive load is adjustable between a minimum of 600 W (one load activated) and a maximum of 3000 W (5 loads activated), corresponding to the nominal ORC power output. Changing the number of loads switched-on will vary the nominal equivalent load impedance of each phase, which is maximum for only 1 load activated (288 Ω), then is halved for 2 loads, divided by three for 3 loads etc., down to the minimum value of 58 Ω for the all in-parallel loads switched-on. The load configuration does not allow setting the generator rotational speed or the load torque, thus the expander shaft is free to achieve the equilibrium between the generator torque and the load resistance. Table 2-5 collects the nameplate specifics of the electric generator.

Table 2-5 – Electric generator specifics

Property	Unit	Value
Model	-	Magnetic NGB 145 M-SA
Rated power	kW	3
Nominal voltage	V_{rms}	380
Nominal current	A_{rms}	5.2
Frequency	Hz	120
Nominal torque	Nm	17.8

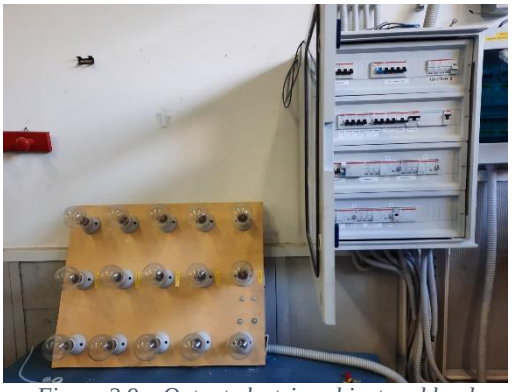

Figure 2.9 – Output electric cabinet and load

2.1.6 Water supply circuits (heat source and cold sink)

The external circuits of hot and cold water, which have been designed for the test bench under investigation as part of the work of this thesis, are represented in the schemes of Figure 2.10 and Figure 2.11. The heat source is supplied by an electric heater (or puffer) with capacity of 500 liters, provided with 5 armored electric heater elements for a total nominal power equal to 40 kW (Figure 2.12a). The resistances can be activated separately in order to regulate the thermal input, with steps of 8 kW. The heater is able to work with pressurized water, up to 5 bar. The water is circulated to the evaporator by a centrifugal pump (P2), usually run at constant speed. The regulation of the hot water flow rate is made by means of an automatic ball valve installed at the evaporator inlet pipe. The hot water loop is also provided with a three-way valve for the regulation of the water temperature at the evaporator inlet. The valve mixes the water heated by the puffer with the return colder stream coming from the evaporator, and it can be controlled automatically by the PID controller. By switching the manual valves MV1 and MV2, the water heated by the puffer can be mixed with tap water, much colder than the return water, allowing more drastic changes in the hot water temperature to the evaporator. The latter configuration, in order to maintain the pressure in circuit in the desired range, requires the control system to open the on-off valve, that allows to discharge the heater water to the drain. The logic and implementation of the control system is presented in detail in a next paragraph.
The cold sink is provided by a water well installed in the laboratory, with a diameter of 1 meter and 11 meters deep (thus with a water capacity close to 11 m^3). Cold water at ambient temperature is extracted by a submerged pump and stored in a cold tank with capacity of 300 liters (Figure 2.12b), then circulated to the condenser using the centrifugal pump P1. The water temperature depends on the ambient temperature, and it shows little variations during the year because the well is located indoor. The drawback of this system is the relatively limited volume of water in the well, which makes increase its temperature in long tests, due to the discharge in the well of the water heated in the condenser. This factor is mitigated by increasing the cold water flow rate, resulting in a low difference

between inlet and outlet temperature (in the order of 2 °C). In any case, it has been observed that tests lasting more than one hour will be inevitably subjected to a rising trend of cold water temperature. An alternative that has been applied in some tests is to use directly tap water to supply the condenser, with the advantage of lower and constant temperature than well water; however, this solution involves the wastefulness of significant amount of water that is discharged to the sewer.

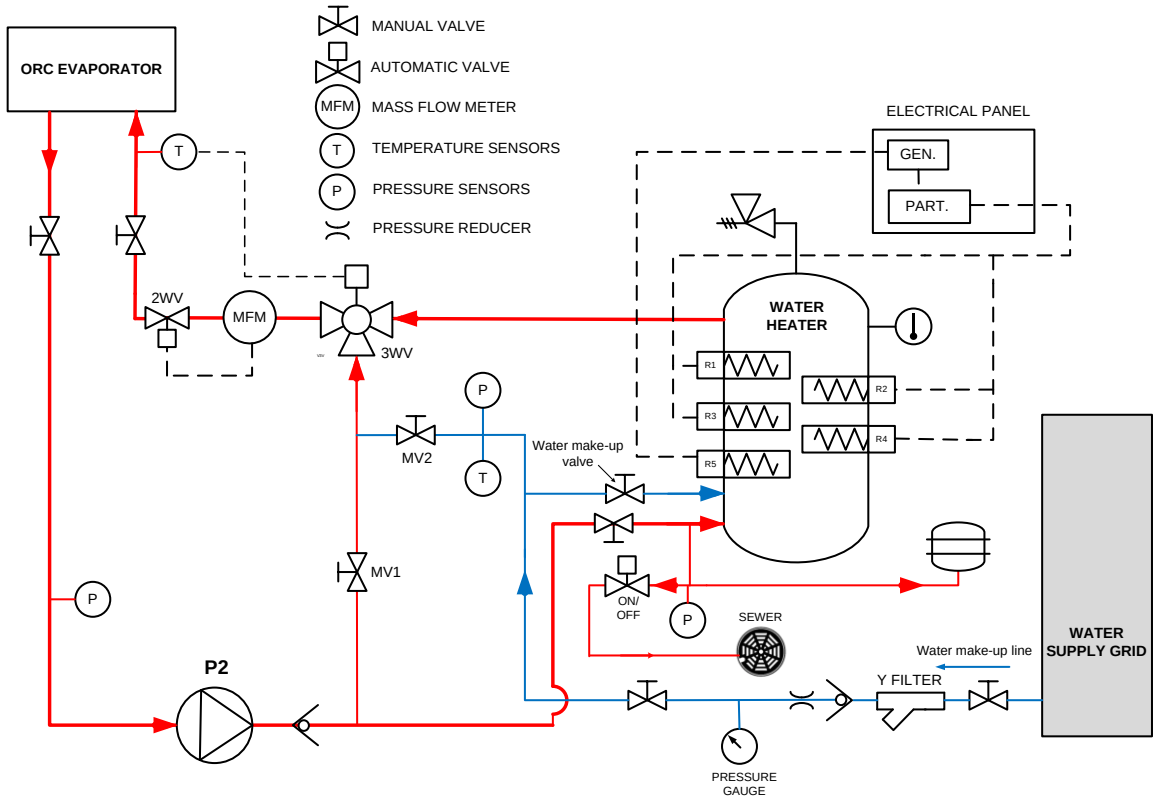

Figure 2.10 – Layout of the hot water circuit

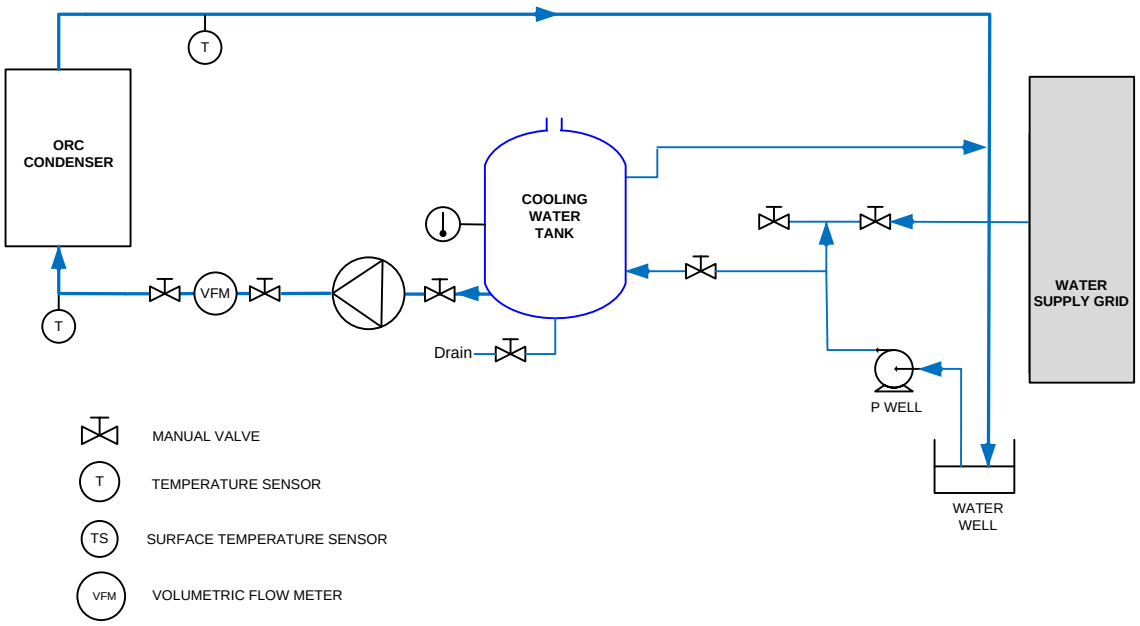

Figure 2.11 - Layout of the cold water circuit

a) *b)*

Figure 2.12 – Photos of electric heater (left) and cold tank (right)

2.2 Working fluid charge

The amount of fluid to be charged inside the system is a critical aspect in the field of ORC system. The mass of fluid in the circuit can affect the system operation in different ways. An overcharge of fluid will cause a decrease in the effective phase change heat transfer area of the heat exchangers, also increasing the fluid cost that is not negligible especially in large-scale systems [83]. The cost of one kilogram of HFC-134a, at the moment this work

is written, is around 10-15 €, with significant market fluctuations in the last years, and is expected to increase during next years due to the phase out of high GWP refrigerants. The cost of new low-GWP fluids, such as olefins, is even higher (20-30 €/kg), since they are new product not really widespread in the market. On the contrary, an insufficient charge of working fluid will increase the risk of cavitation at the feed-pump inlet. Differently from traditional steam Rankine cycles, which are provided with controlled water make-up, ORC systems are closed circuits, and the working fluid is generally charged once at the first plant start-up. Especially when dealing with high-GWP fluids (such as R-134a used in this test bench), all leakages should be avoided according to the F-Gas regulation, which recommends the periodic verification of all the seals by means of leak detectors. Nevertheless, phenomena of small leakages are very difficult to avoid completely, particularly in small-scale plants, which usually are not provided with continuous detection systems. In addition, whether the system is operating or not, the amount of working fluid cannot be assessed directly, since it does not depends from the quantities generally measured, such as temperature and pressure. Hence, a system could have a small leakage somewhere along the circuit, losing a non-negligible amount of fluid after a period of operation of greater or lesser duration (depending on leak magnitude and working pressure), without being detected. Moreover, generally the maintenance procedures cause small leakages from the needle valves used for extracting the fluid, from the component that needs to be repaired or replaced. Even if the reduction of fluid charge is not detected up to a certain amount, it can modify the operating behavior of the ORC cycle, for example inducing pump cavitation. These considerations are particularly important in experimental benches, where often the systems are composed also by prototype elements and deal with frequent maintenance operations.

From the modelling point of view, accounting for the fluid charge allows to avoid making assumptions on the working fluid state (typically, the sub-cooling degree at condenser outlet), thus to model the system performance only based on the components specifics and boundary conditions. This topic have started to be tackled only during the last few years, and the related literature studies are limited. Charge-sensitive models employ different approaches to calculate the fluid mass distribution over the ORC components, depending on the operating conditions. For example, Liu et al. adopts the Lockhart-Martinelli model [84] to calculate the fluid mass as function of the vapor quality and the density and viscosity of saturated liquid and vapor [83]. Dickes et al. considered five of the most used models for assessing the void fraction of the flowing mixture (i.e. the vapor fraction within the two-phase mixture). The latter is defined as function of the fluid quality, according to Equation (2.1):

$$\alpha = \frac{1}{1 + \frac{1-x}{x} \cdot \frac{\rho_V}{\rho_L} \cdot S} \tag{2.1}$$

where α is the void fraction, x is the vapor quality, ρ_L and ρ_L are the saturated vapor and liquid densities at the working fluid pressure, respectively, and S is slip (or speed) ratio between vapor and liquid phase. The different approaches are: i) constant slip ratio equal to 1; ii) slip ratio calculated as $S = \left({}^{\rho_V}/_{\rho_L}\right)^{-1/3}$, as proposed by Zivi [85]; iii) Lockhart-Martinelli empirical correlation; iv) the empirical model introduced by Premoli [86]; v) the empirical model proposed by Hughmark [87]. To validate the models, they compared the charge prediction with the actual mass inside the ORC system [88]. The same authors proposed an novel approach to evaluate the charge distribution experimentally, by suspending and weighting the system components (heat exchangers and liquid receiver) by a bending load cell, and using flexible pipes for connections (Figure 2.13) [89].

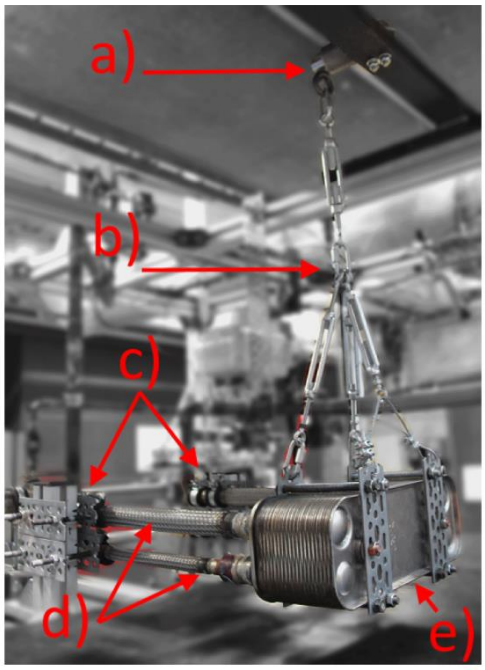

Figure 2.13 – Experimental approach for charge distribution assessment proposed in [89].

In this paragraph, the filling process of an empty tank is described as a simple case of real circuit filling, in order to identify the thermodynamic variables that depends on the fluid charge; also, a simplified empirical procedure to estimate the fluid charge in the circuit during plant downtime is proposed.

2.2.1 Analysis of charge-dependent variables

Figure 2.14 represents a simplification of what happens to the fluid during a charge procedure: a cylindrical tank of capacity equal to 10 l, from empty, is gradually filled with R134a. The fluid source is supposed of infinite capacity. The whole system is at ambient temperature, here supposed constant during the whole procedure and equal to 25 °C. The definition of average density and vapor quality are reported in Equation *(2.2)* and *(2.3)*, where V_{cyl} is the volume of the tank, while m_{cyl} and $m_{cyl,v}$ are the total mass and the vapor mass of fluid inside the tank, respectively.

$$\rho_{avg} = \frac{m_{cyl}}{V_{cyl}} \tag{2.2}$$

$$q_{cyl} = \frac{m_{cyl,v}}{m_{cyl}} \tag{2.3}$$

When introducing a small amount of refrigerant (let us say lower than 0.35 kg) in the empty cylinder, the corresponding average density keeps lower than 35 kg/m^3, which is about the value of the saturated vapor density at a temperature of 25 °C. Hence, the fluid is in the superheated region, there will be no liquid inside the cylinder, and the pressure will depend on the ambient temperature (which is constant) and on the actual mass of fluid charged. The vapor quality (expressed by Equation 2.2) is not defined in this region. If the charged mass rises above 35 kg/m^3, the corresponding average density will increase too, achieving the value corresponding to the saturated state, and the first liquid drops start to form and remain suspended in the vapor. In this phase, pressure value turns to depend only on temperature, while the fluid mass affects only the vapor quality of the fluid (that is reduced as m_{cyl} rises), not further increasing the pressure inside the tank. This will be valid as long as the fluid remains in the two-phase condition. From this point, introducing more fluid into the cylinder, the vapor quality is reduced from 1 to 0 as the density increases from 35 kg/m^3 to 1207 kg/m^3. As showed in Figure 2.15a, the

decreasing curve of quality is not linear, since the quality is reduced of 90% (from 1 to 0.1) as the density increases from the minimum to 260 kg/m3 (which is only the 19% of the maximum value of ρ_{2p}), corresponding to the charge of 2.6 kg of fluid. Continuing to introduce mass of fluid, the variation of the quality is much slower than in the first step. Therefore, in this phase increasing the fluid charge will increase the liquid content (thus reducing the vapor quality), that begins to lay at the bottom of the cylinder. The pressure value, instead, since it is the saturation pressure at the ambient temperature, keeps constant and equal to 6.6 bar. When a mass around 12 kg has been introduced in the tank, the fluid is close to achieve the saturated liquid condition, corresponding to a value of density around 1200 kg/m^3. With more charge, the fluid passes to the subcooled state, and the pressure starts again to increase as the mass inside the cylinder rises. The pressure variation inside a defined volume as function of the fluid density is reported in Figure 2.15b for temperature equal to 15 °C, 25 °C and 40 °C. Since the fluid in the liquid phase is uncompressible, the further increment of mass leads to a very high gradient of pressure rise (around 1.8 $\frac{bar \cdot m^3}{kg}$, which for a tank of 10 l means that the pressure increases of 18 bar for every 0.1 kg of fluid introduced. This can be very dangerous for the risk of tank explosion or damages to junctions and other components. For this reason the regulation on refrigerator storage recommends not to fill the tanks with a mass of fluid that exceed the 80% of the nominal capacity.

In ORC systems, in order to relate the fluid charge to the circuit volume, a charge ratio can be defined as the ratio of the actual mass in the circuit to the maximum theoretical mass that the circuit can hold, that corresponds to the total internal volume multiplied by the liquid density at a reference temperature.

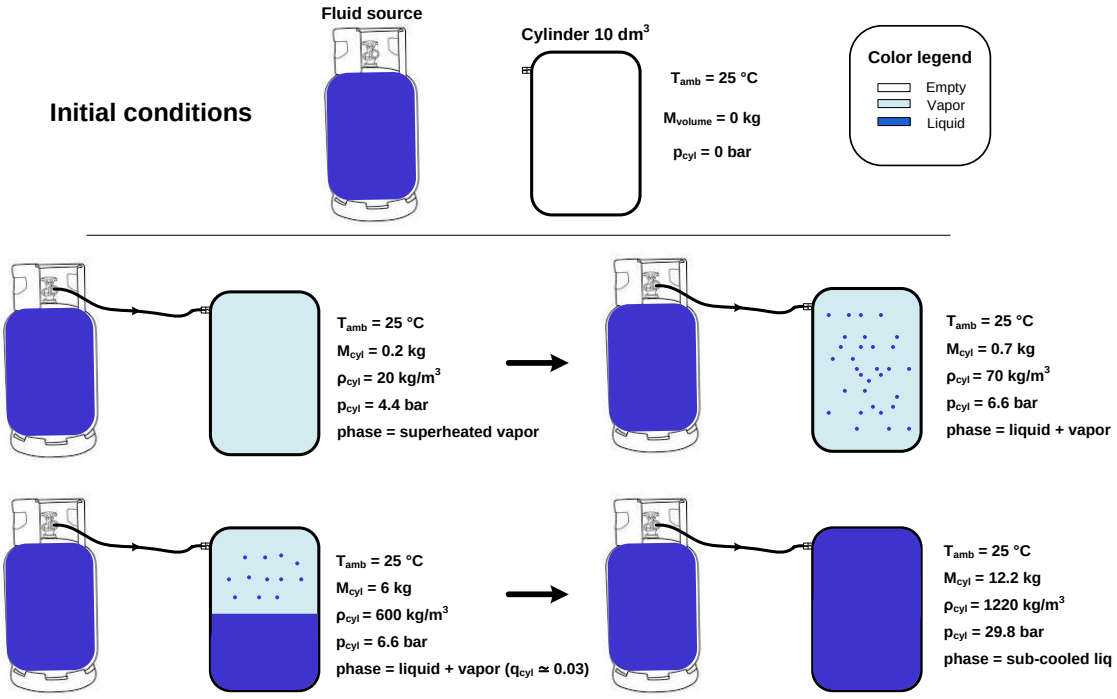

Figure 2.14 – Representation of HFC-134a filling process

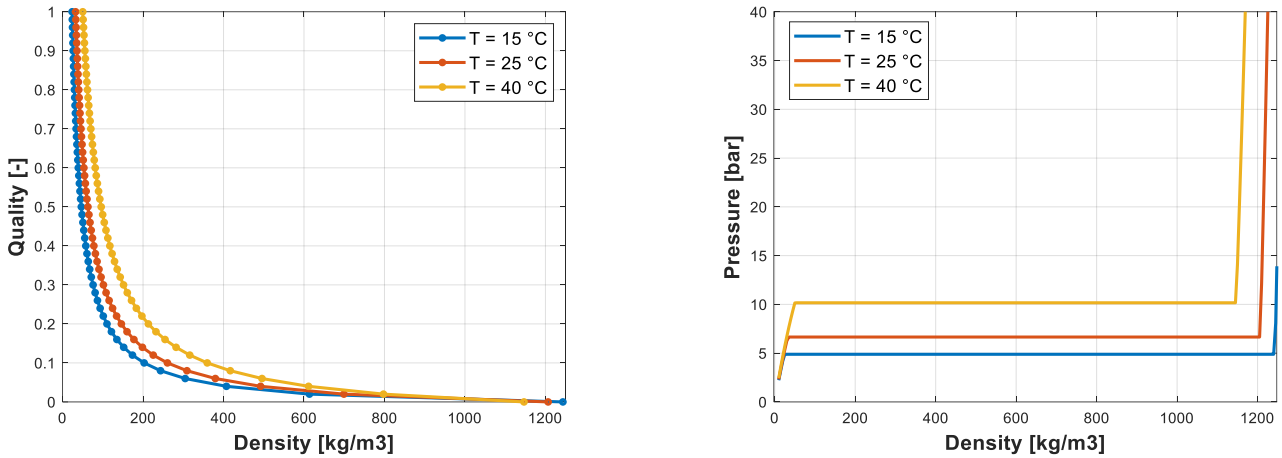

Figure 2.15 – a) HFC-134a vapor quality vs. density at different temperature; b) pressure vs. density at different temperature

2.2.2 Estimation of fluid charge in the circuit

Having pointed out the charge mechanism, an estimation of the fluid charge that is already inside the circuit can be done by applying a similar approach to that above described. The method requires the system to be provided with a liquid receiver installed underneath the condenser, and that both can be closed together from the rest of the circuit by sealed valves to form a large tank (Figure 2.16). The liquid receiver shall have the liquid level indicators. This arrangement is a good practice in the design of micro-ORC systems: the condenser should be above the receiver, in the highest part of the plant, in order to increase the net positive suction head of the pump. The shut-off valves before the condenser and after the recuperator are used as fluid tank during machine maintenance operations, or during periods of inactivity. Moreover, the use of the condenser allows expelling the air that is possibly entered into the circuit. This is done when the pressure and temperature values are not consistent with the values related to a saturated fluid, and in particular if the pressure exceeds the saturation pressure at the fluid temperature, indicating the presence of a certain amount of air in the tank. The air tends to go in the upper point of the circuit, due to the lower density with respect to the working fluid. Thus the air can be expelled by a valve on the top of the condenser, verifying by steps the achievement of the saturation conditions, i.e. verifying that pressure corresponds to the saturation pressure at the ambient temperature. The presence of air should be avoided because air works as non-condensable gas, penalizing the heat transfer at the condenser and increasing the condensation pressure.

The estimation is based on the measurements of the static values of the fluid properties inside the tank, and in particular:

- fluid temperature, generally corresponding to the ambient temperature, T_4
- pressure inside the tank, p_4
- indication of the liquid level inside the receiver, x_{liq}

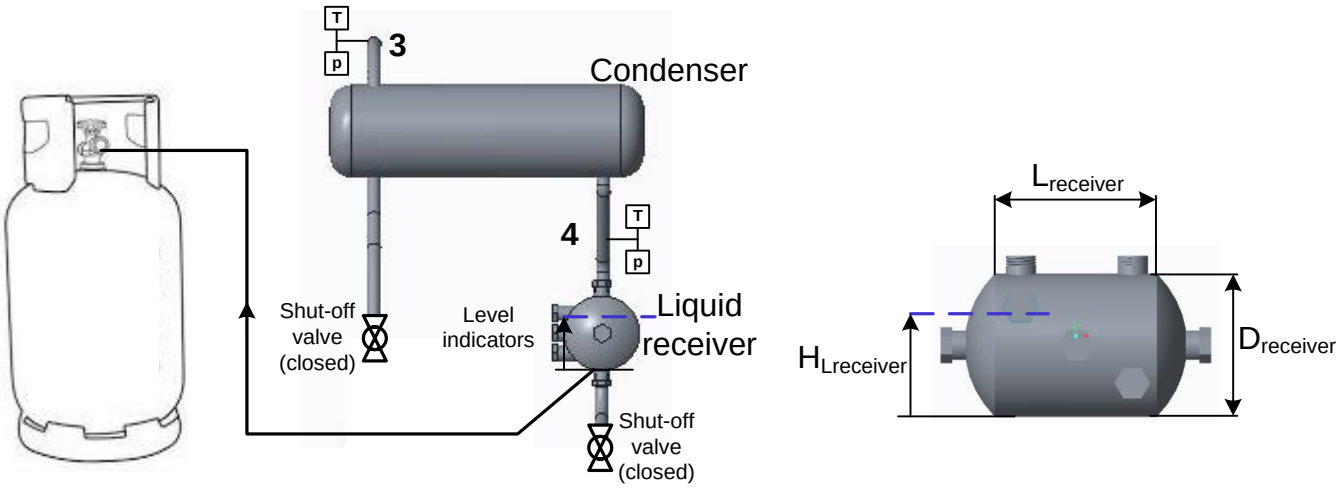

Figure 2.16 – Circuit arrangement for charge estimation and verification

Supposing that the level of the liquid in the tank is the one indicated in Figure 2.16 (blue dashed line), the procedure consists of four steps:

1. calculate the volume of the condenser, of the receiver and of the pipes enclosed within the shut-off valves. The diameter and length of the receiver, that in this case is an horizontal cylinder, are required too. All the values are reported in Table 2-6. It can be noticed how the pipes volumes are very small with respect to the condenser and receiver volumes.

Table 2-6 – Volume of the different part composing the fluid tank

Part	***Volume***
Condenser	0.034 m^3
Liquid receiver	0.019 m^3
Pipe downstream the condenser	0.0008 m^3
Pipe downstream the receiver	0.0005 m^3
Total volume	0.0543 m^3

2. estimate the volume of liquid from the liquid level, by using the formula reported in Equation *(2.4)*:

$$V_{l,receiver} = L_{receiver} \cdot \left[\alpha \cdot \frac{D_{receiver}^2}{4} - \left(\frac{D_{receiver}}{2} - H_{receiver}\right) \cdot \sqrt{D_{receiver} \cdot H_{l,receiver} \cdot H_{receiver}^2}\right] \quad (2.4)$$

where $L_{receiver}$ and $D_{receiver}$ are the length and the diameter of the liquid receiver, $H_{l,receiver}$ is the level of liquid inside the receiver and the coefficient α is determined by the following expression:

$$\alpha = \arccos\left(1 - 2 \cdot \frac{H_{l,receiver}}{D_{receiver}}\right) \quad (2.5)$$

3. calculate via CoolProp the density of saturated liquid and saturated vapor corresponding to the pressure measured in the considered volume (p_4), $\rho_l(p_4)$ and $\rho_v(p_4)$
4. determine the mass of liquid and the mass of vapor by means of Equations *(2.6)* and *(2.7)*.

$$M_l = \rho_l(p_4) \cdot \left(V_{l,receiver} + V_{pipe1}\right) \quad (2.6)$$

$$M_v = \rho_v(p_4) \cdot \left(V_{receiver} - V_{l,receiver} + V_{pipe2} + V_{condenser}\right) \quad (2.7)$$

with V_{pipe1} and V_{pipe1} equal to the volume of the pipe downstream the recuperator (filled with liquid) and the volume the pipe downstream the condenser, respectively. The vapor quality of the two-phase mixture can be calculated as the ratio of the mass of vapor on the total fluid mass, $M_l + M_v$.
The validation of the above-described method has been made by transferring part of the fluid from the circuit to an empty recovery tank, which has been placed on a scale. In order to make the weight procedure quicker, the fluid was extracted until the pressure inside the volume dropped below the saturation pressure at ambient temperature. In this way, the removal of the superheated vapor left in the circuit, which normally requires the use of a recovery pump for relatively long time (due to the high value of the specific volume and to the pressure difference between the circuit and the filled tank), is not completed. The fluid is now in superheated phase, and the density can be obtained from the measured values of pressure and temperature, and then multiplied by the total volume of the circuit. The total mass that was inside the circuit corresponds to the sum of the extracted mass and the left mass, and can be compared to the value of the mass that was estimated. The method has been verified with two values of fluid charge, 20 kg and 25 kg, reporting in both cases an underestimation lower than 1 kg.

2.3 Acquisition and control system

2.3.1 Sensors and actuators

The aim of an accurate experimental characterization of a system that is not commercial – hence it is not provided with detailed fact sheet – is achievable by means of the installation of many sensors to measure the different key properties over the most relevant section of the circuit. For the system under investigation, the operating conditions and performance are evaluated in terms of pressure, temperature, specific enthalpy, density, flow rates and electrical power. In Table 2-7 the detail of the acquisition devices is reported including the type of sensor, range of measurement, the output signal, the rated accuracy and the acquisition module. Temperature is acquired by T-type and K-type thermocouples, respectively in the organic fluid and in the water circuits. Pressure is measured using absolute pressure transducers (model Honeywell FP2000) with accuracy of 0.25% of full scale value and 300 Hz of response frequency. Both thermocouples and pressure sensors are periodically calibrated (once every two years at least) in the laboratory within the operating range indicated in the table. The mass flow rate of the liquid organic fluid is measured at the feed-pump inlet side by a Coriolis flow meter (model Endress+Hauser Promass), that provides the possibility to directly measure also the density of the fluid. Hot and cold water volume flow rates are acquired by two electromagnetic flow meters (model Endress+Hauser Promag) with 0.5% accuracy. Since the hot water circuit operates at higher pressure than the atmospheric value, pressure transducers with appropriate measuring range are also installed at inlet and outlet of the hot water pump. Finally, expander and pump powers are obtained from the acquisition of the three-phase voltage and current by Hall effect electric transducers installed between the generator and the load, and between the inverter and the pump motor. The voltage transducers measure the phase voltages, with reference to a star point realized in the sensor case; thus, to assess the voltage seen by the load (line voltage, since the load is connected in delta), the phase voltage must be multiplied by the square root of 3. Current and voltage transducers are mounted in a printed circuit board (PCB) contained in single plastic cases (one case for the pump and one for the expander), and have been realized and calibrated at the Laboratory of Electrical Measurements of the University of Bologna. The electric transducers are also employed for determining the electric frequency of pump and expander, which are used to calculate the rotating speed of the two machines. All the signals are wired to the acquisition device, which is a National Instruments CompactRIO model cRIO 9022, coupled with a chassis model cRIO 9114 with 8 slots, where the input/output modules are connected (see Figure 2.17).

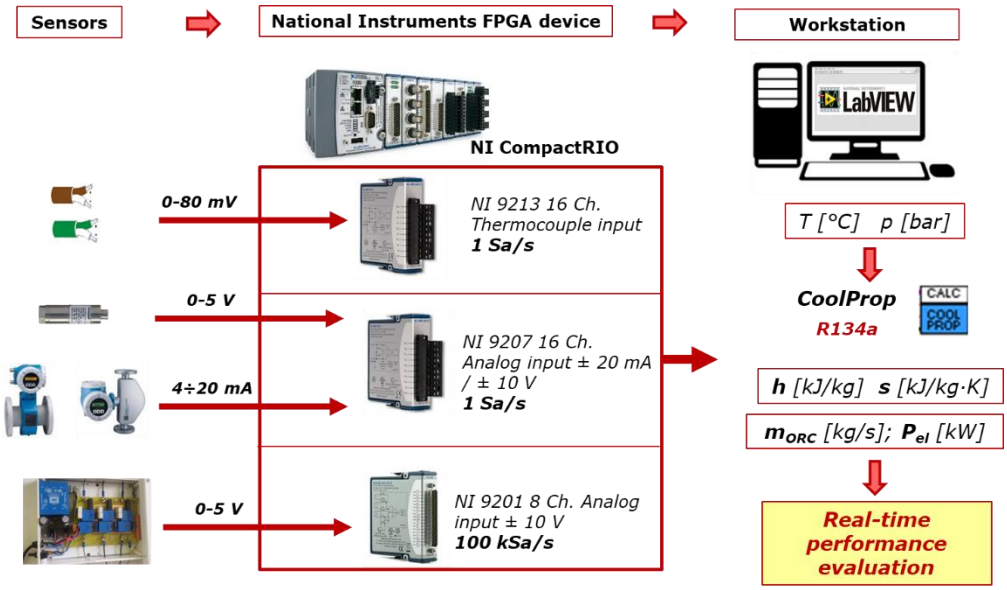

Figure 2.17 – Architecture of the acquisition system

a)

b)

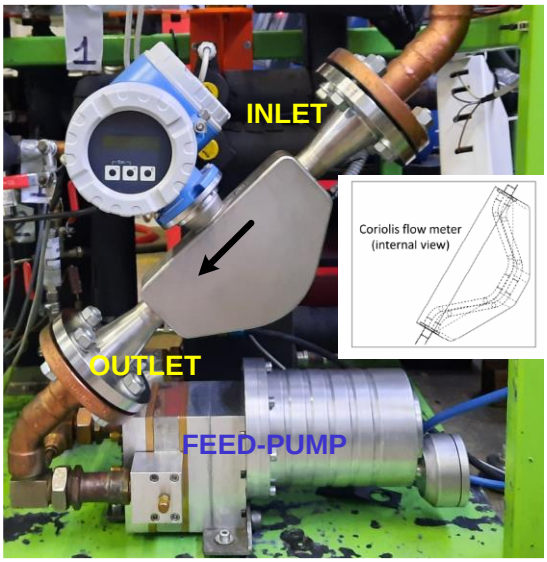

c)

Figure 2.18 – Photos of installed sensors: a) printed circuit board with voltage and current sensors; b) tee-fitting with thermocouple and pressure transducer; c) Coriolis flow meter

Table 2-7 – Specifics of the acquisition/control hardware

Variable	Layout point (Figure 2.2)	Sensor/actuator	Calibration /working range	Output signal	COTS accuracy*	Input module
SENSORS						
ORC Temperatures	1, 1bp, 2, 3, 4, 5, 6, 7	T-type thermocouple	0-90 °C	± 80 mV	±0.5 °C	NI9213-Thermocouple input
Hot water temperatures	10, 11	K-type thermocouple	0-90 °C	± 80 mV	±0.5 °C	
Cold water temperatures	12, 13					
ORC Pressures	1, 6, 7	Pressure transducer Honeywell FP200	0-30 bar	0-5 V	±0.25 % FS	NI9201-Voltage AI
	2, 3, 4		0-10 bar			
Hot water pressure	H_{in}, H_{out}	Pressure transducer	1-6 bar	0-5 V	±0.25 % FS	
ORC mass flow rate	5	Coriolis mass flow meter (H+E Promass)	0.05-1.00 kg/s	4-20 mA	±0.3 % RV	NI9203-Current AI
ORC density			10-1300 kg/m^3	4-20 mA	±0.1 kg/m^3	
Hot water flow rate	Hin	Magnetic flow meter (H+E Promag)	0-6.4 l/s	4-20 mA	±0.5 % RV	
Cold water flow rate	Cin	Magnetic flow meter (H+E Promag)	0-9.8 l/s	4-20 mA	±0.5 % RV	
Electric current and voltage	Expander generator and pump motor supply lines	PCB mounted Hall effect voltage and current transducers	0-400 V 0-5 A	0-4 V	±0.1 % RV ±0.2 % RV	NI9215-Voltage AI
ACTUATORS						
Hot water flow rate	H_{in}	Motorized ball valve	0-100%	0-10 V	-	NI 9263-Voltage AO
Hot water inlet temperature	H_{in}	Motorized three-way valve	0-100%	0-10 V	-	NI 9263-Voltage AO
Hot water drain	H_{out}	Solenoid valve	On-off	Relay	-	NI 9482-Relay output

*Component Off-the-Shelf (COTS) accuracy: it refers to the instrument accuracy as indicated on the data sheet, before individual calibration or calibration of the measurement chain; see section Measurement Uncertainty in Chapter 3.

2.3.2 Acquisition and control software

The acquisition software has been developed in LabVIEW environment by implementing a FPGA project. It is split in two levels, corresponding to as many VIs (virtual instruments, the LabVIEW programs/subroutines) that are executed at the same time when the acquisition system is running: the *Real Time VI*, running in the CompactRIO controller and executing the basic operations such as data extraction and first elaboration with a fixed time-step, and the *Host VI*, running in the host PC and containing more complex calculations, such as the CoolProp functions for calculating enthalpies, entropies and other thermodynamic quantities, as well as the saving functions that register all the acquired data into a TDMS file. The latter that can be read with the tool LabVIEW DIADEM or converted for the use with other common languages. The user interface is also developed in the *Host VI*. Data between the two levels are communicated by means of UDP protocol.
To be rigorous, there is another VI (*FPGA VI*) that is developed at the lowest level with most basic functions. It defines the modules' channels to read and to write, and separates the data in different loops running at different frequency, that is controlled in the *Real Time VI*. The *FPGA VI* is used to generate the *bit file* that is compiled in the FPGA device, programming the instructions for the input/output channels. Thus, it is executed only the first time for the compilation, and it only needs to be re-compiled every time the *FPGA VI* is modified (for example for the introduction of a new I/O module).

Real time VI

A simplified schematization of the block diagram of the *Real Time VI* is presented in Figure 2.19. It is divided into three main loops with different temporizations, depending on the type of signal that has to be processed. **Loop 1** includes all process variables, such as temperatures, pressures and flow rates, all acquired with low frequency ranging from 1 Hz to 10 Hz. The acquisition frequency for these signals is decided by the user and depends on the objective of the test – whether steady-state or dynamic analysis. This frequency can be considered the main (or reference) frequency of the whole acquisition and control system, for reasons that will be clearer in the following. The analogue signals are separated to be converted each in the proper way. The conversion curve of pressure signals was obtained from the calibration of the pressure transducers, accounting for the non-linearity and for the offset. These curves are available only for ORC pressure sensors, while for water pressure no calibration was carried out and the transduction is assumed linear between the minimum and the full scale values of the sensor. The same applies to the conversion of all the flow rate meters, whose calibration curve is given in the data sheets. The conversion of the analogue signals from pressure sensors and from flow meters is implemented in the *Analogue Conversion block*. Regarding the temperature signals coming from the thermocouples, the conversion from mV to degrees Celsius is performed in the *Thermocouple Conversion block*, included in the LabVIEW library. The correction of the values is made in the *Temperature Calibration* block, where the equations resulting from the thermocouples calibration procedure are implemented. The calibration equations are reported both for temperatures and pressures in Table 2-8. The variables named v_{pi} and T_{ri} are, respectively, the voltage output of the pressure sensors and the raw temperatures. In the case the calibration equations is not available, the final temperature value is equal to the output of the *Thermocouple Conversion block*, while the pressure are converted simply multiplying the voltage (v_{pi}) by the ratio of the pressure full scale (10 bar or 30 bar for the ORC sensors) to the voltage signal full scale (5 V), i.e. adopting a linear curve of transduction between 0 and the sensor full scale, without any offset. Loop 1 contains also the commands that perform the control of the valves actuators for hot water flow and temperature regulation, that will be detailed in the following paragraph.

Table 2-8 – Calibration equations for ORC pressures and temperatures

Sensor (with reference to Fig. 2.2)	Equation
p_1	$p_1 = v_{p1} \cdot 5.995140 + 0.003054$
p_2	$p_2 = v_{p2} \cdot 1.999869 + 0.032892$
p_3	$p_3 = v_{p3} \cdot 5 + 0.015$
p_4	$p_4 = v_{p4} \cdot 1.997407 - 0.026502$
p_5	$p_5 = v_{p5} \cdot 5.978277 + 0.054372$
p_6	$p_6 = v_{p6} \cdot 5.999043 + 0.006396$
p_7	$p_7 = v_{p7} \cdot 5.994240 + 0.013500$
T_1	$T_1 = T_{r1} \cdot 1.0051276890 - 0.2844332686$
T_2	$T_2 = T_{r2} \cdot 1.0056740793 - 0.2399085011$
T_3	$T_3 = T_{r3} \cdot 1.0074857527 - 0.1829413593$
T_4	$T_4 = T_{r4} \cdot 1.0041436253 - 0.0307886090$
T_6	$T_6 = T_{r6} \cdot 1.0049238152 - 0.0627281155$
T_7	$T_7 = T_{r7} \cdot 1.0036321750 - 0.0206921998$

Loop 2 performs the conditioning of the analog signals from the electric sensors that measure the electrical power produced by the expander. These sensors measure the instantaneous value of voltage and current of each of the three phases of the electric output line. The product of voltage and current gives the instantaneous power of each phase, which is then averaged over a period equal to the acquisition period of the Loop 1 (the reference period), so that both the two classes of data are synchronized. To be more precise, to perform an accurate average

calculation, the array of the instantaneous power has to be cut in order to obtain a number of elements that compose an integer number of signal periods. The number of elements for the average computation varies depending on the signal frequency, which is proportional to the expander rotating speed. Thus, a routine has been developed in the VI for determining this number on each iteration of the Loop 1. The computed average powers are then summed to obtain the total expander power output. The expression reported in Equation *(2.8)* summarizes the above-mentioned operation.

$$\dot{W}_{\text{exp,el}} = \overline{\imath_1(t) \cdot v_1(t)} + \overline{\imath_2(t) \cdot v_2(t)} + \overline{\imath_3(t) \cdot v_3(t)} \qquad (2.8)$$

where $\dot{W}_{\text{exp,el}}$ is the expander power output, averaged over the reference period, $i_1(t)$ and $v_1(t)$ are the instant current and voltage, respectively. The operating frequency of Loop 2 is set as 100 kHz, being this value a good trade-off between signal accuracy and computational performance.

Loop 3 is dedicated to the conditioning of the signals of the pump electric power sensors, and follows the same logic applied to the expander one. In this case, due to a lower value of the electrical frequency of the measured signals, the imposed value of the acquisition frequency is equal to 50 kHz. For both expander and pump, the voltage signal waveform of the first phase is processed by the LabVIEW function named *Extract Single Tone Information*, which gives as output the electric frequency of the waveform. The latter is then used to evaluate the rotating frequency of the machine shafts. In the case of the expander, no gear is interposed between the expander shaft and the generator, and the mechanical frequency is equal to the ratio of the electrical frequency and the number of pole pairs (4) (Equation *(2.9)*). Differently, between the pump drive shaft and the rotor a speed reducer is interposed, thus the mechanical frequency obtained as for the expander must be further divided by the speed ratio (3) (Equation *(2.10)*).

$$f_{exp} = \frac{f_{exp,el}}{4}\ [Hz] \qquad (2.9)$$

$$f_p = \frac{f_{p,el}}{12}\ [Hz] \qquad (2.10)$$

All the data are collected in an array and sent to the *Host VI* using UDP protocol.

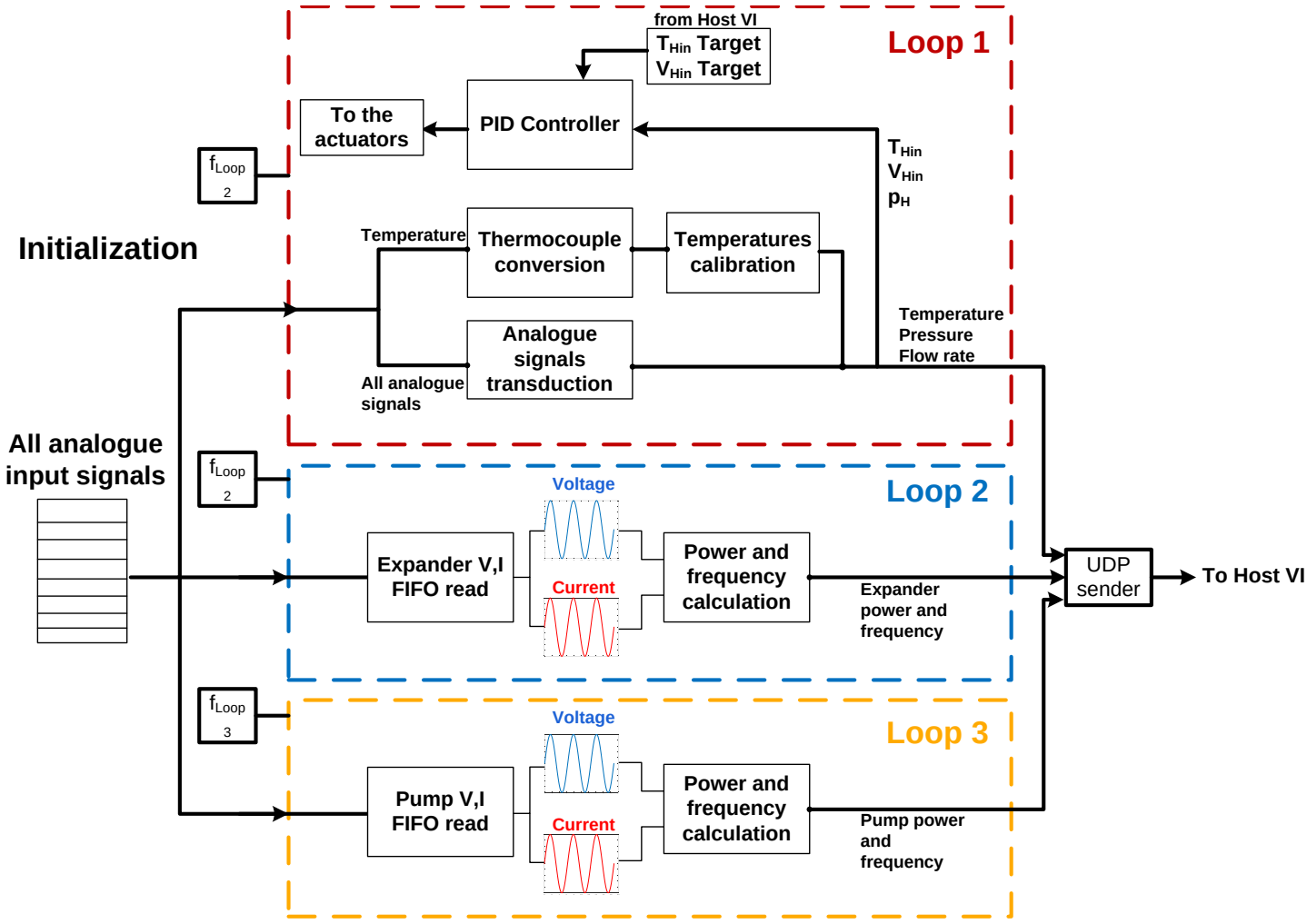

Figure 2.19 – Scheme of the logic implemented in the Real Time VI

Host VI

The Host VI operations are conceptually represented in Figure 2.20. All the charts and indicators visualized in the user interface are created in this VI. In addition, the Host VI contains the computation of all the thermodynamic quantities that are not directly measured. This operation is performed by the CoolProp library, which is called by a specific LabVIEW sub-VI. The latter always requires two variables as input, giving back all the properties corresponding to the thermodynamic state determined by the two input variables. Generally, if the working fluid is in a single phase state (superheated vapor or subcooled liquid), the two inputs are the temperature and pressure of the fluid in that section. If the fluid is in the two-phase region, temperature and pressure are no more sufficient to determine the fluid state; in this case, a different quantity, that can be the vapor quality, density or enthalpy, must replace the temperature or the pressure as one of the inputs. To calculate the fluid properties of a point in the limit curve (saturated liquid or vapor), one variable between temperature and pressure has to be given as input to the CoolProp sub-VI, the other input being a value equal to 0 or to 1 of the fluid quality. The assessment of the thermodynamic state of each section of the ORC circuit allows to draw the thermodynamic cycle on temperature-entropy (T-s) and pressure-enthalpy (p-h) diagrams, that are shown and updated in real time during the tests.

Another main function implemented in the Host VI is the calculation of the instant performance of the ORC system and of its components, useful to better understand the system operation during the course of the test. The rigorous calculation of the performance is performed again in post processing, using the averaged measured values taken in steady-state conditions. Figure 2.21 reports the interface of the acquisition system, programmed in the Host VI. It consists of several pages containing each one the graphical and digital indicators of all the variables.

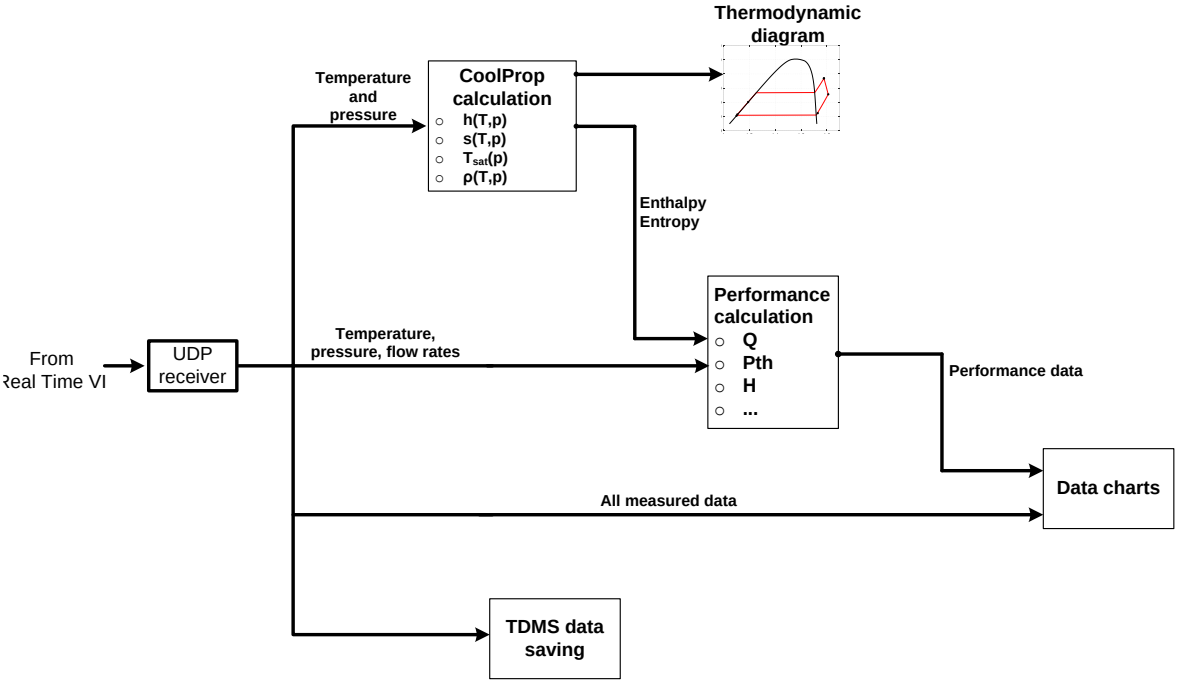

Figure 2.20 - Scheme of the logic implemented in the Host VI

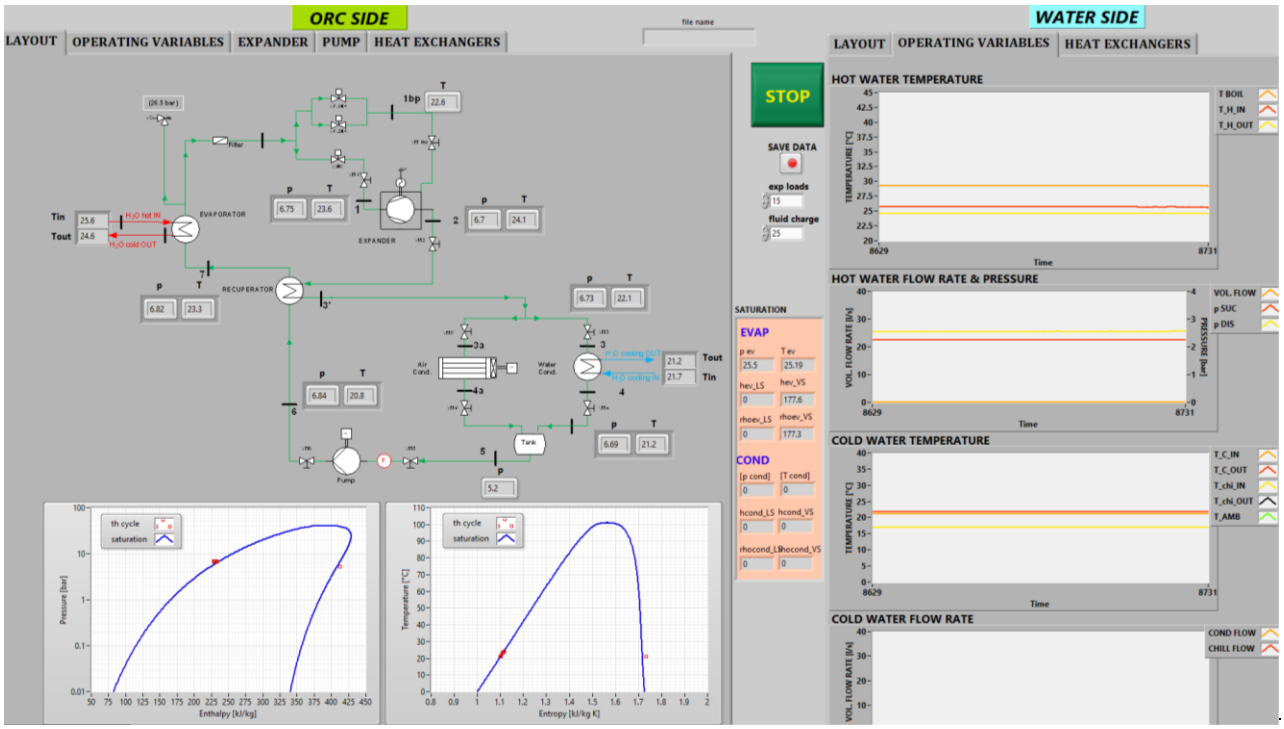

Figure 2.21 – Acquisition system user interface

Control system for hot water loop

The control system implemented on the hot water loop allows regulating automatically the water temperature and flow rate. Since the water pump works at fixed mode, the regulation of the flow rate is performed thanks to a two-way motorized ball valve, installed at the evaporator inlet. This valve is controlled by an analog voltage signal sent by the module NI 9263. The signal to the valve actuator results from a PID controller implemented in LabVIEW. Thus the user sets a constant value of water flow rate, and the system adjusts consequently the position of the ball valve. A dynamic profile of flow rate is also possible by setting as input a time vector instead of a constant value.

The regulation of the hot water temperature is more complex. In the original setup, the regulation was made by manually switching on and off the electric heater elements of the puffer. This was a very basic method, which did not ensure to maintain with sufficient precision a constant value of temperature at the evaporator inlet. Moreover, rapid and controlled variations, both rising and decreasing, were impossible to perform with this procedure.

A more accurate control technique has been implemented in this thesis, by installing a three-way motorized valve, which mixes the water heated by the puffer with colder water. By switching the manual valve VM1, two alternative configurations may be used depending on the test purpose: closed loop, in which the colder water is the water stream returning from the evaporator, that has been cooled by transferring thermal power to the organic fluid for its vaporization (Figure 2.22a), and open loop, that uses tap water at a temperature much lower and not depending on the operating condition (Figure 2.22b). In both cases the valve is controlled by a PID controller, which operates based on the temperature measurement at the evaporator inlet. The **closed loop** is selected in case of steady-state operation. Generally, the temperature of water in the evaporator drops of 2-6 °C, depending on temperature level and on the flow rates of water and working fluid. With this method it is possible to maintain the variation of water temperature at the evaporator inlet within the ± 0.3 °C range, with respect to the value imposed by the user in the front panel. In addition, the closed loop can be used to execute rapid increasing temperature changes, to evaluate the system response to dynamic conditions of the heat source. This condition is achieved by temporarily closing the three-way valve from the heater outlet side (port A of the three-way valve), making the water recirculate from the evaporator outlet to its inlet, by-passing the heater. In this way, the water inside the heater increases its

temperature without any heat transfer in the evaporator. As soon as the water inside the puffer has reached the desired temperature, the port A of the three-way valve is opened and the heated water suddenly flows to the evaporator.

The **open loop** configuration can be implemented by closing the manual valve VM1 and actuating the on-off valve V_{sup}, which is controlled remotely and lets enter tap water into the circuit. Tap water is at a temperature between 10 °C and 15 °C, depending on the season, while the supply pressure can be regulated up to 4 bar gauge. The open loop is mainly suitable in case a fast decreasing variation of the water temperature at the evaporator is required. This option involves a more complex control system in order to perform an efficient control, since more than one actuator must be managed simultaneously. When the user imposes, for example, a temperature drop of 10 °C, the supply valve opens and, at the same time, the port C of the three-way valve starts to open, according to the feedback signal acquired by the thermocouple at evaporator inlet. Cold water starts to enter the circuit, moved by the pressure difference between the supply network and the circuit, reducing the water temperature at the evaporator inlet. By introducing water from outside, the pressure inside the circuit would start to increase, trying to achieve the supply pressure of the water network. Thus, a drain valve is required in order to discharge a certain amount of water and maintain the pressure inside the circuit at its operating value (between 1 and 2 barg). This is an on-off valve remotely actuated by the control system, indicated as V_{drain} in the layout of Figure 2.10. The valve has been installed at the lowest point of the circuit, on the evaporator outlet pipe returning to the electric heater. This choice allows to discharge only the water already cooled by the organic fluid in the evaporator, limiting the waste of thermal power introduced in the heater with the heater elements, that would be higher if the water was discharged from the puffer outlet. Since the loss of thermal power still remains, an additional 10-kW heater element was installed in the puffer to boost the thermal input up to 42 kW.

The first tuning of the gains of the PID controllers have been conducted using the Ziegler-Nichols method [90]. The gains resulting from the field tuning are reported in Table 2-9 for the three controllers. Note that despite the same actuator is used for the closed and the open loop, the tuned gains are different. Moreover, it was observed that the gain values included in Table 2-9, related to the three-way valve control, are valid only for a limited range of hot water flow rate ($\dot{V}_H$), between 2 l/s and 2.7 l/s, corresponding to the range usually operated for the system under investigation (the value of 2.7 l/s corresponds to the maximum water flow rate achievable in the hot water loop). With flow rates lower than 1.5 l/s, if the PID gains are kept unvaried, the controlled variable (T_{Hin}) is forced to repeated overshoots. To restore the normal behavior of the valve controller, the PID gains should be re-tuned. The analysis of the transient response to variations of the heat source conditions can take advantage of this anomaly: indeed, in order to obtain an oscillating signal around the set point of hot water temperature, a systematic overshoot of the controlled variable can be forced by reducing the water flow rate, maintaining the same PID gains schedule tuned for high value of$\dot{V}_H$. This behavior is analyzed more in detail in the transient analysis reported in Chapter 4.

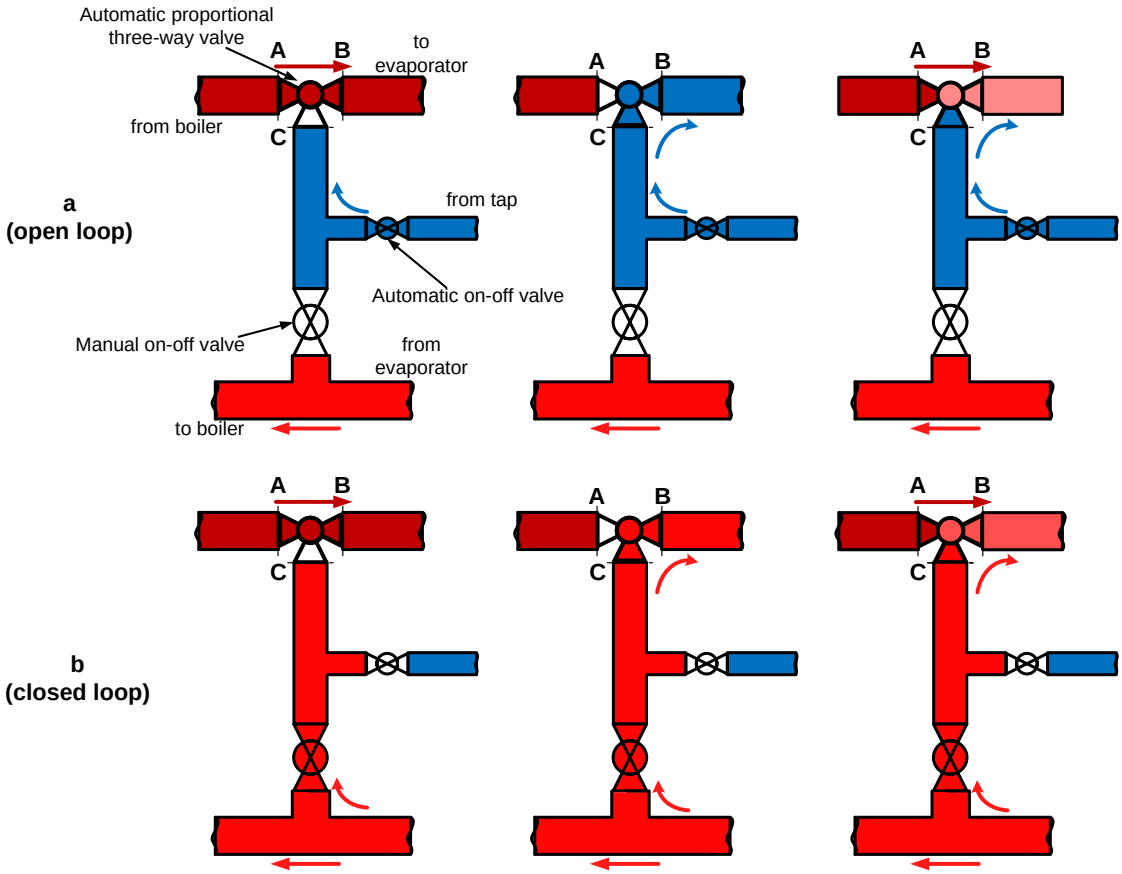

Figure 2.22 – Schematic representation of hot water temperature regulation system

Table 2-9 – Tuned PID gains for hot water circuit

	K_p [-]	K_I [-]	K_d [-]
Ball valve (flow regulation)	1.12	0.25	0
Three-way valve (flow temperature) – closed loop	0.9	0.3	0
Three-way valve (flow temperature) – open loop	1	0.5	0

CHAPTER 3

3 Steady-state experimental analysis

3.1 Test setup

The aim of the steady-state experimental campaign was a full characterization of the operating conditions and of the performance of the micro-ORC system. The tests have been conducted under stationary conditions of the heat source, of the cold sink, of the electric load and of the feed-pump frequency. Hot water temperature has been varied between 65 °C and 85 °C, with hot water flow rate ranging between 1.3 l/s and 2.7 l/s. Cold water flow rate has been regulated between 1.4 l/s and 2.9 l/s, while cold water temperature varied depending on the cold sink used for the specific test. Indeed, when the water well was used, temperature was affected by the ambient conditions, varying between 18 °C in winter up to 27 °C during summertime. When tap water circuit was implemented, cold water temperature ranged between 8 °C and 16 °C, depending on the season as well. In both cases, the user did not have any direct control on the water temperature. The electric load was adjusted between the minimum value of one, corresponding to three light bulbs activated, and the maximum of five, corresponding to 15 light bulbs. Since each bulb has a nominal impedance equal to 288 Ω and the loads are connected in parallel, the total equivalent load impedance of each phase was adjusted by discrete steps between 288 Ω (1 load) and 58 Ω (5 loads). The characteristics of the regulation of the electric load are summarized in Table 3-1. It should be noted that the nominal power related to a certain number of loads refers only to the power absorbed by the light bulbs when supplied with a voltage of 380 V, and it does not correspond to the actual electric power output of the expander. For analogous reason, also the actual load impedance, calculated by means of electric current and voltage measurements, results different from the nominal value of the light bulbs, and in particular is always lower. The load impedance has an important impact on the thermo-fluid dynamics performance of the cycle and on the expander operation, as will be detailed in the next paragraphs.

Table 3-1 – Electric load set points

Number of loads / light bulbs	Nominal power @ 380 V [W]	Nominal equivalent load impedance for each phase [Ω]	Number of operating points acquired
1 / 3	600	288	16
2 / 6	1200	144	15
3 / 9	1800	96	24
4 / 12	2400	72	20
5 / 15	3000	57.6	44

Finally, the feed-pump rotating frequency has been varied between 20 Hz and 55 Hz using the inverter that controls the pump motor. The maximum value of frequency of 60 Hz achievable with the inverter was never tested, due to problems of instability experienced at the highest frequencies. As discussed in the previous chapter, the values of frequency mentioned above refer to the electrical frequency, while the actual mechanical rotating speed is obtained by Equation (3.1), which is reported here again as reference:

$$N_{pump} = \frac{f_p}{n_p \cdot r_s} \cdot 60 \tag{3.1}$$

with f_p pump frequency, n_p number of pole pairs and r_s the speed reduction ratio. After every variation of an operating variable, the system was left for a period longer than 10 minutes in order to achieve the steady-state condition, according to the criteria described in the next paragraph. A total number of 120 steady state operating points have been acquired. Figure 3.1 reports a map of the values of hot and cold water temperature (T_{Hin} and T_{Cin}) and of pump rotating speed (N_{pump}), describing the steady-state operating conditions tested during this campaign. The objectives of the experimental steady-state analysis are different:

- assessing the performance of the micro-ORC system
- understanding how the controlled variables affect the system operation and performance
- providing experimental data to be used for the development and calibration of thermodynamic semi-empirical models

Table 3-2 collects the variables selected as main outputs of the analysis, together with the expected behavior in terms of dependence from the controlled variables of the test bench.

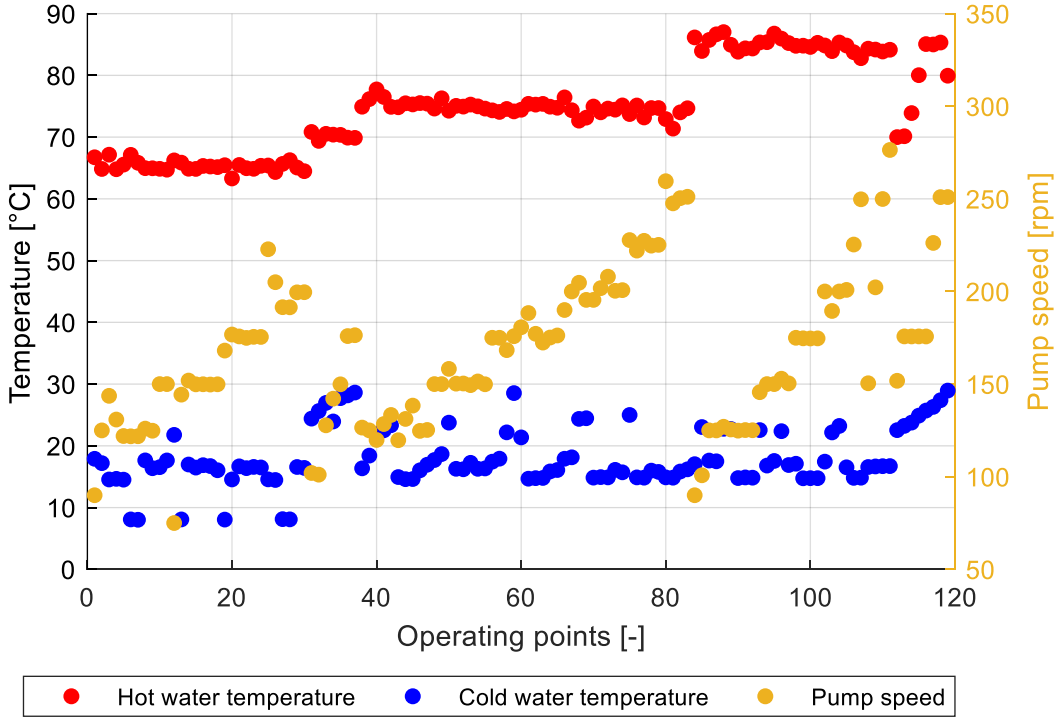

Figure 3.1 – Map of steady-state set points (hot and cold water temperature and pump speed).

Table 3-2 – Experimental analysis main outputs and their dependencies

Variable	Symbol	Expected main dependencies (level of dependency)
Evaporation pressure	p_1, p_6, p_7	Working fluid mass flow rate (strong) and external load (weak)
Condensation pressure	p_2, p_3, p_4	Cooling water temperature (strong) and working fluid mass flow rate (weak)
Superheating degree	ΔT_{sh}	Hot water temperature (strong) and evaporation pressure (strong)
Expander power output	$P_{exp,el}$	Pressure difference (strong), mass flow rate (strong) and external load (weak)
Expander rotating speed	N_{exp}	Working fluid mass flow rate (strong) and external load (weak)
Expander efficiency	η_{exp}	Pressure difference, mass flow rate and external load (weak)
Pump consumption	$P_{pump,el}$	Working fluid flow rate and pressure difference (strong)
Pump efficiency	η_{pump}	Working fluid flow rate and pressure difference (weak)

3.2 Steady-state detection

Accurate methodology for the steady-state detection (SSD) is critical for the correct evaluation of process performance, for the optimization and control purposes. Data used to build empirical or semi-empirical models should always be acquired when steady-state conditions have been achieved, otherwise the risk of erroneous parameters implementation, and the resulting model inaccuracy, increase. The criteria for establishing when a process variable is in stationary conditions may vary depending on the specific application and on the variable nature [91]. Several techniques have been proposed in the literature, mainly applied in process or chemical engineering ([92], [93]). A basic standard for ORC systems was suggested in [94], consisting in considering the variations of the variables trend on a manually identified steady-state time window, through the comparison between simple average values taken at different time. The difference between the average values must be lower than the maximum acceptable variations, defined in Table 3-3 for the typical classes of variables considered in ORC system investigation. It should be noted that temperature probes are in general subjected to several disturbances, such as conduction, radiation, thermal insulation etc., hence the magnitude of the overtime variation should be coupled with the temperature value. The constant value of the acceptable variation reported in Table 3-3 (0.5 °C) can be considered valid within a limited range of measured temperatures, as it is the range analyzed in this work (between 20 °C and 90 °C).

Table 3-3 – Acceptable variation for the steady-state condition according to Woodland et al. [94].

Measured variable	Maximum acceptable variation
Temperature	$\Delta < 0.5$ °C
Pressure	$\Delta < 2$ %
Mass flow rate	$\Delta < 2$ %
Rotational speed	$\Delta < 2$ %

Lecompte [95] applied a steady-state algorithm (derived from the one implemented by Kim et al. on an air conditioner [96]) on the experimental data of an 11 kW ORC system, based on the calculation of the moving standard deviation of the main process variables. In another study, the Authors adopted a similar method on their dynamic analysis of a transcritical CO_2 power cycle for heat recovery from a heavy-duty diesel engine; they computed the absolute deviation on a moving time window equal to 5 seconds and compared it to pre-set thresholds [97]. All the above-mentioned approaches are suitable for the post-processing application. On the other hand, the on-line implementation of a steady-state algorithm presents the advantage of improving the control during the test and of providing better sensitivity to the dynamic phenomena. In addition, the duration of the tests and the efforts for the data post-processing can be significantly reduced.

The on-line detection of the steady-state condition was here implemented by means of the algorithm R-test [98], which was applied to the test bench under investigation in a previous publication of the Author [99]. This approach was selected after a comparison against two other methods found in literature, namely the Moving Standard Deviation (MStD) [96] and the Wavelet transform [91], where the R-test demonstrated to be the most effective between the considered procedures, showing a good time response in all the tested conditions as well as the best match with the mean values calculated with the manual identification of the steady-state operation. It consists in evaluating the variations from the stationary conditions of the process variable trend, through the R_i index, calculated for each i-th process variable. The R_i value is computed in real-time as the ratio of two different estimates of the moving variance of the considered time-series of data, as expressed by Equation (3.2).

$$R_i = \frac{s_{1,i}^2}{s_{2,i}^2} \tag{3.2}$$

The two estimations $s_{1,i}^2$ and $s_{2,i}^2$ are computed by filtering the process variable and its variance, according to Equations (3.3) and (3.4).

$$s_{1,i}^2 = \frac{2-\lambda_1}{2} v_{f,i}^2 \tag{3.3}$$

$$s_{2,i}^2 = \frac{\delta_{f,i}^2}{2} \tag{3.4}$$

$v_{f,i}^2$ is the first filtered variance based on the difference between the process variable and its filtered value (Equation (3.5)), while $\delta_{f,i}^2$ is the variance estimated with the second approach, and is obtained by filtering the standard deviation of two consecutive data, according to Equation (3.6).

$$v_{f,i}^2 = \lambda_2 \cdot \left(x_i - x_{f,i-1}\right)^2 + (1-\lambda_2) \cdot v_{f,i-1}^2 \tag{3.5}$$

$$\delta_{f,i}^2 = \lambda_3 \cdot (x_i - x_{i-1})^2 + (1-\lambda_3) \cdot \delta_{f,i-1}^2 \tag{3.6}$$

$$x_{f,i} = \lambda_1 \cdot x_i + (1-\lambda_1) \cdot x_{f,i-1} \tag{3.7}$$

where x_i is the process variable at the instant i and $x_{f,i}$ is the filtered exponential moving average of the variable (Equation (3.7))). The filtering factors λ_1, λ_2, λ_3 are set as constant and are adjustable between 0 and 1, to adapt the sensitivity of the method to the dynamic characteristics of the specific process. The application of the method implies the calibration of the filtering factors, whose values determine the readiness of the index R_i in detecting the variations of the process variable. The values of the filtering factors are taken according to [98].
The R_i values, computed instant by instant, are then plotted versus time and compared to a threshold, $R_{critical}$. If $R_i < R_{critical}$ for a period at least equal to the minimum required (t_{SS}), the variable is considered to be in steady-state conditions. A value of the threshold $R_{critical}$ must be set for each class of measured quantity, based on the knowledge of the historical data, as the value that guarantees that the variation around the average value of the detected interval is lower than the maximum acceptable. The maximum acceptable variation is determined according to the set of standard thresholds proposed by Woodland et al. [94], summarized in Table 3-3. The minimum duration required for the steady-state interval, t_{SS}, is set based on the characteristic times of stabilization of the measured variables, and more specifically, equal to the characteristic time of the slowest variable in achieving the steady-state conditions (typically a fluid temperature, due to the thermal inertia). The R-test parameters, optimized for the system under investigation, are collected in Table 3-4. Figure 3.2 shows an example of application of the algorithm to an experimental test lasted more than 3 hours. In Figure 3.2a the R-test is applied to the working mass flow rate ($\dot{m}_{ORC}$), identifying three stationary intervals of duration around 1300 s, 1000 s and 4000 s (from left to right). The result of the R-test implemented to the expander inlet and outlet pressure (p_1 and

p_2) is presented in Figure 3.2b. In this case, the algorithm detects only two intervals, corresponding to the first and third interval of the mass flow rate test. The second interval (the one between 2700 s and 3700 s) is ignored due to high noise characterizing the evaporating pressure signal, that makes reduce the duration of the interval during which the value of R is lower than $R_{critical}$.

The achievement of the new stationary conditions after a perturbation depends on the variable and on the magnitude of the perturbation. As will be detailed in the chapter dedicated to the experimental dynamic analysis, mass flow rate requires a minimum duration of 50 s to settle to the new value, while the time needed by the evaporation pressure ranges between 70 s and 300 s. A longer interval is required for the stabilization of the expander outlet temperature (higher than 300 s), which also results the variable with the slowest response, due to the inertia of recuperator that is placed after the expander.

Table 3-4 - Calibrated parameters for R-test

λ_1	λ_2	λ_3	t_{SS}	$R_{critical}$
0.2	0.1	0.1	600 s	6

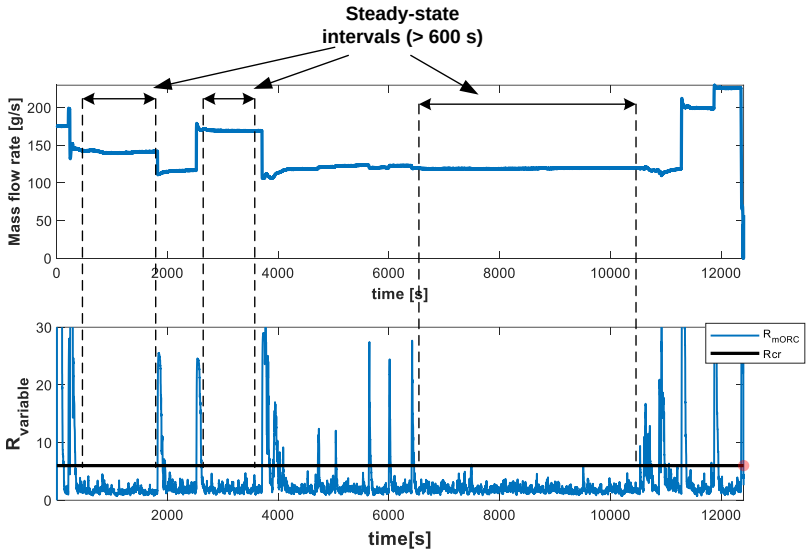

a)

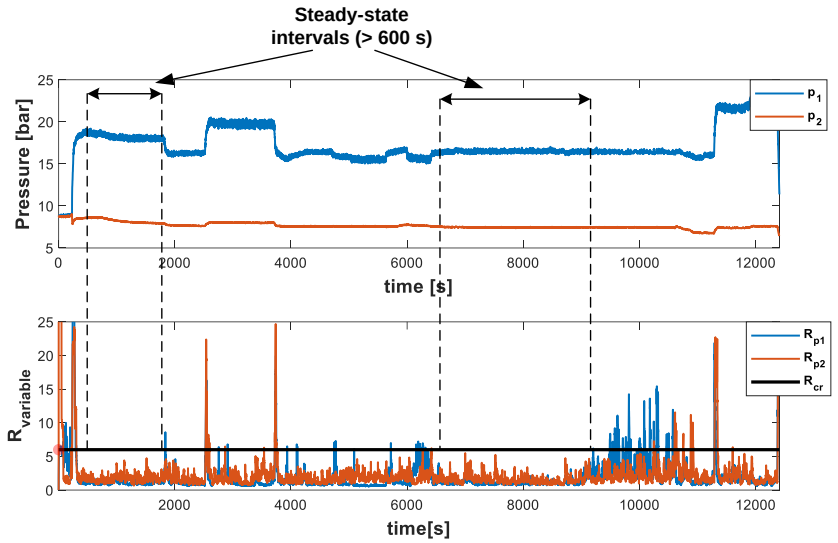

b)

Figure 3.2 – Example of application of the R-Test to mass flow rate, pressure and temperature measured signals.

3.3 Uncertainty analysis

The detailed analysis of the measurement uncertainty, applied to the system under investigation, was presented in a co-authored publication of the Author at the 5th International Seminar on ORC Power Systems (September 9-11, 2019, Athens, Greece) [100].
The uncertainty calculation of the ORC performance parameters is based on the procedure reported in the standard ISO/IEC Guide 98 and EA-4/02M. The propagation of the uncertainty is realized by means of the classic procedure based on propagation rule. According to the ORC performances parameters, the uncertainty of the power thermal input $\dot{Q}$, expander thermodynamic power output $\dot{W}_{th}$, expander specific work W, and thermal efficiency η_{th} can be expressed as follows (Equation *(3.8)*-*(3.11)*):

$$\delta\dot{Q} = \sqrt{\left(\frac{\partial\dot{Q}}{\partial\dot{m}}\right)^2 \cdot \delta\dot{m}^2 + \left(\frac{\partial\dot{Q}}{\partial h_2}\right)^2 \cdot \delta {h_2}^2 + \left(\frac{\partial\dot{Q}}{\partial h_3}\right)^2 \cdot \delta {h_3}^2} \tag{3.8}$$

$$\delta\dot{W}_{th} = \sqrt{\left(\frac{\partial P}{\partial\dot{m}}\right)^2 \cdot \delta M^2 + \left(\frac{\partial P}{\partial W}\right)^2 \cdot \delta W^2} \tag{3.9}$$

$$\delta W = \sqrt{\left(\frac{\partial W}{\partial h_2}\right)^2 \cdot \partial {h_2}^2 + \left(\frac{\partial W}{\partial h_3}\right)^2 \cdot \delta {h_3}^2} \tag{3.10}$$

$$\delta\eta_{th} = \sqrt{\left(\frac{\partial\eta}{\partial P}\right)^2 \cdot \delta P^2 + \left(\frac{\partial\eta}{\partial\dot{Q}}\right)^2 \cdot \delta\dot{Q}^2} \tag{3.11}$$

The last step is to relate the uncertainty of the enthalpy to the thermodynamic measurement of pressure and temperature (Equation *(3.12)*).

$$\delta h = \sqrt{\left(\frac{\partial h}{\partial p}\right)^2 \cdot \delta p^2 + \left(\frac{\partial h}{\partial T}\right)^2 \cdot \delta T^2} \qquad (3.12)$$

where the first derivatives (pressure and temperature) are estimated using the CoolProp library (see for reference [101]). In the CoolProp implementation, the partial derivatives of the state properties with respect to temperature can be calculated directly, because the temperature is one of the independent variables (together with the density) of the Helmholtz energy EoS. By contrast, partial derivatives with respect to dependent variables (such as pressure) cannot be calculated directly. In this case, CoolProp is able to express as a combination of partial derivatives with respect to the independent variables any partial derivative with respect to arbitrary properties [101]. Therefore, using the CoolProp library, the propagation of the uncertainty values related to temperature and pressure measurements can be performed. The calculation method for the assessment of temperature and pressure uncertainty depends on the quality of calibration that has been executed on the acquisition system. For the system under investigation, a field-calibration was implemented on thermocouples and pressure transducers. Each pressure sensor with its correspondent acquisition device has been individually calibrated using a pressure calibrator MicroCal PM200+, representing the in-house laboratory secondary standard which, in turn, is calibrated towards a primary laboratory standard certified in agreement with the Italian Accreditation Body (Accredia). After this procedure, the type B uncertainty is obtained by considering the uncertainty of the primary laboratory standard (that represents the reference uncertainty of the certified laboratory standard) Up,PLS (considered as a Gaussian distribution, and for this reason it is divided by 2 for calculating the standard deviation equivalents) and the residual uncertainty value of the pressure measurement chain Ep,R. The latter value is estimated considering the peak-to-valley amplitude of a set of pressure values obtained during 10 minutes of constant pressure input (generated and controlled by the MicroCal PM200+) and it is considered to have a rectangular probability distribution. This procedure also allows the evaluation of the type A uncertainty by estimating the standard deviation (considered as a Gaussian distribution, and for this reason, it is dived by 2 for calculating the standard deviation equivalents) of the set of data Up,σ. The size of the sample (about 600 pressure measurements) ensures the proper application of the statistic methodology. The final assessment of the pressure measurements uncertainty results (Equation *(3.13)*):

$$\delta p_{field} = \sqrt{\left(\frac{U_{p,PLS}}{2}\right)^2 + \left(\frac{E_{p,R}}{\sqrt{3}}\right)^2 + \left(\frac{U_{p,\sigma}}{2}\right)^2} \qquad (3.13)$$

A similar procedure has been applied to the temperature sensors. The thermocouples are calibrated in a thermostatic static furnace (Isotech Jupiter 650) that introduces an estimated error of ET,F equal to 0.10 K (related to the non-ideal uniform temperature of the bath) and a first order (linear) calibration curve was obtained in the range of 288 K – 365 K. The reference temperature was obtained with a Pt100 Class A thermistor (4-wire) coupled with the Microcal 200+ calibrator. This reference temperature chain represents the in-house laboratory secondary standard calibrated towards a primary laboratory standard certified in agreement with the Italian Accreditation Body (Accredia), characterized by an uncertainty equal to UT,PLS = 0.09 K. Type A and Type B uncertainty contributions are established by means of a similar procedure used for pressure sensors. The on-field calibration does not allow the proper control of the environmental conditions, and, the variability encountered in the ambient temperature could affect the calibration process (variation of ice-point reference, and thermocouple signal noise). Finally, the uncertainty related to the installation and radiation effects (Benedict, 1984) was neglected considering the similar temperature between the duct walls and the tip of the thermocouple. The uncertainty associated to temperature is therefore calculated according to Equation *(3.14)*.

$$\delta T_{field} = \sqrt{\left(\frac{U_{T,PLS}}{2}\right)^2 + \left(\frac{E_{T,F}}{\sqrt{3}}\right)^2 + \left(\frac{E_{T,R}}{\sqrt{3}}\right)^2 + \left(\frac{U_{T,\sigma}}{2}\right)^2} \qquad (3.14)$$

In Table 3-5, the values of uncertainty resulting from the application of the on-field calibration analysis to evaporator thermal power, expander power output and thermodynamic efficiency, are reported in two cases, A and B, characterized by a different rate of thermal input, higher in case B. Except for the uncertainty of the evaporator thermal power, which is basically equal in both cases, both the uncertainties of the expander power and cycle efficiency present a slight increment in case B, i.e. with increased thermal power input. For power and efficiency, the uncertainty is lower if the electric power output is considered, since the part of uncertainty related to the CoolProp library is avoided. Being the efficiency value small, even if the efficiency shows a relatively high uncertainty, the global accuracy can be still considered satisfactory, as the efficiency interval results 5.8% ± 0.27% in case A, and 4.6% ± 0.29% in case B, meaning that the absolute variation is almost negligible.

Table 3-5 – Uncertainty values of evaporator thermal power, expander power and thermal efficiency for two operating conditions

Variable	**Case A**		**Case B**	
	Value	Uncertainty	Value	Uncertainty
Evaporator thermal power	17519 W	131 W (0.75%)	25829 W	153 W (0.59%)
Expander thermodynamic power	1010 W	47 W (4.61%)	1179 W	74 (6.28%)
Thermal efficiency	0.058	0.0027 (4.67%)	0.046	0.0029 (6.31%)

3.4 Experimental results and discussion

3.4.1 Operating conditions

The performances of the micro-ORC system are mostly affected by the levels of evaporation and condensation pressures, which determines the pressure difference across the expander influencing the specific work. For each heat source condition and heat exchanger sizing/behavior, the value of vaporization pressure has an upper limit given by the vaporization temperature (which is mainly affected by the hot water inlet temperature), and by the value of the minimum superheating degree, which can be controlled regulating the flow rate of the working fluid. In other words, for given conditions of the hot water inlet temperature, heat exchanger characteristics and superheating degree, the maximum achievable value of the evaporation pressure is determined. The condensation pressure is mainly affected by the cold sink condition, with less important effect given by the working fluid flow rate. Hence, the condensation pressure cannot be regulated. As reference, the graph of the saturation pressure versus the saturation temperature of HFC-134a is reported in Figure 3.3.

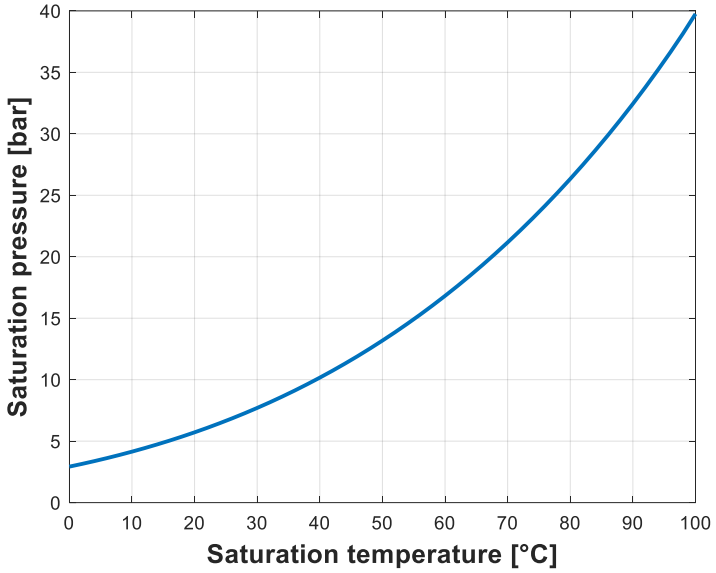

Figure 3.3 – Saturation pressure as function of temperature for HFC-134a.

Therefore, the variables that identify the operating points of the ORC system are the expander inlet and outlet pressures (corresponding to evaporation and condensation pressures, except for the pressure losses) and the expander inlet temperature (T_1), which is the maximum temperature of the cycle. The evaporating pressure p_1 is affected by the working fluid mass flow rate and by the resistance of the circuit, which is determined by the number of resistive loads (n_{loads}) connected to the expander generator. A direct correlation between the pump speed and the ORC mass flow rate ($\dot{m}_{ORC}$) has been experimentally observed (Figure 3.4). At constant pump speed, the ORC mass flow rate achieves slight different values, that are related to the variation of the fluid density and of the actual pump swept volume (as explained in Eq. 18). More in details, the fluid density, which is acquired by the Coriolis flow meter, reveals modest variations depending on the condensation pressure values, and accounts for a variation of only 1 % of the $\dot{m}_{\mathrm{ORC}}$ value, at constant speed; the actual pump volume, instead, causes a variation up to the 9 % of the mass flow rate value. The expander inlet pressure (p_1) as well is determined indirectly by the pump speed, since it is mainly affected by the mass flow rate. At constant value of $\dot{m}_{ORC}$, the pressure p_1 depends on the actual load impedance, which represents the circuit hydraulic main resistance. As shown in Figure 3.5, the expander inlet pressure varies from 11.4 bar to 22.5 bar as the mass flow rate increases from 80 g/s to 210 g/s. The lowest values of p_1 are obtained with the maximum load impedance, due to poor expander filling performance. It is clear already, and it will be confirmed in the following, that the system works better at lower values of the phase impedance (thus at higher nominal electric load), as the fluid is able to achieve higher pressure at equal mass flow rate.

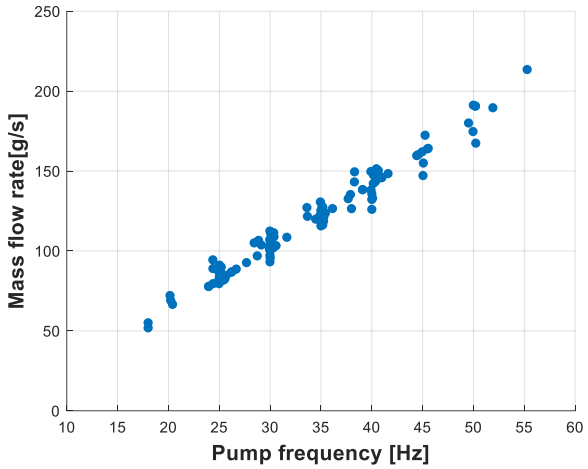

Figure 3.4 – Mass flow rate vs. pump frequency.

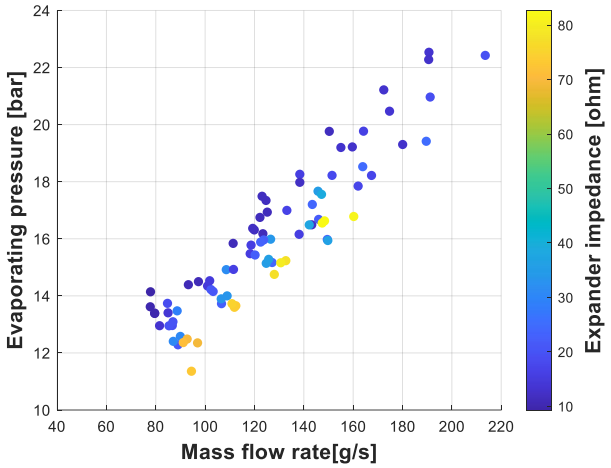

Figure 3.5 – Evaporation pressure vs. mass flow rate varying the expander load impedance.

The temperature T_1 is mostly influenced by the heat source temperature ($T_{H,IN}$) and quite close to it. In fact, the difference between $T_{H,IN}$ and T_1 keeps almost constant and very small (lower than 1.5 °C) for all the working conditions (Figure 3.6). The reason of this behavior lies in the high ratio between the mass flow rate of water and that of the working fluid, ranging between 10 and 50, assuring a high effectiveness (close to 1) of the superheating zone of the evaporator (see section 3.4.3). This feature will result convenient in the development of the micro-ORC steady-state model (section 3.5), since the temperature difference between water and working fluid at the evaporator hot terminal can be assumed constant.
The superheating degree (ΔT_{sh}) is expressed by Equation *(3.15)*), where the term $T_{sat}(p_1)$ is the saturation temperature at calculated by the CoolProp function, using as input the evaporation pressure and any value of the quality between 0 and 1.

$$\Delta T_{sh} = T_1 - T_{sat}(p_1) \qquad (3.15)$$

The superheating degree is a useful parameter that is used to identify the operating condition at a given value of the maximum temperature of the cycle. It can be used for control purposes as target value to adjust the pump rotating speed to regulate the working fluid mass flow rate, thus the evaporation pressure. Indeed, at given heat source temperature, the superheating degree explicitly determines the target value of the evaporating pressure, that can be achieved with feedback control system by acting on the feed-pump. A minimum value of the superheating degree should be always assured in order to avoid wet expansion. At the available hot source temperature, a low value of ΔT_{sh} is preferred when high power output is requested, since it is generally related to high mass flow rate and pressure difference. In the case of applications with variable heat source temperature, the regulation based on a map of target values of ΔT_{sh} can be used to maintain a constant output power, to maximize it, or to obtain the optimum value of thermal efficiency for the specific condition. Obviously, this is possible only within the operating boundaries of the system. Figure 3.7 shows the trend of the superheating degree versus the mass flow rate for the different values of heat source temperature tested. At the maximum temperature of 85 °C, the lowest value of ΔT_{sh} was around 11 °C, corresponding to an evaporation pressure close to 22.5 bar. It was not possible to further reduce the superheating degree due to safety concerns. In facts, the system is designed for working with maximum pressure around 25 bar, and a mechanical safety valve is installed to release the fluid in case the pressure reaches values higher than 26 bar. Moreover, an unstable operation of the feed-pump was experienced at high pump frequency, as will be cleared hereinafter. The minimum value close to zero was achieved with the lowest hot source temperature (65 °C), while the maximum of 41 °C was observed at the lowest value of mass flow rate and the highest temperature.

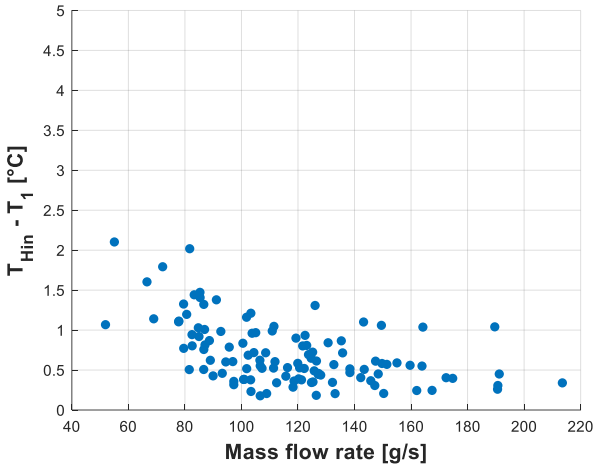

Figure 3.6 – Terminal temperature difference between water and working fluid for the evaporator vs. mass flow rate.

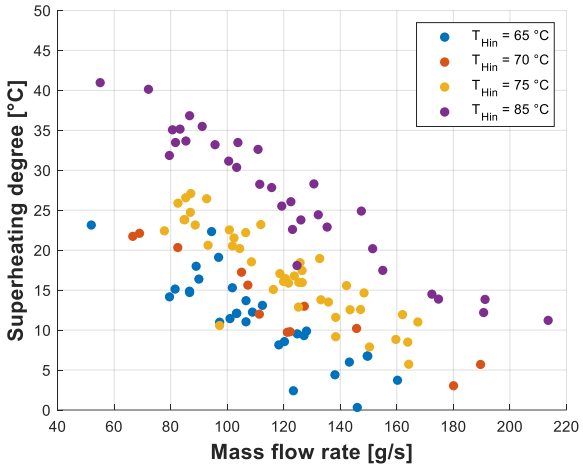

Figure 3.7 – Superheating degree at expander inlet vs. mass flow rate at different hot water temperature.

The expander outlet pressure p_2, that differs from the properly named condensing pressure by the pressure losses in the vapor side of the recuperator (not negligible), is mainly influenced by the cold water temperature at the condenser inlet, but increases also with the mass flow rate of the working fluid (Figure 3.8). It resulted around between 5.8 bar and 6.4 bar, depending on the mass flow rate, for cold water temperature up to 16 °C, while with cold sink temperature higher than 24 °C ranges between 7.5 bar and 10 bar. The results relative to the expander outlet temperature (T_2) are showed in Figure 3.9, as function of the mass flow rate and of the expander inlet temperature. T_2 is increases with the expander inlet temperature, while presents decreasing trends with the increment of $\dot{m}_{ORC}$. A lower value of T_2, at the same inlet temperature T_1 and pressure levels, indicates higher performance of the expansion machine, and in particular its specific work and isentropic efficiency increase as the enthalpy difference increases.

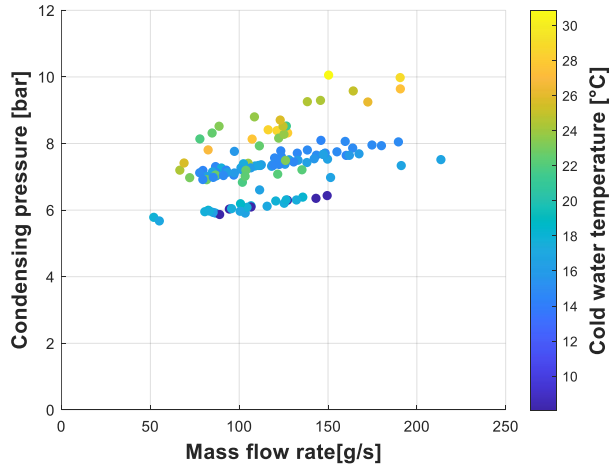

Figure 3.8 – Condensing pressure vs. mass flow rate varying cold water temperature.

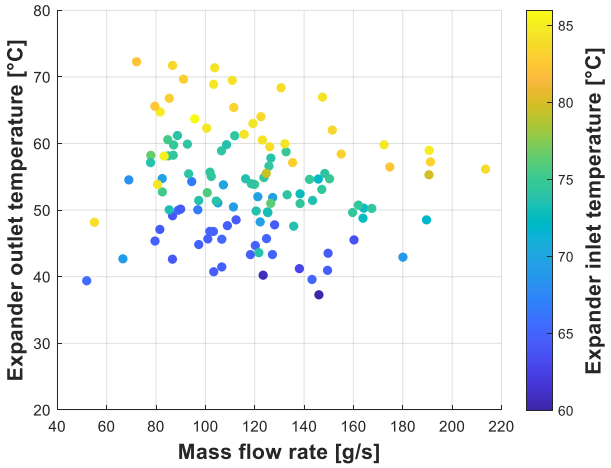

Figure 3.9 – Expander outlet temperature vs. mass flow rate varying cold expander inlet temperature.

Figure 3.10 and Figure 3.11 present the thermodynamic diagram temperature-specific entropy for some typical operating conditions. Figure 3.10 reports the comparison of two cases at the same load number and at equal temperatures of heat source (75 °C) and cold sink (18 °C), where the feed-pump speed has been regulated

differently in order to obtain two different values of the superheating degree. As can been seen, the value of the evaporation pressure rises from 14.5 bar to 17 bar as the superheating degree decreases from 20 °C to 13.5 °C. This is obtained by increasing the pump speed from 150 rpm and 200 rpm, corresponding to a frequency of 30 Hz and 40 Hz on the inverter, respectively. The electric power output results 810 W for case 1 and 1120 W for case 2, while the overall gross efficiency is 4.1% and 4.3%, respectively. Thermodynamic diagrams for two further operating points (case 3 and case 4) are compared in Figure 3.11. In this example, the cold sink temperature is still the same, but two different values of the heat source temperature are considered, namely 65 °C and 85 °C, respectively for case 3 and case 4. The superheating degree, instead, is equal to 14 °C for both cases, corresponding to a pressure equal to 13.5 bar for case 3 and 20.6 bar for case 4, that are achieved with pump speed of 122 rpm and 250 rpm. The resulting power output is 450 W and 1360 W, with overall gross efficiency equal to 3.1% and 4.2%, respectively. It is observed a higher value of the condensing pressure for case 3 and case 4 with respect to the two previous cases, even though the cold water temperature is slightly lower. This anomaly is probably due to the fluid charge inside the circuit, that was higher during case 1 and case 2 testing. Also, since case 3 and case 4 tests were carried out in a subsequent period, phenomena of fouling and clogging may have worsened the heat transfer performance of the condenser. The accidental air intake inside the system may be another cause of condensation pressure increase.

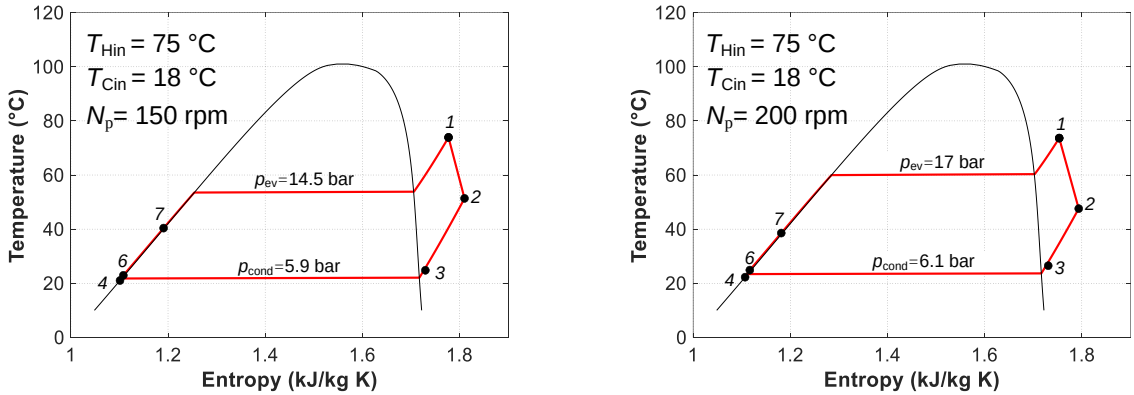

Figure 3.10 – Temperature-specific entropy diagram for two tests at equal hot and cold water temperature and different mass flow rate.

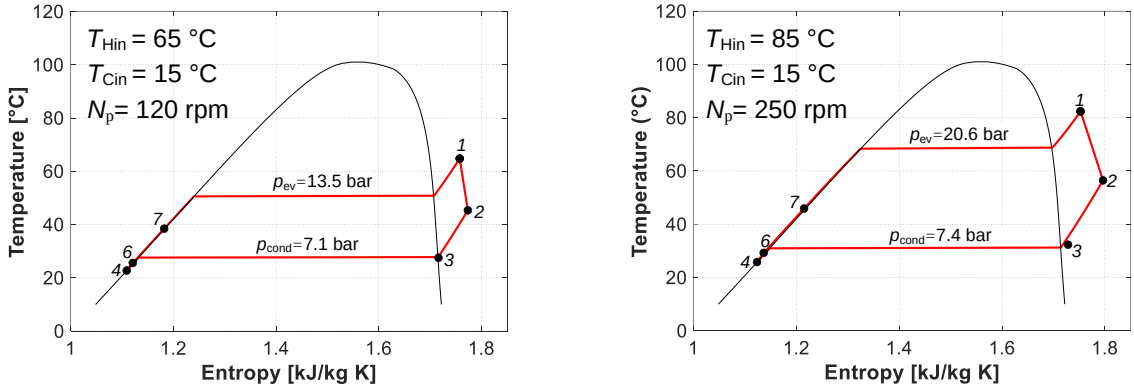

Figure 3.11 – Temperature-specific entropy diagram for two tests at equal superheating degree and hot water temperature.

3.4.2 Expander performance

When an engine is connected to the electric grid, its rotating speed is determined by the grid frequency (50 Hz in Europe) and by the number of poles of the electric generator. Since the operating voltage is also set by the grid

(230 V or 400 V), the regulation of the engine corresponds to the variation of its torque, which affects the output current.
Differently, in the test bench under investigation, the electric load consists of a pure resistive load that does not impose the electric frequency nor the voltage. Hence, as a free-rotating displacement machine, the expander rotational speed depends on the working fluid volumetric flow rate flowing through the cylinders, which is a function of the mass flow rate (set by the pump speed) and of the density at the expander inlet (Equation *(3.16)*). The density is determined by the working fluid pressure and temperature, measured at the expander inlet.

$$\dot{V}_1 = \frac{\dot{m}_{ORC}}{\rho_1(T_1, p_1)} \tag{3.16}$$

The expander rotating speed (N_{exp}, in revolutions per minute (rpm)) is computed from the electric frequency according to Equation *(3.17)*, where the term n_p is the number of pole pairs of the electric generator, equal to 4 in this specific case. The frequency is calculated using the LabVIEW function called *Extract Single Tone Information*, which receives as input the waveform signal of the current of the phase 1 of the expander output line.

$$N_{exp} = \frac{f_{exp}}{n_p} \cdot 60 \tag{3.17}$$

As shown in Figure 3.12, the rotating speed depends also on the loads number. When only one load is activated, the resistance applied to the rotation of the expander shaft is the lowest possible, and in fact the range of variation of the speed shifts to highest values, between 650 rpm and 1150 rpm as the pump rotates between 100 rpm and 220 rpm. Conversely, at the highest value of n_{loads} (five), the resistance is maximum and the expander speed ranges between 320 rpm and 900 rpm with pump speed between 90 rpm and 250 rpm. A characteristic of the electric load is represented by the plot in Figure 3.13, in terms of load impedance (Z_{load}) as function of the number of loads, for different values of the expander speed. The value of Z_{load} is proportional to the ratio of the expander voltage and the current, according to Equation *(3.18)*.

$$Z_{load} = \sqrt{3} \cdot \frac{V_{exp}}{I_{exp}} \tag{3.18}$$

The multiplication factor $\sqrt{3}$ derives from the fact that the measured voltage is the phase voltage, i.e. that referred to the neutral, while the loads are connected in delta, thus without the neutral. A lower number of loads corresponds to higher values of the actual phase impedance, whose range of variation increases, at constant n_{loads}, with the expander speed. It can be observed that the range of variation of the impedance is larger at lower number of loads, even if the range of tested conditions (temperatures and mass flow rates) is more limited.

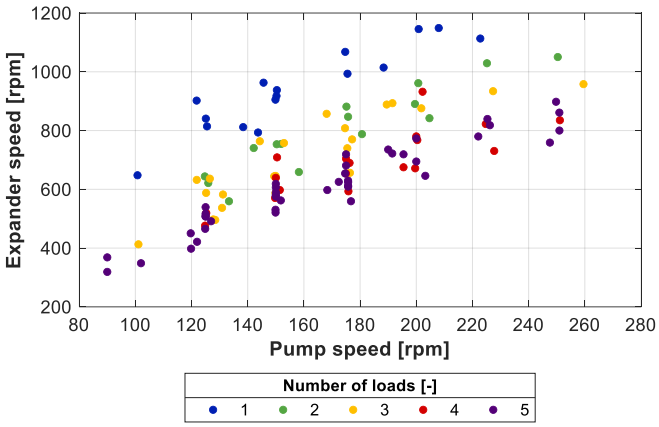

Figure 3.12 – Expander rotating speed vs. pump speed at different loads number.

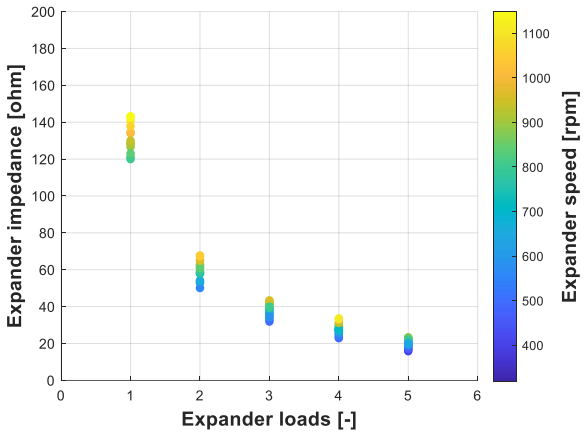

Figure 3.13 – Phase load impedance vs. loads number varying the expander speed.

The expander output voltage (phase voltage, V_{exp}) is an increasing function of the rotating speed (Figure 3.14). It can be observed that the voltage presents different linear curves, one for each value of the loads number. All the curves present approximately the same slope. At constant speed, the output voltage is higher for a lower number of loads, and achieves the maximum value of 130 V for 1 load, corresponding to the maximum expander speed tested during this campaign. In Figure 3.15, the root mean square value of the expander phase current is reported versus the voltage. The slope of the curves of current increases with the number of loads varying from 4 A up to 6 A at N_{loads} equal to 5, while at one load the current varies only between 1.3 A and 1.6 A.

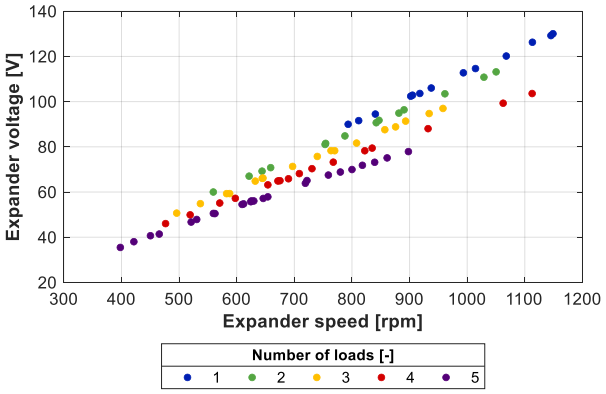

Figure 3.14 – Expander phase voltage vs. expander speed at different loads number.

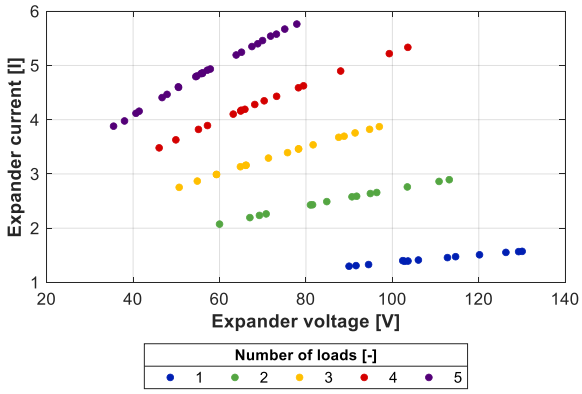

Figure 3.15 – Expander phase current vs. expander speed at different loads number. -

The expander electric power ($\dot{W}_{\mathrm{exp,el}}$) is computed according to Equation *(3.19)*, as the sum of the electric power of each phase of the expander electric output line. The terms $i_i(t)$ and $v_i(t)$ represent the instant values of current and voltage, respectively, hence their product is the instantaneous power. The expression $\overline{\imath_1(t) \cdot v_1(t)}$ is the electric power averaged over a reference period (see Chapter 2).

$$\dot{W}_{\mathrm{exp,el}} = \overline{\imath_1(t) \cdot v_1(t)} + \overline{\imath_2(t) \cdot v_2(t)} + \overline{\imath_3(t) \cdot v_3(t)} \qquad (3.19)$$

The trend of $\dot{W}_{\mathrm{exp,el}}$ is reported in Figure 3.16 a) as function of the expander speed, at different number of electric loads activated. It can be observed that also the power-speed plot presents five different curves, corresponding to the different values of the load impedance activated. At constant rotational speed, the power produced is higher for higher number of loads (or for lower load impedance value). At fixed impedance, the electrical output increases with the expander rotational speed; the figure also shows that the slope of the curves at constant number of loads increases with the load impedance decrease (or with the number of loads increase). The graph of Figure 3.16 b) presents the expander power output as function of the pressure difference across the expander (Δp_{exp}) and of the rotating speed. A strong dependency of $\dot{W}_{exp,el}$ from Δp_{exp} is evident, while a minor effect is due to the variation of the rotating speed at constant value of pressure difference. The range of variation of the electric power is between 250 W and 1650 W, as the pressure difference increases from 4 bar to 15 bar. The bunch of yellow points around 7-9 bar at a speed higher than 100 rpm are related to a working condition with only one load activated. It is interesting to analyze how the ratio of power output on the pressure difference across the expander (power-to-pressure ratio, $\dot{W}_{bar}$) varies depending on the operating conditions. As showed in Figure 3.17, the value of $\dot{W}_{bar}$ ranges from 60 W/bar to 115 W/bar, increasing with the expander speed (N_{exp}) and (slightly) with the heat source temperature. When a number between 3 and 5 loads is activated, the loads number does not seem to affect the parameter $\dot{W}_{bar}$. With loads number equal to 2, the values of the power-to-pressure ratio are down-shifted, still depending on the expander speed. With only 1 load, the influence of N_{exp} on $\dot{W}_{bar}$ is negligible, and only a slight effect of the hot water temperature can be observed. In this case, even if the values of rotating speed achieved by the expander are high (between 800 rpm and 1200 rpm), the power-to-pressure ratio keeps rather low, between 65 W/bar and 75 W/bar. This result confirms that the performance of the expander is strongly penalized by the high values of the load impedance achieved when only 1 load is activated. The maximum value of $\dot{W}_{bar}$ express a first indication of how much power can be extracted at given thermal source and cold sink conditions. The expander torque (M_{exp}) is calculated according to the following equation (Eq.*(3.20)*), referred to the electrical quantities:

$$M_{exp} = \frac{\dot{W}_{exp,el} \cdot 60}{N_{exp} \cdot 2 \cdot \pi} \qquad (3.20)$$

where the expression $\frac{2 \cdot \pi}{60}$ is used to convert the speed from rpm to rad/s. The torque is plotted in Figure 3.18 a) versus the expander speed. The slope of the different trends at constant load number is characterized by small differences. Decreasing the value of n_{loads}, the same value of the expander torque is achieved at a higher rotating speed. With the highest loads number (five), the expander torque varies between 9.0 Nm and 14.5 Nm, while with only one load the range of M_{exp} is between 3.7 Nm and 5.0 Nm. Figure 3.18 b) describes the influence of the pressure difference on the expander torque, showing different curves depending on the loads number. The highest curve regards the maximum loads number (five), with a pressure difference ranging between 5.1 bar and 12.9 bar, while the lowest is related to one load between 3.7 bar and 9.1 bar. For all the cases of loads number the curve of the expander torque rises with the pressure difference up to a maximum, which occurs at different value of the pressure difference. Both the maximum torque and the corresponding value of Δp_{exp} increase with the loads number.

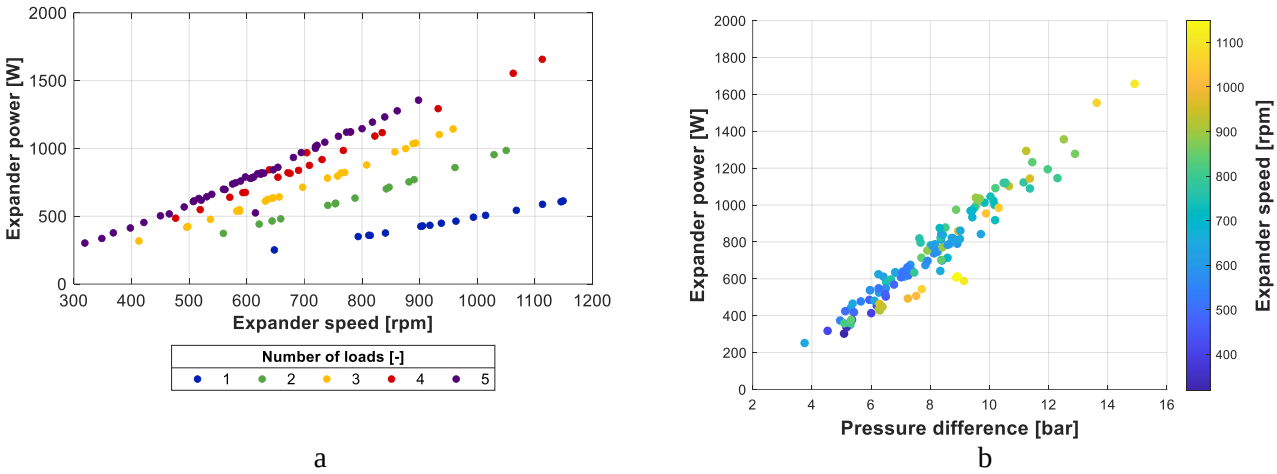

a b

Figure 3.16 – Expander power output vs. a) expander speed at different loads number; b) pressure difference varying the expander speed.

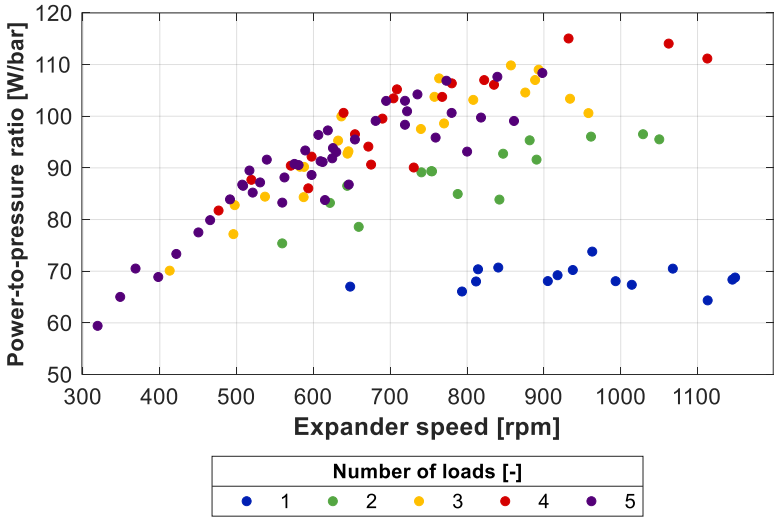

Figure 3.17 – Power-to-pressure ratio vs. expander speed at different loads number.

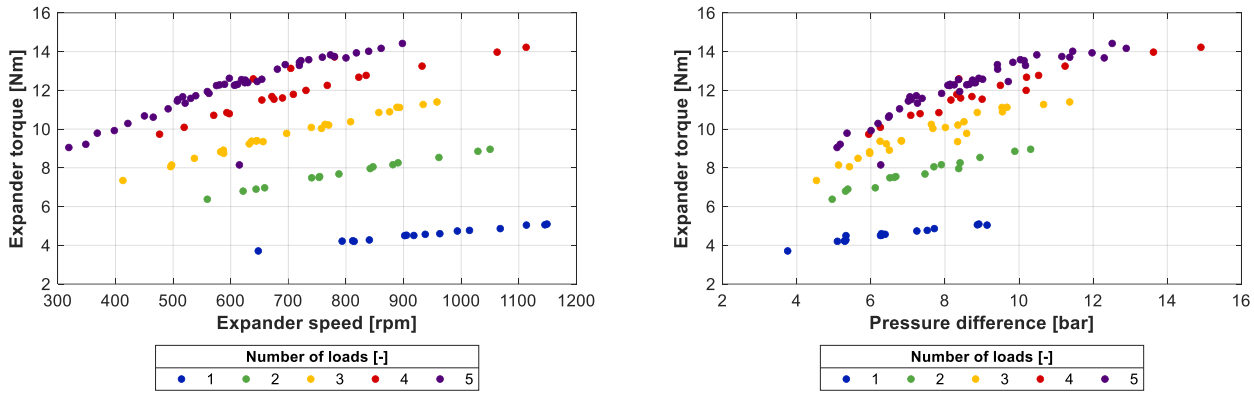

a) b)

Figure 3.18 – Expander torque vs. a) expander speed at different loads number; b) pressure difference at different loads number.

The filling factor (FF_{exp}) is used to evaluate the volumetric performance of the displacement expanders. It is defined as the ratio of the actual volume flow rate at the expander inlet and the ideal flow rate, estimated by the product of the rotating speed and the expander displacement (Equation *(3.21)*).

$$FF_{exp} = \frac{\dot{V}_1}{\dot{V}_{1,id}} = \frac{\dot{m}_{ORC}}{\rho_1 \cdot N_{exp}/60 \cdot V_{\exp}} \qquad (3.21)$$

where ρ_1 is the density of the fluid at the expander inlet, estimated via CoolProp from pressure and temperature measured values. A decreasing trend of FF_{exp} is observed when it is plotted versus the expander speed Figure 3.19 a). The maximum value of the filling factor is close to 0.95 at the minimum value of the expander rotating speed around 350 rpm, while the minimum close to 0.45 is obtained at the maximum expander speed of 1150 rpm. The filling performance is also affected by the pressure difference across the expander, describing different decreasing trends depending on the number of loads activated (Figure 3.19 b). The worst performance is obtained with only one load, with FF_{exp} varying from 0.7 to 0.45 as the pressure difference increases from 4 bar to 9 bar. In all the load conditions, the FF_{exp} drops below 0.6 when pressure difference exceeds 10 bar. These results suggest that the fluid intake and/or discharge in the expander should be improved, perhaps by means of a modification of the valves shape and timing. Further studies, with the aid of three-dimensional computational fluid dynamics (CFD) techniques are planned yet.

The expander total efficiency, expressed by Equation *(3.22)* as the ratio of the electric power output and the ideal (or isentropic) power, is presented in Figure 3.20 as function of the expander rotating speed at different number of loads.

$$\eta_{\exp} = \frac{\dot{W}_{\exp,el}}{\dot{m}_{ORC} \cdot (h_1 - h_{2,is})} \qquad (3.22)$$

where h_1 is the enthalpy estimated via CoolProp at the expander inlet, and $h_{2,is}$ is the enthalpy of the isentropic expansion, calculated using the expander outlet pressure (p_2) and the entropy evaluated at the expander inlet ($s1$) as input of the CoolProp block. The expander efficiency shows very modest variations around the average value of 40% within a large range of expander speed, with a slightly decreasing tendency with the increment of N_{exp}. Very low performance is obtained when only one load is activated, a condition that corresponds also to high values of the rotating speed, as the efficiency curve stands in the range between 30% and 22%. The value of n_{loads}, when comprised between 2 and 5 loads, does not seem to affect substantially the total efficiency.

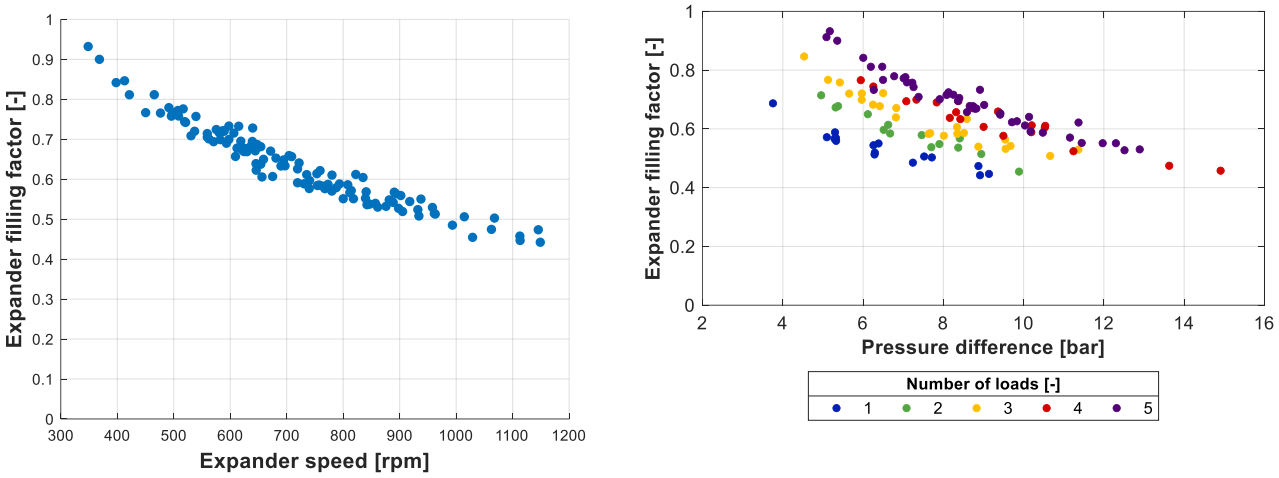

a) b)

Figure 3.19 – Expander filling factor vs. a) expander speed; b) pressure difference at different loads number.

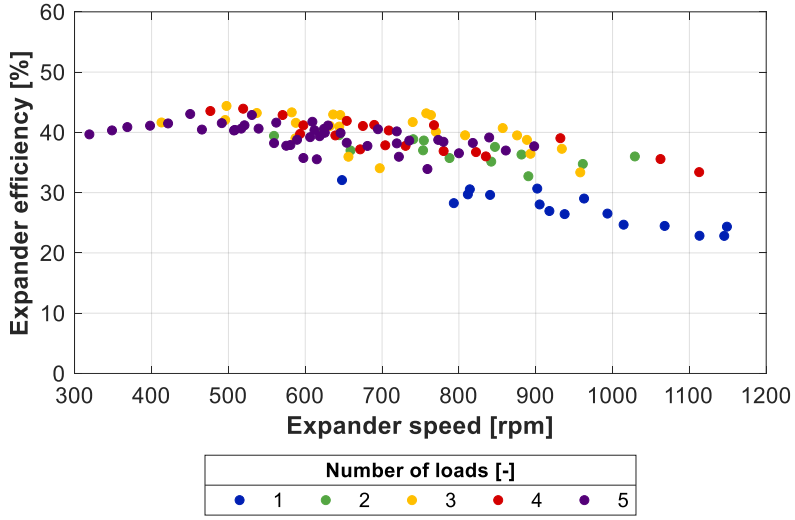

Figure 3.20 – Expander total efficiency vs. expander speed at different loads number.

3.4.3 Pump performance

As discussed in the first chapter, the performance of the feed-pump is very relevant to the performance of the whole ORC system, especially if considering small scale applications where the pump consumption covers a significant fraction of the expander power output. The hydraulic power ($\dot{W}_{p,hy}$) is the product of the volumetric flow rate and the pressure difference across the pump (Equation *(3.23)*), and represents the minimum theoretical power required to move that specific flow rate from the ambient at low pressure to another at high pressure.

$$\dot{W}_{p,hy} = \dot{V}_5 \cdot (p_6 - p_4) = \frac{\dot{m}_{ORC}}{\rho_5} \cdot (p_6 - p_4) \qquad (3.23)$$

As it is clear from Eq. *(3.23)*, at given values of mass flow rate and pressure difference, the rate of the hydraulic power is influenced by the fluid density at the pump inlet (ρ_5), which depends on the pump inlet pressure (p_4) and

on the sub-cooling degree downstream the condenser (ΔT_{sc}). The latter parameter is determined by means of Equation *(3.24)*:

$$\Delta T_{SC} = T_{cond}(p_4) - T_4 \qquad (3.24)$$

where T_{cond} is the condensation temperature evaluated by CoolProp as function of the condensing pressure. The sub-cooling degree is an important index that plays a fundamental role when dealing with problems of cavitation at the pump inlet. A higher value of ΔT_{sc} helps to avoid cavitation phenomena, since it reduces the risk of achieving the condition of saturation at the pump suction side. Several studies have dealt with pump cavitation in ORC systems, revealing that a minimum value of the sub-cooling degree should be always assured to prevent cavitation. The minimum value of ΔT_{sc} recommended for a secure pump operation varies from study to study, ranging from 2 °C up to 11 °C [10] depending on the characteristics of the specific application (working fluid, pump model and rotating speed). As shown in Figure 3.21, the inlet density decreases from 1240 kg/m^3 to 1160 kg/m^3 as the suction pressure increases from 5.6 bar to 9.8 bar, while at constant pressure ρ_5 is higher for larger values of the sub-cooling degree.

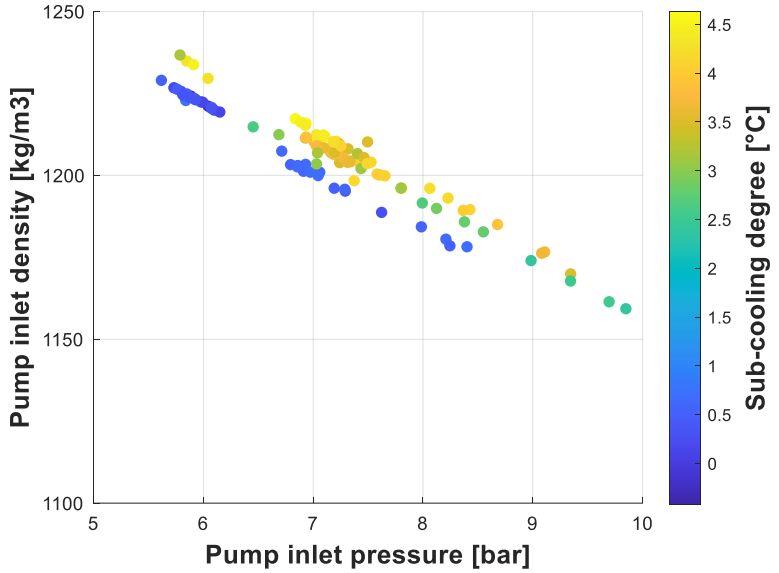

Figure 3.21 – Pump inlet density vs. inlet pressure varying the sub-cooling degree.

The characteristic curves of the pump in the pressure head versus volume flow rate diagram is showed in Figure 3.22. The experimental points that describe the curves at different pump speed have been acquired with the pump operating in the ORC circuit with the expander by-passed, and by partially closing in different position a manual ball valve located in the high pressure side of the circuit. For completing the curves at the highest pressures, the operating points with the expander activated were used. It was impossible to acquire the free flow rate of the pump, since a minimum rate of pressure losses (related to the piping and the heat exchangers) cannot be avoided. Hence, the volume flow rate at null pressure head was estimated from the curves trend. The hydraulic resistance of the ORC circuit during its normal operation is represented by the red curves that are related each to a different number of loads connected to the expander generator. It can be observed that the volumetric losses are considerable, causing the need to impose a higher pump speed to achieve higher pressure difference and higher expander specific work. The estimated values of the free flow rate at each rotating speed are slightly lower than the displacement calculated from the reverse engineering procedure mentioned in Chapter 2, suggesting that the pump sides and sealing are not optimized in order to avoid internal leakages.

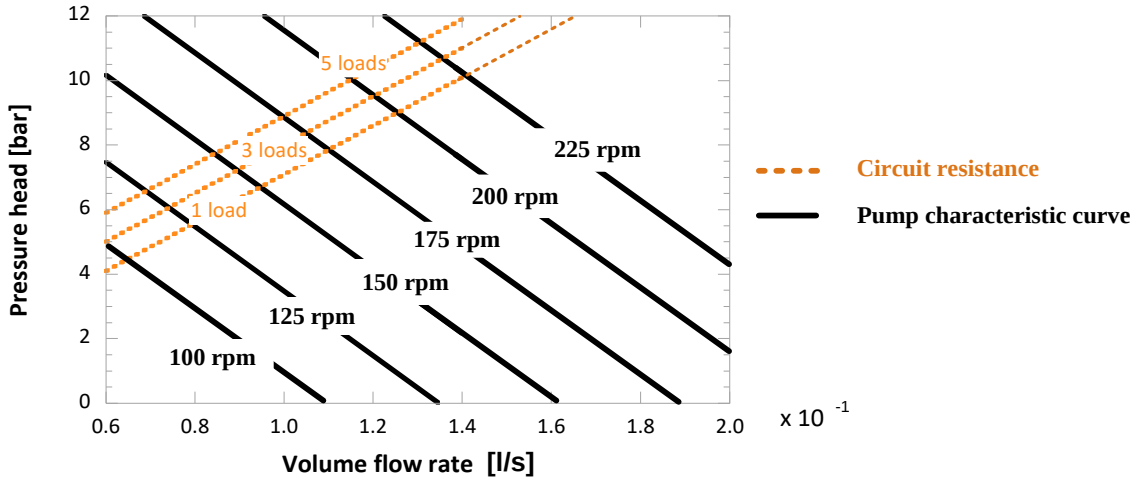

Figure 3.22 – Pump characteristic curves: pressure head versus volume flow rate diagram, at different pump speed and circuit hydraulic resistance (load number).

The hydraulic power ($\dot{W}_{p,hy}$) follows a rising trend versus the working fluid volume flow rate (which affects also the pressure rise), from 20 W to almost 300 W, as showed in Figure 3.23. In Figure 3.24 the pump electric power ($\dot{W}_{p,el}$), computed in the same way of the expander electric power, is reported as function of the volume flow rate, showing a large range of variation, between 200 W and 1200 W, increasing with the flow rate value.

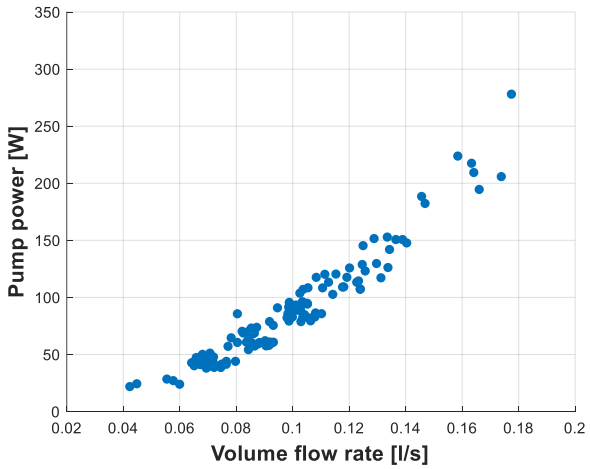

Figure 3.23 – Pump hydraulic power vs. volume flow rate.

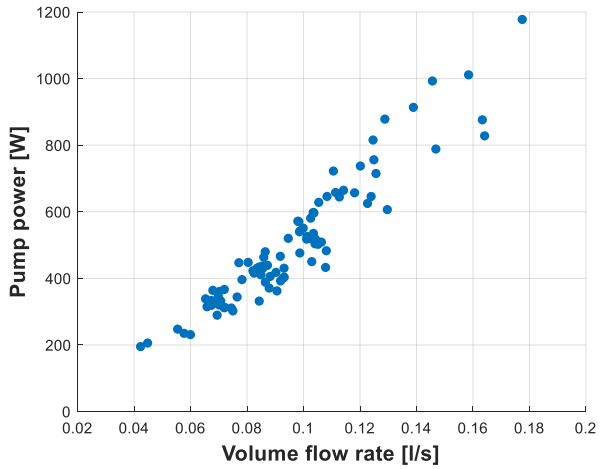

Figure 3.24 – Pump electric power vs. volume flow rate.

The main terms of losses in the displacement pump operation are the fluid leakages, the mechanical and the electric losses. Leakages from the supply side to the suction side are taken into account by the volumetric efficiency ($\eta_{p,vol}$), defined by Equation *(3.25)* as the ratio of the actual volume flow rate moved by the pump and the ideal flow rate, determined using the pump displacement (V_p) and the rotating speed (N_p).

$$\eta_{p,vol} = \frac{\dot{V}_5}{\dot{V}_{5,id}} = \frac{\dot{m}_{ORC}}{\rho_5 \cdot N_p/60 \cdot V_p} \quad (3.25)$$

As shown in Figure 3.25, at a given pressure difference across the pump, the volumetric efficiency increases with the volume flow rate (i.e. with the pump speed). The mechanical losses include the bearing frictions, the friction of the speed reducer and the friction of the pick head against the pump case and of the teeth side against the fixed bronze sides. In the pump under investigation, the latter term of losses is significant, probably because the manufacturing tolerances of the prototype are not sufficiently tight. Moreover, the need of reducing the fluid leakages to the pump inlet and to eliminate those to the ambient, leads to a very tight assembly of the fixed bronze sides to the flank of the teeth. In addition, a poor lubrication can further worsen the sliding friction of the pump gears. The electric losses are related to the conversion of the electrical power into mechanical. The nameplate efficiency of the installed motor is 90% (see Chapter 2), but it must be considered that most of the time the motor works regulated in an operating point that is far from its nominal condition, with negative effect to its performance. The oversizing of the electric motor of the feed pump is a common practice in this kind of systems, as well as the loss of efficiency in off-design conditions is a common related issue [39]. Since in this test bench the pump torque is not measured, it is not possible to distinguish the power losses related to the friction and those of the electric motor. Nevertheless, it is possible to estimate the combination of mechanical and electric loss contributions by evaluating the thermodynamic power ($\dot{W}_{p,th}$) of the pump, expressed as the product of the mass flow rate and the enthalpy difference across the pump. The electromechanical efficiency ($\eta_{p,em}$) is therefore defined in Equation *(3.26*). However, the relatively high error introduced by the enthalpy calculation, especially if considering the low temperature difference between the inlet and outlet of the pump, causes a high risk of inaccuracy of these data, that becomes unacceptable when the acquired variables are not completely in stationary conditions. The overall performance of the feed-pump is expressed by the pump total efficiency, that corresponds to the ratio of the hydraulic to the electric power (Equations *(3.27*)).

$$\eta_{p,em} = \frac{\dot{W}_{p,th}}{\dot{W}_{p,el}} = \frac{\dot{m}_{ORC} \cdot (h_6 - h_4)}{\dot{W}_{p,el}} \quad (3.26)$$

$$\eta_{p,tot} = \frac{\dot{W}_{p,hy}}{\dot{W}_{p,el}} \quad (3.27)$$

The trends of the pump total efficiency ($\eta_{p,tot}$) and of the electromechanical efficiency ($\eta_{p,em}$), are presented in Figure 3.26 as function of the fluid volume flow rate. Due to the inaccuracy issue above described, a lower number of operating points, selected after a data filtering, have been considered for the plotting of the electromechanical efficiency. As it can be noticed, the pump total efficiency is in general very low, ranging between 10% and 25%, resulting in a high penalization of the overall performance of the ORC system. This is represented more explicitly in Figure 3.27, where the back work ratio (*BWR*), defined by Equation *(3.28*) as the ratio of the pump power to the expander power, both electric, is plotted versus the expander power at different loads number.

$$BWR = \frac{\dot{W}_{\mathrm{p,el}}}{\dot{W}_{\mathrm{exp,el}}} \quad (3.28)$$

Plus the substantially high rate of the index BWR, lowest values around 50% corresponding to an expander power output between 600 W and 900 W can be observed. At low number of loads, and especially at one load, BWR presents the highest values, in some cases exceeding the 90%. This last result further confirm that the value of the impedance associated to a low loads number (one and two) is not optimal for most operating conditions of this specific ORC system (even when low power rates are involved), and leads to the deterioration of the performance and operational instability.

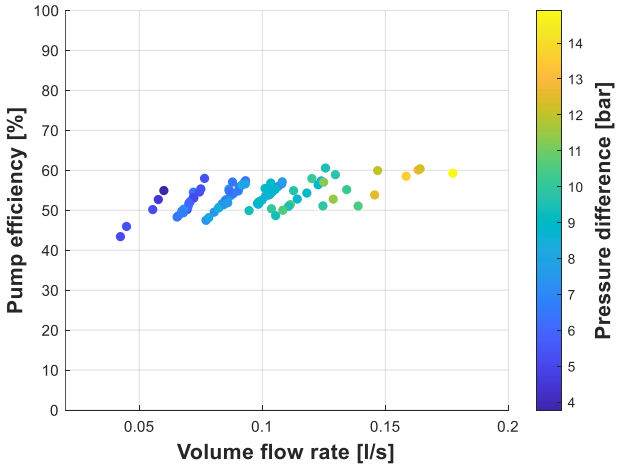

Figure 3.25 – Pump volumetric efficiency vs. volume flow rate varying the pressure difference.

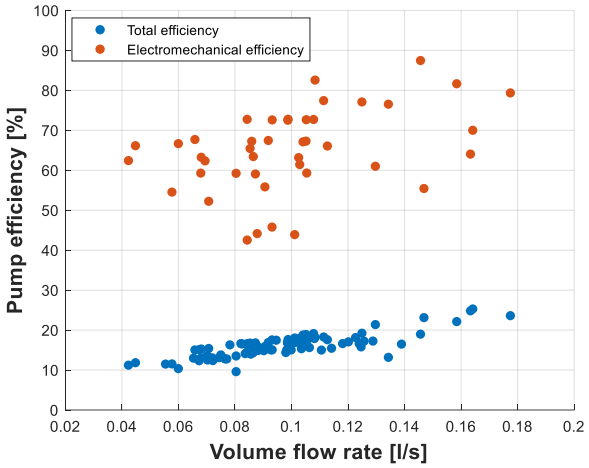

Figure 3.26 – Pump total and electro-mechanical efficiency vs. volume flow rate.

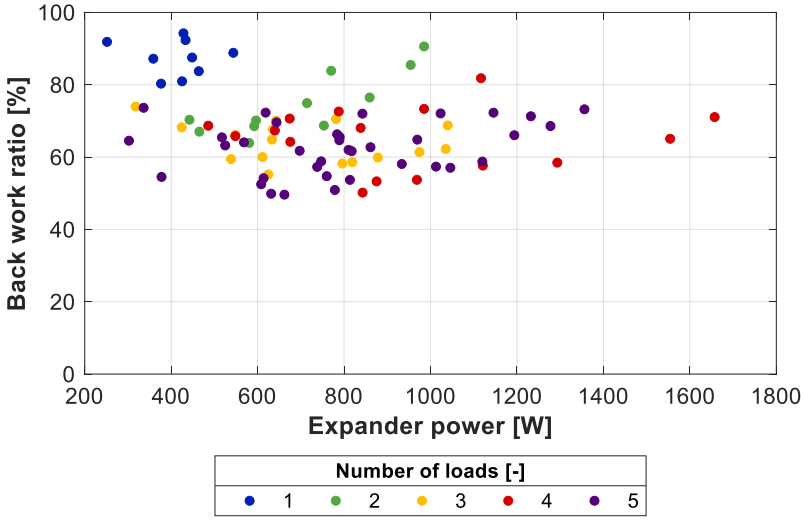

Figure 3.27 – Back work ratio vs. expander power output at different loads number.

Pump cavitation

The pump cavitation occurs when the fluid pressure at the pump inlet drops below the saturation pressure, causing the formation of vapor bubbles at the pump suction that, at some conditions, explode as they are moved to the pump outlet side at higher pressure. This phenomenon can be the cause of important damages and deterioration, leading to a short operating life of the pump. The slight cavitation, even if does not cause fatal damages, has a negative effect on the performance and operation stability of the feed-pump, as it is associated to a decrease of the fluid flow rate and to pump vibrations [42]. Generally, the parameter that define the margin to the fluid saturation at the pump suction is the available Net Positive Suction Head, corresponding to the difference between the pump suction pressure and the saturation pressure at the fluid temperature ($NPSH_{av} = p_{in} - p_{sat}(T_{in})$). Within the ORC

analysis, also the sub-cooling degree ($\Delta T_{sc} = T_{sat}(p_{in}) - T_{in}$) can be used to express the cavitation limits. They both refer to the same concept, the former expressed in terms of pressure and the second as function of temperatures. The pump inlet pressure (p_{in}) is in general the sum of different contributions, according to Equation *(3.29*) [103]:

$$p_{in} = p_{tank} + \left(H_z - H_f - H_a\right) \cdot \frac{g}{v_{in}} \qquad (3.29)$$

where:

- p_{tank} is the pressure measured at the liquid receiver, in Pa;
- H_z is the vertical distance in meters between the pump inlet and the liquid level;
- H_f corresponds to the head associated to the pressure losses in the suction piping (including friction and local resistances) [m];
- H_a is the acceleration head at pump inlet, usually provided by the pump manufacturer [m];
- g is the gravitational acceleration $\left[\frac{m}{s^2}\right]$;
- v_{in} is the fluid specific volume at the pump suction $\left[\frac{m^3}{kg}\right]$

Generally, the pump manufacturers provide the curve of the required net positive suction head ($NPSH_{req}$), as function of the pressure head and flow rate. The value of $NPSH_{av}$ should be always higher than the prescribed one ($NPSH_{req}$) , at least of a quantity equal 0.1 bar. In case the pump is a prototype not provided with values of required *NPSH*, cavitation limits should be assessed experimentally.
With systems presenting cavitation issues, there are several actions that can be implemented to increase the value of the net positive suction head, but some of the methods require relatively important intervention to the test bench. These techniques have been summarized in [10], and are the following:

- introducing an additional heat exchanger (sub-cooler) after the condenser or after the liquid receiver, to reduce the temperature value at the pump inlet;
- introducing a pre-feed pump, characterized by low required NPSH), before the main feed pump, to provide the required pressure head at the main pump inlet;
- placing the pump at the lowest point of the circuit, with high vertical distance from the condenser (or the receiver);
- increasing the fluid charge, that would increase the liquid level above the pump suction.

The introduction of a sub-cooler results surely effective to the purpose of increasing the sub-cooling degree, but has the disadvantages of the modifications needed in the plant to install the new component, higher costs and the addition of further pressure losses in the low-pressure side of the circuit [103]. Similar consideration can be done on the pre-feed pump. The increase of the vertical distance between pump and condenser can be difficult to implement in an existing plant, and in new systems is usually already considered in the design phase, compatibly with the installation constraints. The additional charge of working fluid inside the circuit is the simplest procedure to implement, not requiring any modification on the system. However, the fluid charge should be assessed carefully, as the overcharge should be avoided [10].
Regarding the system under investigation, cavitation takes place at high pump rotating speed, as the pressure losses increase at the pump inlet (in the whole circuit) due to the increase of the mass flow rate. It can be facilitated by a sudden variation on the thermal power transferred in the evaporator, for example after a change of the working fluid mass flow rate or of the hot water temperature. The reaction of the condenser, due to the thermal inertia of the system, is not instantaneous, and the resulting condenser outlet flow will be characterized by lower sub-cooling degree [102].
As the cavitation starts, the working fluid flow rate begins to reduce slowly at constant pump speed, and persisting the conditions that have caused the phenomenon, it can lead to the full block of the flow rate, and to the sudden collapse of the pressure difference of the cycle. The expander stops to rotate and the electric power output falls to zero. The Coriolis flow meter reports the warning *non-homogeneous fluid*, resulting in oscillations of the acquired $\dot{m}_{\mathrm{ORC}}$ that make the measurement not reliable. Cavitation can be facilitated by a sudden variation on the thermal

power transferred in the evaporator, for example after a change of the working fluid mass flow rate or of the hot water temperature. The reaction of the condenser, due to the thermal inertia of the system, is not instantaneous, and the resulting condenser outlet flow will be characterized by lower sub-cooling degree [102]. Among the above-mentioned techniques to solve this issue, only the increment of the fluid charge is viable in the present case. Two conditions of fluid mass have been evaluated systematically, to recognize if any significant modification is observed in the pump operation. First, the micro-ORC has been tested with a charge close to 20 kg, for which cavitation events occur quite frequently, especially at high pump speed; then the charge was increased up to 25 kg to evaluate if this solution is sufficient to limit or completely cancel the phenomenon. Please note that the estimated total volume of the circuit (V_{tot}) is close to 70 liters, meaning that the maximum theoretical charge corresponds to $M_{th} = V_{tot} \cdot \rho = 84\ kg$. The fluid charge ratio for these tests resulted therefore close to 23% in the first case and 30% in the second case.

Cavitation test with 20-kg charge and 10 Hz pump frequency increment

The first case regards a test conducted at average working conditions, namely with constant hot water temperature (around 75 °C) and cooling water temperature (close to 14.5 °C), and with a working fluid charge equal to 20 ± 0.5 kg. Starting from a stable operation, characterized by pump speed of 125 rpm (25 Hz on the pump inverter), mass flow rate around 85 g/s and evaporating pressure close to 13.5 bar (see Figure 3.28), the pump speed is rapidly increased up to 175 rpm (35 Hz) at a time = 1540 s, causing an almost simultaneous increment of the mass flow rate, followed by a slower variation of the evaporation pressure. After the peak due to the sudden variation of the pump speed, the value of $\dot{m}_{ORC}$ decreases quite rapidly before trying the stabilization, then starts to decrease slowly, achieving the reduction of 3% with respect to the case of absence of cavitation in about 150 s. The mass flow rate begins then to decrease more rapidly and to show oscillations, until the collapse of $\dot{m}_{ORC}$ after about 400 s from the start of cavitation. The evaporation pressure follows the trend of the flow rate with little delay, as it is reduced slowly as the cavitation event occurs, with a more sudden drop with respect to the flow rate, at time close to 2000 s. After the system collapses, the normal operation of the feed pump can be restored by switching the expander by-pass valves to the idle mode, to set to zero the main hydraulic load resistance of the circuit. If the expander is left in active mode, the effect of the cavitation progressively vanishes, and in about 100 s after the collapse the system restarts its operation, without any intervention on the controlled variable of the test bench.

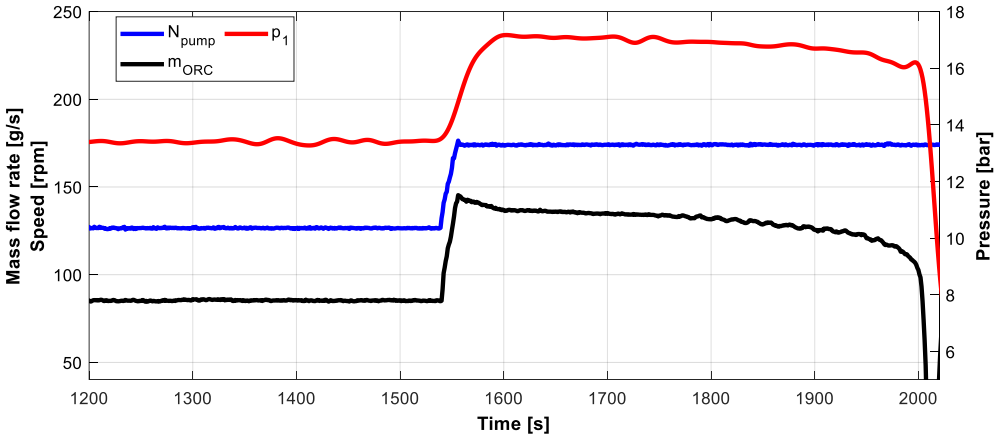

Figure 3.28 – Mass flow rate, evaporation pressure and pump frequency with fluid charge ≈ 20 kg.

Cavitation test with 25-kg charge and 10 Hz pump frequency increment

The second case is related to an experimental test executed with working fluid charge equal to 25 ± 0.5 kg. Hot and cold water inlet temperature are kept close to 75 °C and 20 °C respectively. The starting condition is characterized by pump speed equal to 150 rpm, mass flow rate close to 116 g/s and evaporation pressure around 16.2 bar. At time = 2518, an increment of 10 Hz is imposed to the inverter frequency, and the pump rotating speed

rises up to 200 rpm (see Figure 3.29). The first response of the working fluid mass flow rate and evaporating pressure is substantially similar to the previous case, with a slight peak before the attempt to the stabilization. However, both $\dot{m}_{\mathrm{ORC}}$ and p_1 achieve the stabilization in about 100 s after the imposed variation of N_{pump}. The two measured variables remain stable for a time longer than that required by the R-test method (see Section 3.2), and the average values of the steady-state interval can be registered. Please note that the rotating speed of the pump is higher in this example than in the previous one, suggesting that the addition of fluid charge had a positive effect on the cavitation issue since, as mentioned, high pump speed values tend to push the phenomenon.

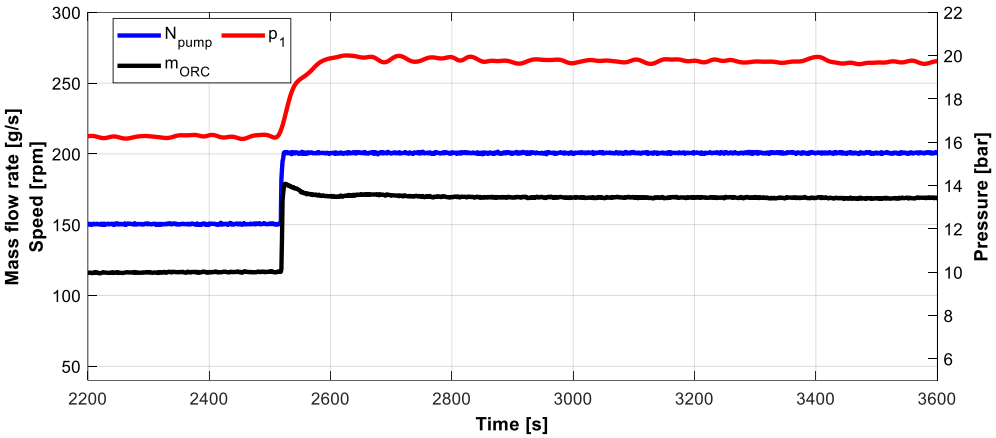

Figure 3.29 - Mass flow rate, evaporation pressure and pump frequency with fluid charge ≈ 25 kg.

3.4.4 Heat exchangers

Thermal power exchanged in the evaporator ($\dot{Q}_{\mathrm{ev}}$) and in the condenser ($\dot{Q}_{\mathrm{cond}}$) are reported in Figure 3.30, as function of the working fluid flow rate. Both present an almost linear dependence from the mass flow rate, while a minor influence is made by the saturation pressures, which determine the heat of vaporization, that increases as the pressure is reduced. The trend of the thermal power exchanged in the recuperator ($\dot{Q}_{\mathrm{rec}}$) is influenced by the mass flow rate and by the hot water temperature, increasing with their increment (Figure 3.31). Please note that the recuperator thermal power can be evaluated on both flows (liquid and vapor, Equations *(3.32)* and *(3.33)*) but, in stationary conditions, the values of $\dot{Q}_{\mathrm{rec,l}}$ and $\dot{Q}_{\mathrm{rec,v}}$ can be considered coincident. The heat transferred in the recuperator ranges between 1 kW and 2.5 kW with $T_{h,in}$ around 65 °C, between 2 kW and 3.5 kW with a $T_{h,in}$ of 75 °C, and from 3 kW up to more than 5 kW for a water temperature around 85 °C. It must be highlighted that the value of mass flow rate, affecting the recuperator thermal power, at lower temperature is limited by the minimum superheating degree, that imposes a limit to the evaporating pressure and hence on the mass flow.

$$\dot{Q}_{\mathrm{ev}} = \dot{m}_{\mathrm{ORC}} \cdot (h_1 - h_7) \qquad (3.30)$$

$$\dot{Q}_{\mathrm{cond}} = \dot{m}_{\mathrm{ORC}} \cdot (h_3 - h_4) \qquad (3.31)$$

$$\dot{Q}_{\mathrm{rec,l}} = \dot{m}_{\mathrm{ORC}} \cdot (h_7 - h_6) \qquad (3.32)$$

$$\dot{Q}_{\mathrm{rec,v}} = \dot{m}_{\mathrm{ORC}} \cdot (h_3 - h_2) \qquad (3.33)$$

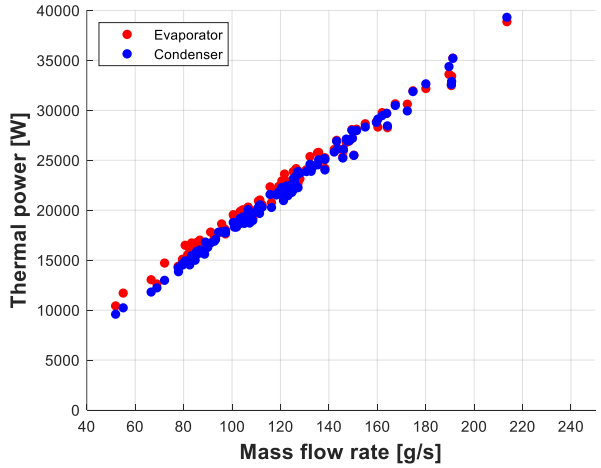

Figure 3.30 – Evaporator and condenser thermal power vs. mass flow rate.

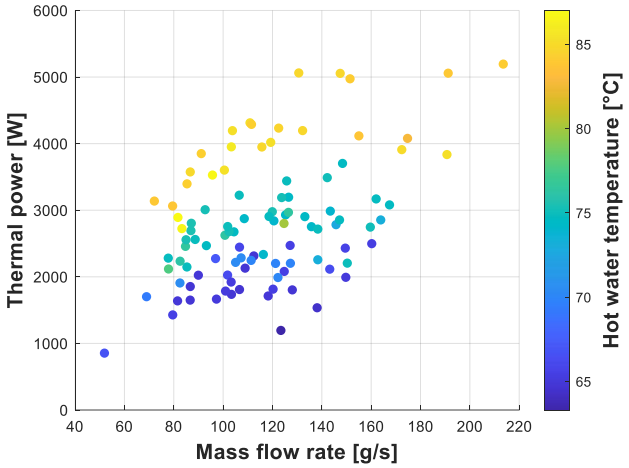

Figure 3.31 - Recuperator thermal power vs. mass flow rate varying hot water temperature.

In Figure 3.32 and Figure 3.33 the heat transfer diagrams are presented for the evaporator, with the purpose to make a comparison of the evaporator behavior at different operating conditions. In the construction of the diagrams, the pressure losses have been neglected as well as the thermal losses to the ambient. Both the assumptions are acceptable for this purpose, as the pressure losses in the evaporator are in the order of 0.1 bar, while the heat losses, although they have not been estimated, can be considered negligible since the heat exchanger is thermally insulated. The first comparison (Figure 3.32) is made at different heat source temperature (T_{Hin} around 65 °C and 85 °C for Figure 3.32) and at equal superheating degree close to 14 °C. As already mentioned, to obtain the same superheating degree, the mass flow rate must be increased when the evaporator outlet temperature increases. This leads to an increment of the evaporation pressure from 13.4 bar to 20.5 bar, corresponding respectively, to an evaporation temperature close to 51 °C and 69 °C. On the other hand, the thermal power transferred from the hot water to the working fluid increases from 15 kW to 32 kW. It can be noticed that the fraction of thermal power needed for the heating of the fluid to the saturation temperature on the total thermal power is larger for the case with heat source temperature of 85 °C (20%), than with a temperature of 65%, for which it accounts for only the 10% of the total power transferred. Differently, the share of the thermal power used for the superheating keeps similar for both conditions, around the 10%. As expected, the majority of the heat is needed for the vaporization of the working fluid, and it accounts for 80% and for 69% of the total thermal power for the 65 °C and the 85 °C cases respectively. In Figure 3.33 the comparison is made between two operating conditions characterized by same thermal power exchanged between hot water and working fluid (25 kW), related to similar values of the working fluid flow rate, and different heat source temperature (65 °C and 85 °C respectively in Figure 3.32). Evaporation pressure is slightly different between the two conditions (16.2 and 16.8 bar). The superheating degree of 4.4 °C in the case of 65 °C is close to the minimum acceptable value to avoid wet expansion and the resulting instability. The thermal power needed for the vaporization is slightly higher in case a, due to the larger value of the heat of vaporization related to the lower saturation pressure with respect to case b. Higher rate of the economizing power is also observed in case of lower heat source temperature. The heat of superheating, on the contrary, accounts for only the 3% of the total power, much less than case b where it accounts for the 16% (0.8 kW versus 4 kW). The slope of the curve of hot water is higher for case *a*, as the temperature difference is around 4.5 °C against 2.4 °C of case *b*. This is also due to the lower value of the water flow rate maintained during the test of case a.

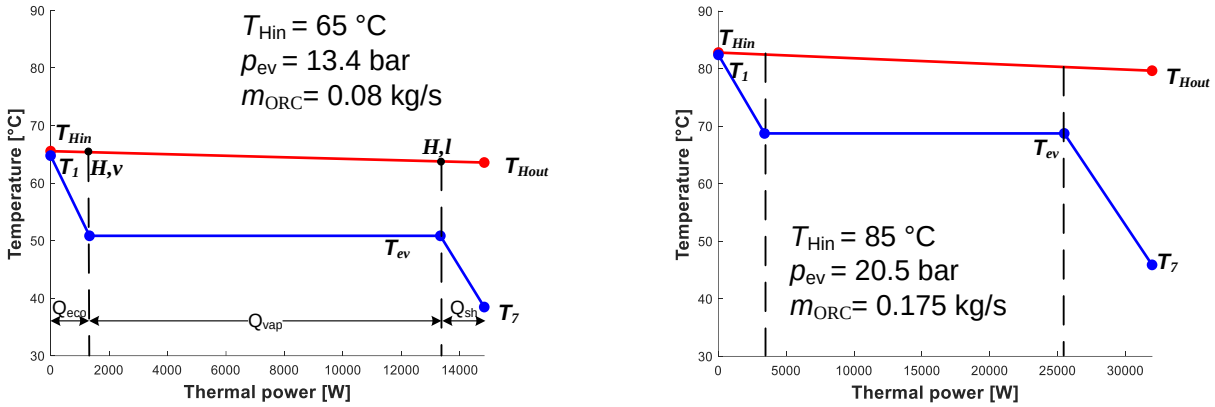

Figure 3.32 – Heat transfer diagram for the evaporator in two working conditions similar superheating degree.

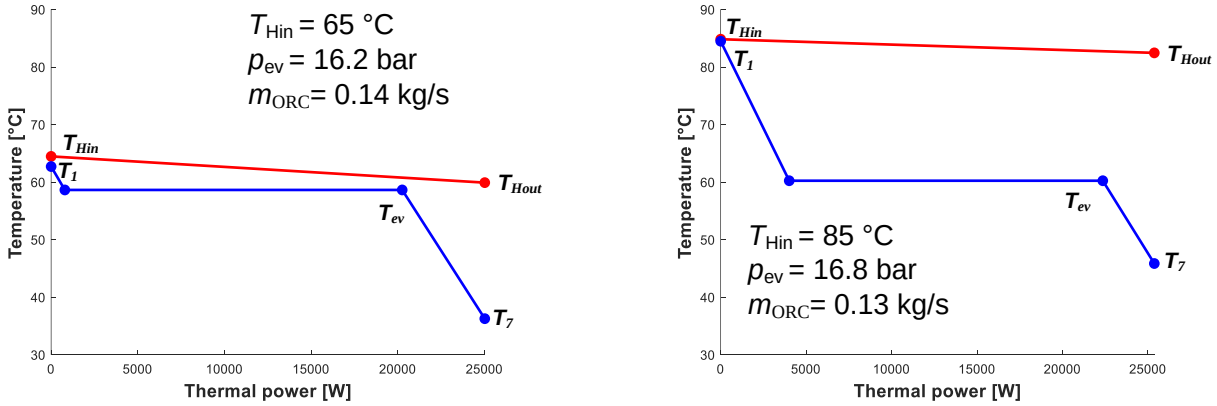

Figure 3.33 – Heat transfer diagram for the evaporator in two working conditions with similar mass flow rate.

The general expression of the heat exchanger effectiveness (ε_{HE}) is reported in Equation *(3.34)*, defined as the ratio of the thermal power actually transferred ($\dot{Q}_{HE}$) on the ideal thermal power that would be transferred with an infinite exchange area ($\dot{Q}_{HE\infty}$) or, in other words, if the temperature of the hot fluid at the outlet of the heat exchanger achieved the cold fluid inlet temperature [104]. The thermal power are expressed using the enthalpy difference evaluated at the terminals of the heat exchanger, determined from pressure and temperature values measured experimentally. The assumptions needed for this approach are:

- steady-state heat transfer conditions and no thermal losses to the ambient (thermal power discharged by hot flow is equal to that absorbed by cold flow)
- pressure losses between inlet and outlet of the heat exchanger are neglected
- for water, constant value of the specific heat c_p
- heat exchanger modeled as counter flow type
- temperature variation is linear between inlet and outlet temperature values

Two explicit forms of Equation *(3.34)* can be conveniently expressed for a general case: the adoption of the form of Equation *(3.34)* a), where the heat transfer is referred to the cold flow, is preferred when the lower terminal temperature difference occurs at the hot side outlet. The opposite, i.e. the heat transfer calculated on the hot flow, makes the use of Equation *(3.34)* b more convenient.

$$\varepsilon_{HE} = \frac{\dot{Q}_{HE}}{\dot{Q}_{HE\infty}} \qquad (3.34)$$

$$\varepsilon_{HE} = \frac{T_{out,cold} - T_{in,cold}}{T_{in,hot} - T_{out,cold}} \quad \text{with} \quad T_{out,hot} - T_{in,cold} > T_{in,hot} - T_{out,cold} \qquad \text{(a)}$$

$$\varepsilon_{HE} = \frac{T_{in,hot} - T_{out,hot}}{T_{in,hot} - T_{in,cold}} \quad \text{with} \quad T_{out,hot} - T_{in,cold} < T_{in,hot} - T_{out,cold} \qquad \text{(b)}$$

where the subscripts *in*, *out*, *hot* and *cold* refer to the inlet, the outlet, the hot flow and the cold flow, respectively. The equation of the efficiency thus defined cannot be applied directly to the evaporator, which is a once-through boiler, since it is suitable for a heat transfer without any passage of phase, while in the evaporator the fluid is preheated, vaporized and superheated. Therefore, a new definition by separating the heat transfer in three steps, namely the economization, the vaporization and the superheating. The amount of thermal power associated to each step is expressed, considering the organic fluid flow, by Equations *(3.35*), *(3.36*), *(3.37*).

$$\dot{Q}_{eco} = \dot{m}_{ORC} \cdot (h_{vap,l} - h_7) \quad (3.35)$$

$$\dot{Q}_{vap} = \dot{m}_{ORC} \cdot (h_{vap,v} - h_{vap,l}) \quad (3.36)$$

$$\dot{Q}_{sh} = \dot{m}_{ORC} \cdot (h_1 - h_{vap,v}) \quad (3.37)$$

with $\dot{Q}_{eco}$, $\dot{Q}_{vap}$ and $\dot{Q}_{sh}$ respectively the thermal powers of economizer, vaporizer and super-heater, while the subscripts *vap,l* and *vap,v* are referred to saturated liquid and vapor points. The definitions of the effectiveness for the evaporator under investigation are those reported in Equations *(3.38*), *(3.39*), *(3.40*). The values of the variable $\dot{Q}_{HE\infty}$ are calculated considering the three steps of the heat transfer as separate heat exchangers. The global evaporator effectiveness can be then computed according to Equation *(3.41*), as the ratio of the total evaporator thermal power on the sum of the thermal powers of the single sections. The subscript *H* refers to hot water and the temperatures $T_{H,v}$ and $T_{H,l}$ are those corresponding to the points *a* and *b* indicated in the heat transfer diagram of Figure 3.33. The variable named h_{Hb} represents the enthalpy that the fluid would have at the economizer outlet if it achieved the water temperature at the same terminal (T_{Hb}). The global effectiveness can also be expressed using the single zones' effectiveness, as their average weighted on the ideal thermal powers (Equation *(3.42*)).

$$\varepsilon_{eco} = \frac{(h_{vap,l} - h_7)}{(h_{Hb} - h_7)} \quad (3.38)$$

$$\varepsilon_{vap} = \frac{T_{Ha} - T_{Hb}}{T_{Ha} - T_{vap}} \quad (3.39)$$

$$\varepsilon_{sh} = \frac{(h_1 - h_{vap,v})}{(h_{Hin} - h_{vap,v})} \quad (3.40)$$

$$\varepsilon_{ev} = \frac{\dot{Q}_{ev}}{\dot{Q}_{ev\infty}} = \frac{\dot{Q}_{eco} + \dot{Q}_{vap} + \dot{Q}_{sh}}{\dot{Q}_{eco\infty} + \dot{Q}_{vap\infty} + \dot{Q}_{sh\infty}} = \frac{\dot{m}_{ORC} \cdot (h_1 - h_7)}{\dot{m}_{ORC} \cdot (h_{H,l} - h_7 + h_{Hin} - h_{vap,v}) + \dot{m}_H \cdot c_{pH} \cdot (T_{H,v} - T_{H,l})} \quad (3.41)$$

$$\varepsilon_{ev} = \frac{\varepsilon_{eco} \cdot \dot{Q}_{eco\infty} + \varepsilon_{vap} \cdot \dot{Q}_{vap\infty} + \varepsilon_{sh} \cdot \dot{Q}_{sh\infty}}{\dot{Q}_{eco\infty} + \dot{Q}_{vap\infty} + \dot{Q}_{sh\infty}} \quad (3.42)$$

In Figure 3.34 the effectiveness of the single sections of the evaporator are reported versus the evaporator thermal power. As expected, the effectiveness of the superheating section (ε_{sh}) presents very high values (higher than 90%) for most of the tested conditions. The vaporizer effectiveness (ε_{vap}) shows values lower than 20% for all conditions characterized by an evaporator thermal power lower than 17 kW, while at a power larger than 20 kW, also values of ε_{vap} close to 50% are achieved. The effectiveness of the economizer keeps quite low for all the working conditions, increasing slightly up to the maximum of 25% with the thermal power. Figure 3.35 shows the global evaporator effectiveness (ε_{ev}) resulting from the application of Equation *(3.42*) on the measured data, as function of the evaporation pressure and hot water temperature. The evaporation pressure rise leads to the increment of the value of ε_{ev} at all the conditions of hot water temperature, as both pressure and thermal power are related to the mass flow rate of the organic fluid. At constant pressure, the global effectiveness is higher for lower values of the hot water temperature. The maximum value of ε_{ev} with T_{Hin} around 65 °C is close to 45% at a

pressure of 16 bar. With T_{Hin} of 85 °C, the maximum is only 27% and corresponds to a value of the evaporating pressure close to 22.5 bar. With a pressure lower than 18 bar and T_{Hin} around 85 °C, the values of ε_{ev} is always lower than 10%. Indeed, the low value of hot temperature together with the high pressure of vaporization (thus low superheating degree), make reduce the temperature difference at the pinch point ($\Delta T_{pp,ev}$), improving the effectiveness of both economizer and vaporizer sections of the heat exchanger. This is well explained in the comparison of the heat transfer diagrams of Figure 3.33, obtained with similar pressure at hot water temperature of 65 °C and 85 °C. It must be pointed out that the low values of superheating degree tested at 65 °C are not achievable at 85 °C, since the pressure in the circuit would be too high for the system. For example the saturation pressure at evaporation temperature of 80 °C, (corresponding to a ΔT_{sh} around 5 °C) results close to 26.3 bar, which is close to the maximum pressure of the circuit for safe operation. Moreover, as described in the previous paragraph, at high pump speed, required to achieve high evaporation pressure, phenomena of cavitation have been experienced, causing instable operation of the ORC system.

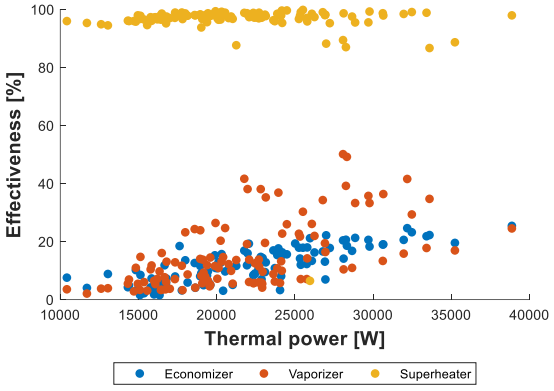

Figure 3.34 – Evaporator zones effectiveness vs. evaporator thermal power.

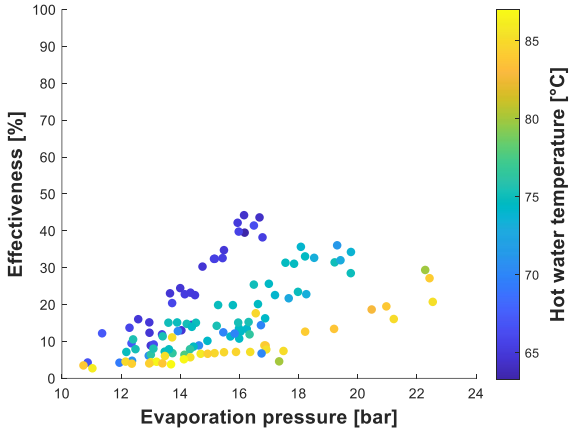

Figure 3.35 – Evaporator global effectiveness vs. evaporation pressure varying hot water temperature.

Separating the evaporator into the three zones allows also to calculate the product of the heat transfer surface (*A*) and the global heat transfer coefficient (*U*). This parameter, that is usually referred as *UA*, is characteristic of the behavior of the heat exchanger and depends also on the operating conditions. The parameter UA is defined, for counter flow heat exchangers, as the ratio of the thermal power exchanged to the value of the logarithmic mean temperature difference (*LMTD*). In the case of an evaporator, in which the fluid passes from subcooled liquid to superheated vapor, the expression to calculate the parameter *UA* must be applied to each zone (economizer, vaporizer and super-heater), assuming the form reported in Equations *(3.43)*, *(3.44)*, *(3.45)*, valid for the heat exchanger under investigation.

$$UA_{\text{eco}} = \frac{\dot{Q}_{\text{eco}}}{LMTD_{eco}} = \frac{\dot{m}_{\text{ORC}} \cdot (h_{ev,l} - h_7)}{(T_{H,l} - T_{ev}) - (T_{H,out} - T_7)} \cdot \ln\left(\frac{T_{H,l} - T_{ev}}{T_{H,out} - T_7}\right) \qquad (3.43)$$

$$UA_{\text{vap}} = \frac{\dot{Q}_{\text{vap}}}{LMTD_{vap}} = \frac{\dot{m}_{\text{ORC}} \cdot (h_{ev,v} - h_{ev,l})}{(T_{H,v} - T_{ev}) - (T_{H,l} - T_{ev})} \cdot \ln\left(\frac{T_{H,v} - T_{ev}}{T_{H,l} - T_{ev}}\right) \qquad (3.44)$$

$$UA_{\text{sh}} = \frac{\dot{Q}_{\text{sh}}}{LMTD_{sh}} = \frac{\dot{m}_{\text{ORC}} \cdot (h_1 - h_{ev,v})}{(T_{H,in} - T_1) - (T_{H,v} - T_{ev})} \cdot \ln\left(\frac{T_{H,in} - T_1}{T_{H,v} - T_{ev}}\right) \qquad (3.45)$$

where the subscripts *H,l* and *H,v* refer to the points indicated in the heat transfer diagram of Figure 3.32

Knowing the value of the parameter UA allows to estimate the heat transfer actual surface of the heating, vaporizing and superheating zones, using the correlations applied in the literature to calculate the heat transfer coefficient. The latter is a function of the Nusselt number (*Nu*), according to Equation *(3.46*).

$$U = \left(\frac{Nu \cdot \lambda}{D_{hy}}\right) \tag{3.46}$$

with λ thermal conductivity, D_{hy} hydraulic diameter. The Nusselt number is affected by the flow regime, and it is computed with different correlation if the flow is laminar – thus with Reynolds number (Re) lower than 2000) – rather than turbulent (Re > 4000). With turbulent flow, if the working fluid is in the subcooled liquid or superheated vapor zones, the Nusselt number is calculated with the Gnielinski correlation [105], reported in Equation *(3.47*):

$$Nu = \frac{\frac{f}{8} \cdot (Re - 1000) \cdot Pr}{1 + 12.7 \cdot \sqrt{\frac{f}{8}} \cdot (Pr^{\frac{2}{3}} - 1)} \tag{3.47}$$

where *Pr* is the Prantdl number of the fluid and f is the Darcy friction factor. If the fluid is in the two-phase zone, the correlation used is the one introduced by Cavallini and Zecchin [106], shown in Equation *(3.48*):

$$Nu = 0.05 \cdot \left[(1 - x + x \cdot \sqrt{\frac{\rho_{sl}}{\rho_{sv}}}) \cdot Re_{sl}\right]^{0.8} \cdot Pr_{sl}^{0.33} \tag{3.48}$$

where the subscripts *sl* and *sv* refer to saturated liquid and saturated vapor.
The trends of the *UA* for the different zones are presented in Figure 3.36 a as function of the working fluid mass flow rate. As expected, the highest values of *UA* are registered in the vaporizer zone, followed by the super-heater and then by the economizer, in all cases increasing with the flow rate. In Figure 3.36 b- Figure 3.36 c, the effect of the hot water inlet temperature on *UA* is presented for each zone separately. In the economizer zone (subcooled liquid) the value of UA_{eco} ranges between 5 kW/K and 700 kW/K, and at constant flow rate it results higher with lower hot water temperature. The same effect of $T_{H,in}$ on *UA* is observed in the vaporization zone, where the parameter UA_{vap} increases with $\dot{m}_{\mathrm{ORC}}$ from 200 kW/K to 2700 kW/K with hot water temperature of 85 °C, while at the lowest temperature (65 °C), the increment is exponential up to 6000 kW/K. At constant mass flow rate, the reduction of UA is due to the increment of the logarithmic mean temperature difference, that is related to the increase of $T_{H,in}$ and of the evaporator inlet temperature (T_7). In the superheated zone the effect of hot water temperature is mitigated from the fact that the hot terminal temperature difference is maintained quite constant and low among all conditions. Hence the main effect is given by the mass flow rate, and the UA value ranges between 180kW/K and 1200 kW/K as $\dot{m}_{\mathrm{ORC}}$ increases from 50 g/s to 210 g/s.

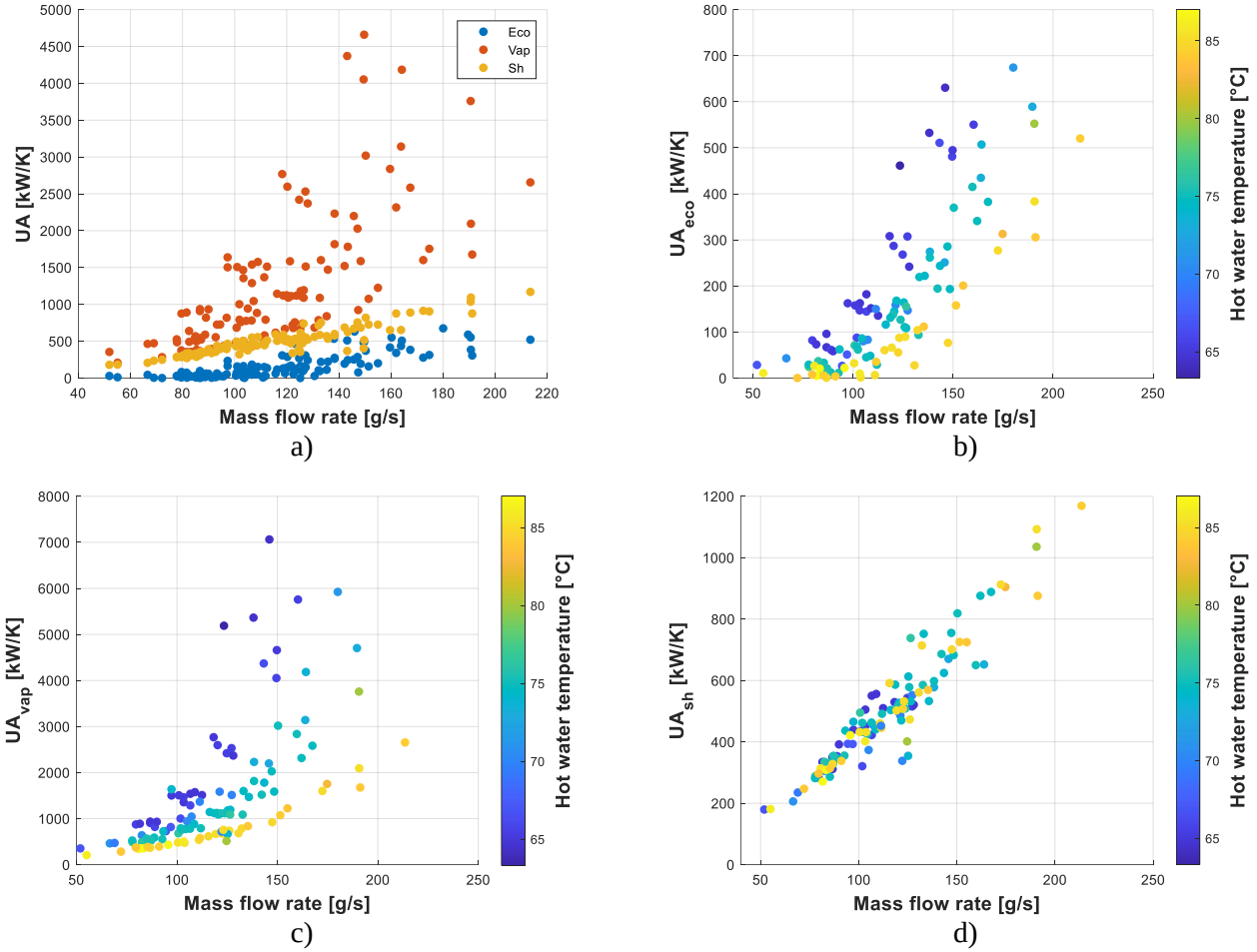

Figure 3.36 – Trends of the parameter UA vs mass flow rate varying the hot water temperature.

In Figure 3.37 the heat transfer diagrams are reported for the recuperator in two cases, with same mass flow rates around 0.14 kg/s (thus similar evaporation pressure), different hot water temperature (65 °C and 85 °C), and different value of condensation pressure, namely 7.4 bar and 6.3 bar for case *a* and case *b* respectively (same working conditions presented in Figure 3.32 for the evaporator). Confirming the trend reported observed for the evaporator, the recuperator thermal power is mainly affected by the hot water temperature than by the working fluid flow rate, being significantly higher in case *b* (4.2 kW) than in case *a* (1.5 kW). Looking at Figure 3.37, it can be noticed that the curves of the hot and cold streams are close to be parallel with hot water temperature equal to 65 °C, while with T_{Hin} equal to 85 °C the slope of the curve of the hot stream is substantially higher, determining a higher recuperator effectiveness that varies from 84% of case a to 93% of case b. The resulting contribution to the total heat input varies from 6% of case *a*, to almost 17% of case *b*. In other words, the benefit of the adoption of the recuperator is more limited, although not negligible, when the system works with low values of the heat source temperature. The recuperator effectiveness (ε_{rec}) is expressed by Equation *(3.49)*, where the temperature differences are used instead of the enthalpies to perform an easier calculation of the ideal thermal power. Indeed, since the outlet of the recuperator is generally characterized by very low superheating degree, the calculation via CoolProp of the enthalpy corresponding to liquid inlet temperature may give as result an enthalpy value related to the subcooled region (that is generally between 240 kJ/kg and 280 kJ/kg), leading to incorrect results for ε_{rec}.

$$\varepsilon_{rec} = \frac{\dot{Q}_{rec}}{\dot{Q}_{rec\infty}} = \frac{T_2 - T_3}{T_2 - T_6} \qquad (3.49)$$

Under certain conditions, it is observed that the vapor flow of working fluid starts to condense already in the recuperator. This circumstance cannot be directly detected from simply observing the acquired data of temperature and pressure. The first warning is given by imbalance between the stationary thermal powers of the recuperator calculated on liquid and vapor side. If the value of $\dot{Q}_{\mathrm{rec,v}}$ is lower than $\dot{Q}_{\mathrm{rec,l}}$, it is possible that there is an error in the estimation of the vapor thermal power, because the latter should be equal to the thermal power on liquid side, or higher in case of thermal losses to the ambient. In this case, the outlet enthalpy ($h_3{}'$) is computed by means of the energy balance at the recuperator, using the thermal power referred to the liquid side, according to Equation *(3.50)*. The vapor quality (x_3) is then calculated using the enthalpy $h_3{}'$ and the pressure p_3, resulting very close to one in all the cases analyzed. The heat transfer diagram remains quite similar to the case of non-condensation in the recuperator, as the amount of latent heat transferred in the recuperator is very small. However, from the comparison between points with similar operating conditions, an increase of the condensation pressure is observed for the tested points with saturation condition at the recuperator outlet. Looking at Figure 3.38, the two heat transfer diagrams (case *a* and case *b*) have close heat source temperature of 74 °C and 70 °C, while cold water temperature and working fluid flow rate are nearly equal. However, the condensation pressure results significantly higher in case *a* (8.7 bar) than in case *b* (7.3 bar). It can be observed that the recuperator outlet temperature (T_3) of case *a* is close to 35 °C, and corresponds to the condensation temperature, while in case *b* T_3 is lower (near 30 °C), with a condensation temperature of 28 °C that is achieved inside the condenser. The minimum saturation pressure in case of start of condensation in the recuperator is limited by the pinch point temperature difference and by the value of the inlet temperature on liquid side, that is always higher than the cold water temperature. Regarding the condenser, the sub-cooling degree at its outlet is 3.9 °C in case *a* and 0.6 °C in case *b*, suggesting that the cooling power that is saved from the intake of saturated fluid in case *a*, is used for the sub-cooling at the condenser outlet. Moreover, the heat of condensation is lower at higher pressure, resulting in a value of ΔT_{sc} near zero. Even if this may be considered an advantage in terms of cavitation problems, the increment of the condensation pressure has negative impact on the performance of the system, reducing the specific work and thus the power output. Moreover, no significant benefits in terms of cavitation have been demonstrated experimentally, as some events has occurred in both cases eventually. The power output is higher in case *b* (580 W vs. 480 W), even if the evaporation pressure is one-bar lower than in case *a* (13.9 bar and 14.9 bar, for case *a* and case *b* respectively). The expression of the recuperator effectiveness should be modified according to Equation *(3.51)*, to take into account the latent heat transferred. However, since the value of the vapor quality is very close to one, using the form reported in Eq. *(3.49)* leads to very small errors for most of the cases analyzed.

$$h_3{}' = h_2 - h_7 + h_6 \tag{3.50}$$

$$\varepsilon_{\mathrm{rec}}{}' = \frac{(T_2 - T_6) + (h_a - h_6)}{(T_2 - T_{pp}) + (h(T_{sat}, p_6) - h_6)} \tag{3.51}$$

where the quantity T_{pp} is the temperature of the liquid flow that corresponds to the pinch point of the condensing zone of the vapor flow (see Figure 3.38a).

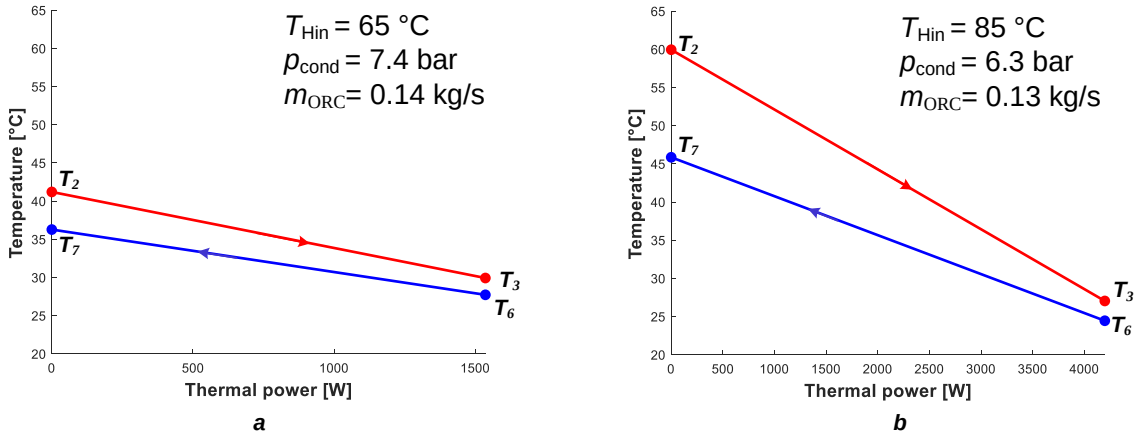

Figure 3.37 – Comparison of heat transfer diagrams for the recuperator between two working conditions.

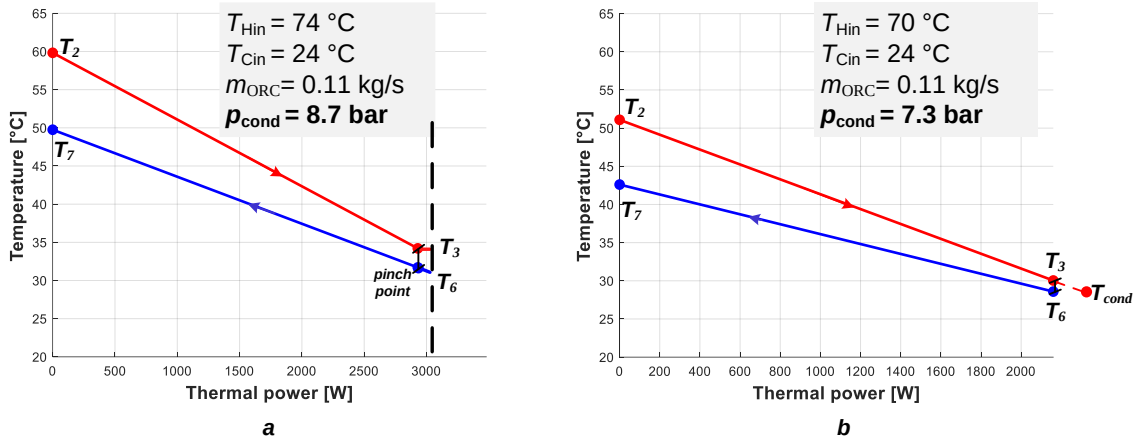

Figure 3.38 – Comparison of heat transfer diagram for two similar conditions, in case of saturated vapor at the outlet (case a) and superheated vapor (case b).

The dependency of the recuperator effectiveness from the working fluid mass flow rate and from the heat source temperature is presented in Figure 3.39, showing a decreasing trend as the value of $\dot{m}_{ORC}$ increases. The figure confirms that, at constant mass flow rate, the effectiveness is higher for higher values of hot water temperature, as confirmed by the slopes of the heat transfer curves in the T-Q diagram comparison of Figure 3.37. The increment of the expander outlet temperature T_2 (related to the increment of the inlet temperature, T_1) determines a higher rate of available thermal power for the recuperator heat recovery, since the expander discharges a fluid with higher superheating degree, corresponding to higher enthalpy content. Indeed, the recuperator outlet temperature is influenced by the condenser conditions, such as the cooling water temperature, and shows more limited variations varying the working conditions. Hence, the temperature difference across the recuperator ($T_2 - T_3$) increases mostly with the increment of T_{Hin}. In any case, the recuperator effectiveness is high, above 80% in all the tested conditions.

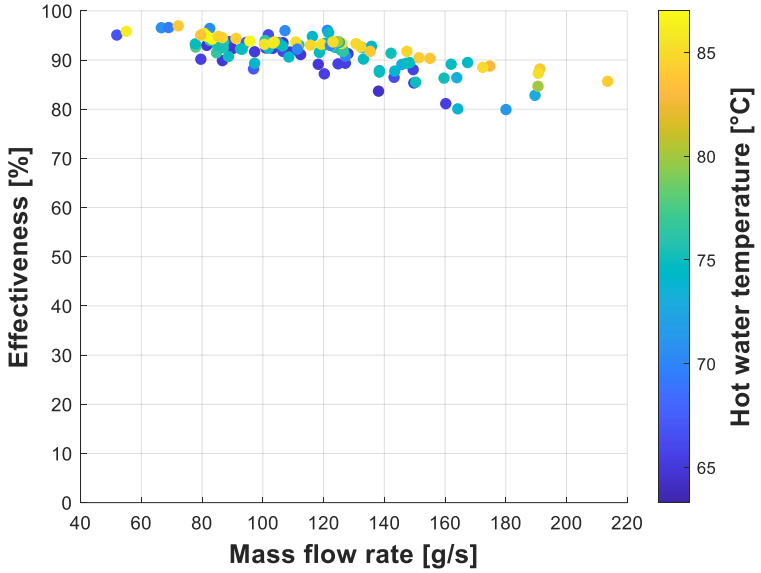

Figure 3.39 – Recuperator global effectiveness vs. mass flow rate varying hot water temperature.

Figure 3.40 a-d show two comparisons of the condenser heat transfer performance in the temperature-thermal power diagram. The diagrams of Figure 3.40 a and b refer to two operating conditions characterized by same value of the cold water inlet temperature, T_{Cin} (15 °C) and different flow rate and transferred thermal power. The water temperature rises more in the case of higher mass flow rate (case *b*), but the minimum temperature difference (T_4 – T_{Cout}) is instead higher in case *a*. However, the temperature difference at the pinch point is substantially similar between the two cases, since the working fluid at the condenser outlet in case *a* presents a larger value of the sub-cooling degree. The fluid enters the condenser almost as saturated vapor in the case with lower mass flow rate, while it has a superheating of about 4 °C with high mass flow rate (case *b*). The comparison of Figure 3.40 c) and d) is made between two working points with same cold water inlet temperature and organic fluid mass flow rate (hence with similar transferred thermal power), but in case c the fluid has started to condense inside the recuperator and thus enters the condenser in saturated conditions. Confirming the behavior already observed in Figure 3.38, the condensation pressure is significantly higher in case *c* (8.7 bar) than in case *d* (7.3 bar), with consequent diminution of the expander available pressure ratio and specific work. For case *c*, the pinch point occurs at the recuperator hot terminal, with a pinch point temperature difference close to 9 °C; for case *d*, the pinch point is located after the cooling phase (that requires around 200 W) and the temperature difference is equal to 2.3 °C. The value of the sub-cooling degree varies between 3.9 °C in case *c* and 0.6 °C in case *d*. In all the cases analyzed, almost the entire cooling power transferred from the cold water is used for the phase of condensation of the working fluid, as a minimum fraction is needed by the sub-cooling process and by the cooling of the superheated vapor to the saturated state. For this reason, the calculation of the condenser effectiveness is simplified considering only the condensing zone and using the water temperatures (Equation *(3.52)*). The condenser effectiveness varies between 13% and 50% with condensing pressure and cold water temperature (Figure 3.41). The low performance (condenser effectiveness below 30%) of a significant amount of operating points can be deduced also from the high value of the condenser pinch point temperature difference on the heat transfer diagram of Figure 3.40, case a, b and c. For all the operating conditions, the effectiveness of the condenser is limited by the low variation of the cold water temperature, whose heat transfer curve is rather flat. With regards to the conditions presented in Figure 3.40, the values of the effectiveness is 22% for case *a*, 29.5% for case *b*, 17% for case *c* and 45% for case *d*.

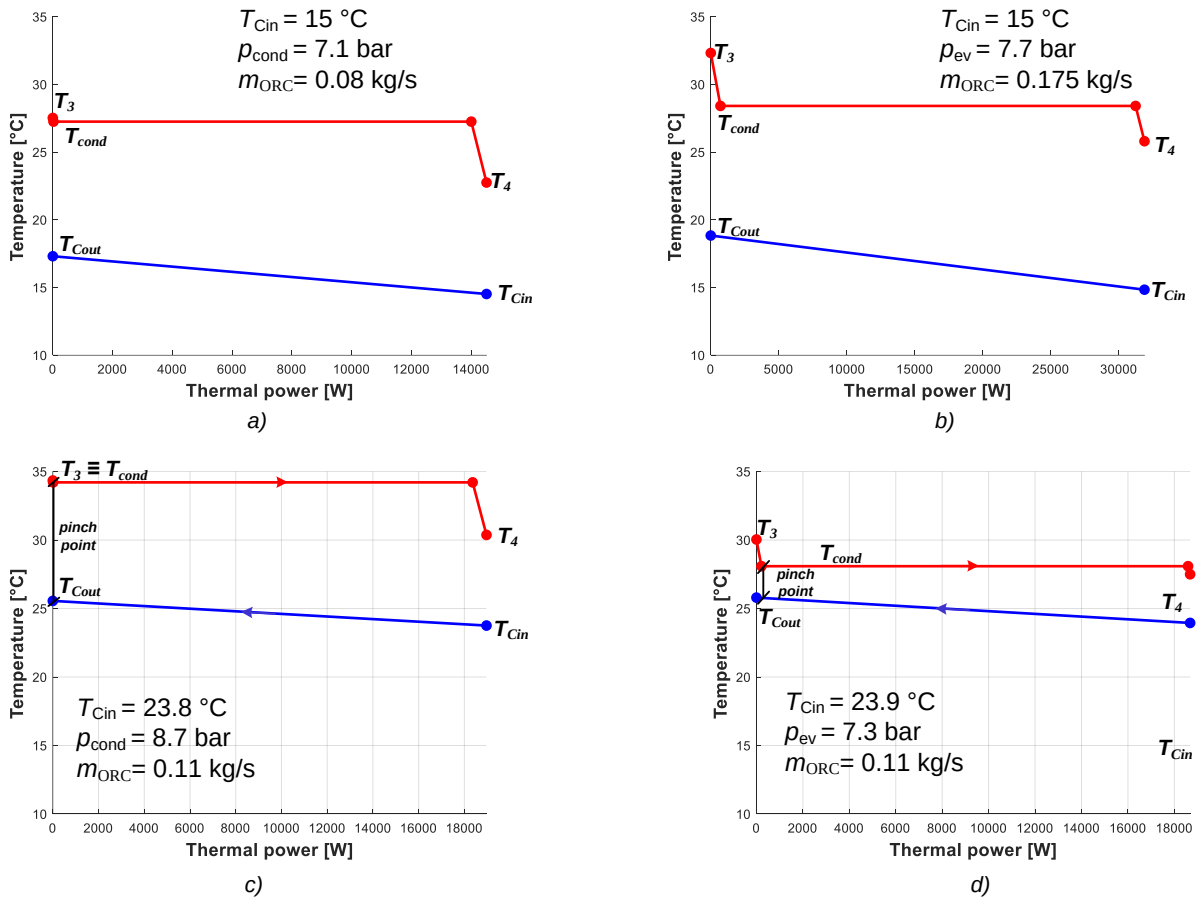

Figure 3.40 – Heat transfer diagram for the condenser at different working conditions: cases a and b, comparison with different mass flow rate; cases c and d, comparison with and without condensation started in the recuperator.

$$\varepsilon_{\text{cond}} = \frac{\dot{Q}_{\text{cond}}}{\dot{Q}_{\text{cond}\infty}} = \frac{T_{Cout} - T_{Cin}}{T_{cond} - T_{Cin}} \tag{3.52}$$

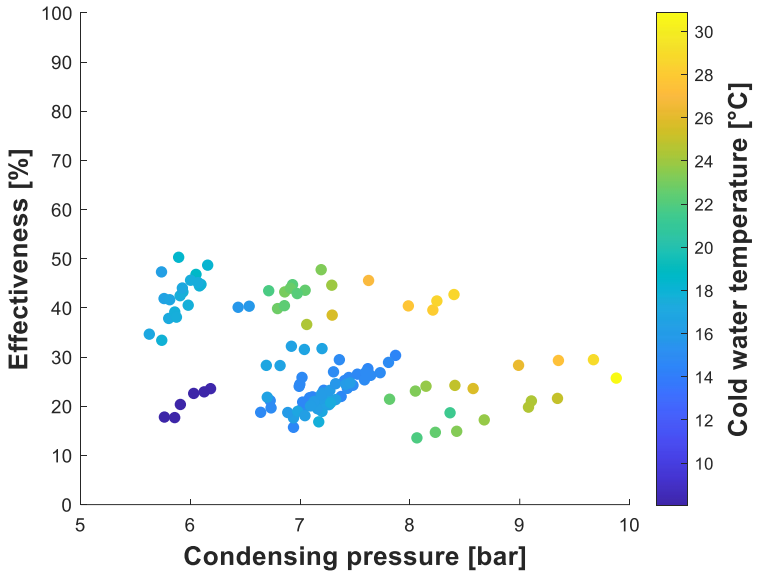

Figure 3.41 – Condenser effectiveness vs. condensing pressure varying cold water temperature.

In Figure 3.42 the pressure losses (Δp_{loss}) in the different heat exchangers are plotted versus the mass flow rate. It was observed that the most relevant values of pressure losses are registered on the vapor side of the recuperator, ranging from 0.1 bar up to 0.35 bar. In the evaporator, they vary between 0.05 bar and 0.15 bar, while in the condenser and especially in the liquid side of the recuperator, Δp_{loss} presents very small values, lower than 0.05 bar. Except for the recuperator, pressure losses in the other heat exchangers do not seem to be very much influenced by the value of $\dot{m}_{ORC}$. Table 3-6 summarizes the ranges of variation of the pressure losses in the heat exchangers as percentage of the inlet pressure. The hot stream of the recuperator, which works at low pressure, is interested by the higher range of percent pressure losses, with an average value around 2.5%.

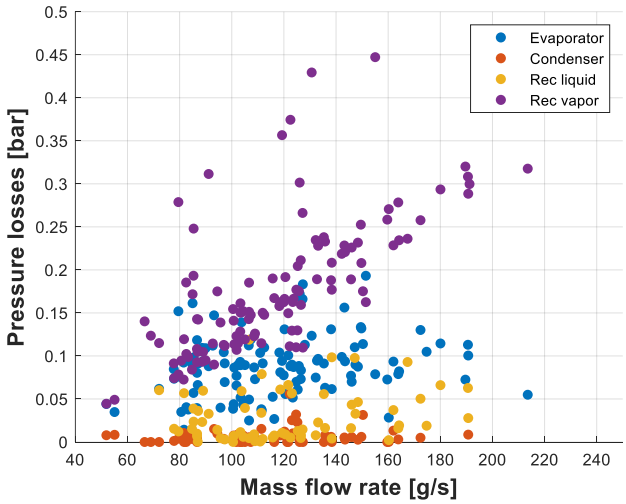

Figure 3.42 – Heat exchangers pressure losses vs. mass flow rate.

Table 3-6 – Range of percentage variation of pressure losses for the different heat exchangers

Heat exchanger	Pressure losses [%]
Evaporator	0.1-1.5
Condenser	0.05-0.7
Recuperator (liquid)	0.05-1
Recuperator (vapor)	1-8

3.4.5 Overall performance

The overall net power output ($\dot{W}_{\mathrm{exp,el}} - \dot{W}_{\mathrm{p,el}}$) is presented in Figure 3.43, as function of the working fluid mass flow rate and pressure difference across the expander. The plot confirms the strong penalization related to the low efficiency of the feed-pump and to its consequent high consumption. The net power ranges from few watts for the worst case to more than 500 W at high flow rate and pressure difference. In order to improve the overall performance, plus the increase of the pump efficiency, a possible solution would be to connect mechanically the shafts of the pump and of the expander, to avoid the losses related to the electro-mechanical conversion on pump motor and expander generator. However, this configuration requires a precise design and sizing of the two machines geometry. Moreover, the flexibility on speeds regulation that is guaranteed by the use of inverters, should be accomplished by implementing a variable speed reducer or variable displacement pump (and/or expander), involving more complexity and mechanical losses.

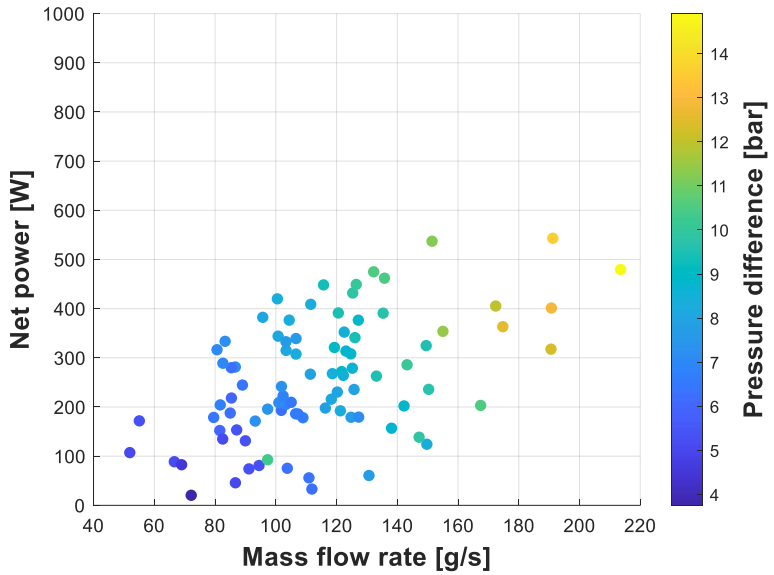

Figure 3.43 – The overall net power output as function of the working fluid mass flow rate and pressure difference across the expander.

The global performance of this kind of ORC systems is strongly limited by the difference between the temperature at which the heat is introduced to the cycle and the temperature of cold sink, which is very low if compared to the traditional thermal system employed for electricity generation. The efficiency of the equivalent Carnot cycle (η_{carnot}) is evaluated as the ratio of the difference between the heat source and the cold sink temperature to the heat source temperature (Equation *(3.53)*), and represents the ideal efficiency achievable by a thermal cycle between the temperature of hot source and cold sink. As showed in Figure 3.44 as function of T_{Hin} and T_{Cin}, the Carnot efficiency of the system under investigation ranges between 10% and 18%.

$$\eta_{\mathrm{carnot}} = \frac{T_{Hin} - T_{Cin}}{T_{Hin}} \qquad (3.53)$$

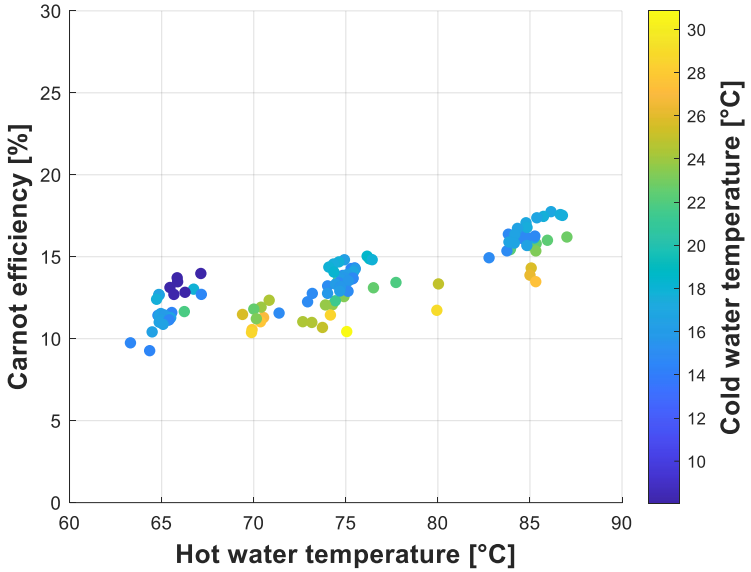

Figure 3.44 – Carnot equivalent efficiency vs. hot water temperature varying cold water temperature.

The overall efficiency of the micro-ORC system is evaluated as the ratio of the power output to the heat input. Two version are indicated, depending on whether the power output is considered gross (the total power produced by the expander) or net (subtracting the power consumed by the feed-pump). Equation *(3.54)* and *(3.55)* represent the two expressions of the overall efficiency. In Figure 3.45 a) the gross overall efficiency ($\eta_{\mathrm{ORC,gross}}$) is plotted versus the pressure difference across the expander, with the loads number indicated with different colors. The rate of $\eta_{\mathrm{ORC,gross}}$ increases slightly with the value of Δp_{exp}. The maximum value results close to 5% with a pressure difference of 11.2 bar. In the case of one load, the gross efficiency does not seem to have significant variation with the pressure difference, establishing around the 2%. The best efficiency trends are obtained with 3, 4 and 5 loads activated. Figure 3.45 b) shows the same plot for the overall net efficiency ($\eta_{\mathrm{ORC,net}}$), revealing that the maximum value of the net efficiency is obtained in correspondence of medium level of pressure difference (between 7 bar and 9 bar), while it decreases at higher values of Δp_{exp}. The net efficiency is strongly penalized by the high electric consumption of the feed-pump, which in some cases covers almost the entire amount of expander power output. It can be observed that in case of one load the net efficiency is extremely scarce, not achieving the value of 1% for the whole range of pressure difference. Since it is clear that the performance of this specific pump are not acceptable for this application, an additional evaluation of the overall net efficiency ($\eta_{\mathrm{ORC,net}}$) has been made by using a reference value of the pump total efficiency ($\eta_{p,tot}$), taken as the average of those found in the literature regarding similar application of ORC system [42]. The reference pump efficiency is taken equal to 50%, and is multiplied to the pump hydraulic power to obtain the electric power consumed by the pump. The overall net efficiency trend resulting from this artificial operation is reported in Figure 3.46 as function of the pressure difference.

$$\eta_{\mathrm{ORC,gross}} = \frac{\dot{W}_{\mathrm{exp,el}}}{\dot{Q}_{\mathrm{ev}}} \tag{3.54}$$

$$\eta_{\mathrm{ORC,net}} = \frac{\dot{W}_{\mathrm{exp,el}} - \dot{W}_{\mathrm{p,el}}}{\dot{Q}_{\mathrm{ev}}} \tag{3.55}$$

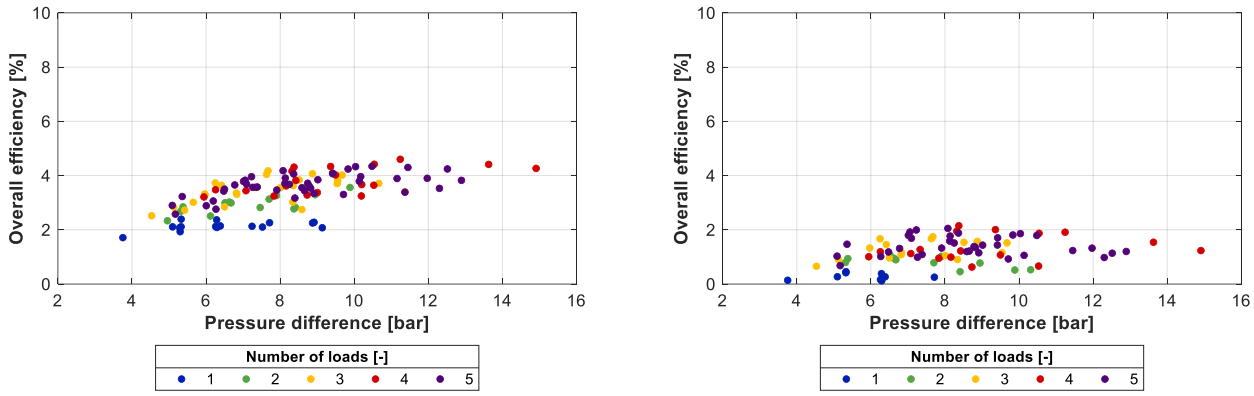

Figure 3.45 – Overall efficiency of the ORC vs pressure difference at different loads number: a) gross efficiency; b) net efficiency.

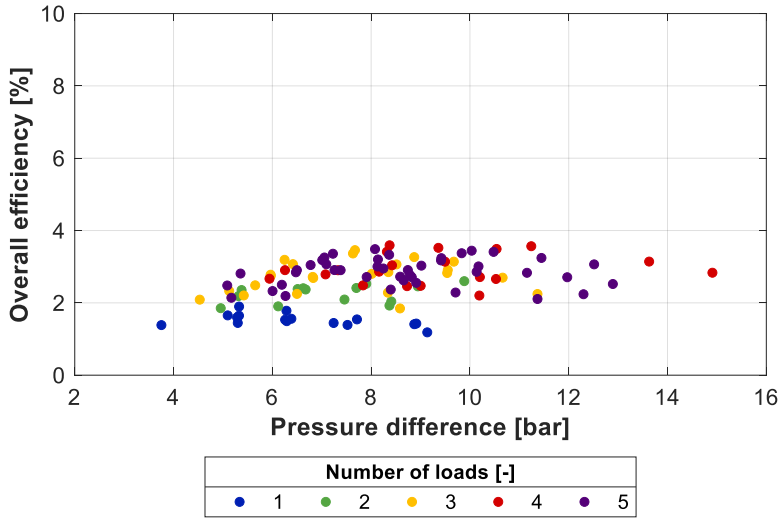

Figure 3.46 – Overall net efficiency vs pressure difference at different loads number, in case of pump efficiency equal to 0.5.

A schematic representation of the heat fluxes is presented in the Sankey diagrams of Figure 3.47, for an average working conditions characterized by a hot water temperature set-point equal to 85 °C and a pump speed of 200 rpm. Almost all the power introduced is discharged to the cold sink, as the ideal power available for the expansion work is only 10.7% of the heat input. The irreversibility includes also the thermal losses through the expander surfaces, which have been estimated below 50 W, thanks to the thermal insulation. The diagram highlights the penalizations due to the relatively low expander efficiency (lower than 45%), and to the pump consumption, which absorbs 50% of the gross expander electric output.

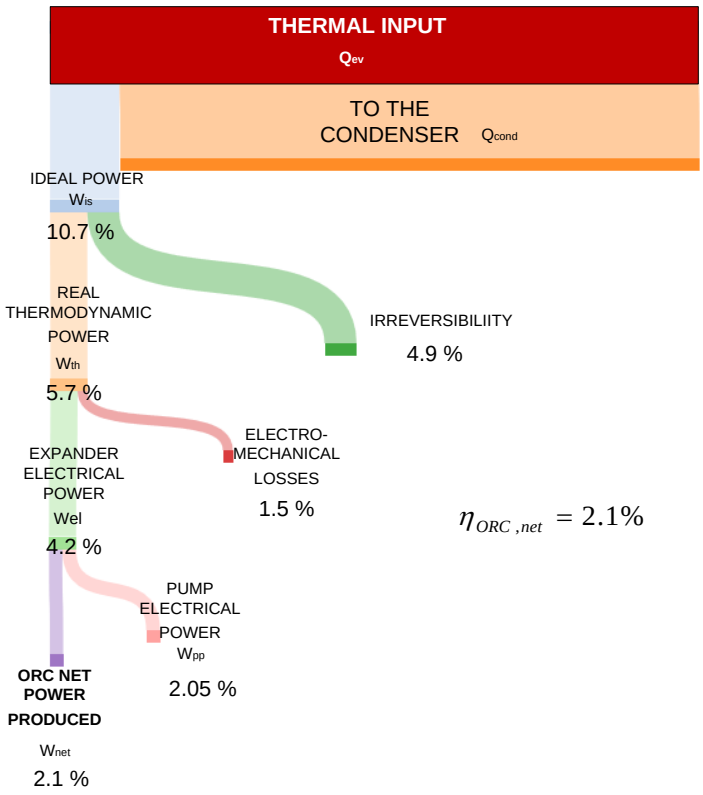

Figure 3.47 - Sankey diagram

Finally, Table 3-7 collects the optimum operating conditions obtained during the steady-state test campaign, in terms of expander power output and overall gross efficiency. The optimum points are identified for each level of heat source temperature (65 °C, 75 °C, 85 °C), and the values of mass flow rate, cooling temperature and loads number corresponding to the best performance are indicated.

Table 3-7 – Optimal tested operating conditions at different hot source temperature

Heat source temperature	T_{Hin} = 65 °C	T_{Hin} = 75 °C	T_{Hin} = 85 °C
Condition of maximum power output			
$P_{exp,el}$	1000 W	1120 W	1660 W
$\eta_{ORC,gross}$	3.7%	3.9%	4.3%
$\dot{m}_{ORC}$	0.15 kg/s	0.16 kg/s	0.21 kg/s
Δp_{exp}	9.5 bar	11.2 bar	14.9 bar
T_{Cin}	8.1 °C	14.9 °C	16.7 °C
Condition of maximum overall efficiency			
$\eta_{ORC,gross}$	4.1%	5.6%	4.6%
$P_{exp,el}$	970 W	990 W	1290 W
$\dot{m}_{ORC}$	0.13 kg/s	0.10 kg/s	0.15
Δp_{exp}	8.9 bar	10.3 bar	11.2 bar
T_{Cin}	8 °C	15.8 °C	16.7 °C

3.5 Micro-ORC analytical model

The knowing of the experimental data of the micro-ORC system allows to make some a-priori consideration on its real behavior. An analytical steady-state model of empirical type can be used to perform a first estimation of the performance of the system, for example to evaluate its feasibility in case of application different from that the system was designed for. The empirical model has the advantage of being robust and easy to implement, requiring a limited number of experimental data to work (lower than the amount of operating points acquired in the experimental campaign above described). The main disadvantage is the low accuracy when applied to operating conditions that are significantly different for those on which the model is calibrated. A schematic block diagram representing the flow chart of the analytical model is reported in Figure 3.48. The model input variables are the hot water inlet temperature (T_{Hin}), the cold water inlet temperature (T_{Cin}), and the working fluid mass flow rate ($\dot{m}_{\mathrm{ORC}}$). The assumed parameters are the temperature difference between T_{Hin} and the evaporator outlet temperature (T_1), the pinch point temperature difference at the condenser ($\Delta T_{pp,cond}$) , the superheating and sub-cooling degrees (ΔT_{sh} and ΔT_{sc}), and the expander and pump isentropic efficiencies ($\eta_{\mathrm{exp,is}}$ and $\eta_{\mathrm{p,is}}$). A constant value of both the efficiencies is assumed, equal to 0.5 and to 0.3 for expander and pump efficiencies, respectively. It must be pointed out that the efficiency to use in this calculation is the isentropic efficiency, expressed by Equation *(3.56*) and *(3.57*), since they are used not only to estimate the power output but also to determine the thermodynamic state of the fluid at the expander and pump outlets.

$$\eta_{\mathrm{exp,is}} = \frac{\dot{W}_{\mathrm{exp,th}}}{\dot{W}_{\mathrm{exp,is}}} = \frac{(h_1 - h_2)}{(h_1 - h_{2,is})} \qquad (3.56)$$

$$\eta_{\mathrm{p,is}} = \frac{\dot{W}_{\mathrm{p,hy}}}{\dot{W}_{\mathrm{p,th}}} = \frac{\dot{V}_5 \cdot (p_6 - p_4)}{\dot{m}_{ORC} \cdot (h_6 - h_4)} \qquad (3.57)$$

The routine starts calculating the values of the maximum temperature of the cycle, T_1, and of the condensing temperature (T_{cond}), by means of Equation *(3.58*) and *(3.59*), respectively.

$$T_1 = T_{Hin} - \Delta T_{ev,pp} \qquad (3.58)$$

$$T_{cond} = T_{Cin} + \Delta T_{cond,pp} \qquad (3.59)$$

The vaporization temperature (T_{ev}) is obtained with the imposed value of superheating degree (Equation *(3.60*)). The corresponding evaporation and condensation pressures (p_{ev} and p_{cond}) are computed via CoolProp. To evaluate the mass flow rate of the working fluid, a first order equation, obtained using the experimental trend of $\dot{m}_{\mathrm{ORC}}$ versus p_{ev}, is applied (Equation *(3.61*)).

$$T_{ev} = T_1 - \Delta T_{sh} \qquad (3.60)$$

$$\dot{m}_{ORC} = \frac{p_{ev} - a}{b} \qquad (3.61)$$

where the empirical coefficients *a* and *b* have been obtained from experimental trend of mass flow rate versus the evaporation pressure.
Now that the expander inlet state is fully determined by pressure and temperature values, the expander isentropic efficiency definition is applied to calculate the expander inlet enthalpy. Note that the quantity $\eta_{exp,is}$ is the isentropic efficiency defined in Eq. *(3.62*) and not the expander total efficiency, since it takes into account the enthalpy difference (or specific work) instead of the electrical power.

$$h_2 = h_1 - (h_1 - h_{2,is}) \cdot \eta_{exp,is} \qquad (3.62)$$

Moving the calculation on the condenser side the sub-cooling degree is then used to compute the condenser outlet temperature (Equation *(3.63*)).

$$T_4 = T_{cond} - \Delta T_{sc} \tag{3.63}$$

Once the thermodynamic state at pump inlet is fully determined, the pump outlet enthalpy (h_6) is calculated supposing the process isenthalpic. Hence, the pump outlet temperature (T_6) is computed via CoolProp as function of evaporation pressure and pump inlet enthalpy (h_4). The definition of recuperator effectiveness (ε_{rec}) and the heat balance to the recuperator can be used now to obtain the evaporator inlet temperature and the condenser inlet temperature (Equations *(3.64)* and *(3.65)*).

$$h_3 = h_2 - (h_2 - h(T_6, p_{cond})) \cdot \varepsilon_{rec} \tag{3.64}$$

$$h_7 = h_6 + h_2 - h_3 \tag{3.65}$$

As all the cycle is fully determined, the performance of the system can be estimated, the electrical power produced by the expander is evaluated according to Equation *(3.66)*), where the expander total efficiency is taken constant and equal to 40%, as average value derived from the experimental data showed in Figure 3.20. The group of data characterized by one electric load has been neglected in the calculation of the average, as it was demonstrated that the expander performance is lower in this particular condition. The feed-pump electric consumption is computed in similar way (Equation *(3.67)*), with a value of the pump efficiency that has been taken constant and equal to 50%.

$$\dot{W}_{exp,el} = \dot{W}_{exp,is} \cdot \eta_{exp} = (h_1 - h_2) \cdot \eta_{exp} \tag{3.66)}$$

$$\dot{W}_{p,el} = \frac{\dot{W}_{p,hy}}{\eta_p} = \frac{\dot{V}_5 (p_6 - p_4)}{\eta_p} \tag{3.67}$$

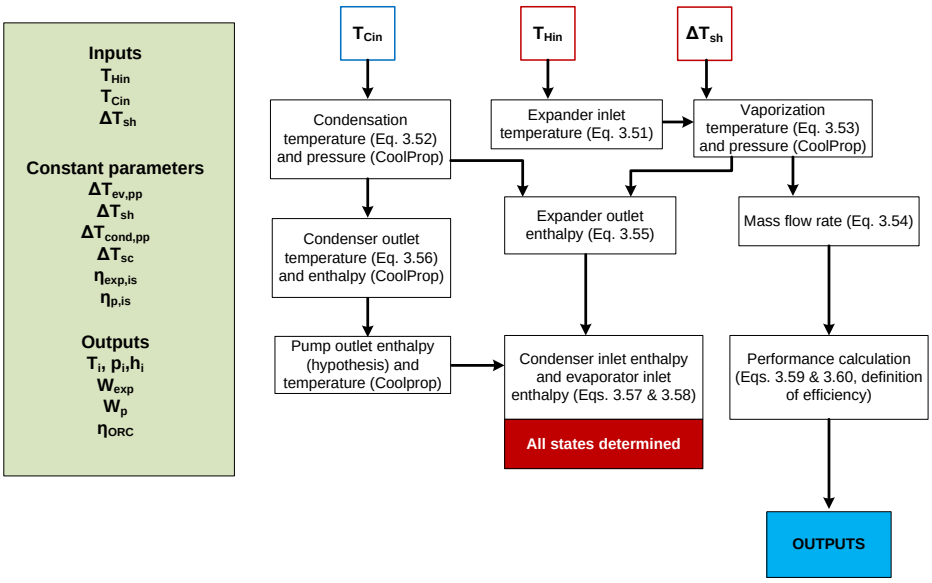

Figure 3.48 – Flow chart of the ORC empirical model.

The so-described model has been used in [25] as sub-routine of a TRNSYS model developed for simulating a combined cooling heating and power (CCHP) system for supplying a near zero energy building (NZEB), made of photovoltaic panels, solar thermal collectors, an absorption chiller and a heat pump. The study is fruit of the collaboration with the National Research Center (CNR ITAE) of Messina, that developed the absorption chiller.

The thermal collectors transfer thermal energy to the micro-ORC system and to in cascade to the chiller, which was designed for being supplied with hot water at a temperature compatible with those at the outlet of the ORC evaporator. A thermal energy storage (TES) is provided between the solar collectors and the ORC system. The layout of the system investigated in [25] is reported in Figure 3.49.

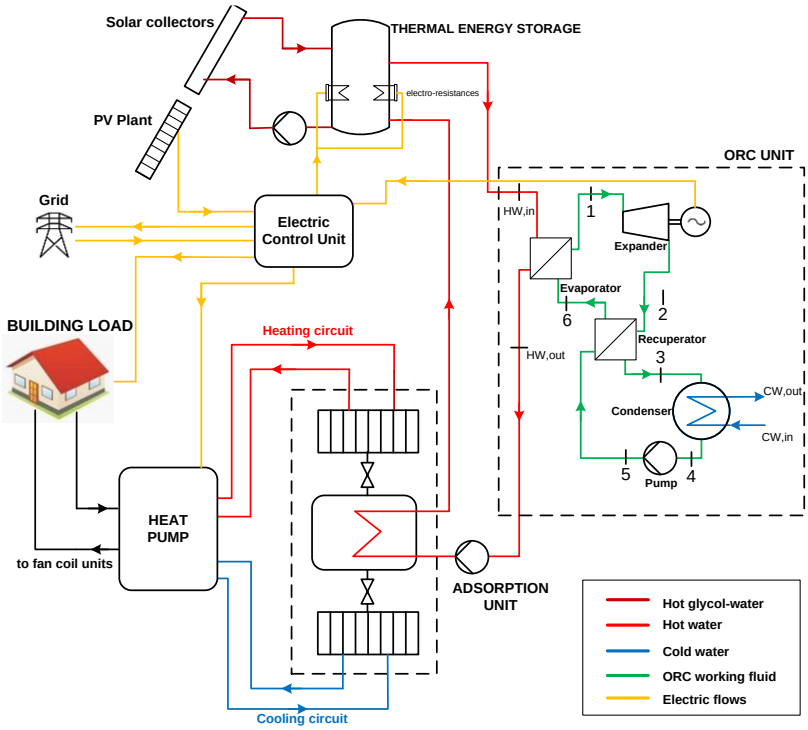

Figure 3.49 – Layout of the system analysed in [25].

CHAPTER 4

4 Experimental transient analysis

Although the ORC system is originally conceived for working in stationary conditions, it is of interest to evaluate its behavior during the transients, in terms of response of the key variables to the modification of the input conditions. The assessment of the dynamic characterization is crucial to the definition of the control strategy and the development of the control system for the ORC plant.

4.1 Dynamic indexes

Two indexes are defined to assess the response behavior to a modification of a controlled variable: the response time and the settling time.
The **response time** (τ_r) is defined as the time required by a variable that changes after an input variations, to achieve the 90% of its total variation; the total variation is intended as the difference between the new and the old average steady-state values. The parameter τ_r indicates the reactivity of the variable, that undergoes a change caused by a perturbation of a controlled input. The response time is generally lower for fast-response variables, such as mass flow rate and pressure, while it results rather high for the temperatures and temperature-derived quantities, which are affected by higher inertia.
The **settling time** (τ_{ss}) is defined as the time needed to achieve the start of the steady-state condition for the changed variable. The starting time of the stationary interval is determined by applying the R-Test described at the beginning of the previous chapter. For a specific variable, the value of τ_{ss} is generally substantially higher than that of τ_r, also for fast-settling quantities such as the mass flow and the pressure. In some cases, on the other hand, the values of τ_r and τ_{ss} result very close. The index τ_{ss} corresponds to the time required by the variable to extinguish the transient after the perturbation. In the evaluation of the two parameters related to the pressures in the cycle, as well as in the graphs included in this chapter, the acquired pressure signals have been filtered using a 4th order Butterworth filter, in order to clean up the characteristic noise (mostly electrical) of such signals.

4.2 Start-up transient

The assessment of the ORC operation during the start-up transient process can be useful to determine whether to develop a specific control strategy for this phase. Moreover, knowing the time of stabilization of all the working variables after the system activation helps to better evaluate the global performance and the usability of the system as intermittent facility for electricity production (for example, if the system is supplied by non-programmable heat sources, or if it must operate under intermittent electric load). It can already be said that, despite the system under investigation requires a certain time interval to warm up (as every thermal conversion technology), the relatively low size of the plant components reduces in general the startup time with respect to larger facilities. The limited heat exchangers volume and surface to be heated allows to achieve the working regime in a time interval in the order of minutes.
In Figure 4.1 a), the time-based experimental data of pump speed, mass flow rate and evaporation and condensation pressure are showed for a startup operation of the micro-ORC. The conditions of hot water temperature and flow rate and the pump speed are kept constant and equal to 65 °C, 1.5 l/s and 125 rpm, respectively. As soon as the hot water has been heated to the desired temperature in the boiler, the pump is activated and starts to elaborate a certain amount of mass flow rate, that depends almost exclusively on the pump speed. In this phase, the expander cylinders are by-passed, and the fluid flows directly to the recuperator. The mass flow rate is the highest achievable at that specific value of the pump speed, since the only hydraulic resistance of the circuit are the pressure losses (see Figure 3.22, with pump characteristic curves). Hence, the condensation pressure level is very close to the evaporation pressure, and the fluid is sucked as subcooled liquid by the pump. Generally, after few minutes (the

time required by the evaporator outlet temperature in by-pass mode, T_{1bp}, to heat up), the expander is activated, the fluid enters the cylinders and the expander starts to rotate and to produce electricity (time = 1260 s). At constant pump speed, the mass flow rate drops very quickly and then continue to decrease slowly till the steady-state value. The evaporation pressure rises fast to a level that depends on the mass flow rate and on the expander load, which affects the new hydraulic resistance of the circuit. The condensation pressure has a slight and quick decrease, then increases slowly to stabilize at a value close to that achieved before the activation of the expander. In Figure 4.1 b), the values of temperature of hot water evaporator inlet and outlet (T_{Hin} and T_{Hout}), and of working fluid expander inlet and outlet (T_1 and T_2), acquired during the startup process, are showed for the same test. As far as the expander is in idle mode, the working fluid heated in the evaporator flows through the by-pass line, while the thermocouple is located right next to the expander (see Fig. 2.2). Therefore, the temperature T_1 remains low, and the increment with respect to the ambient temperature is due only to the thermal conduction through the pipe and the valve. After the switch of the by-pass valves, T_1 increases until it achieves a value very close to the water inlet temperature, as it was observed in the heat transfer analysis of the previous paragraph. A very modest perturbation is observed in the hot water inlet temperature trend in correspondence to the start of increasing of temperature T_1. The water outlet temperature shows a peak after few seconds and then it settles to the steady state value around 62.5 °C. Hot water temperature difference between inlet and outlet decreases with respect to the previous value with the expander in idle mode, since the transferred thermal power is reduced by the drop of the mass flow rate. The expander outlet temperature (T_2), which was increasing within the idle mode, shows a sudden drop and then is stabilized after about 320 s. The trends of the expander speed and power output is showed in Figure 4.1 c). After the valves switch, the rotating speed responds in about 40 seconds, similarly to the power. The time employed to achieve full stabilization (τ_{ss}) results close to 400 s and 600 s, respectively for N_{exp} and $\dot{W}_{exp,el}$. The values of the parameters τ_r and τ_{ss} are collected in Table 4-1 for the variables presented in Figure 4.1a), b) and c).

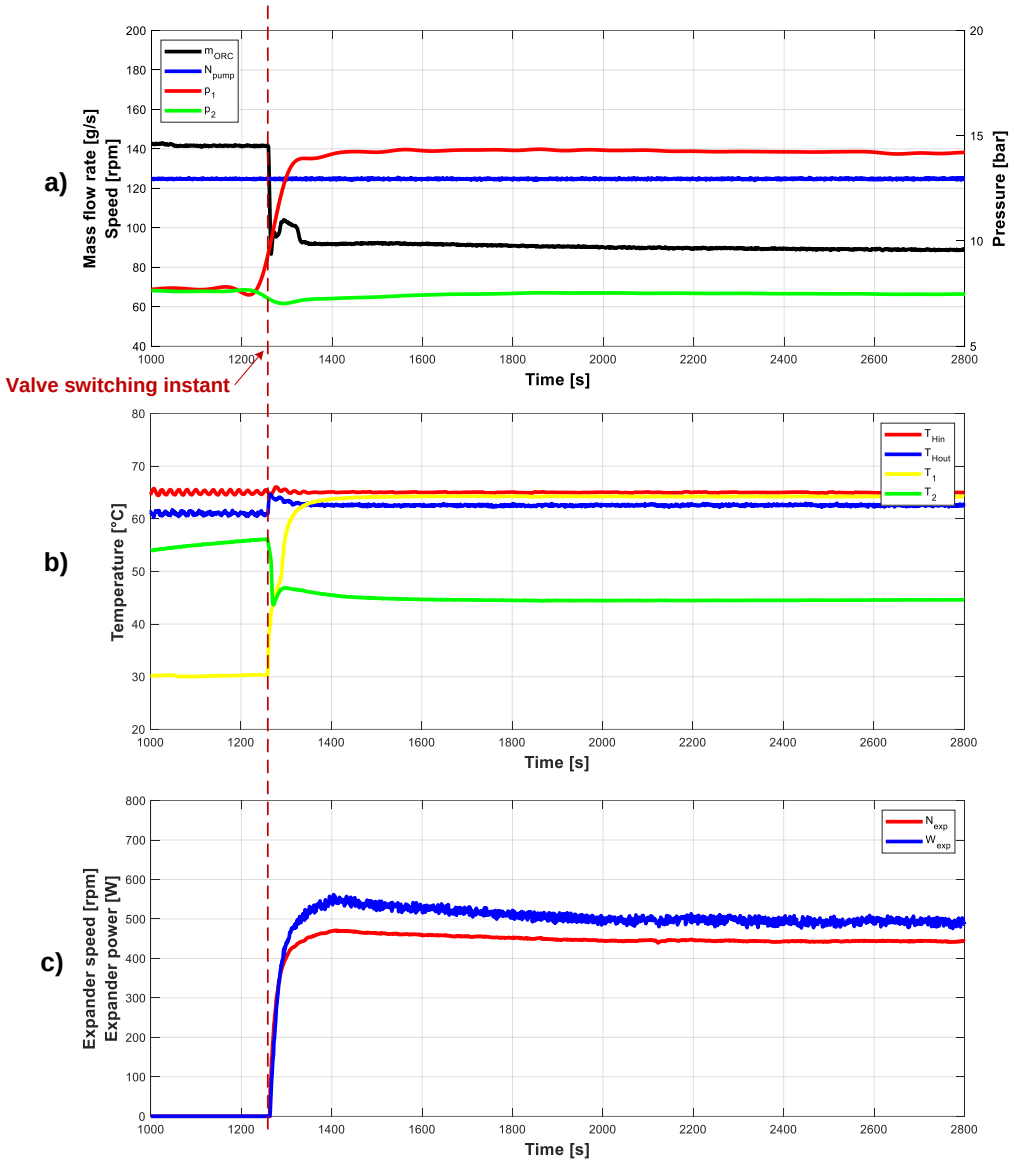

Figure 4.1 – Dynamic response in case of start-up transient: a) pump rotating speed, mass flow rate, evaporation and condensation pressure; b) hot water inlet and outlet temperature and expander inlet and outlet temperature; c) expander electric power output and speed.

Table 4-1 – Response time and settling time for a start-up transient

Variable	τ_r	τ_{ss}
Pump speed (N_{pump})	-	-
Mass flow rate ($\dot{m}_{ORC}$)	4	85
Evaporation pressure (p_1)	48	110
Condensation pressure (p_2)	5	170
Expander inlet temperature (T_1)	55	100
Expander outlet temperature (T_2)	10	320
Expander speed (N_{exp})	39	410
Expander power ($\dot{W}_{exp,el}$)	42	580

4.3 Input variation transient

To analyze the transient response of the key variables to an input variation, starting from a stationary condition, the controlled variable (hot water temperature and flow rate, pump speed, expander loads), of which the dynamic effect is to be evaluated, is varied and the indexes τ_r and τ_{ss} are calculated on the transient process. In the following, several cases are discussed with variation of N_{pump} at constant T_{Hin}, and n_{loads}, of T_{Hin} at constant N_{pump} and n_{loads}, and of n_{loads} at constant T_{Hin} and N_{pump}. Varying the hot water temperature or the pump speed (keeping constant the other variables) has a direct effect on the superheating degree at the expander inlet. Indeed, increasing T_{Hin} at constant N_{pump} makes increase the superheating degree, which decreases instead with a rise of N_{pump} at constant T_{Hin}. In the following, different cases are described for each of the changed variable. The results presented in this paragraph have been acquired during two dedicated test sessions, with a total duration close to 6 hours.

4.3.1 Pump frequency variation

This first instance is referred to the regulation of the feed-pump rotating speed, keeping constant the set point of hot water inlet temperature and the number of loads connected to the expander electric generator. The regulation is performed by acting manually on the inverter of the pump motor. Both rising and decreasing variations are analyzed looking at the effect they have on the key variables of the system, with special attention to the expander-related quantities. From case 1 to case 3, a step variation of N_{pump} was performed, while in case 4 the new value of pump speed is achieved by a ramp. The variation is considered a step if the pump speed passes from the starting to the new value in less than 3 seconds, the minimum material time to manually set the new value of the inverter frequency.

Case 1 – rising step of N_{pump}

The case of a rising step of the pump speed is reported in Figure 4.2. The value of N_{pump} is changed from 150 rpm to 200 rpm, corresponding to an increase of 10 Hz of the inverter frequency. The set point of hot water temperature to 75 °C and the number of loads are constant and equal to 75 °C and to 5 loads, respectively. Figure 4.2 a) shows the trends of pump speed, organic fluid mass flow rate, evaporating and condensing pressure. The pump speed (blue line) passes from the starting to the new value in 5 seconds. The mass flow rate (black line) presents the fastest variation from 116 g/s to 170 g/s, with a response time τ_r equal to 4 s, and it achieves the stabilization in about 50 s. It was observed that the value of $\dot{m}_{ORC}$ always presents an overshoot for a few seconds after the pump speed variation, before starting the stabilization. However, the difference between the peak and the steady-state values is in general rather low (in the order of 10 g/s). The evaporation pressure (red line) begins to increase instantaneously as the mass flow is changed, but its response time results higher ($\tau_r \approx 40$ s). The transient of p_1 is fully extinguished in about 160 s from its first variation. The values of p_1 before and after the transient are, respectively, 16.3 bar and 19.7 bar. As expected, the condensation pressure (p_2) presents only a slight increment, from 7.6 bar to 8.0 bar, due to the increase of the mass flow rate, with a transient completed in a time comparable

to the settling time of the evaporation pressure (170 s), but its response is slightly slower (60 s). Figure 4.2 b) shows the corresponding value of the evaporator water inlet and outlet temperatures (T_{Hin} and T_{Hout}) and of organic fluid at expander inlet and outlet (T_1 and T_2). On water side, the only effect of the increase of the mass flow rate is the increment of the evaporator thermal power, and thus the reduction of the hot water outlet temperature, which decreases from 73.2 °C to 71.2 °C. The barely perceivable variation of the water inlet temperature is only due to the change of the temperature of the outlet flow (which enters the three-way valve to maintain the set-point of T_{Hin}), and to the delay of the PID controller that commands the valve opening. The temperature T_1, as already demonstrated in the previous chapter, depends on the water inlet temperature, and for most operating conditions it is almost coincident to T_{Hin}. Differently, the expander outlet temperature, T_2 (green line) is reduced of about 5 °C, with a slow response ($\tau_r \approx 340$ s) and achieving the stabilization in almost 500 s. The increase of the evaporation pressure at constant water temperature has a direct effect on the superheating degree at the evaporator outlet (ΔT_{sh}), which is showed in Figure 4.2 c), where also the sub-cooling degree at the condenser outlet is included. The value of the superheating degree decreases from 16 °C to 7 °C, with a response time close to 55 s. The sub-cooling degree, on the contrary, keeps constant during the transient analyzed in this case. In the plot of Figure 4.2 d), the signals of the recuperator inlet and outlet temperature are reported, on vapor (T_2 and T_3, red lines) and liquid (T_6 and T_7, blue lines) sides. The highest variation is observed on the recuperator inlet temperature (that corresponds to the expander outlet one, T_2). At the same time, the vapor outlet temperature has a slight increment of about 1.5 °C. On liquid side, the opposite trend occurs, as the outlet temperature T_7 is reduced of about 2.5 °C, and the inlet temperature increases of less than 1 °C. The latter increment is related to the rise of the pump frequency, which makes increase the pump outlet enthalpy and the thermodynamic power. Both before and after the variation that causes the perturbation, the temperature difference is higher on vapor side, since, assuming that the power balance on the heat exchanger is maintained, the specific heat at constant pressure (c_p) results higher in the liquid phase. Amongst the cycle operating variables, the expander outlet temperature (T_2) results the slowest both in term of response and stabilization in this case. Figure 4.2 e) shows the signals of expander rotating speed and power output, together with the value of the load impedance. As expected, both N_{exp} and $\dot{W}_{exp,el}$ increase with similar response trend and settling time. The electric power passes from 820 W to 1180 W, while the speed rises from 630 rpm to 810 rpm. The response time (τ_r) and settling time (τ_{ss}) are, for power and speed respectively, equal to 44 s, 40 s, 180 s and 140 s. The load impedance, Z_{load}, since it mostly depends on the loads number, presents only a slight increment with similar response time to N_{exp} and $\dot{W}_{exp,el}$, remaining in the range of impedance corresponding to 5 loads (see Fig. 3.13).

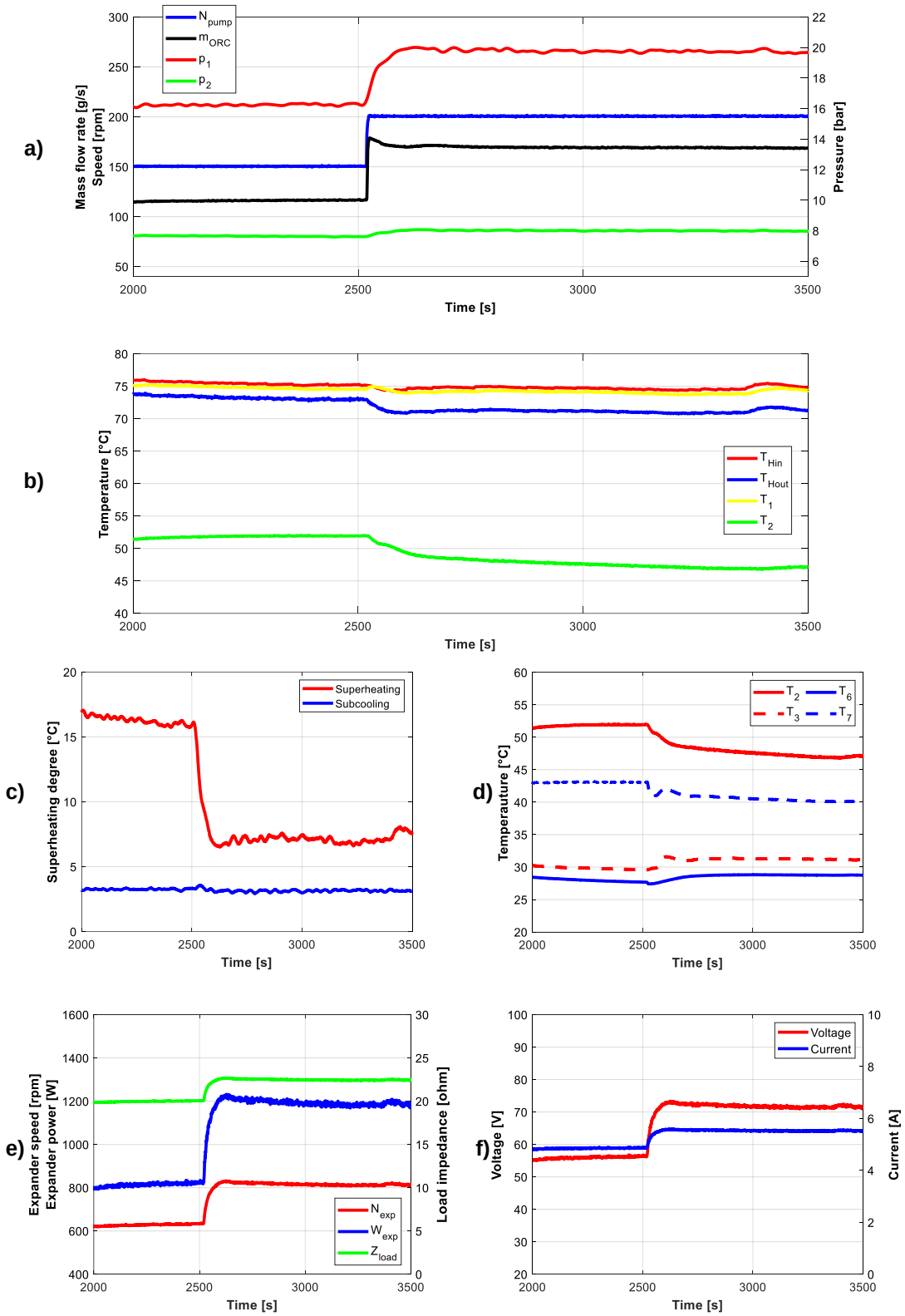

Figure 4.2 – Dynamic response in case of 10-Hz pump frequency increment: a) pump rotating speed, mass flow rate, evaporation and condensation pressure; b) hot water inlet and outlet temperature and expander inlet and outlet temperature; c) superheating degree at evaporator outlet and sub-cooling degree at condenser outlet; d) recuperator inlet and outlet temperatures; e) expander electric power output, speed and load impedance; f) expander output voltage and current.

Case 2 – rising step of N_{pump} to saturation condition

In this case, the transition is performed to an operating condition characterized by a value of the superheating degree close to zero. The main difference with the previous case is that a slight reduction is observed as well on the trend of the expander inlet temperature, T_1. The hot water temperature set-point is fixed to 65 °C, and the load number is set to 5 loads. The cold water temperature is close to 21 °C. The starting condition is characterized by superheating degree close to 11 °C, electrical power output around 515 W, and expander speed close to 460 W. At time equal to 5498 s, the pump speed is varied from 125 rpm to 175 rpm, corresponding to an increase of 10 Hz of the inverter frequency. In Figure 4.3 a), the transient response is reported for the working fluid mass flow rate and the evaporation and condensation pressures. The stationary starting and ending values of mass flow rate are, respectively, 89 g/s and 149 g/s, while the evaporating pressure increases from 14.2 bar to 17.3 bar. The condensing pressure presents a slight increase from 7.5 bar to 8.0 bar. The rising rate of $\dot{m}_{ORC}$ is close to that of N_{pump}, as it achieves the 10% of the new stationary value within only 2 seconds, but the settling time (τ_{ss}) results much larger, around 50 seconds. The increment of the evaporation pressure is significantly slower, as the indexes τ_r and τ_{ss} result, respectively, 22 s and 100 s. The superheating degree is showed in Figure 4.3 b), with ΔT_{sh} decreasing from 11 °C to the saturation ($\Delta T_{sh} \approx 0$). The response time is similar to that found in the previous case. In Figure 4.3 c), where the transient is analyzed from the point of view of the hot water temperatures and of the expander inlet and outlet temperature (T_1 and T_2). As already observed, the water inlet temperature remains constant around the imposed set-point. The water outlet temperature presents a small decrease of almost one degree Celsius, due to the increase of the evaporator thermal power related to the increment of the mass flow rate. The expander inlet temperature is reduced of about 2 °C, from a value almost coincident to the hot water inlet temperature to the saturation temperature related to the new value of the evaporation pressure. This is the main effect that makes this case different from the previous (and from the general trend of experimental data for this power plant), where the evaporator outlet temperature basically depended only on the water inlet temperature. This behavior has a negative effect on the evaporator effectiveness, due to the increment of the temperature difference at the hot terminal. The expander outlet temperature decreases of about 6 °C. The time required for the stabilization (τ_{ss}) resulted high for both temperatures T_1 and T_2, equal respectively to 110 s and 220 s. The response time of the two temperatures is 70 s and 100 s for T_1 and T_2 respectively. In Figure 4.3 e) the signals of the expander rotating speed and power output, acquired during the transient of case 2, are reported versus time. They present a similar behavior in terms of rising rate and settling time, close respectively to 30 s and 130 s. Regarding Z_{load}, a similar comment of the case 1 above described is valid also in this case. In Figure 4.3 d) the trends of the temperature at the inlet/outlet of the recuperator in both sides (T_2, T_3, T_6, T_7) are plotted versus time. On vapor flow, the temperature at the inlet presents a substantial decrease, as T_2 decreases from 45.0 °C to 38.7 °C after the transient, that is due to the reduction of the expander inlet temperature and of the isentropic efficiency. On the other hand, the outlet temperature T_3 has a slight increase from 28.9 °C to 31.0, resulting in a considerable reduction of the sensible heat transferred from the vapor to the liquid side (from 1450 W to 1050 W). On the liquid side, the inlet temperature T_6 increases from 27.5 °C to 29.0 °C, while the outlet temperature T_7 decreases from 38.7 °C to 35.4 °C. Therefore, the inlet-outlet temperature difference and the resulting reduction of the thermal power, as indicated in Figure 4.3 f) is higher for the vapor than for the liquid side. These results suggest that a condition such as that described in section 3 of the previous chapter is occurring: part of the vapor thermal power is transferred as latent heat, as the fluid at the condenser inlet has achieved the saturation.

Even with an expander of piston type, which tolerates wet expansion better than turbines, this condition should be avoided in general, in order to preserve the machine from deterioration and keep good performance. To this purpose, a good practice could be to include a map in the control system, reporting the maximum value of pump speed achievable at a given expander inlet temperature (T_1), to maintain a minimum safe value of superheating degree (between 3 °C and 4 °C). The map, which must be obtained from experimental tests or calibrated models, should take into account the external load connected to the expander, as it influences significantly the value of the evaporation pressure at given pump speed.

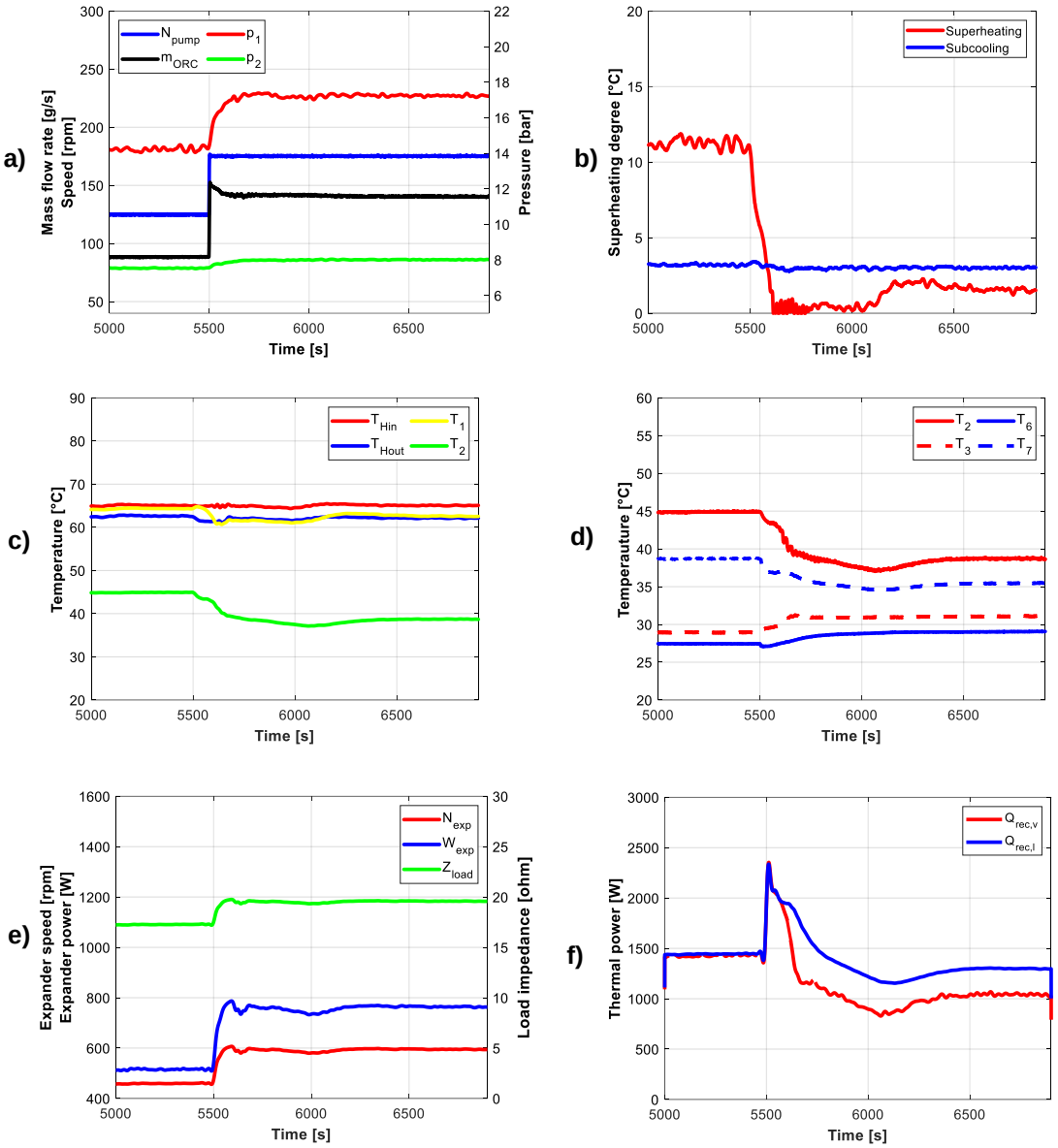

Figure 4.3 - Dynamic response in case of 10-Hz pump frequency increment, with final point at saturation: a) pump rotating speed, mass flow rate, evaporation and condensation pressure; b) superheating degree at evaporator outlet and sub-cooling degree at condenser outlet; c) hot water inlet and outlet temperature and expander inlet and outlet temperature; d) recuperator inlet and outlet temperatures; e) expander electric power output, speed and load impedance; f) recuperator thermal power on liquid and vapour side.

Case 3 – Decreasing step of N_{pump}

Figure 4.4 shows the dynamic effect of the decreasing variation of the feed-pump rotating speed from 175 rpm to 150 rpm (Figure 4.4 a), blue line), corresponding to a regulation of 5 Hz on the inverter. An immediate effect is observed on the mass flow rate measured value (black line), which decreases from 141 g/s to 116 g/s, with response time of only 3 s and settling time close to 300 s. The response of the evaporation pressure (red line) is slower ($\tau_r = 60\ s$), but the stabilization is achieved very fast, in only 70 s from the speed variation. The variation of the condensation pressure (green line) is very low, as it depends mainly on the cooling water temperature and only marginally on the working fluid mass flow rate. The reduction of the mass flow rate causes a drop of the thermal power transferred in the evaporator, resulting in the increment of the water outlet temperature (T_{Hout}), as observed in Figure 4.4 b). This variation reflects on the value of the hot water inlet temperature (T_{Hin}), which presents a slight increment due to the entrance of hotter water at the port C of the mixing three-way valve. The expander inlet

temperature (T_1) basically follows the temperature T_{Hin}, as the terminal temperature difference is maintained substantially constant and lower than 1 °C. The expander outlet temperature (T_2) has a little increment of about 2 °C, with slow response time close to 300 s. As expected, the superheating degree increases of about 5 °C, with a response time close to 70 s, due to the evaporating pressure increment at quasi-constant superheating temperature (Figure 4.4 c), red line). The sub-cooling degree remains constant during the entire transient interval. Figure 4.4 d) shows the curves of expander power output, rotating speed and load impedance. The electric power is reduced from almost 1 kW to 800 W with relatively fast response ($\tau_r \approx 30\ s$). A similar response time is obtained for the expander rotating speed, which decreases between 720 rpm and 620 rpm before and after the pump speed reduction. The value of Z_{load} decreases of small amount with similar characteristic time indexes of power and speed.

Table 4-2 summarizes, for case 1 and case 3, the response time, settling time, absolute and percentage variation of each variable analyzed as consequent of pump frequency variation.

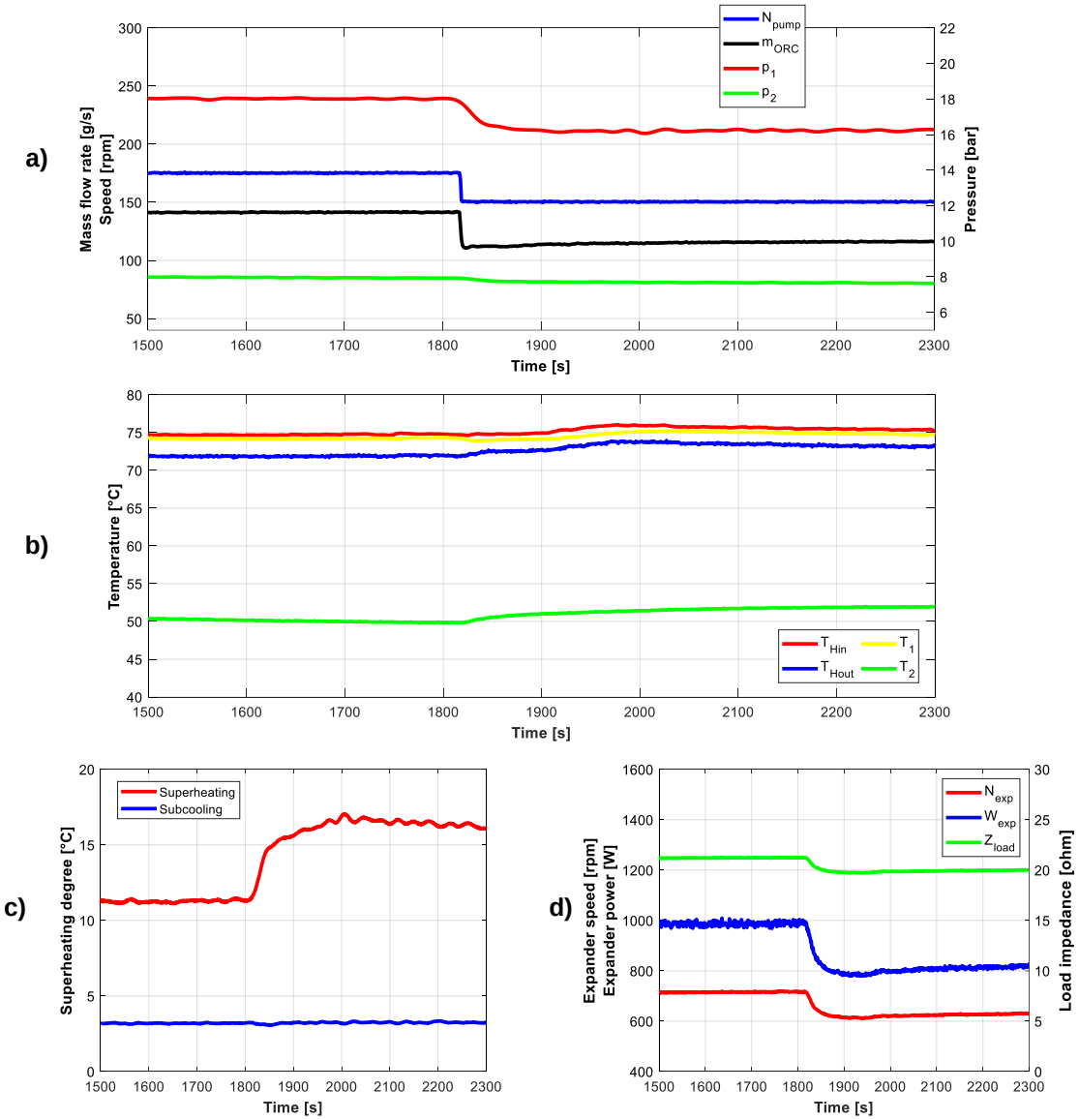

Figure 4.4 - Dynamic response in case of 5-Hz pump frequency decrease: a) pump rotating speed, mass flow rate, evaporation and condensation pressure; b) hot water inlet and outlet temperature and expander inlet and outlet temperature; c) superheating degree at evaporator outlet and sub-cooling degree at condenser outlet; d) expander electric power output, speed and load impedance.

Table 4-2 – Response time and settling time for pump frequency variations. The absolute and percentage variation of each variable is reported. The arrows in the % variation columns indicate if the variation is increasing (↑) or decreasing (↓).

	10 Hz increment (case 1)				**5 Hz decrease (case 3)**			
Variable	*Abs. var.*	*% var.*	τ_r *[s]*	τ_{ss} *[s]*	*Abs. var.*	*% var.*	τ_r *[s]*	τ_{ss} *[s]*
Pump speed (N_{pump})	50 rpm	33% ↑	2	5	25 rpm	14.3% ↓	2	3
Mass flow rate ($\dot{m}_{ORC}$)	53 g/s	45% ↑	4	50	25 g/s	18% ↓	3	300
Evaporation pressure (p_1)	3.6 bar	22% ↑	40	165	1.8 bar	10% ↓	60	70
Condensation pressure (p_2)	0.4 bar	5.2% ↑	60	170	0.3 bar	3.8% ↓	-	-
Expander inlet temperature (T_1)	-	-	-	-	-	-	-	-
Expander outlet temperature (T_2)	5 °C	9.6% ↓	340	490	2 °C	4% ↑	200	300
Superheating degree (ΔT_{sh})	8.3 °C	52% ↓	52	145	5.1 °C	45% ↑	70	180
Expander speed (N_{exp})	188 rpm	29.8% ↑	38	140	88 rpm	12.3% ↓	40	60
Expander power ($\dot{W}_{exp,el}$)	374 W	45.4% ↑	40	180	175 W	17.8% ↓	50	80

4.3.2 Hot water temperature variation

The regulation of the evaporator water inlet temperature is performed using the three-way valve located in line right outside the boiler, with the control logic described in Chapter 2. Four cases are analyzed for this process: increasing step of, decreasing step, increasing ramp and fluctuating signal of T_{Hin}. Here the step is intended as an instantaneous variation of the set-point of T_{Hin}, which leads to the actual variable's change within a time interval lower than 15 s. The that factors influence the time delay from the imposition of the new set-point to its achievement are the PID control system delay, the actuation time of the motorized valve and the water thermal inertia. The inertia of the temperature sensors can be considered negligible with respect to the other element of influence, since the sheath diameter of the thermocouples is equal to 1 mm, resulting in a relatively fast response of the sensors with response time in the order of 0.2-0.5 s.

Case 1 – Increasing step of T_{Hin}

An increasing step of the water temperature at the evaporator inlet is performed by employing the closed loop configuration on the hot water circuit (see Fig. 2.20), thus mixing the water coming from the boiler with the colder water returning from the evaporator. The procedure consists of keeping switched-on all the heater elements and setting the valve to a position that allows a larger passage from the return line (C-B) than from the main line(A-B). This condition allows the water inside the boiler to increase its temperature, with limited cooling effect related to the water cooled in the evaporator. The actual water temperature inside the boiler is double-checked by means of two thermocouples, one located at the boiler outlet and the other inside the boiler at a middle height. This solution limits the error on the actual boiler temperature estimation, related to phenomena of temperature stratification inside the boiler. In the example of Figure 4.5, the initial set-point of T_{Hin} is 75 °C, while the boiler temperature is close to 85 °C. At instant equal to 6010 s, the set-point is changed to 80 °C, and the valve starts to open the A-B way, partially closing the return passage. It is important that the power provided by the heater elements is higher than that transferred in the evaporator, in order to guarantee a sufficient total thermal power source required to maintain the higher value of water temperature during the transient. Since no variation on the mass flow rate, evaporating and condensing pressure was observed, the relative graph is not showed for this case. As observed in Figure 4.5 a), the response of the water outlet temperature (T_{Hout}) substantially follows that of the inlet temperature, both presenting a rising step right after the set-point variation and then a slower increasing trend up to the new stationary value. The response of the expander inlet temperature, T_1, presents a little delay with respect of that of the water inlet temperature (for which τ_r results around 50 s), with a value of the index τ_r close to 70 s. Due to this time delay, during the transient the hot terminal temperature difference (T_{Hin} - T_1) is slightly

higher than the value acquired in steady-state condition. The value of the expander outlet temperature (T_2) shows an increment of about 2 °C, with very high response time around 400 s. The expander electric power and rotating speed are reported in Figure 4.5 c). The trend of the load impedance does not display significant variation and hence it was not included in the figure. Both $\dot{W}_{exp,el}$ and N_{exp} are affected by little increase related to the variation of the heat source temperature, with response time lower than that of the controlled variable that causes the perturbation, T_{Hin}.

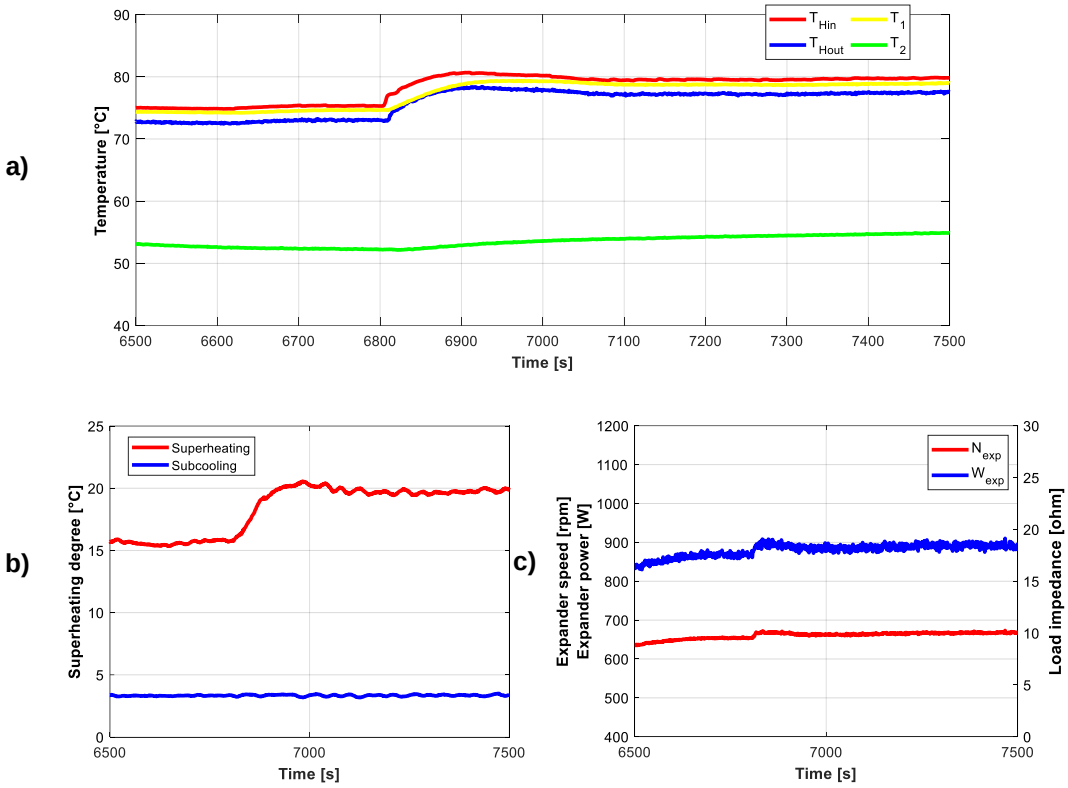

Figure 4.5 - Dynamic response in case of 5 °C increment on hot water temperature set-point: a) hot water inlet and outlet temperature and expander inlet and outlet temperature; b) superheating degree at evaporator outlet and sub-cooling degree at condenser outlet; c) expander electric power output, speed and load impedance.

Case 2 – Decreasing step of T_{Hin}

The case of decreasing variation of the hot water inlet temperature is presented in Figure 4.6. The starting value of T_{Hin} is 80 °C and, around time = 8690 s, it is reduced by imposing the new set point to 75 °C. Because the variation of $\dot{m}_{ORC}$, p_1 and p_2 are not significant, in this case too their trends are not showed. The response time of the hot water inlet and outlet temperature are close to 100 s (Figure 4.6 a). Similarly to the previous case, the response of the organic fluid expander inlet temperature (T_1) is slower than that of the water, but in the present case this determines a higher value of T_1 than T_{Hin} during the transient. The expander outlet temperature T_2 (green line) is reduced of almost 4 °C, with very slow response ($\tau_r \approx 600\ s$). The superheating degree is decreased of about 4 °C with same response time of the expander inlet temperature T_1 (Figure 4.6 b), as the evaporation pressure remains substantially constant. The sub-cooling does not show significant variation during the transient analyzed in this case. The expander electric power output and the rotating speed, as depicted in Figure 4.6 c), present a small decrease corresponding to the change interval of the hot water temperature, but the new steady-state values are more or less the same of the starting ones, close respectively to 870 W and 670 rpm, respectively.

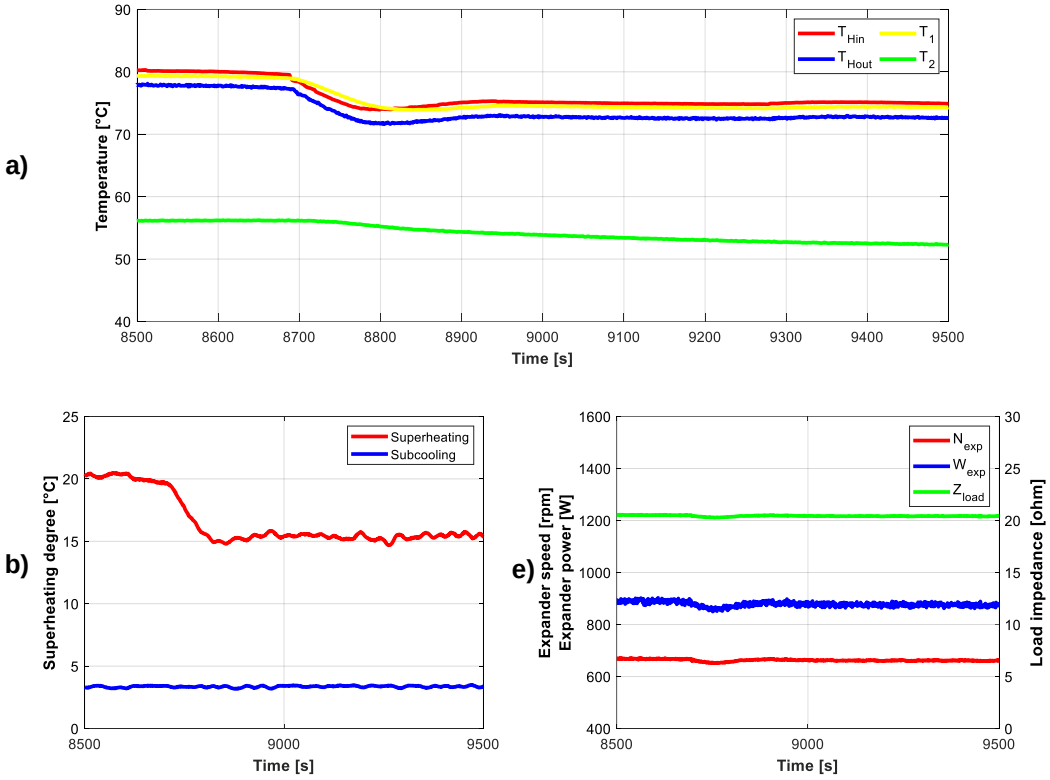

Figure 4.6 – Dynamic response in case of 5 °C decrease on hot water temperature set-point: a) hot water inlet and outlet temperature and expander inlet and outlet temperature; b) superheating degree at evaporator outlet and sub-cooling degree at condenser outlet; c) expander electric power output, speed and load impedance.

Case 3 – Fluctuation of T_{Hin}

When dealing with fluctuating heat input conditions, it is important to assess whether the evaporator is able or not to dampen the oscillation of the heat source or, in other words, if its response is slow enough to assure a constant or quasi-constant value of the ORC maximum temperature (evaporator outlet temperature, T_1). Heat exchangers with high mass and high internal volume are characterized by higher thermal inertia, hence by high response time to the input variations. Depending on the application the ORC system must operate, low or fast response evaporators can be selected. For example, if the heat source temperature oscillates with low-amplitude around a constant or slowly variable average value, an evaporator with slow response time, able to dampen the temperature fluctuation, could be more appropriate to achieve a more stable operation of the system and easier control strategy. On the contrary, a heat source characterized by frequent and irregular changes of temperature and/or flow rate may require an evaporator heat exchanger with fast response, to be able to follow the variation of the source conditions in order to maintain the maximum performance over the whole operation. In [77], the authors used an index called *dynamic regime number*, Γ, to identify the operational regime of the heat source. The index Γ is defined, for the system under investigation, as the ratio between the response time of the evaporator (in terms of working fluid outlet temperature, T_1), to the characteristic time of the oscillating signal of the heat source temperature (Equation (4.1). The latter corresponds, in case of fluctuating signal comparable to a sinusoid, to half the period of oscillation of the heat source. The response time $\tau_{r,T1}$ is calculated, in this case, as the time interval between a valley and the next peak of the signal of working fluid temperature at the evaporator outlet.

$$\Gamma_{ev} = \frac{\tau_{r,T1}}{T_{Hin}/2} \tag{4.1}$$

The parameter Γ_{ev} defines the characteristic regime of the fluctuating heat source: a value lower than 1 is characteristic of a quasi-steady regime (Figure 4.7a), with the working fluid temperature. If Γ_{ev} is higher than 10, the dynamic regime can be defined quasi-constant, meaning that the fluctuation of the heat source conditions does not reflect to the working fluid evaporator outlet temperature, which remains slightly constant and close to the average value of the sinusoidal signal of the heat source temperature (Figure 4.7 c). The case of Γ_{ev} higher than 1 and lower than 10 (Figure 4.7 b) is a middle ground between the quasi-steady and quasi-constant response regime [77]. A heat exchanger with transient response similar to that shown in Figure 4.7 c) ($\Gamma_{ev} > 10$) should be selected as evaporator if an oscillation dampening of the fluctuating heat sources is required, while in case of fast response needed, the evaporator behavior should be more similar to that reported in Figure 4.8 a) and b).

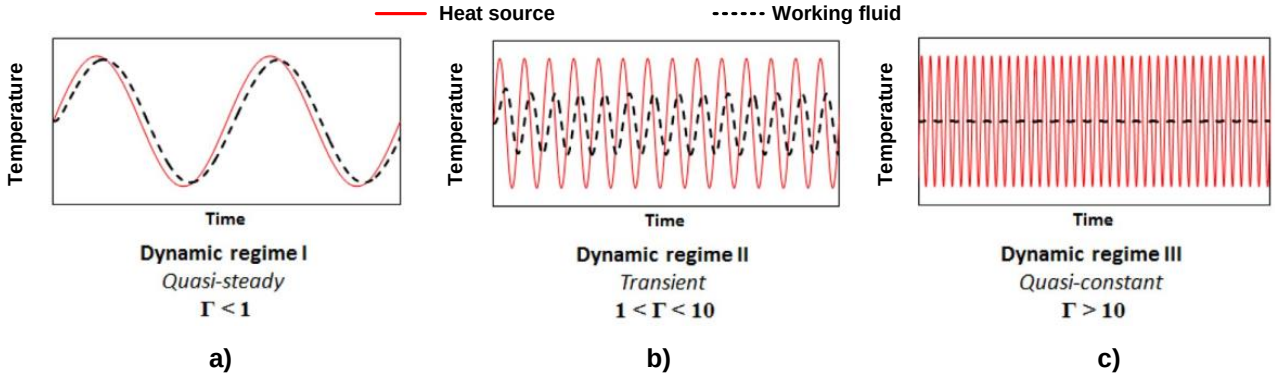

Figure 4.7 – Dynamic regimes depending on heat source fluctuating period and evaporator response time [77].

Figure 4.7 a) shows the experimental trends of hot water temperatures and expander inlet/outlet temperatures in the case of oscillating hot water inlet temperature. The fluctuation of T_{Hin} (red line, zoomed in Figure 4.7 b) can be considered as a sinusoid characterized by a rather constant amplitude and frequency, oscillating around the set-point value of 65 °C. Such condition of the hot water temperature can be obtained by modifying the constant gains on the three-way valve PID controller, to such values that cause a systematical overshoot of the controlled variable. Indeed, increasing the value of the proportional constant K_p and integral constant K_I with respect to the values reported in Table 2.9, and introducing the derivative effect of the PID controlled (i.e. imposing a non-null value of the constant K_D), an oscillating effect can be obtained. Due to the relatively high response time of water temperature, this setting assures a sufficiently regular oscillation of the variable around the imposed set point. Alternatively, the oscillation of T_{Hin} can be obtained by exploiting the non-linear behavior of the two controllers of the hot water flow rate and temperature, which requires a different gain schedule for working properly with different value of the water flow rate. Indeed, if the volume flow rate is reduced substantially, without adjusting the three-way valve PID gains, the valve member starts to move up and down without achieving the steady-state. To return to the normal operation of the valve for achieving the set point of evaporator inlet temperature, one must set the PID gains to the scheduled values for the new water volume flow rate. The lower is the flow rate with respect to the starting steady value, the higher will be the T_{Hin} oscillation amplitude. The latter approach was the one used for this analysis of fluctuating T_{Hin}. This last approach has been applied in the present analysis of fluctuating heat source.

In the case of Figure 4.8 the water flow rate was first reduced from 2.0 l/s to 1.0 l/s (kept from time = 3580 s to time 4063 s), then it was increased to 1.5 l/s. Within the first interval ($\dot{V}_H = 1\ l/s$), the T_{Hin} signal is characterized by a period close to 35 s and an average amplitude close to 8 °C around the set-point of 65 °C. With $\dot{V}_H$ equal to 1.5 l/s, the oscillation period is reduced to 23 s and the amplitude to about 4.5 °C. The signal of water outlet temperature (blue line) presents an amplitude that is about the half of the inlet temperature one, but the oscillation period is substantially similar, even if it is delayed with respect to the T_{Hin} sinusoid. Due to the thermal inertia, the resulting value of the expander inlet temperature fluctuates with an amplitude close to only 1 °C and a period of 37 s, with a volume flow rate of 1.0 l/s. Within the second interval, the oscillation of the T_1 acquired signal is still

visible, but it keeps lower than 0.5 °C, while the period results around 12 s. On the other hand, the fluctuation of the expander outlet temperature can be barely detected, as it can be considered to remain constant and close to the value measured before the perturbation (except for the first transient, for which T_3 presents a slight variation when the water flow rate is suddenly changed). In the first interval, the response time of the temperature T_1 is around 17 s, and corresponds, for this hot water temperature fluctuation period, to a dynamic regime number, Γ_{ev}, very close to 1, thus falling into the case of Figure 4.7 b). In the second interval (starting from time ≈ 4100 s), as observed in Figure 4.8 a), the evaporator is able to completely dampen the heat source fluctuation, mostly because the amplitude of the latter results very small, and the temperature T_1 can be assumed quasi-constant. These results suggest that the evaporator installed in the ORC system under investigation is suitable for dampening low-amplitude (< 10 °C) fluctuation of the hot water temperature as heat source. Indeed, with a maximum amplitude of T_{Hin} close to 8 °C, the resulting smoothed amplitude of T_1 is lower than 5 °C, while it is nearly negligible with T_{Hin} amplitude lower than 5 °C.

In Figure 4.7c, the acquired signals of pump speed, organic fluid mass flow rate and evaporation and condensation pressures are showed versus time, on the interval characterized by fluctuating hot water temperature. The values of mass flow rate and pressures oscillate with a sinusoid as well, but with larger noise than the temperature one. The mass flow oscillation amplitude keeps lower than 3 g/s with the higher temperature fluctuation, with a period around 36 s (similar to the period of the oscillation that caused it). However, in this interval the mean value of the sinusoid does not remain strictly constant, as it can be observed looking at Figure 4.7 d). During the second interval, the mean value keeps rather constant at 88 g/s, with amplitude lower than 2 g/s and an oscillation period around 21 s. Evaporation pressure (p_1) presents oscillation of about one bar around the average value of 14.2 bar, in the first interval (see Figure 4.7 d). The period is the same observed for the mass flow rate but the signal of pressure is delayed of half a period with respect to that of $\dot{m}_{ORC}$. In other words, the times corresponding to the peaks of p_1 are the same of those of the valleys of $\dot{m}_{ORC}$.

For the same case, Figure 4.7 e) presents the acquired signals of expander rotating speed and electric power, with the detail of the interval between 3800 s and 4000 s showed in Figure 4.7 f). Both the signals present almost the same period, that corresponds to the fluctuating period imposed by the hot water temperature, and they are synchronized. With regard to the first interval, the amplitude results close to 100 W and to 50 rpm, for power and speed respectively.

One important conclusion that has been assessed is that the dynamic response of the operating variables to the fluctuation of the hot water inlet temperature is quasi-linear. This is deduced from the similarity of the characteristic indices (amplitude and period) of the different variables signals (temperature, pressure, mass flow rate), that are proportional to the indices of the cause of the perturbation (the fluctuation of the hot water temperature). This aspect generally simplifies the control system development, as it allows to consider the dynamic behavior as linear and to adopt simple control techniques.

Table 4-3 collects the response time and settling time for the main variables in case of variation of hot water temperature set-point, for the cases 1 and 2 above discussed.

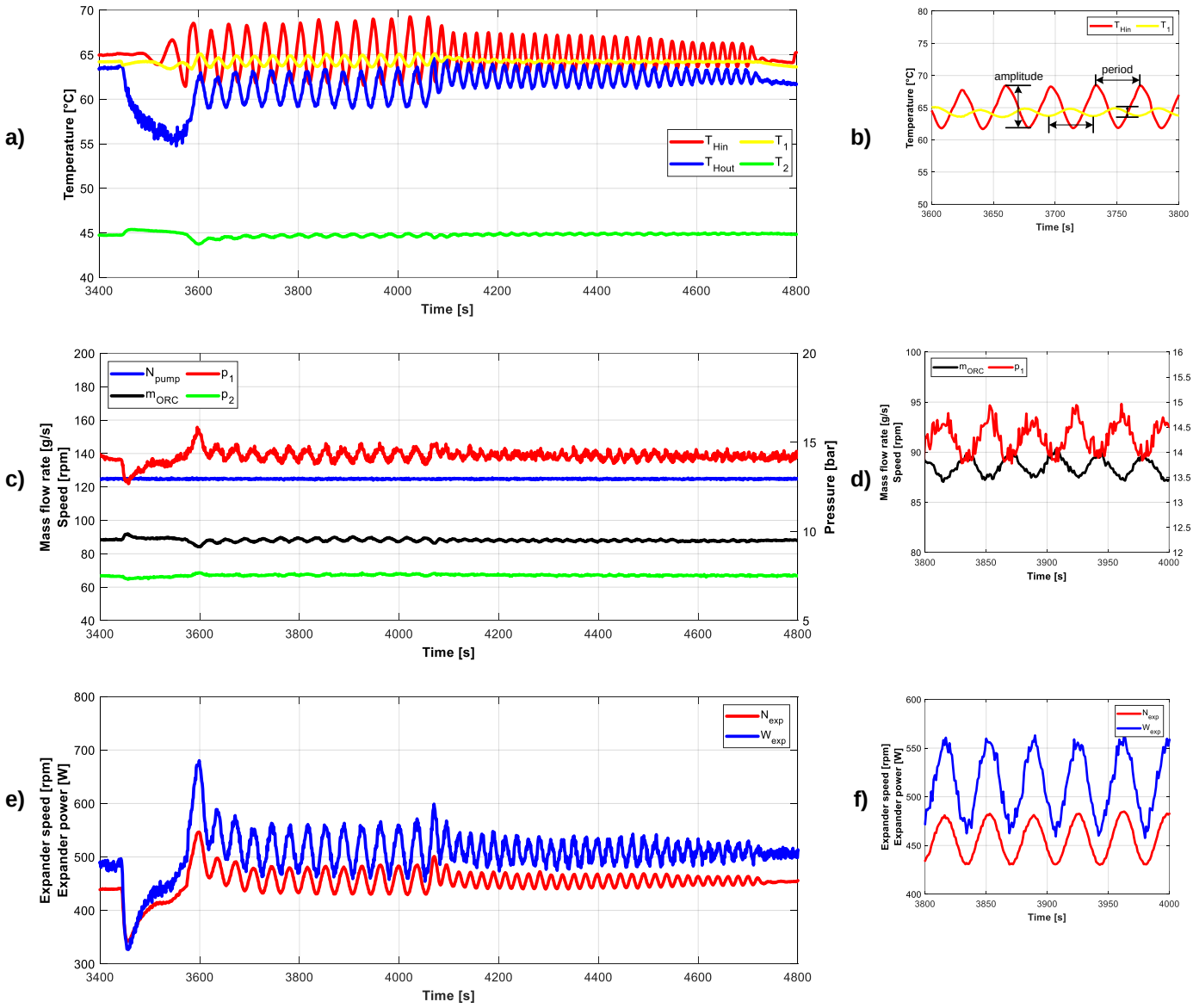

Figure 4.8 – Dynamic response in case of fluctuating hot water temperature: a) hot water inlet and outlet temperature and expander inlet and outlet temperature; b)) pump rotating speed, mass flow rate, evaporation and condensation pressure; c) expander electric power output and speed.

Table 4-3 – Response time and settling time in case of variation of hot water temperature (T_{Hin}) set-point. The absolute and percentage variation of each variable is reported. The arrows in the % variation columns indicate if the variation is increasing (↑) or decreasing (↓).

	5 °C increment (case 1)				5 °C decrease (case 2)			
Variable	*Abs. var.*	*% var.*	τ_r [s]	τ_{ss} [s]	*Abs. var.*	*% var.*	τ_r [s]	τ_{ss} [s]
Pump speed (N_{pump})	-	-	-	-	-	-	-	-
Mass flow rate ($\dot{m}_{ORC}$)	-	-	-	-	-	-	-	-
Evaporation pressure (p_1)	-	-	-	-	-	-	-	-
Condensation pressure (p_2)	-	-	-	-	-	-	-	-
Expander inlet temperature (T_1)	4.3 °C	5.7% ↑	75	150	4.8 °C	6.1% ↓	70	80
Expander outlet temperature (T_2)	2.6 °C	5% ↑	440	455	4.6 °C	8.2% ↓	600	800
Superheating degree (ΔT_{sh})	4.5 °C	29% ↑	100	200	5	25% ↓	95	165
Expander speed (N_{exp})	15 rpm	2.3% ↑	7	7	-	-	-	-
Expander power ($\dot{W}_{exp,el}$)	30 W	3.5% ↑	8	8	-	-	-	-

4.3.3 Expander load variation

As depicted in the previous chapter, the loads number influences the value of the phase load impedance, Z_{load}, which produces a relevant effect on the performance of expander (filling factor, speed, torque and power output) and of the overall system (evaporation pressure). It was already demonstrated that the expander operates with poor performance if a low loads number is connected to the generator (especially one and two loads), i.e. if the load impedance assumes the larger values among those tested (higher than 50 ohms). This parameter mainly reflects on the expander rotating speed, increasing N_{exp} to values that are not optimized for the machine under investigation, thus reducing the expander filling factor. As consequences, the power output and the torque at constant expander speed and pressure difference result lower. In this section, the aim is to analyze the system response to a variation of the expander load. With the equipment available for this investigation, the n_{loads} variation can be only a sudden, discrete step (rising or decreasing), as they are controlled by manual switches that activate one load at a time. The effect of the variation of the loads number, first decreasing from 5 to 2, then increasing from 2 to 5, is presented in Figure 4.9 and in Table 4-4. The resulting trend of the load impedance, Z_{load} (calculated according to Equation *(3.18)*), together with the expander electric power and rotating speed is showed in Figure 4.9 a). The value of Z_{load} passes from 20 ohms to 62 ohms as the load is reduced from 5 to 2. The power output is reduced from 850 W to 720 W, with a response time (τ_r) close to 30 s, and a settling time of 40 s. The response to the reduction of the load impedance (or the increment of the loads number), is similar, but the full stabilization requires more time to be achieved. The change of the expander speed is almost instantaneous, both with the rise and reduction of the Z_{load} value. Indeed, the rotating speed depends on the expander voltage which, as shown in Figure 4.9 b), increases (decreases) immediately as the impedance is increased (decreased). In both cases (rising and decreasing), the voltage presents an overshoot before the stabilization, which reflects also on the expander rotational speed. On the other hand, the expander output current is reduced from 5 A to 2.5 A, and then increased back to the starting value. The settling time is very low for the current, while the voltage requires longer time due to the first peak after the variation.

The electrical perturbation has an impact also on the fluid dynamics of the system, as it can be noticed looking at Figure 4.9 c), where mass flow rate, evaporation and condensation pressure are reported. With constant pump speed, the mass flow rate has a slight increment when the expander is connected to 2 loads only. This behavior can be related to the raise of the expander speed, which makes increase the volumetric flow at the expander inlet. However, the corresponding value of the evaporation pressure is about 1 bar lower. The modification of the condensing pressure can be barely perceived, as it remains below 0.2 bar. The superheating degree (ΔT_{sh}) and the

sub-cooling degree are plotted in Figure 4.9 d), with red line and blue line respectively. The trend of ΔT_{sh} presents two variations corresponding to the instants of loads number change, depending to the decrease of the evaporation pressure during the operation with 2 loads connected. Also, in this case, the sub-cooling degree at the condenser outlet does not show substantial variations.

Table 4-4 – Response time and settling time in case of external load variation.

	From 5 to 2 loads		**From 2 to 5 loads**	
Variable	τ_r [s]	τ_{ss} [s]	τ_r [s]	τ_{ss} [s]
Pump speed (N_{pump})	-	-	-	-
Mass flow rate ($\dot{m}_{ORC}$)	10	30	10	35
Evaporation pressure (p_1)	10	60	15	55
Condensation pressure (p_2)	-	-	-	-
Expander inlet temperature (T_1)	-	-	-	-
Expander outlet temperature (T_2)	250	370	220	400
Expander speed (N_{exp})	1	50	2	65
Expander power ($\dot{W}_{exp,el}$)	25	50	40	120

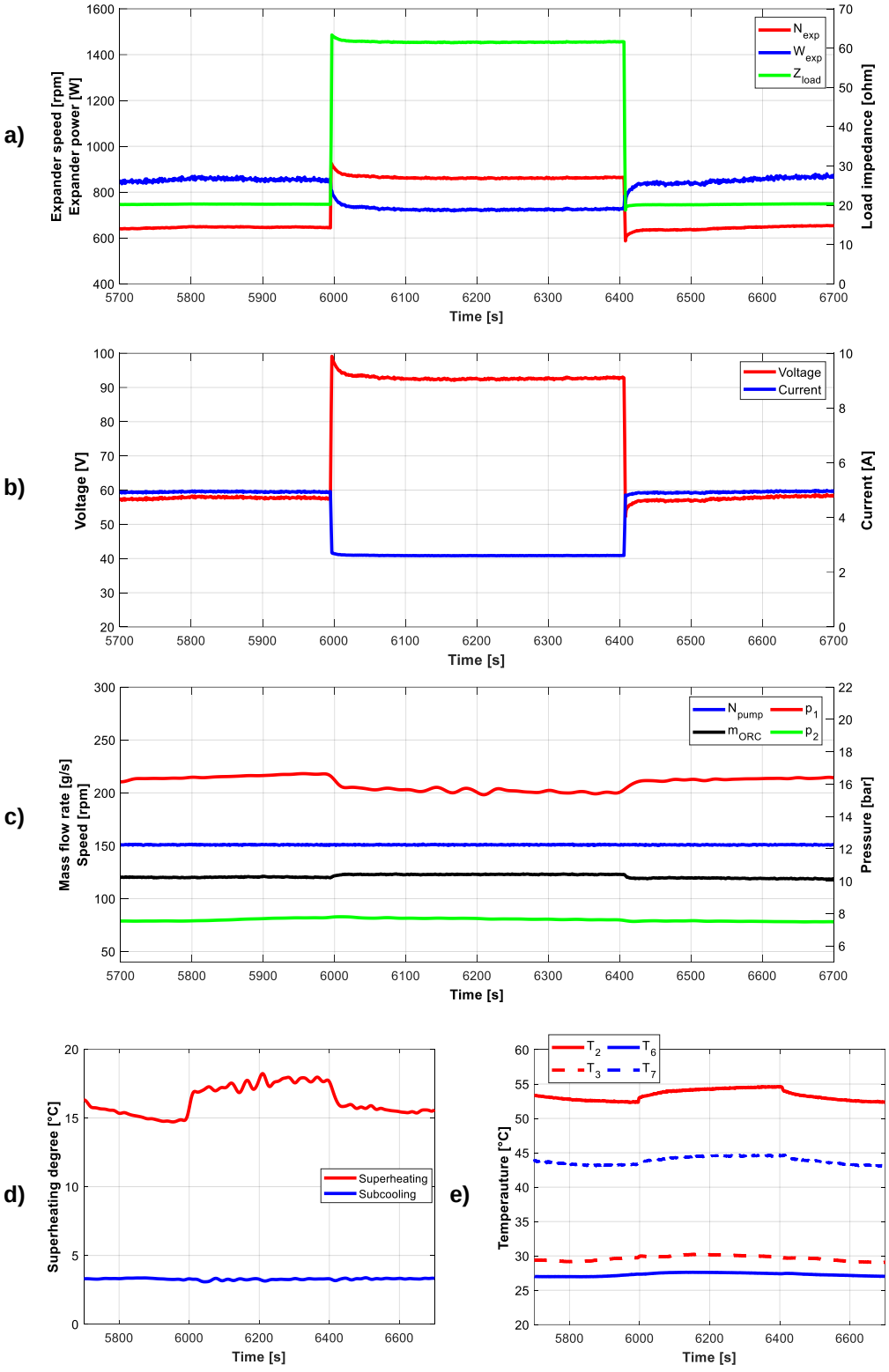

Figure 4.9 – Dynamic response in case of external load variation: a) expander electric power output, speed and load impedance; b) expander output voltage and current; c) pump rotating speed, mass flow rate, evaporation and condensation pressure; d) superheating degree at evaporator outlet and sub-cooling degree at condenser outlet; e) recuperator inlet and outlet temperatures.

4.4 Control-oriented results discussion

The transient conditions analyzed in this chapter are related to the variation of pump rotating speed, hot water inlet temperature and external electric load, which are the main controlled variables of the test bench. Depending on the nature of the heat source, the temperature can be either constant (as in geothermal plants), dynamic (WHR from internal combustion engines) or quasi-stationary (solar thermal plants). If the system is connected to the electric grid, the expander speed can be maintained constant and equal to a submultiple of the electric frequency, in case the generator has more than one pole pair, or if a speed reducer is placed between the generator and the expander shafts. If the regulation of the expander speed is required, an inverter between the generator and the electric station should be used, or, in alternative, a gearbox with variable speed ratio should be located between the expander and generator shafts. If a system connected to the grid is supplied by constant temperature heat source, it can be operated continuously at the design point. In this case, a simple control system able to manage start-up / shut-down operations and alarms, should be adequate. With quasi-stationary heat source, the ORC is required to vary its working conditions several times a day, such as the working fluid mass flow rate and the evaporation pressure, in order to pursue the optimal performance at every off-design condition. The control strategy in this case requires the employment of a PID controller, which acts on the feed pump speed that affects the evaporation pressure, based for example on a target value of the superheating degree (ΔT_{sh}) at the expander inlet. When dealing with very frequent and large variations of the heat source temperature, especially with fast-response evaporator, a linear PID controller might not be effective for a real-time adaptation of the ORC working conditions to the frequent perturbations. This is the situation where a more complex control system should be implemented, employing for example a PID with gain scheduling, or model-based predictive techniques working in a combination of closed (feedback) and open control loop.
Some consideration on the control implementation can be made looking at Figure 4.10 a) and Figure 4.10 b), which show two possible configurations of the control system referred to the system under investigation, to be implemented in a test bench and in a real application, respectively.

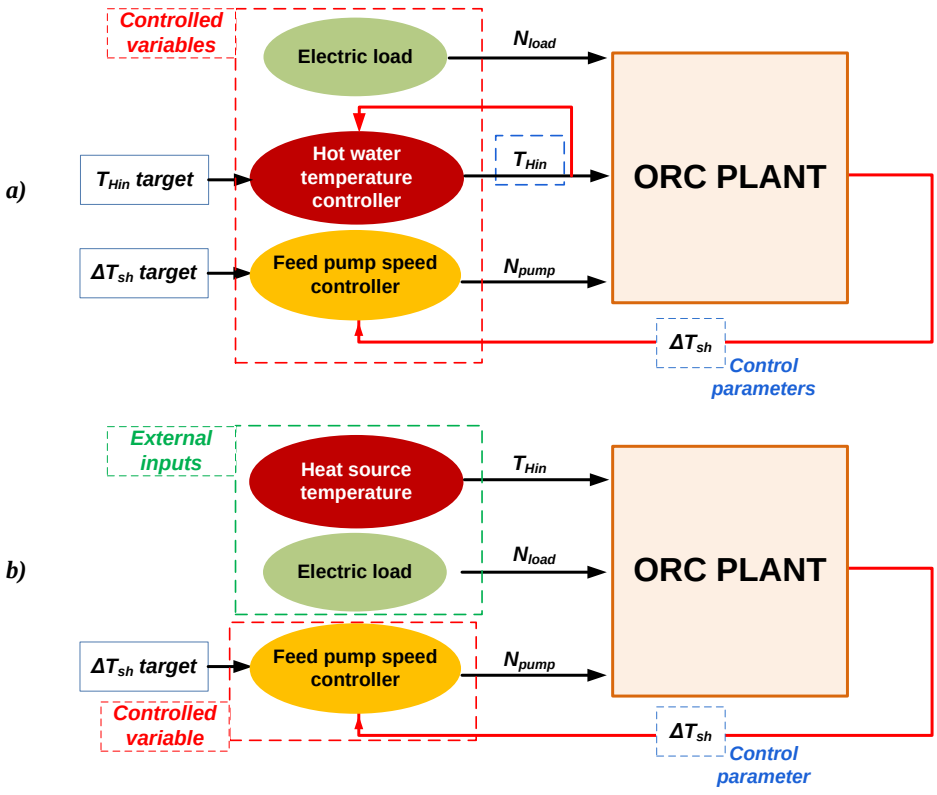

Figure 4.10 – Control system architecture: a) test bench; b) real application.

In the case of the test bench, the controlled variables coincide with the main external inputs to the ORC system, in order to be able to test controlled boundary conditions. The controller of the hot water temperature, as well as that of the expander load (if present), are used to reproduce artificially the highest possible number of real operating conditions. In the present case, the control parameters (i.e. the system outputs used as feedback parameters for the closed-loop controller) are the measured hot water temperature at the evaporator inlet, T_{Hin}, and the superheating degree at the expander inlet (ΔT_{sh}). On the contrary, in real applications the heat source temperature and the electric load are external inputs, and cannot be regulated, while the only controlled variable remains the feed pump rotating speed. In this second case, the only control parameter is the superheating degree.
The comparison of the response time of the output variables is therefore conducted considering the hot water temperature as external input. This assumption allows to include the dynamics of the temperature controller in case of variation of T_{Hin}, and compare the response time of the control parameter, ΔT_{sh}, with the case of variation of the pump speed. To this aim, The response factor (F_r) is defined as the ratio of the response time to the variation magnitude of a variable, and can help to compare the different responses even if they are not related to the same input variations.
The results for hot water temperature variations, reported in Table 4-3, reveal that the response time of the expander inlet temperature (T_1) is similar for the two conditions tested: the value of $\tau_{r,T1}$ results nearly the same in both the cases of increasing and decreasing T_{Hin} (around 100 s, case 1 and case 2). This trend is reflected on the response of the superheating degree at the expander inlet ($\tau_{r,\Delta Tsh}$), which results very close in the two conditions. The corresponding response factors results similar, close respectively to 22 s/°C and 19 s/°C. These values are slightly lower than the response of ΔT_{sh} to the modification of the pump rotating speed in case 3 (5-Hz decreasing step), characterized by τ_r close to 70 s and response factor around 14 s/°C. On the other hand, a much faster response of the superheating degree is obtained with the 10-Hz increment (case 1), in which the value of the ΔT_{sh} response factor results close to 6.5 s/°C. In conclusion, it can be affirmed that the control parameter selected for this ORC system is more sensitive to the variation of the controlled variable (N_{pump}), than to the modification of the external input (T_{Hin}). These results confirm that the control strategy based on a target value of the superheating degree can be performed efficiently by regulating the rotating speed of the feed-pump, under moderately fast input variations. If the heat source is characterized by fluctuating trend, such that reported in case 3 of the hot water temperature variation (section 4.3.2), the design of the control system should take into account the period and amplitude of the oscillation, and also assess the dynamic regime of the evaporator response (Figure 4.7).

CHAPTER 5

5 Simulink model of micro-ORC system

5.1 Introduction

As mentioned in the first chapter of this thesis, an ORC concept as the one here analyzed could be suitable for a number of applications, which can be different from case to case. Except for geothermal, which can be considered a stationary energy source, other applications may require the ORC system to work in off-design conditions for most of the time, and in some cases even in dynamic conditions. The most representative example of dynamic ORC system is the waste heat recovery from internal combustion engines in transport field. In this case, the thermal load at the ORC evaporator (i.e. the thermal power discharged by the engine to the ORC) is strongly irregular, as it depends from the engine load which changes temperature and pressure of the exhaust gases. The ORC system presented in this investigation, due to the low critical temperature of the working fluid, is not suitable for exhaust gas thermal recovery in combustion engines. However, it could be applied for recovering the heat discharged by the engine cooling circuit. In this case, the fluctuations of temperature and flow rate, even if still present, have lower impact on the bottoming cycle than those of the exhaust gas. A large quantity of thermal power is wasted also in the small industry sector, as many manufacturing plants use heat to complete their production processes. Some main examples regard iron and steel, ceramic, paper, food and chemical industries. The quality and working conditions of the heat in these applications strongly depend on the features of the specific case. Therefore, the profiles over time of temperature and mass flow rate should be carefully analyzed, at the system and control design phase. A different example is the solar thermal collectors, with or without concentration, which presents a behavior laying in the middle between stationary and dynamic heat resource. Indeed, due to the high intermittency and variability of the solar source, the system is forced to work in strongly off-design conditions, and to operates within relatively slow transient intervals of variation of the energy supply.
Regardless of the specific application, the dynamic modelling is considered a powerful tool for the design of energy systems, as it helps to establish the response of the key operating variables to variation of input and boundary conditions, for component design and control development purposes [76].

5.2 Model description

5.2.1 Introduction to Simulink Simscape

The model proposed in this study has been developed in MATLAB Simulink environment, using the library of physical components Simscape [107]. The library allows to reproduce the behavior of simple elements with no need of implementing the equations governing the physical processes. A schematic of the structure of the Simscape library is presented in Figure 5.1. As main categories, the sub-libraries include electrical, mechanical, and thermo-fluid dynamic components. The latter is divided in turn based on the domain, into *Gas* (G), *Thermal Liquid* (*TL*), *Liquid isothermal (L)*, Moist Air (*MA*), *Two-Phase* (*2P*). The sub-libraries used for this study are the *two-phase fluid* (*2P*) for the components where the organic working fluid circulates, the *thermal liquid* (*TL*) for water pipes and the *thermal* (*T*) for heat transfer elements. A component belonging to a fluid domain cannot be part of the same hydraulic circuit of a component of a different domain. This is not valid for the thermal ports of the components that are enabled to transfer thermal power the environment. For example, see the block diagram reported in Figure 5.2, with a simple case of heat exchange between a gaseous and a liquid fluid inside tubes. The

pipe of the *Gas* domain (purple lines) can be linked only to another pipe or to a reservoir of the same library, but its thermal port (H, orange) can be connected to the thermal port of the *Thermal Liquid* pipe (yellow), in order to model the heat transfer between the two fluids. Any element of the *Thermal* (*T*) library (thermal resistance, conductive/convective/ radiative heat transfer, etc.) can be located between the thermal ports of the two components. In some cases, interface elements such as heat exchangers or actuators, are provided with ready blocks. The calculation of the fluid properties is executed inside the Simscape blocks, and then is transferred to the connected blocks through their conserving ports.

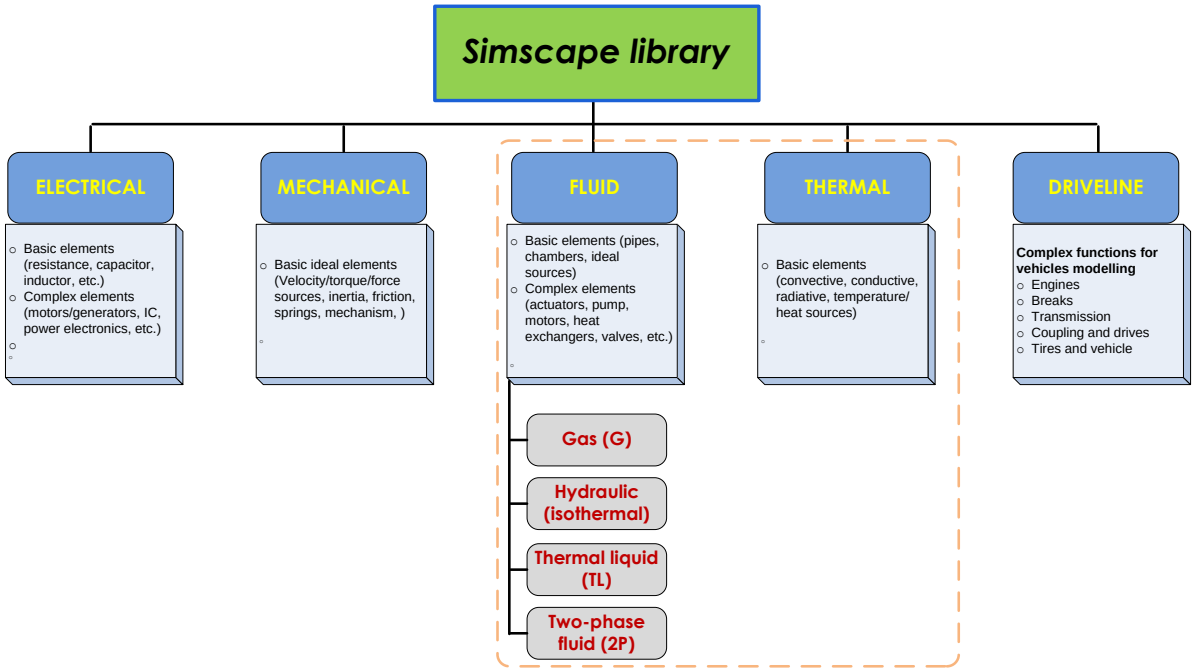

Figure 5.1 – Conceptual structure of the Simscape library (dashed frame indicates sub-libraries used in this study).

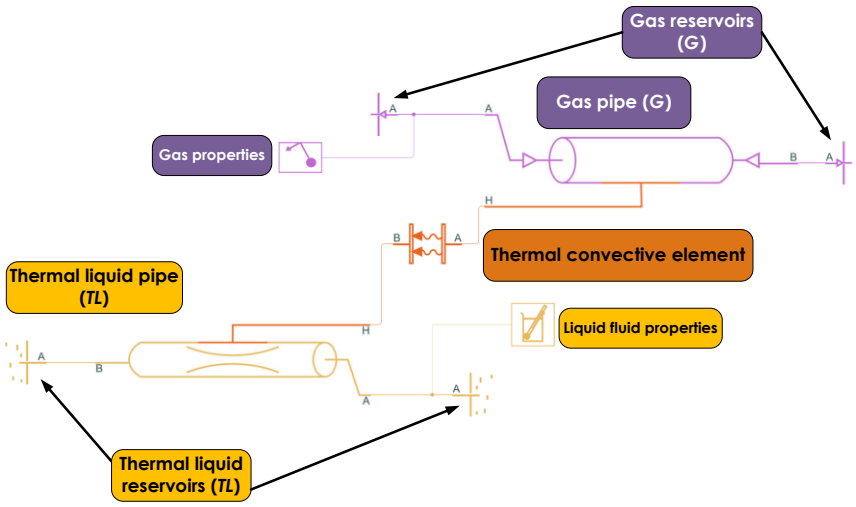

Figure 5.2 – Example of basic Simscape network with heat transfer between gas and liquid

5.2.2 Model framework

The implemented model is based on a combination of regular Simulink blocks and Simscape components. Basically, the software implements the equations of Navier-Stokes with a lumped parameters approach, meaning that the equations are applied to the nodes of each component. The type of equations implemented depends on the function and features of the specific component. Within the Simscape Fluid domains, the are two categories of components: quasi-steady and dynamic. In quasi-steady blocks, the properties are calculated at the block ports. There is no internal volume in these blocks, and he equations implemented are only algebraic. On the contrary, dynamic blocks implements both algebraic and differential equations, and compute the properties at the block ports and at its internal nodes. Examples of quasi-steady blocks are valves, local restrictions and some types of actuators. Among the dynamic components there are pipes, tanks, chambers, all characterized by an internal volume. In hydraulic network, since the volume of fluid is contained only in dynamic components, the initial conditions are set in the block parameters of these components. The initial conditions of models in Simscape Fluid depend on the component domain: for thermal liquid blocks, initial temperature and pressure must be provided, while two-phase components requires the initial pressure and either the temperature, vapor quality (in case of vapor-liquid mixture), the specific enthalpy, or internal energy. Note that inside the organic fluid pipes the initial conditions determines, together with the volume of the pipes, the charge of working fluid inside the circuit.
Fluid properties are evaluated through the relative block connected to the circuit, which is compiled with the vectors of thermodynamic quantities previously generated via CoolProp. It applies both to water and HFC-134a, so in each network the *Fluid Properties* block must be included.
Empirical correlations, such as those for heat transfer and pressure calculation, are used for coefficients computing, depending on the specific block function. For the calculation of pump and expander thermodynamic power, the corresponding semi-empirical sub-models are built with regular Simulink blocks and coupled to the library components, as will be clarified. From the Author's point of view, the adoption of the physical library Simscape, compared to the implementation of the equations, allows a faster model building process and a major robustness, since the source code of each block is already provided with functions to optimize the numerical performance and to solve possible singularities (like, for example, the density calculation close to the saturation curve).
Some simplifications have been assumed in order to reduce the complexity of the model:

- Heat source and cold sink are modelled as infinite water reservoirs, which provide for infinite thermal power at given temperature
- The liquid receiver is not modelled
- Connecting pipes of the ORC circuit are not modelled
- Thermal losses to the ambient are neglected

Given these general hypotheses, the layout of the micro-ORC system assumes the simplified form shown in Figure 5.3, which contains only evaporator, expander, recuperator, condenser and feed-pump. The hot source and cold sink are open loops. The full list of the input and output variables of the model is reported in Table 5-1. In most simulated cases, the flow rates of hot and cold water are kept constant, so the model input variables are limited to hot and cold water temperature and working fluid flow rate. Model outputs are the expander power and rotating speed, and all the thermo-dynamic properties that define the state of the fluid in each section of the cycle.

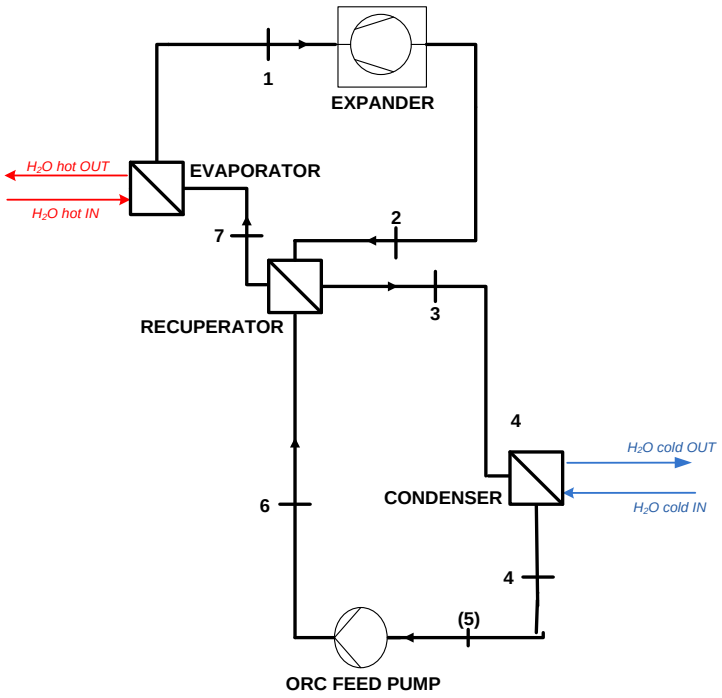

Figure 5.3 – Simplified layout considered for Simscape model

Table 5-1 – Inputs, outputs and parameters for the Simscape model

Inputs	***Outputs***	***Parameters***
○ Water temperature at evaporator inlet, T_{Hin} ○ Water flow rate at evaporator inlet, $\dot{V}_H$ ○ Water temperature at condenser inlet, T_{Cin} ○ Water flow rate at condenser inlet, $\dot{V}_C$ ○ Working fluid mass flow rate at the pump outlet, $\dot{m}_{ORC}$	○ Expander power output, $\dot{W}_{exp}$ ○ Expander rotating speed, N_{exp} ○ Fluid state in all cycle sections (temperature and pressure)	○ Diameter and length of the pipes representing the heat exchangers (D_{ev}, L_{ev}, D_{cond}, L_{cond}, etc.) ○ Coefficients for the expander empirical correlations for efficiency and speed ○ Feed-pump efficiency (η_{pump})

The model layout is reported in Figure 5.4. Each block is a Simulink Subsystem that represents one main component of the micro-ORC system (evaporator, expander, recuperator, condenser and feed pump), and contains the Simscape elements that reproduce the behavior of the component simulated. The solid blue lines represent the fluid connections between the model components; hence, all the fluid properties are held by the solid blue lines and transferred from a component to another. The dashed blue lines are the connections of the circuit branches with the virtual sensors, which are located all along the circuit, to acquire all thermodynamic properties during the model execution. The virtual sensors are used to measure the fluid temperature, pressure, flow rate, specific enthalpy, specific volume of all the points between two consecutive subsystems. Measurements have the function of monitoring the model outputs during the simulation, streaming the data to the MATLAB workspace for post-processing. In addition, the sensors provide the input data needed by some components to calculate the output of the model, such as the expander (as will be described hereinafter). The signal from the sensor can be also used to perform the feedback control of the operating variables of the cycle, for example with a PID controller. In the following, the single developed subsystems are detailed.

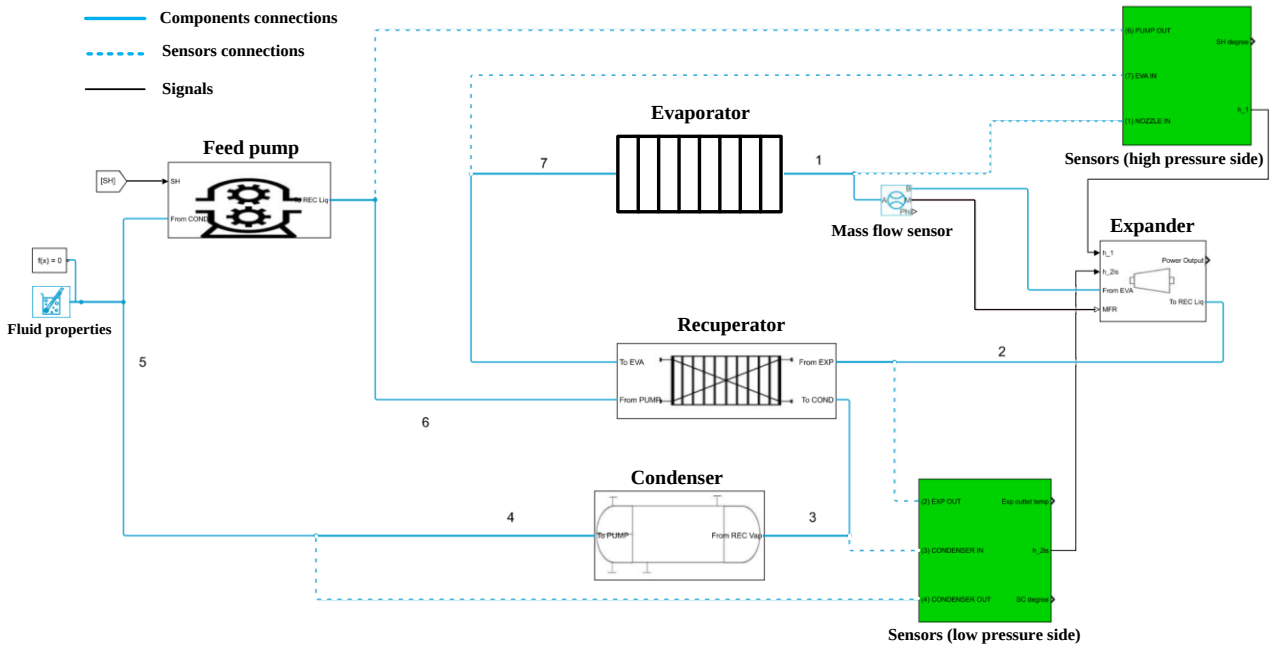

Figure 5.4 – Layout of the Simulink Simscape model

5.2.3 Evaporator block

The evaporator is one of the most important components in the modelling of ORC system, especially when the model is used to simulate transient conditions. In case of fluctuating heat source, indeed, the understanding of the evaporator dynamic response to a variation of the heat source conditions is a crucial step for the development of an efficient control strategy. The evaporator is characterized by a slow response to dynamic inputs, due to its high thermal inertia. For the present case study, the input variables that mostly influence the evaporator behavior are:

- hot water inlet temperature, that influences the superheating temperature of the cycle, thus the maximum evaporation pressure achievable with the minimum value of superheating degree to avoid wet expansion. The maximum achievable expander power output
- hot water flow rate, which affects the hot water outlet temperature and hence is related to the evaporator performance (such as the slope of the heat transfer curves and the pinch point)
- working fluid flow rate, which controls the evaporation pressure and affects the evaporator transferred thermal power

The evaporator is modelled by means of counter flow pipes that transfer thermal power between them. In its basic configuration, it consist of two pipes, one for the hot fluid (water), taken from *Thermal Liquid* domain, the other for the cold one (HFC-134a), from the *Two-Phase* domain. The two pipes are connected by their thermal ports H, which represent the external connection to the environment, and are used to exchange the thermal power between the fluids. In each pipe the fluid properties are calculated at a limited number of nodes (inlet and outlet ports, internal node) with a lumped parameters approach. Thus, to improve the calculation, each side of the heat exchanger shall be split in more pipes in series, in order to realize a discretization of the component and to increase the number of nodes in which the conservation equations are applied. In the case of the evaporator, three tubes are connected in series for each fluid.
The block parameters of the pipes requires to insert several quantities, related to the pipe dimensions, the heat transfer between the pipe wall and the external environment (port H), the flow friction and the initial conditions.

Some of these parameters are set to their defaults values, while others have been selected as calibrated parameters, as they influence substantially the performance of the pipe used as heat exchanger. Pressure losses across the evaporator are taken into account.
The layout of the evaporator sub-model is presented in Figure 5.5. The main Simscape elements that compose it are depicted in Table 5-2. The *3-Zone Pipe* is a block used to model a tube with phase-changing fluid. The total volume inside the pipe is divided in three zones, related to sub-cooled liquid (L), liquid-vapor mixture, and superheated vapor, tracked by a boundary-following model. Each zone is characterized by a *zone length fraction*, that corresponds to the fraction of volume occupied by the zone to the total volume of the pipe.

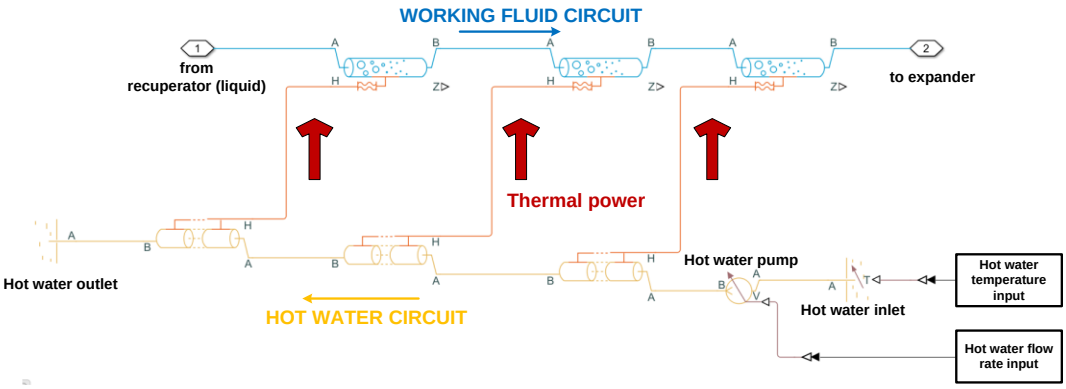

Figure 5.5 – Layout of evaporator model sub-system

Table 5-2 – Elements included in the evaporator sub-system

Element name	Domain	Quantity	Function
3-Zone Pipe	*2P*	3	Working fluid side of the heat exchanger
Pipe	*TL*	3	Water side of the heat exchanger
Controlled Reservoir	*TL*	1	Inlet environment of hot water, with controlled temperature
Reservoir	*TL*	1	Outlet environment of hot water
Controlled Volumetric Flow Rate Source	*TL*	1	Hot water pump

In the following, the main equations implemented inside the *3-Zone Pipe (2P)* and in the *Pipe (TL)* are recalled from the MATLAB Help [107] and briefly described.

Mass conservation

The mass conservation is expressed by Equation 5.1, where $\dot{m}_A$ and $\dot{m}_B$ are the mass flow rates at the inlet and outlet ports of the pipe, and *m* is the total mass of fluid inside the pipe.

$$\frac{dm}{dt} = \dot{m}_A + \dot{m}_B \tag{5.1}$$

The mass variation can be expressed also in terms of fluid zones, as function of the density variation with pressure (p) and specific internal energy, u, according to Equation 5.2.

$$\frac{dm}{dt} = \left[\left(\frac{d\rho}{dp}\right)_u \cdot \frac{dp}{dt} + \left(\frac{d\rho}{du}\right)_p \cdot \frac{du_{out}}{dt} + \rho_L \cdot \frac{dz_L}{dt} + \rho_M \cdot \frac{dz_M}{dt} + \rho_V \cdot \frac{dz_V}{dt}\right] \cdot V_{pipe} \tag{5.2}$$

where u_{out} is the internal energy at the end of the heat transfer and V_{pipe} is the internal volume of the pipe, i.e. the total volume of fluid.

Energy conservation

The energy conservation in the 3-Zone Pipe is expressed through Equation 5.3:

$$m \cdot \frac{du_I}{dt} + \frac{dm}{dt} \cdot u_I = \phi_A + \phi_B + Q_H \tag{5.3}$$

where m is the mass of fluid inside the pipe, u_I is its internal energy, ϕ is the energy flow rates at inlet (A) and outlet (B) ports of the pipe, and Q_H is the thermal power transferred through the pipe wall. The thermal power Q_H is expressed as function of the enthalpy difference in each zone, according to Equation 5.4. Such enthalpy change is defined by Equation 5.5 and 5.6, for the single-phase zones and for the two-phase zone, respectively.

$$Q_H = \dot{m}_{in} \cdot (\Delta h_L + \Delta h_V + \Delta h_{2P}) \tag{5.4}$$

$$\Delta h_L = c_p \cdot (T_H - T_{in}) \cdot \left[1 - exp\left(-\frac{z_L \cdot A}{\dot{m}_{in} \cdot c_p \cdot (\alpha_F^{-1} + \alpha_E^{-1})}\right)\right] \tag{5.5}$$

$$\Delta h_{2P} = (T_H - T_{in}) \cdot \frac{z_{2P} \cdot A}{\dot{m}_{in} \cdot (\alpha_F^{-1} + \alpha_E^{-1})} \tag{5.6}$$

where:

- Δh_L is the enthalpy difference in the liquid zone
- Δh_{2P} is the enthalpy difference in the two-phase zone
- c_p is specific heat at constant pressure;
- T_H temperature at the port *H* of the pipe, associated to the external heat source or sink;
- T_{in} is the temperature at the inlet of the zone, i.e. the temperature of the liquid or vapor in Eq. 5.5, and the saturation temperature of the mixture in Eq. 5.6;
- z is the zone length fraction;
- $\dot{m}_{in}$ is the mass flow rate at the inlet of the zone;
- α_F is the convective heat transfer coefficient between the fluid and the wall;
- α_E is the convective heat transfer coefficient between the wall and the external source/sink;
- A is the surface area of external wall, that depends on the pipe hydraulic diameter and length.

The evaluation of the convective transfer coefficient between fluid and wall, α_F, depends on the fluid phase, having the general form reported in Equation 5.7.

$$\alpha_F = \frac{\lambda \cdot Nu}{D} \tag{5.7}$$

where λ is the average thermal conductivity of the working fluid in the pipe (tabulated), *D* is its hydraulic diameter (to be calibrated) and *Nu* is the Nusselt number. With turbulent flow, the value of *Nu* is obtained from the Gnielinski correlation (Equation 5.8) for single-phase conditions (liquid and vapor) [105], as a function of Reynolds number (*Re*), Prandtl number (*Pr*) (tabulated) and Darcy friction factor *f*; in the two-phase region *Nu* follows from the Cavallini and Zecchin correlation (Equation 5.9) [106], depending also on fluid quality *x*.

$$Nu = \frac{\frac{f}{8} \cdot (Re - 1000) \cdot Pr}{1 + 12.7 \cdot \sqrt{\frac{f}{8}} \cdot (Pr^{\frac{2}{3}} - 1)} \tag{5.8}$$

$$Nu = 0.05 \cdot \left[(1 - x + x \cdot \sqrt{\frac{v_{SV}}{v_{SL}}}) \cdot Re_{SL} \right]^{0.8} \cdot Pr_{SL}^{0.33} \tag{5.9}$$

where the subscript *SL* and *SV* are referred respectively to saturated liquid and saturated vapor. The heat transfer coefficient between the wall and the exterior, α_E, is expressed by Equation 5.10. The conduction coefficient of the wall α_W is defined by Equation 5.11, while the heat transfer coefficient of the external source, α_{ext}, must be specified in the block parameters of the component.

$$\frac{1}{\alpha_E} = \frac{1}{\alpha_W} + \frac{1}{\alpha_{ext}} \tag{5.10}$$

$$\alpha_W = \frac{\lambda_W}{D \cdot \ln(1 + \frac{s_w}{D})} \tag{5.11}$$

Where λ_W is the wall thermal conductivity and s_W is the wall thickness. It is clear that, in order to remove the effect of the pipe wall on the heat transfer, the value of s_W shall be set to zero in the block parameters.

Momentum conservation

Two factors determine the pressure variation along the pipe: the change of density and the pressure losses due to friction at the pipe wall.

Pressure losses in turbulent regime are computed as function of the Darcy friction factor, *f*. The latter is computed by the Haaland correlation, expressed by Equation 5.12, as function of the pipe hydraulic diameter (*D*), internal surface absolute roughness (ε), and Reynolds number (*Re*).

$$\frac{1}{\sqrt{f}} = -1.8 \cdot log \left[\left(\frac{\varepsilon/D}{3.7} \right)^{1.11} + \frac{6.9}{Re} \right] \tag{5.12}$$

The pressure differential over the pipe is computed with two analogous equations, one for pressure change between inlet port *A* and internal node *I*, the other between port *B* and internal node *I* (Equation 5.13, here reported only in the case of port *A*).

$$p_A - p_I = \left(\frac{1}{\rho_I} - \frac{1}{\rho_A} \right) \cdot \left(\frac{\dot{m}_A}{S} \right)^2 + \frac{f_A \cdot \dot{m}_A^2}{2 \cdot \rho_I \cdot D \cdot S^2} \cdot \left(\frac{L + L_{add}}{2} \right) \tag{5.13}$$

where ρ_I and ρ_A are the values of fluid density at the internal node and the inlet port, respectively, *S* is the pipe cross sectional area, *L* is the pipe length and L_{add} is the aggregate equivalent length of local resistances, whose value can be set in the block parameters.

The above-presented equations, even if not exhaustive of the functions implemented in the *3-Zones Pipe*, provide for a basic understanding of the effect that the calibrated parameters to be set have on the heat transfer and friction inside the pipe. The properties that must be specified in the *Geometry* page of the block parameters are the pipe length (L), Cross-sectional area (S) and Hydraulic diameter (D). These parameters have been reduced to two (pipe length and diameter), since the cross-sectional area is related to the hydraulic diameter (through the expression $S = \frac{\pi \cdot D^2}{4}$), assuming that the pipe has circular section. *L* and *D* are therefore selected as calibration parameters for the pipes that compose the heat exchangers. From the analysis of Eqs. 5.1-5.13, it is clear that the parameters *L* and *D* have effect on both the heat transfer and the pressure losses. Indeed, increasing the hydraulic diameter D makes decrease the convective transfer coefficient of the fluid inside the pipe (α_F), and also the heat transfer coefficient related to the wall and the external environment heat exchange, α_E. On the contrary, if *D* decreases, the heat transfer surface area, or the wall surface ($A = \pi \cdot D \cdot L$) is reduced proportionally. The same effect on the value of the wall surface *A* is observed for the pipe length, *L*, which instead does not influence the heat transfer coefficients, α_F and α_E. The coefficient α_E is also affected by the pipe wall thickness (s_w) and by the imposed value of the external environment heat transfer coefficient, α_{ext}. Besides the working conditions (density and flow rate), pressure losses depend on the Darcy friction factor, on the pipe length and on the equivalent length of local resistances. The friction factor *f* is a function of the hydraulic diameter and on the Reynolds number, increasing both with the increment of *D* and *Re*. On the other hand, the reduction of the diameter *D* causes an increment of the pressure loss, as indicated in Equation 5.13 (where *D* affect also the cross sectional area, *S*). The pipe length is one of the calibrated parameters, while the equivalent length of the local resistance is set in the block parameters, usually expressed as a fraction of the pipe length. To recap, the heat transfer coefficients are enhanced by the reduction of the hydraulic diameter (*D*), which however makes decrease the heat transfer surface area (*A*). A higher value of the pipe length (*L*) increases the surface area, but have negative effect on the pressure losses.

The evaporator water pipes follow similar rules to those just described for the organic fluid pipes, with some differences related to the not inclusion of phase change. In this case, the heat transfer between the fluid and the wall is expressed by two terms, one accounting for conduction (Q_{cond}) and the other for convection (Q_{conv}), displayed respectively in Equations 5.14 and 5.15.

$$\mathrm{Q}_{cond} = \frac{\lambda \cdot A}{D} \cdot (T_H - T_I) \tag{5.14}$$

$$\mathrm{Q}_{conv} = c_{p,avg} \cdot \dot{m}_{avg} \cdot (T_H - T_{in}) \cdot \left[1 - exp\left(-\frac{\alpha_F \cdot A}{\dot{m}_{avg} \cdot c_{p,avg}}\right)\right] \tag{5.15}$$

where λ is the water thermal conductivity, T_H is the pipe wall temperature, T_I is the water temperature at the pipe internal node, $c_{p,avg}$ and $\dot{m}_{avg}$ are the average values of the specific heat and water mass flow rate, respectively, T_{in} is the fluid temperature taken at the pipe inlet port. The expression used for determining the convective coefficient is the same reported in Eq.5.7. The Nusselt number is calculated by Gnielinski correlation, that assumes the form used for the single-phase organic fluid (Eq. 5.8). Alternative computations approaches are the Dittus-Boelter correlation, or the look-up table parametrization of the heat transfer based on user-supplied data (nominal temperature differential versus nominal mass flow rate, or Colburn factor versus Reynolds number, or Nusselt number versus Reynolds number and Prandtl number).

5.2.4 Condenser

The condenser model is substantially similar to the evaporator one, having exactly the same components listed in Table 5-2. The main difference is that in this case the heat source is the organic working fluid, flowing in the *3-Zone Pipes* of *2P* domain, and discharging its thermal power to the cooling water, which flows inside the *Thermal Liquid* Pipes. The same discretization of the evaporator, i.e. with three elements in series, is used. Equations 5.1-

5.13 used for the evaporator are valid also in this case. The condenser sub-system is presented in Figure 5.6. The organic fluid (hot side) comes from the vapor side of the recuperator and flows in the blue pipes, then exits the condenser towards the feed-pump. The cold water is pumped from an ideal reservoir to the in-series pipes of the condenser, then exits towards the outlet ideal reservoir. Cold water temperature and volumetric flow rate are imposed at the inlet reservoir and at the water pump, respectively.

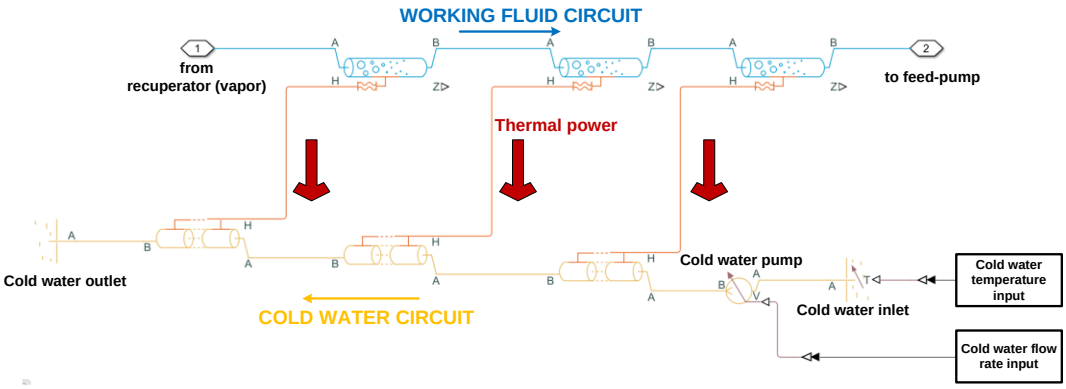

Figure 5.6 - Layout of condenser model sub-system

5.2.5 Recuperator

The recuperator sub-model presents the same structure of evaporator and condenser, but this time both sides of the heat exchanger are interested by the organic working fluid. This means that both the pipes of hot and cold fluid are *3-Zone Pipes (2P)*, that are governed by the same equations reported for the evaporator. Differently from the other heat exchangers, and also from pump and expander as will be explained, the recuperator does not receive any external input. Indeed, its calculation is performed on variables (flow rate, pressure and internal energy) that are transferred internally from the other sub-system through the Simscape blocks. For this reason, the calibration of the recuperator parameters is more challenging than that of the other heat exchangers. Figure 5.7 shows the basic structure of the recuperator sub-system: on the hot side, the low-pressure vapor comes from the expander outlet and flows through the recuperator towards the condenser inlet. On cold side, the liquid high-pressure fluid pumped by the feed-pump flows towards the evaporator inlet.

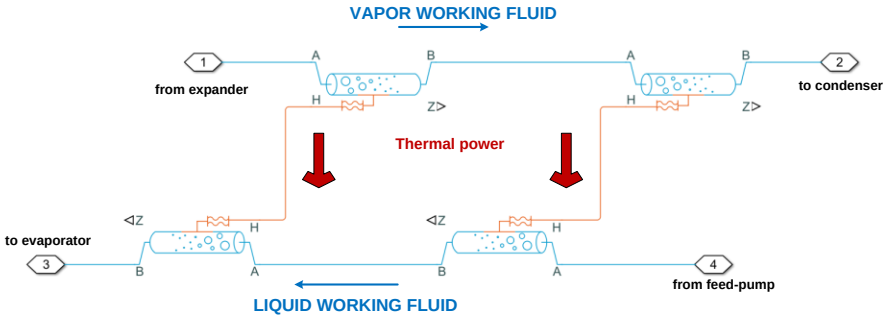

Figure 5.7 - Layout of recuperator model sub-system

5.2.6 Expander block

The expander sub-system includes all the functions that model the expansion process. This is composed by a combination of Simscape blocks and regular Simulink blocks, performing the steps that simulate the expander operation. The expansion process is modelled in two virtual stages (see Figure 5.8 and Figure 5.9):

1) **1-2h:** pressure drop at constant enthalpy
   In this first stage of the expansion, the pressure is reduced from the value at the head of the expander (evaporation pressure) to the expander outlet pressure, which corresponds to the condensation pressure except for the pressure losses in the recuperator. The element operates with no exchange of thermal power with the environment and with no work done on or by the fluid. In addition, since a quasi-steady block is employed, the element volume is considered negligible. Hence, the pressure drop occurs without any enthalpy change between the inlet and outlet of the component (isenthalpic process). The process is performed by the component called *Flow Resistance* of the *Two-Phase* domain. The values of the following parameters must be specified in its block parameters:

   - Nominal pressure drop, Δp_{nom}
   - Nominal mass flow rate, $\dot{m}_{avg}$
   - Nominal specific volume, v_{nom}

   These values are set equal to experimental data of pressure difference, working fluid mass flow rate and specific volume at the expander inlet, taken from a test point selected as design conditions. This point is characterized by the maximum value of pressure difference acquired during the test campaign. The *Flow Resistance* block applies static equations of mass, energy and momentum balance, to the inlet and outlet ports of the component (port *A* and port *B*). The conservation of mass and energy is expressed by Equation 5.16 and 5.17, where $\dot{m}_A$ and $\dot{m}_B$, ϕ_A and ϕ_B, p_A and p_B are the mass flow rates, heat fluxes and pressure value at port A and port B of the *Local Resistance*, respectively.

$$\dot{m}_A + \dot{m}_B = 0 \tag{5.16}$$

$$\phi_A + \phi_B = 0 \tag{5.17}$$

$$p_A - p_B = \Delta p \tag{5.18}$$

   The pressure drop Δp is evaluated by means of a semi-empirical expression that calculates the friction losses in terms of a loss coefficient, ξ, defined according to Equation 5.19.

$$\Delta p = \frac{\xi \cdot v \cdot \dot{m}^2}{2 \cdot S^2} \tag{5.19}$$

   where the value of v and $\dot{m}$ are generic. The loss coefficient ξ is not required as input parameter for the block, but it is calculated using Eq. 5.19, based on the nominal values of pressure drop, mass flow rate and specific volume specified by the user.

2) **2h-2:** heat transfer at constant pressure
   The second stage of the expansion process is represented by a heat transfer that occurs at constant pressure. that is used to account for the release of thermodynamic power output due to the fluid expansion. This is performed by adding a *3-Zone Pipe (2P)*, which allows to transfer the expander thermodynamic power to the external environment through its port H. To absorb this power from the pipe, the block named *Controlled Heat Flow Rate Source (2P)* is connected to the port H. This component represents an ideal heat source, able to maintain the specified heat flow rate value regardless of the temperature difference. The input value to the heat flow source is the output result of the calculation performed inside the block

called *Expander Semi-Empirical Model*. The latter is based on semi-empirical correlations (polynomial fitting functions) for calculating the expander isentropic efficiency (η_{is}) and the filling factor (*FF*) as function of the pressure ratio over the expander (Equations 5.20 and 5.21). The empirical constant coefficients a, b, c and d have been calibrated applying the polynomial function method to the expander only [108]. The isentropic efficiency is then used to estimate the expander outlet enthalpy, h_2, from the balance relation shown in Equation 5.22 and, finally, the thermodynamic power output, input of the ideal heat flow source, is defined as the mass flow rate multiplied by the enthalpy difference over the expander ($\dot{W}_{exp,th} = \dot{m}_{wf} \cdot (h_1 - h_2)$). The electric power produced by the expander (Equation 5.23), which is one of the outputs of the model, is computed using the expander electromechanical efficiency ($\eta_{exp,em}$), defined as the ratio of the electric to the thermodynamic power.

$$\eta_{is} = a \cdot \left(\frac{p_2}{p_1}\right) + b \cdot \left(\frac{p_2}{p_1}\right)^2 \tag{5.20}$$

$$FF = c \cdot \left(\frac{p_2}{p_1}\right) + d \cdot \left(\frac{p_2}{p_1}\right)^2 \tag{5.21}$$

$$h_2 = h_1 - (h_1 - h_{2,is}) \cdot \eta_{is} \tag{5.22}$$

$$\dot{W}_{exp,el} = \dot{W}_{exp,th} \cdot \eta_{exp,em} = \dot{m} \cdot (h_1 - h_2) \cdot \eta_{exp,em} \tag{5.23}$$

Once the filling factor *FF* is determined, the expander rotating speed can be calculated according to Equation 5.24, where V_{exp} is the expander total displacement and ρ_1 is the density at the expander inlet.

$$N_{exp} = \frac{\dot{m}_{wf} \cdot 60}{V_{exp} \cdot \rho_1 \cdot FF} \tag{5.24}$$

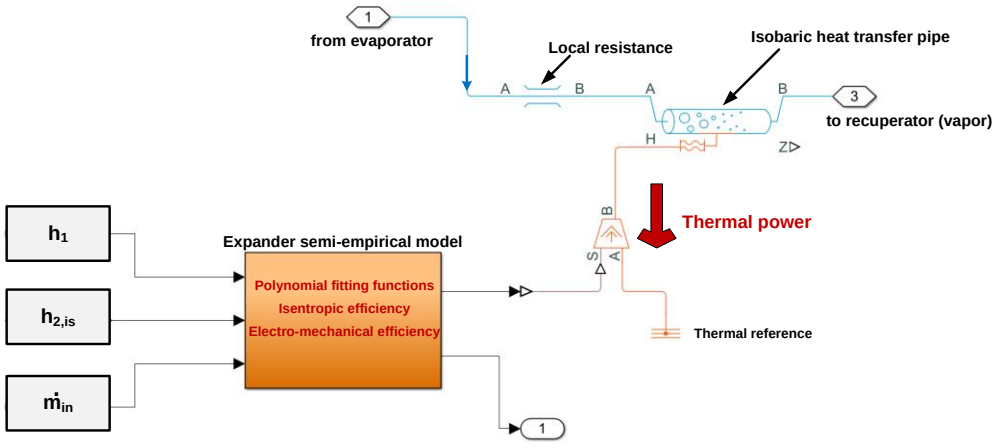

Figure 5.8 - Layout of expander model sub-system

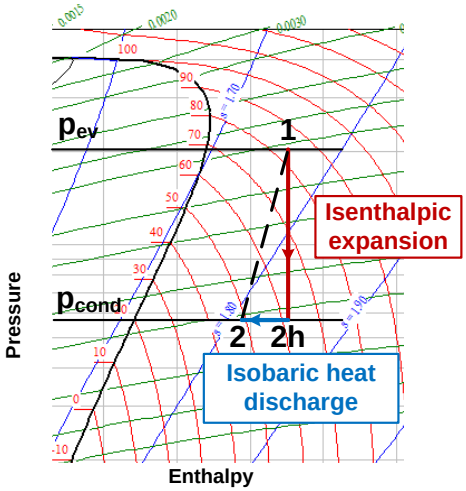

Figure 5.9 – Representation of the modelled expansion process in pressure-specific enthalpy diagram

5.2.7 Feed-pump block

The feed-pump model follows a similar approach to the expander one, consisting in the coupling of Simscape blocks with Simulink functions. The pumping process is split in the following two steps, corresponding to as much Simscape elements (Figure 5.10): an ideal flow rate source (*Controlled Mass Flow Rate Source (2P)*), which provides for a user-imposed value of mass flow rate, regardless of the pressure differential over the component. The second step accounts for the change of enthalpy that occurs between the inlet and outlet sections of the pump. On the pressure-specific enthalpy diagram of Figure 5.11, pumping is represented by two virtual processes:

1) Isenthalpic pressure rise
   Increase from low pressure at the pump suction to high pressure at pump discharge. The pressure rise occurs at constant enthalpy (isenthalpic transformation). The value of mass flow to maintain is determined by the block input S, and is an input variable of the model. To express the input in terms of pump rotational speed (which is the actual controlled variable), Equation 5.24 is used, function of the pump volumetric efficiency.
2) Heat transfer at constant pressure
   A *3-Zone Pipe* is used for accounting the increase of internal energy in the pumped fluid. The virtual pipe absorbs an amount of heat equal to the thermodynamic power consumed by the pump. The heat transfer is realized with an ideal heat source (*Controlled Heat Flow Rate Source (2P)*). The input to the heat source, i.e. the thermodynamic power added by the pumping process, is calculated according to Equation 5.26, as the ratio of the hydraulic power to the pump efficiency, which is assumed constant and equal to 0.25, according to the average measured value.

$$\dot{V}_{wf} = V_p \cdot N_p \cdot \eta_{vol,p} \tag{5.25}$$

$$P_{p,th} = \frac{\dot{V}_{wf} \cdot (p_6 - p_4)}{\eta_p} \tag{5.26}$$

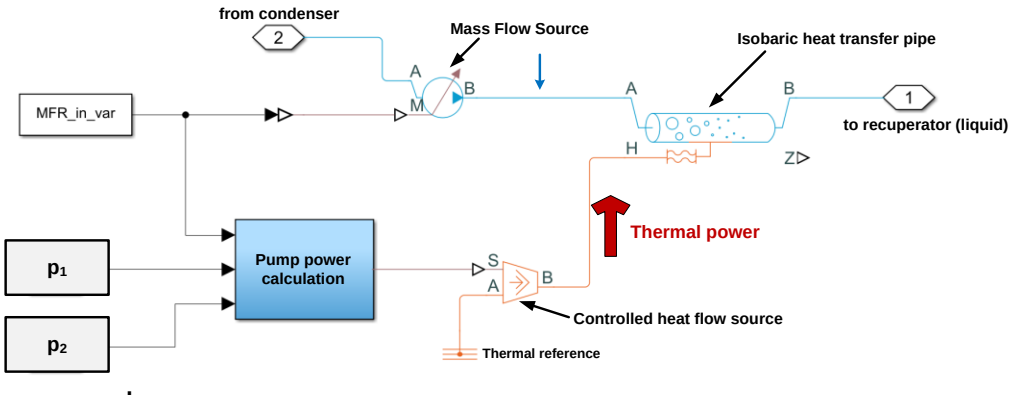

Figure 5.10 – Layout of pump model sub-system

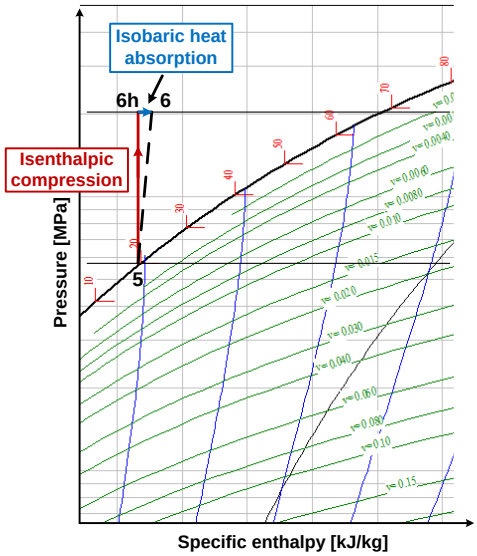

Figure 5.11 – Representation of the modelled pumping process in pressure-specific enthalpy diagram

5.3 Calibration procedure

The calibration procedure was realized on the single model components, implementing a routine on a MATLAB script and launching the Simulink model from the script itself, every time with a different set of parameters. The simulation results have been acquired in terms of temperature and pressure at different operating conditions. The relative errors have been compared and the configuration associated with the lowest average error has been selected. The main calibration is performed on the heat exchangers geometries, as depicted in the following.

5.3.1 Heat exchangers calibration

A parametric analysis was conducted with the aim of assessing the value of the geometrical parameters included in the calibration process. For an easier procedure, the heat exchangers have been simulated separately, in order to isolate and understand the effect of their fixed parameters on the heat transfer. Hence, some modifications are

needed in the layout of Figure 5.5, as an inlet and an outlet environment for the working fluid must be defined if the sub-model needs to work disconnected from the rest of the circuit. The layout of the evaporator model used for the calibration process is reported in Figure 5.12. A controlled reservoir is added at the evaporator inlet, setting the inlet pressure and temperature, while a normal reservoir is used at the evaporator outlet. An ideal mass flow rate source is used as ideal pump at the evaporator inlet. The water side remains substantially the same, since it is an independent open loop all contained inside the evaporator block. The same considerations apply to the condenser. The following heat exchangers parameters are the objects of the calibration:

- Hydraulic diameters of the *3-Zone Pipes* (working fluid side of evaporator and condenser, both sides of recuperator), D_{ev}, D_{cond}, $D_{rec,v}$, $D_{rec,l}$;
- Length of the heat exchangers *3-Zone Pipes*, L_{ev}, L_{cond}, L_{rec};

The length of water pipes (L_H, L_C) is not included in the calibrated parameters since it is assumed equal to the length of working fluid pipe. The same applies to the length of the recuperator, which is assumed equal at both liquid and vapor sides. Also the hydraulic diameters of the water pipes are excluded from calibration, and taken equal to 0.04 m and 0.05 m for the evaporator pipes diameter (D_H) and for the condenser one (D_C).The calibration procedure is here detailed only for the case of the evaporator, being substantially similar for the other heat exchangers.
The input variables to the evaporator sub-model are the organic fluid mass flow rate ($\dot{m}_{ORC}$), the inlet temperature (T_7), the outlet pressure (p_1), the water flow rate ($\dot{V}_H$) and water inlet temperature (T_{Hin}). The outputs are the outlet temperatures of organic fluid and water (T_1 and T_{Hout}), that define the thermal power transferred in the heat exchanger, and the organic fluid inlet pressure (p_7). The latter is obtained by imposing the outlet pressure at both the inlet and outlet reservoir, and then acquiring the pressure value at the actual pipe inlet, after the ideal pump. In this way, the pump perform the exact pressure rise required to overcome the pressure losses inside the pipes in series (see Figure 5.12).

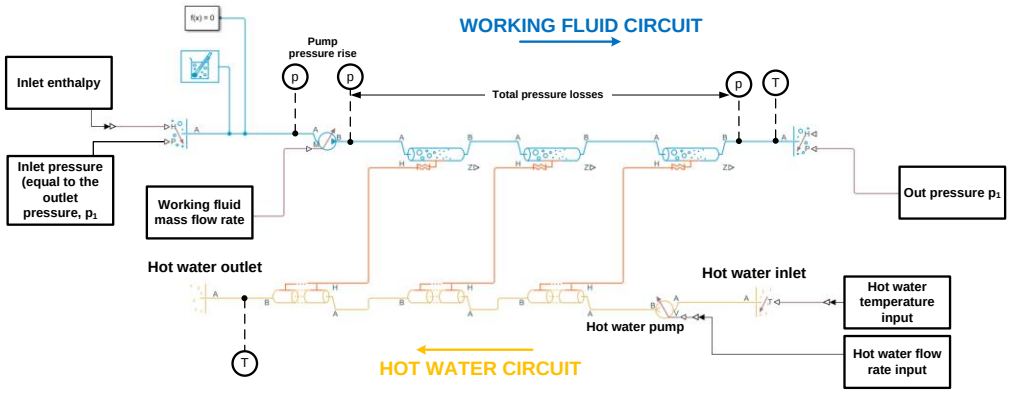

Figure 5.12 – Layout of the evaporator model, modified for the calibration

The calibration is performed by imposing constant inputs to the block, and registering the output results as they achieve steady-state conditions. The output variables are then compared to the experimental values, defining a relative error calculated as the difference between the simulated and the experimental value divided by the experimental value. At the start of calibration, a first attempt of heat exchangers pipe geometry must be provided, which can be obtained from the real geometry in terms of surface area and volume. Then, the values of the parameters are adjusted in order to reduce the error of the output variables. A DOE (Design Of Experiment) matrix has been created, including the variable values of organic fluid pipe diameter and length. Each combination of length and diameter defines an element of the DOE matrix, which corresponds to one simulation of the model. The simulations have been launched from the MATLAB Editor, in order to run the model progressively and

changing the geometry parameters at each execution, according to the DOE matrix. The calibration was conducted at several operating points, characterized by different working conditions in terms of heat source and cold sink temperature, and working fluid mass flow rate. The combination of diameter and lengths that determines the lowest global error has been determined for each heat exchanger. An example of DOE matrix used for the evaporator is reported in Table 5-3. Generally, the procedure requires more than one calibration stage, resulting in more DOE matrixes: in the first stage, a relatively large range of variation for each parameter is considered around the first-attempt geometry. In the next stages, the range of variation is reduced and is centered around the best value found in the previous stage.
The calibration results, in terms of relative errors with respect to the experimental steady-state data, are reported in Figure 5.13, where the selected configuration is indicated. Table 5-4 collects the calibrated geometrical parameters of the three heat exchanger.

Table 5-3 – DOE matrix for evaporator calibration

		Evaporator pipe diameter D_{ev} [m]			
DOE		*0.022*	*0.023*	*0.024*	*0.025*
Evaporator pipe length L_{ev} [m]	*30*	1	6	11	16
	35	2	7	12	17
	40	3	8	13	18
	45	4	9	14	19
	50	5	10	15	20

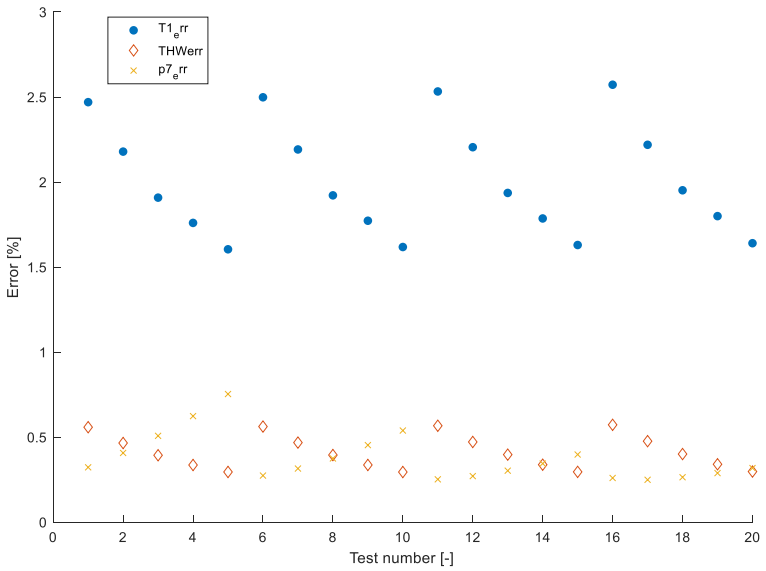

Figure 5.13 – Simulation errors of T_1, p_7 and T_{Hin}, varying the combination of D_{ev} and L_{ev} (see Table 5-3)

Table 5-4 – Geometrical parameters resulted from calibration

Component	Number of pipes	Equivalent diameter, *D* [m]		Equivalent length *L* [m]	
		WF (vap)	H2O (liq)	WF (vap)	H2O (liq)
EVAPORATOR	3	0.025	0.05	35	35
CONDENSER	3	0.025	0.04	60	60
RECUPERATOR	2	0.027	0.02	25	25

5.3.2 Expander parameters

The expander sub-system requires to set several constant coefficients, in each of the different elements that perform the expansion virtual stages. The *Local Resistance* block requires the nominal values of pressure drop, mass flow and specific volume. The experimental operating point with maximum value of mass flow rate was selected as nominal condition, and the corresponding pressure difference and specific volume are imposed in the *Local Resistance* block parameters.

5.3.3 Initial conditions

All the Simscape dynamic blocks, i.e. the components with non-null volume of fluid (such as the pipes), require the initial conditions of the fluid in the Block Parameters. Regarding the water pipes, initial conditions are set in terms of temperature and pressure. In this study, pressure value was imposed equal to the atmospheric pressure, while the temperature is set equal to the initial value of the temperature input signal, T_{Hin} and T_{Cin} for hot and cold water pipes, respectively. In two-phase *3-Zone Pipes*, the initial conditions are defined by the fluid pressure, and one property that can be selected between temperature, specific enthalpy, specific energy or vapor quality. With temperature and pressure, the initial state of the fluid is imposed in single-phase (subcooled liquid or superheated vapor). The other pairs allows to define the initial conditions in the two-phase mixture. In the organic fluid loop, the initial conditions, together with the dimensions of the pipes, define the mass of fluid inside the closed ORC circuit, since they determine the uniform density in each volume. Here, the property pairs pressure-temperature has been selected. Pressure values have been set to 12 bar and 6 bar for high pressure and low pressure components of the cycle, respectively. Temperature has been imposed uniform in the whole circuit and equal to 35 °C. With these conditions, the charge ratio results 35%, which is consistent with the actual value of charge ratio around 30%, corresponding to a mass of 25 kg (see Section 3.4.3 – *Pump Cavitation*).

5.4 Steady state validation

The parameters obtained with the above-described procedure have been fixed inside the block parameters of the components in the whole layout of Figure 5.4. The first comparison of the simulated results with measured one was performed in stationary conditions, to assess the ability of the integrated model to predict the ORC operating conditions and performance. A set of operating points was selected among the available tested conditions, as representative of the main off-design working conditions of the system. The simulation was conducted with heat source temperature varying from 65 °C to 85 °C, the cold water temperature in the interval 20-24 °C, and the mass flow rate ranging between 50 g/s and 150 g/s. Figure 5.14 show a map of the input set points for the steady-state simulations. The results of the validation are reported in terms of parity plots of the main output variables.

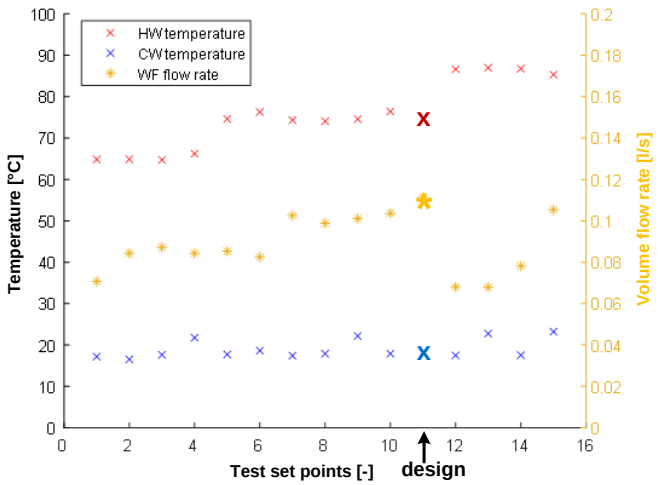

Figure 5.14 – Input set points for simulations

Figure 5.15a and Figure 5.15b report the parity plots for the expander inlet and outlet pressure (p_1 and p_2), and for the expander inlet and outlet temperature (T_1 and T_2). Inlet pressure p_1 shows a good match with experiments especially at the conditions characterized by high evaporation pressure and low heat source temperature, while it is affected by higher inaccuracy with low values of evaporation pressure, especially at high temperature. In other words, the model performs better with low value of superheating degree at the evaporator outlet. In almost all the tested points, p_1 remains inside the ± 5% error band. The expander outlet pressure p_2, related to the condensing pressure of the cycle, shows a low relative error (within ± 5% error band), revealing only a little overestimation with respect to the experiments. Regarding the inlet temperature (T_1), the model reproduces properly the conditions of the experiments, with an error within the ± 2% band, demonstrating a good calibration of the evaporator subsystem. Conversely, the outlet temperature (T_2) is characterized by a more significant error, particularly at high heat source temperature and low mass flow of the working fluid, condition that determines also a higher value of the outlet temperature (between 58 °C and 65 °C). This uncertainty is related, on one hand, to the inaccuracy of the expander sub-model, on the other to the nature itself of the variable T_2. The latter indeed, is the most affected by dynamic phenomena due to the operation of the recuperator (placed after the expander). This anomaly can be observed also experimentally, from two energy balances not being respected at some operating points: the expander thermodynamic power ($\dot{W}_{exp,th} = \dot{m}_{wf} \cdot (h_{in} - h_{out})$), that should be higher than the electrical one ($\dot{W}_{exp,el}$), due to the electromechanical losses, and the recuperator thermal power on vapor side ($\dot{Q}_{rec,V}$), that is supposed to be equal or higher than that on liquid side ($\dot{Q}_{rec,L}$), due to the eventual heat losses to the ambient. Both these conditions, in steady-state operation, should be satisfied. These deviations can be related to transients not being extinguished completely and to measurement uncertainties, which lead to higher error for calculated quantities (like the enthalpies) than for purely measured ones (as temperature, pressure and electric power), due to the propagation of the uncertainties through the data acquisition and elaboration processes (see Chapter 2). The above-presented consideration suggests one of the main limits of the semi-empirical approach, which introduces the errors related to the experiments uncertainties.

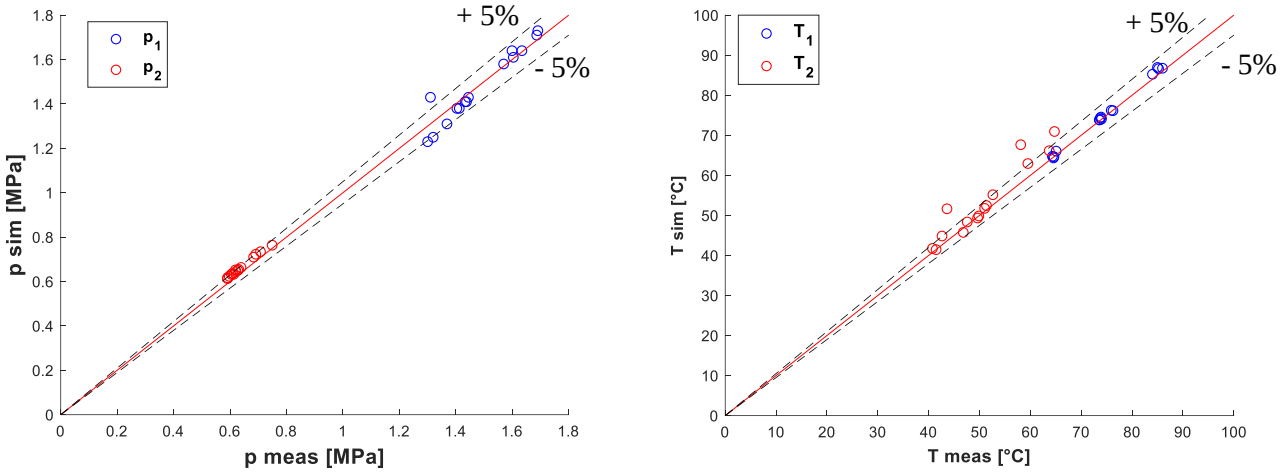

a) b)

Figure 5.15 - Parity plot for expander inlet and outlet pressure (a) and expander inlet and outlet temperature (b)

In Figure 5.16a and Figure 5.16b the comparisons for the expander electric power output ($\dot{W}_{exp,el}$) and rotational speed are presented. As expected, a better correspondence to experimental data is found at higher values of the power output. For expander power higher than 700 W, the error for this quantity is estimated within 10 %. At lower power, the error increases, due to the pressure miscalculation already observed in Figure 5.15a. The rotational speed (N_{exp}) is calculated from the definition of volumetric efficiency of the expander, which was obtained through the polynomial fitting function correlation (Eq. 6), similarly to the isentropic efficiency. It shows an error within the 20% for most the data tested. There is, in most operating conditions, an underestimation of the output variable N_{exp}, whose inaccuracy derives also from the uncertainties related to the experimental measurement of the actual volumetric efficiency, which may not take into account the internal leakage of fluid that is not involved in the expansion process. Introducing a different approach for the expander model (see the Lumped parameters model used in [108]), could improve the empirical correlation of the volumetric efficiency.

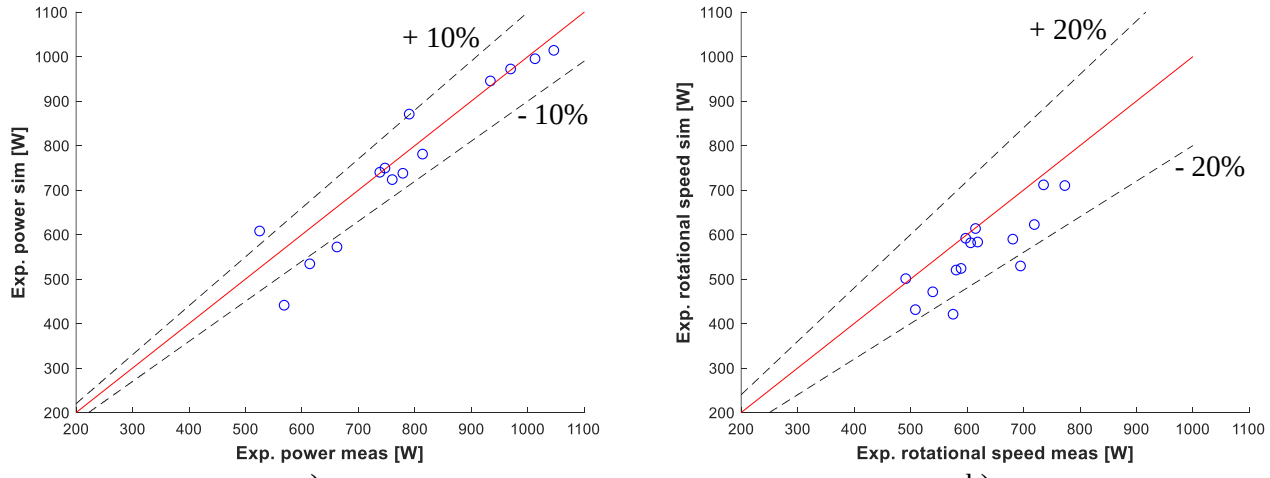

a) b)

Figure 5.16 – Parity plot for expander electric power output (a) and rotating speed (b)

Finally, the comparison of the thermal power exchanged in the three heat exchangers has been made. The simulation on evaporator showed good accuracy, while the condenser has slightly higher error which reflects on the condensation pressure and on the sub-cooling degree. The recuperator is the component with highest inaccuracy, reporting an error bar within the 30% with respect to the experimental results. The same considerations on transient effects made for the expander outlet temperature applies on recuperator thermal power. This component is the one who shows most uncertainties in the calibration phase, due to the mutual dependence of the two flows involved, differently from HEs exchanging with water. This is one of the main causes of the anomalies on expander outlet temperature discussed above.

5.5 Dynamic simulations

The validation of the model has been conducted also with transient input conditions. The cases of increasing variation of the pump speed and of the hot water temperature are here analyzed, by means of the comparison of the simulated results with the experimental data of evaporation and condensation pressure, expander inlet and outlet temperature, and expander power output.

Case 1: variation of pump speed

The first instance regards the case of the increasing variation of the organic fluid pump speed, and its effect on the key output variables of the model. The experimental signal of the mass flow rate ($\dot{m}_{ORC}$), related to a 10-Hz increment pump frequency (see Case 1 of Section 4.3.1), is given as variable input to the feed pump subsystem. The signal is filtered with a 4th order Butterworth filter, in order to dampen any signal noise, which would cause higher time required by the model computations. The other model inputs (T_{Hin}, T_{Cin}, $\dot{V}_H$, $\dot{V}_C$) are kept constant, and equal to the average values calculated on the steady-state experimental signal referred to the selected interval. The variation of the input occurs at time = 1990 s, when the mass flow rate is changed from 0.115 kg/s to 0.169 kg/s, with an increasing ramp.

Figure 5.17 a) shows the response of the evaporation and condensation pressure to the 10-Hz pump speed increment. The mass flow rate, as mentioned, is one of the inputs of the model, inserted at the inlet port of pump ideal flow source (see Figure 5.10). In the graph of Figure 5.17 a), two signals for the mass flow rate are shown, namely the input mass flow rate (black solid line) and the signal measured by the virtual flow rate sensor located at the expander inlet (Figure 5.4). As expected, in stationary conditions the two values substantially coincide. On the contrary, during the transient the response of $\dot{m}_{ORC}$ simulated value is delayed with respect to the input one. The response time (τ_r) of $\dot{m}_{ORC}$ *sim* results close to 280 s, against the time of 60 s related to the $\dot{m}_{ORC}$ *input* variation. This effect cannot be validated directly with experimental data, because in the test bench under investigation the mass flow is measured at the pump inlet and can be different from the mass flow after the evaporator, due to phenomena of liquid fluid accumulation during transient operation. The simulated and measured values of evaporation pressure are reported in Figure 5.17 a) for the two points at the inlet and outlet sides of the evaporator (p_7 and p_1, magenta and red lines respectively). The simulated values (solid lines) are in line with the measured ones (dashed lines) in stationary conditions, while a slower response is observed on the simulation, as expected, due to the delay of the mass flow rate variation. The response time of the variable p_1 is close to 260 s, comparable to that of the expander inlet flow rate, $\dot{m}_{ORC}$ *sim*, while the measured value of $\tau_{r,p1}$ results around 90 s. Condensation pressure is represented in Figure 5.17 a) by the blue and yellow lines corresponding to p_2 and p_3 (expander outlet and condenser inlet pressures, respectively). The simulated value of p_2 is slightly underestimated during the steady-state operation, with an average error close to 8% with respect to the measured pressure. However, the absolute variation after the change of mass flow input, around 0.35 bar, is comparable with the experiments, as well as the response time, close to 70 s (see Table 4-2). Looking at Figure 5.17 b), reporting the temperature trend at the expander inlet and outlet (T_1 and T_2), it can be noticed that the simulated temperature T_1 *sim* (dashed red line) has a good match with the experimental value (T_1 *meas*, solid red line), with maximum error lower than 1%. Only a very small variation due to the change on pump speed is observed for the expander inlet temperature trend, and is related to the increment of the ratio of working fluid to hot water flow rates. Note that the hot water temperature is maintained constant for the entire interval analyzed in this case. The expander

outlet temperature resulting from the model simulation, (T_2 *sim*), is overestimated during the first steady-state interval (before the input change), with an error lower than 5%, while a good match is detected in the second interval after the mass flow variation, with a maximum error close to 1%. In this case, the dynamic reaction results slightly faster than that of experiments, with simulated response time of T_2 *sim* close to 170 s, versus the value of τ_r close to 250 s for the measured expander outlet temperature, T_1 *meas*. The comparison for the expander gross power output ($\dot{W}_{exp,el}$, Figure 5.17 c)) reveals a perfect match of simulated value within the first interval (before the instant equal to 2000 s), while a small overestimation is observed in the second stationary interval, after the input change, with average error around 6%. On the other hand, the response speed of the simulated power is underestimated, with response time close to 160 s, versus only 60 s of the measured power. As depicted in Figure 5.17 c), the trend of simulated $\dot{W}_{exp,el}$ matches the experimental one during the first 50 seconds of variation; then, around the instant = 2050 s, it reduces its slope to achieve the new stationary value more gradually than the measured power.

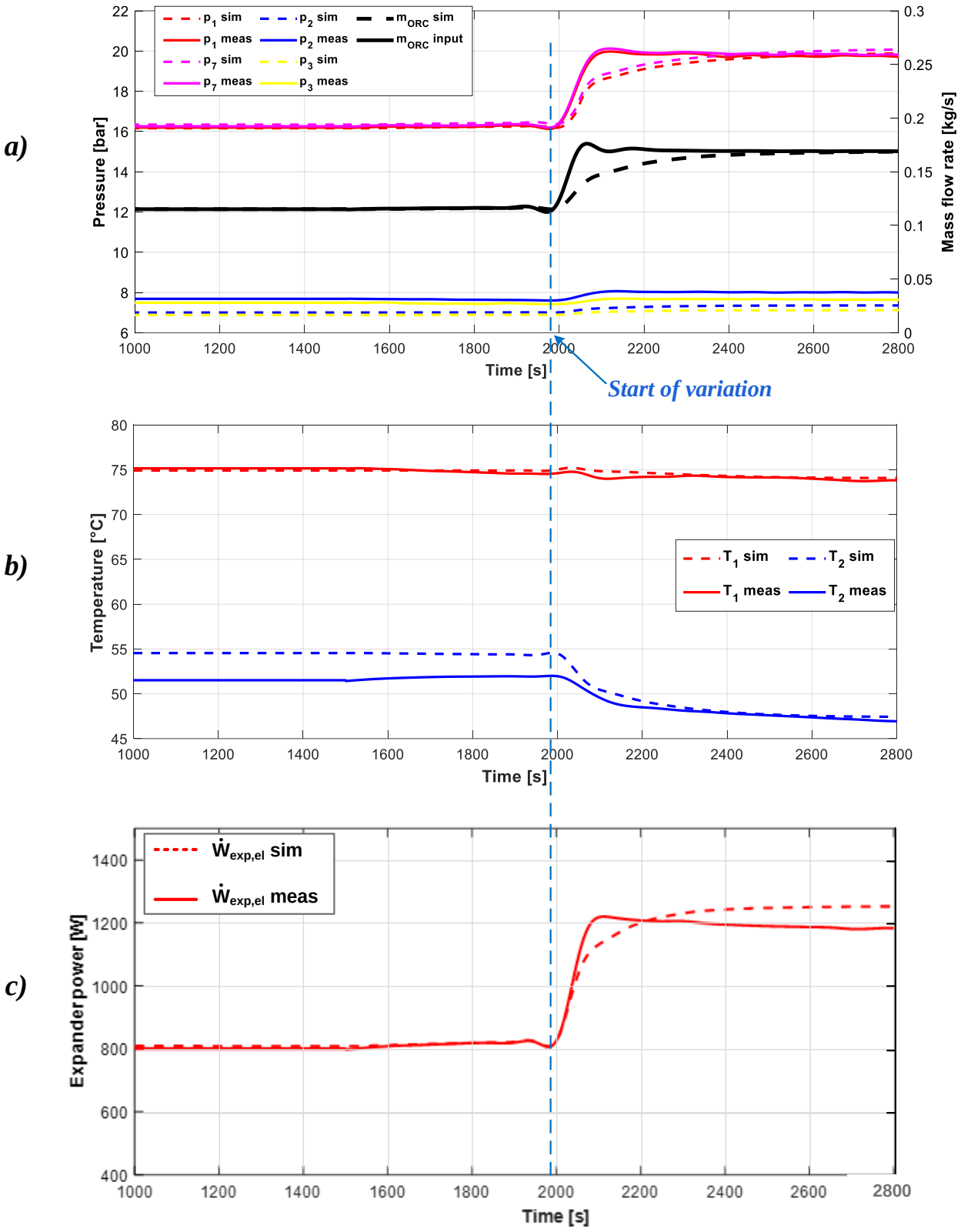

Figure 5.17 – Results of simulation with increasing step of the mass flow rate and comparison with experiment: a) pressures and mass flow rate; b) expander inlet and outlet pressure; c) expander power output

Case 2: variation of hot water temperature

The second case is referred to an increasing variation of the hot water temperature at the evaporator inlet (T_{Hin}). The temperature input signal is taken from the experimental test described in Case 1 of Section 4.3.2. Also in this case, the acquired signal of T_{Hin} is filtered in order to clean up the oscillation that would decrease the computational performance of the model. The other input variables ($\dot{m}_{ORC}$, T_{Cin}, $\dot{V}_H$, $\dot{V}_C$) are kept constant and equal to the experimental average made on the selected interval. The variation of the input temperature T_{Hin} starts at time = 1280 s, with an increment of 5 °C from 75 °C to 80 °C. Figure 5.18 a) shows the results of the simulation for the expander inlet and outlet temperature (T_1 and T_2). The response of the inlet temperature signal (T_1 *sim*, dashed red line*)* is almost coincident with the characteristic time of the perturbation (T_{Hin} *input*, black line), with a response time close to 60 s, which is lower than the actual response time of the variable (T_1 *meas*), around 80 s. In both the intervals before and after the hot temperature variation, the simulated value of T_1 is overestimated of less than 1 °C, corresponding to a relative error around 1%. The model result for the expander outlet temperature (T_2 *sim*) presents low error in the first interval (< 1%), while after the variation the value of T_2 *sim* is overestimated, with higher relative error (4.5%). Indeed, the effect of the hot water temperature rise on T_2 is an increment with similar magnitude and response time to that of the expander inlet temperature. Figure 5.18 b) presents the simulated and measured signals of working fluid mass flow rate ($\dot{m}_{ORC}$), evaporation pressure (p_7, p_1) and condensation pressure (p_2, p_3). Both high and low simulated pressures are slightly lower than measured ones: average errors for p_7 and p_1 are close to 1.5% and 3% respectively, while for p_2 and p_3 the error results around 8.5% and 7.5%, respectively. The perturbation related to the hot water temperature variation has limited impact on the quantities reported in Figure 5.18 b), as only a small change of the evaporation pressure signal is observed, in the interval 1300 s-1500 s. Both in measured and simulated variables, the new steady-state value differs by a negligible amount from the condition before the perturbation. Finally, measured and simulated signals are reported in Figure 5.18 c) for the expander power output. As the input temperature variation starts (time = 1280 s), the simulated value of $\dot{W}_{exp,el}$ achieves a peak after about 100 s, then decreases and settles to a value slightly lower than the measured one (error ≈ 2.5%). This trend is similar to the experimental one, which however presents a lower peak at an earlier time.

5.6 Model weaknesses and potential improvements

In conclusion, the model developed in Simulink Simscape can predict with acceptable precision the thermodynamic performance of the ORC system under investigation, within a relatively wide range of steady-state off-design conditions. The lowest errors are obtained on the expander inlet temperature and on evaporation and condensation pressure, while highest errors are related to the expander outlet temperature, power output and rotating speed. The application of the model to dynamic conditions reveals that the modelled cycle is less reactive than the actual system to the variation of the mass flow, presenting higher response time on both evaporation pressure and expander inlet mass flow rate signals. On the contrary, the modelled evaporator is more sensitive to the variation of hot water temperature than the real one, since the organic fluid temperature at the evaporator outlet is almost coincident with the water inlet temperature. The discrepancy between the experiments and the simulations of the system response to transient conditions, are related to the simplified geometries used to model the heat exchangers. The latter indeed, in order to be able to exchange the required thermal power, are much longer than the actual heat exchangers, resulting in higher fluid mass inertia and causing a slower response to mass flow transients. A solution to this issue could be the disposition of the pipes in parallel instead that in series, but a new calibration procedure would be required. Also, if a larger number of parallel pipes are needed, the model numerical performance are affected negatively.

The main drawback of the presented approach is the calibration of the components of the model, which can be time consuming and difficult to perform, especially if limited amount of information and experimental data are available. Also, the model execution results quite slow especially at the beginning of the simulation, due to the first stabilization of the variables from their initial states to the values determined by the model inputs.

Possible improvements of the proposed model may regard: i) testing different heat exchangers configurations, with parallel pipes or by using one of the complex components included in the Simscape library, mostly dedicated to

refrigeration systems; ii) replacing the polynomial function model of the expander with a more accurate semi-empirical model; iii) accounting for the expander load and speed in the calculation of the fluid dynamic properties of the micro-ORC.

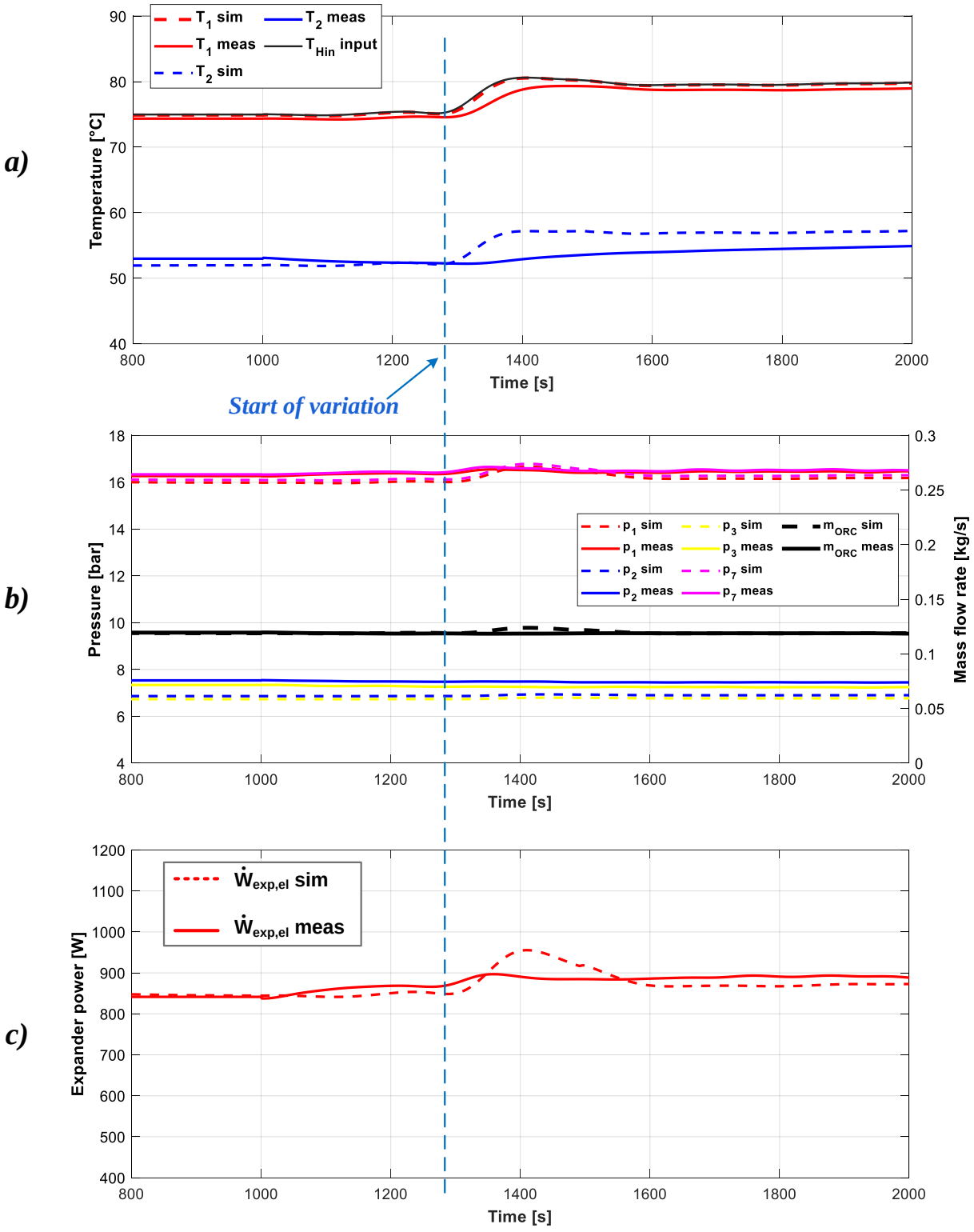

Figure 5.18 - Results of simulation with increasing hot water temperature and comparison with experiment: a) expander inlet and outlet pressure; b) pressures and mass flow rate; c) expander power output

Conclusions

The aim of the study presented in this Ph.D. thesis was the detailed analysis of the operation and performance of a recuperated micro-organic Rankine cycle (ORC) system working with low-temperature heat source. Although the results presented in this manuscript are mainly related to the specific test bench installed at the University of Bologna, main outcomes can be generalized to other systems with similar characteristics. The power plant is rated for a power output in the range 1-3 kW, with heat source temperature between 60 °C and 90 °C. The system operates with a sub-critical cycle with HFC-134a (R-134a) as working fluid, and is driven by a reciprocating piston expander prototype. The micro-ORC has been investigated under several points of view. First, since the development of the experimental equipment has been part of the Ph.D. three-year period, the details of the test bench various solutions have been depicted. These involve the implementation of the external circuits of hot and cooling water, including the in-house developed controllers, and the architecture of the data acquisition and control system, with special focus to the software realized in LabVIEW platform. An experimental approach for the assessment of the working fluid charge is introduced, only based on pressure, temperature and liquid level measurements with the system switched off. The experimental analysis has been conducted both in steady-state and dynamic conditions. Within the steady-state campaign, nearly 130 experimental points have been acquired in off-design conditions, by changing the hot water temperature, the ORC feed pump rotating speed and the external load connected to the expander. The expander load is an electric pure resistive load with discrete regulation, which does not allow imposing a value of rotating frequency or load torque, but only influences the hydraulic resistance of the circuit, by modifying the electric load impedance. With this load configuration, the expander operates as a free-piston machine, as its rotational speed depends on the working fluid flow rate, and therefore on the pump speed. Hence, the rotations of pump and expander, even if their shafts are not mechanically connected, are fluid-dynamically coupled. The other controlled variables of the test bench are the hot and cold water flow rate, while the cold water temperature depends on the ambient conditions and cannot be regulated. The measured variables allowed to evaluate the performance indexes for each component. At given heat source and cold sink temperatures and external load, the mass flow rate determines the operating pressures of the cycle, and thus its power output. The flow rate is proportional to the feed pump rotating speed, which is controlled by the pump inverter. The organic fluid evaporating pressure increases from 11 bar and 23 bar, as the mass flow rate is raised from 80 g/s to 220 g/s, showing higher trends with lower impedance. The performance of the expander has been assessed as function of the expander speed and load impedance. The latter is mainly influenced by the load number (from 1 to 5 loads), but shows also a dependence from the expander speed, due to the variation of the phase voltage with the frequency. The expander rotates at low speed, ranging between 400 rpm and 1150 rpm. The electric power output varied from 300 W to 1650 W, depending on pressure difference and on the loads number. A power-to-pressure ratio between 60 W/bar and 120 W/bar was observed. The expander filling factor decreases with the rotating speed, from 0.95 to 0.45, depending also on the loads number. The expander total efficiency shows modest variations over a wide range of operating conditions, ranging between 38% and 43%, slightly decreasing with the expander speed increment. At high speed and especially with one load, the expander efficiency drops below 30%. Pump electric power and total efficiency are in the ranges 200-1000 W and 10-25%, respectively, both increasing with the pump speed. Cavitation phenomena at the pump suction have been solved by increasing the working fluid charge from 20 kg to 25 kg, achieving an increment of the pump pressure rise at same flow rate and the avoidance of the pumping instability and system collapse. Evaporator behavior has been investigated extensively by assessing the heat transfer effectiveness according to each zone of the heat exchanger (sub-cooled liquid, superheated vapor, two-phase mixture). The evaporator global effectiveness is mostly penalized by the economizer and vaporizer zones of the heat transfer, while the super-heather shows effectiveness close to 100% in most operating points. At some conditions, the fluid starts to condensate inside the recuperator, and enters the condensed in saturated state. These conditions are related to a drop of performance, due to the increment of the condensation pressure at constant cold water temperature and the reduction of the pressure difference across the expander. The overall gross efficiency of the system varies between 2% and 5%, but the net efficiency is strongly penalized by the low pump performance, as it achieves a maximum of 2.1%.

Further experimental tests have been conducted for evaluating the system transient response to step variations of the controlled variables. The cases analyzed are related to the expander start-up transient, pump speed, hot water temperature and electric load variations. The fluid flow rate presents the fastest response to the modification of the pump speed, followed by the evaporation pressure and then by the condensing pressure, which shows a modest variation. The slowest variable is the expander outlet temperature, which in general requires minutes to achieve the new steady-state point. A case of fluctuating hot water temperature has been tested, revealing a relatively slow response of the evaporator heat transfer, suggesting that the evaporator is able to dampen heat source temperature fluctuations with amplitude lower than 5 °C.

A thermodynamic model has been developed using the Simscape library included in MATLAB Simulink, for both steady-state and dynamic simulations of the micro-ORC system. The model is of charge-sensitive type, meaning that no assumptions are made on the fluid states, and the operating conditions depend only on the boundary conditions (hot and cold water temperature and flow rate) and on working fluid flow rate. Heat exchangers are modelled with Simscape blocks as counter-flow pipes, while expansion and pumping processes are divided in two virtual stages a modelled with both Simscape blocks and regular Simulink blocks to implement empirical correlations. The model validation in steady-state conditions reports low error in predicting the pressures of the cycle and the expander inlet temperature (< 5%), while the expander outlet temperature and the expander power output and rotating speed present lower precision. The final step has been the application of the Simscape model to dynamic conditions, in order to validate the system simulated response to transient inputs. First, the simulations have been conducted with an increment of the mass flow rate at the pump outlet, keeping constant all the other inputs. The resulting response of the evaporation pressure and of the expander inlet mass flow rate is slower than the response observed experimentally, but the precision in predicting the stationary values before and after the perturbation is satisfactory. In the second instance, with constant flow rate, the hot water temperature has been increased from 75 °C to 80 °C. In this case, the transient response of the expander inlet temperature is faster than the measured one, as the temperature is almost coincident with the hot water inlet temperature. In conclusion, the proposed model has demonstrated acceptable accuracy in predicting the behavior of the micro-ORC system, both in steady-state and dynamic regime, but some upgrades could help to achieve better precision in reproducing the actual response speed in case of transient input conditions.

Some final remarks can be stated from the analysis reported in this thesis. A micro-ORC system like the one under investigation has a potential as energy conversion technology in the residential sector, coupled with renewable thermal source and heat storage. The cogenerative arrangement is suitable, allowing saving primary energy to supply thermal and electric demands. This solution becomes more attractive for off-grid applications in rural areas. However, the main limits to its spread are high costs of installation and relatively low efficiency, resulting in long payback period. In addition, the large amount of fresh water required for the heat rejection in the ORC condenser may not be available in some locations; this lack can be overcome by using an air condenser, which leads to a reduction of thermodynamic performance. Moreover, the performances of the expander and especially of the feed pump need a substantial improvement. Indeed, a challenging objective would be the significant reduction of the ratio of pump consumption to expander power output (back work ratio) in micro-scale ORC systems, to values lower than 20%. Finally, the operation under slightly dynamic conditions of the heat source is possible, but the variation profile of the heat source should be evaluated carefully, as an efficient control strategy must account for it.

References

[1] Our World in Data based on BP Statistical Review of World Energy & Ember (2020) https://ourworldindata.org/energy, visited in December 2020.

[2] International Energy Agency (IEA), World Energy Outlook 2018.

[3] International Energy Agency (IEA), Emissions from Fuel Combustion, 2020.

[4] Our World in Data based on World Bank, Sustainable energy for All (SE4ALL) & UNWPP https://ourworldindata.org/energy, visited in December 2020.

[5] Health Effects Institute, State of *Global Air 2018*, Boston, MA., United States.

[6] Production of Electricity, 2007. In: Sustainable Nuclear Power. Elsevier, pp. 185–200. https://doi.org/10.1016/B978-012370602-7/50024-7

[7] Rahbar, K., 2017. Review of organic Rankine cycle for small-scale applications. Energy Conversion and Management 21.

[8] REN21, Renewables 2017: Global Status Report., 2017.

[9] Macchi, E., 2017. Theoretical basis of the Organic Rankine Cycle, in: Organic Rankine Cycle (ORC) Power Systems. Elsevier, pp. 3–24. https://doi.org/10.1016/B978-0-08-100510-1.00001-6

[10] Quoilin, S., Broek, M.V.D., Declaye, S., Dewallef, P., Lemort, V., 2013. Techno-economic survey of Organic Rankine Cycle (ORC) systems. Renewable and Sustainable Energy Reviews 22, 168–186. https://doi.org/10.1016/j.rser.2013.01.028

[11] Bell, I.H., Lemmon, E.W., 2017. Organic fluids for Organic Rankine Cycle systems, in: Organic Rankine Cycle (ORC) Power Systems. Elsevier, pp. 91–119. https://doi.org/10.1016/B978-0-08-100510-1.00004-1

[12] Aboelwafa, O., Fateen, S.-E.K., Soliman, A., Ismail, I.M., 2018. A review on solar Rankine cycles: Working fluids, applications, and cycle modifications. Renewable and Sustainable Energy Reviews 82, 868–885. https://doi.org/10.1016/j.rser.2017.09.097

[13] Bao, J., Zhao, L., 2013. A review of working fluid and expander selections for organic Rankine cycle. Renewable and Sustainable Energy Reviews 24, 325–342. https://doi.org/10.1016/j.rser.2013.03.040

[14] Eyerer, S., Dawo, F., Kaindl, J., Wieland, C., Spliethoff, H., 2019. Experimental investigation of modern ORC working fluids R1224yd(Z) and R1233zd(E) as replacements for R245fa. Applied Energy 240, 946–963. https://doi.org/10.1016/j.apenergy.2019.02.086

[15] Feng, Y., Hung, T., Zhang, Y., Li, B., Yang, J., Shi, Y., 2015. Performance comparison of low-grade ORCs (organic Rankine cycles) using R245fa, pentane and their mixtures based on the thermoeconomic multi-objective optimization and decision makings. Energy 93, 2018–2029. https://doi.org/10.1016/j.energy.2015.10.065

[16] Bamorovat Abadi, G., Kim, K.C., 2017. Investigation of organic Rankine cycles with zeotropic mixtures as a working fluid: Advantages and issues. Renewable and Sustainable Energy Reviews 73, 1000–1013. https://doi.org/10.1016/j.rser.2017.02.020

[17] Bianchi, M., Branchini, L., De Pascale, A., Melino, F., Ottaviano, S., Peretto, A., Torricelli, N., 2020. Replacement of R134a with low-GWP fluids in a kW-size reciprocating piston expander: Performance prediction and design optimization. Energy 206, 118174. https://doi.org/10.1016/j.energy.2020.118174

[18] Lemmon, E.W., Bell, I.H., Huber, M.L., McLinden, M.O. NIST Standard Reference Database 23: Reference Fluid Thermodynamic and Transport Properties-REFPROP, Version 10.0, National Institute of Standards and Technology, Standard Reference Data Program, Gaithersburg, 2018.

[19] Pereira, J.S., Ribeiro, J.B., Mendes, R., Vaz, G.C., André, J.C., 2018. ORC based micro-cogeneration systems for residential application – A state of the art review and current challenges. Renewable and Sustainable Energy Reviews 92, 728–743. https://doi.org/10.1016/j.rser.2018.04.039

[20] Guercio, A., Bini, R., 2017. Biomass-fired Organic Rankine Cycle combined heat and power systems, in: Organic Rankine Cycle (ORC) Power Systems. Elsevier, pp. 527–567. https://doi.org/10.1016/B978-0-08-100510-1.00015-6

[21] Turboden, https://www.turboden.com/solutions/1051/biomass, visited in December 2020.

[22] Baharoon, D.A., Rahman, H.A., Omar, W.Z.W., Fadhl, S.O., 2015. Historical development of concentrating solar power technologies to generate clean electricity efficiently – A review. Renewable and Sustainable Energy Reviews 41, 996–1027. https://doi.org/10.1016/j.rser.2014.09.008

[23] Pramanik, S., Ravikrishna, R.V., 2017. A review of concentrated solar power hybrid technologies. Applied Thermal Engineering 127, 602–637. https://doi.org/10.1016/j.applthermaleng.2017.08.038

[24] Garcia-Saez, I., Méndez, J., Ortiz, C., Loncar, D., Becerra, J.A., Chacartegui, R., 2019. Energy and economic assessment of solar Organic Rankine Cycle for combined heat and power generation in residential applications. Renewable Energy 140, 461–476. https://doi.org/10.1016/j.renene.2019.03.033

[25] Lombardo, W., Sapienza, A., Ottaviano, S., Branchini, L., De Pascale, A., Vasta, S., 2021. A CCHP system based on ORC cogenerator and adsorption chiller experimental prototypes: Energy and economic analysis for NZEB applications. Applied Thermal Engineering 183, 116119. https://doi.org/10.1016/j.applthermaleng.2020.116119

[26] Moya, D., Aldás, C., Kaparaju, P., 2018. Geothermal energy: Power plant technology and direct heat applications. Renewable and Sustainable Energy Reviews 94, 889–901. https://doi.org/10.1016/j.rser.2018.06.047

[27] Spadacini, C., Xodo, L.G., Quaia, M., 2017. Geothermal energy exploitation with Organic Rankine Cycle technologies, in: Organic Rankine Cycle (ORC) Power Systems. Elsevier, pp. 473–525. https://doi.org/10.1016/B978-0-08-100510-1.00014-4

[28] Zhang, H.G., Wang, E.H., Fan, B.Y., 2013. A performance analysis of a novel system of a dual loop bottoming organic Rankine cycle (ORC) with a light-duty diesel engine. Applied Energy 102, 1504–1513. https://doi.org/10.1016/j.apenergy.2012.09.018

[29] Imran, M., Usman, M., Park, B.-S., Lee, D.-H., 2016. Volumetric expanders for low grade heat and waste heat recovery applications. Renewable and Sustainable Energy Reviews 57, 1090–1109. https://doi.org/10.1016/j.rser.2015.12.139

[30] Lemort, V., Legros, A., 2017. Positive displacement expanders for Organic Rankine Cycle systems, in: Organic Rankine Cycle (ORC) Power Systems. Elsevier, pp. 361–396. https://doi.org/10.1016/B978-0-08-100510-1.00012-0

[31] Zhao, Y., Liu, G., Li, L., Yang, Q., Tang, B., Liu, Y., 2019. Expansion devices for organic Rankine cycle (ORC) using in low temperature heat recovery: A review. Energy Conversion and Management 199, 111944. https://doi.org/10.1016/j.enconman.2019.111944

[32] Desideri, A., Hernandez, A., Gusev, S., van den Broek, M., Lemort, V., Quoilin, S., 2016. Steady-state and dynamic validation of a small-scale waste heat recovery system using the ThermoCycle Modelica library. Energy 115, 684–696. https://doi.org/10.1016/j.energy.2016.09.004

[33] Shen, L., Wang, W., Wu, Y., Lei, B., Zhi, R., Lu, Y., Wang, J., Ma, C., 2018. A study of clearance height on the performance of single-screw expanders in small-scale organic Rankine cycles. Energy 153, 45–55. https://doi.org/10.1016/j.energy.2018.02.004

[34] Jia, X., Zhang, B., Pu, L., Guo, B., Peng, X., 2011. Improved rotary vane expander for trans-critical CO2 cycle by introducing high-pressure gas into the vane slots. International Journal of Refrigeration 34, 732–741. https://doi.org/10.1016/j.ijrefrig.2010.12.005

[35] Zheng, N., Zhao, L., Wang, X.D., Tan, Y.T., 2013. Experimental verification of a rolling-piston expander that applied for low-temperature Organic Rankine Cycle. Applied Energy 112, 1265–1274. https://doi.org/10.1016/j.apenergy.2012.12.030

[36] Belardinelli R.; Bianchi M.; Branchini L.; De Pascale A.; Dimaiuta A.; Mancini G.; Melino F.; Ottaviano S.; Peretto A. Preliminary Experimental Investigation On A Hydraulic Piston Pump Driven By A Solar Micro-ORC Prime Mover. Proceedings of 16th International Conference on Sustainable Energy Technologies – SET 2017. http://hdl.handle.net/11585/619917

[37] Hou, X., 2017. Free piston expander-linear generator used for organic Rankine cycle waste heat recovery system. Applied Energy 11.

[38] Bianchi, M., Branchini, L., Pascale, A.D., Melino, F., Ottaviano, S., Peretto, A., Torricelli, N., Zampieri, G., 2018. Performance and operation of micro-ORC energy system using geothermal heat source. Energy Procedia 148, 384–391. https://doi.org/10.1016/j.egypro.2018.08.099

[39] Zeleny, Z., Vodicka, V., Novotny, V., Mascuch, J., 2017. Gear pump for low power output ORC – an efficiency analysis. Energy Procedia 129, 1002–1009. https://doi.org/10.1016/j.egypro.2017.09.227
[40] Quoilin, S., Lemort, V., Lebrun, J., 2010. Experimental study and modeling of an Organic Rankine Cycle using scroll expander. Applied Energy 87, 1260–1268. https://doi.org/10.1016/j.apenergy.2009.06.026
[41] Reid A.D. Low temperature power generation using HFE-7000 in a Rankine cycle, Master thesis, San Diego State University, 2010
[42] Landelle, A., Tauveron, N., Revellin, R., Haberschill, P., Colasson, S., Roussel, V., 2017. Performance investigation of reciprocating pump running with organic fluid for organic Rankine cycle. Applied Thermal Engineering 113, 962–969. https://doi.org/10.1016/j.applthermaleng.2016.11.096
[43] Yang, X., Xu, J., Miao, Z., Zou, J., Yu, C., 2015. Operation of an organic Rankine cycle dependent on pumping flow rates and expander torques. Energy 90, 864–878. https://doi.org/10.1016/j.energy.2015.07.121
[44] Turunen-Saaresti, T., Uusitalo, A., Honkatukia, J., 2017. Design and testing of high temperature micro-ORC test stand using Siloxane as working fluid. J. Phys.: Conf. Ser. 821, 012024. https://doi.org/10.1088/1742-6596/821/1/012024
[45] Tartière, T., Astolfi, M., 2017. A World Overview of the Organic Rankine Cycle Market. Energy Procedia 129, 2–9. https://doi.org/10.1016/j.egypro.2017.09.159
[46] Turboden, Concentrated Solar Power. https://www.turboden.com/solutions/1056/concentrated-solar-power, visited in December 2020.
[47] Air Squared, Introducing the Plug and Play Micro-ORC. https://airsquared.com/, visited in December 2020.
[48] Rank. https://www.rank-orc.com/rank-micro-2/, visited in December 2020.
[49] Enogia. http://enogia.com/wp/7-2-5/, visited in December 2020.
[50] Visorc. https://www.visorc.fi/#Technology, visited in December 2020.
[51] ElectraTherm, https://electratherm.com/products__trashed/power-plus-generator-4400b-series/, visited in December 2020.
[52] Zuccato Energia, https://zuccatoenergia.it/it/prodotti/serie-chp/, visited in December 2020.
[53] Li, Y.-M., n.d. Experimental investigation of 3-kW organic Rankine cycle (ORC) system subject to heat source conditions: A new appraisal for assessment 11.
[54] Bianchi, M., Branchini, L., Casari, N., De Pascale, A., Melino, F., Ottaviano, S., Pinelli, M., Spina, P.R., Suman, A., 2019. Experimental analysis of a micro-ORC driven by piston expander for low-grade heat recovery. Applied Thermal Engineering 148, 1278–1291. https://doi.org/10.1016/j.applthermaleng.2018.12.019
[55] Taccani, R., Obi, J.B., De Lucia, M., Micheli, D., Toniato, G., 2016. Development and Experimental Characterization of a Small Scale Solar Powered Organic Rankine Cycle (ORC). Energy Procedia 101, 504–511. https://doi.org/10.1016/j.egypro.2016.11.064
[56] Desideri, A., Gusev, S., van den Broek, M., Lemort, V., Quoilin, S., 2016. Experimental comparison of organic fluids for low temperature ORC (organic Rankine cycle) systems for waste heat recovery applications. Energy 97, 460–469. https://doi.org/10.1016/j.energy.2015.12.012
[57] Carraro, G., Rech, S., Lazzaretto, A., Toniato, G., Danieli, P., 2019. Dynamic simulation and experiments of a low-cost small ORC unit for market applications. Energy Conversion and Management 197, 111863. https://doi.org/10.1016/j.enconman.2019.111863
[58] Mascuch, J., Novotny, V., Vodicka, V., Zeleny, Z., 2017. Towards development of 1-10 kW pilot ORC units operating with hexamethyldisiloxane and using rotary vane expander. Energy Procedia 129, 826–833. https://doi.org/10.1016/j.egypro.2017.09.196
[59] Bouvier, J.-L., Lemort, V., Michaux, G., Salagnac, P., Kientz, T., 2016. Experimental study of an oil-free steam piston expander for micro-combined heat and power systems. Applied Energy 169, 788–798. https://doi.org/10.1016/j.apenergy.2016.01.122
[60] Torregrosa, A., Galindo, J., Dolz, V., Royo-Pascual, L., Haller, R., Melis, J., 2016. Dynamic tests and adaptive control of a bottoming organic Rankine cycle of IC engine using swash-plate expander. Energy Conversion and Management 126, 168–176. https://doi.org/10.1016/j.enconman.2016.07.078

[61] Jung, H.-C., Taylor, L., Krumdieck, S., 2015. An experimental and modelling study of a 1 kW organic Rankine cycle unit with mixture working fluid. Energy 81, 601–614. https://doi.org/10.1016/j.energy.2015.01.003
[62] Feng, Y., Hung, T.-C., Su, T.-Y., Wang, S., Wang, Q., Yang, S.-C., Lin, J.-R., Lin, C.-H., 2017. Experimental investigation of a R245fa-based organic Rankine cycle adapting two operation strategies: Stand alone and grid connect. Energy 141, 1239–1253. https://doi.org/10.1016/j.energy.2017.09.119
[63] Gusev, S., Ziviani, D., Vierendeels, J., De Paepe, M., 2019. Variable volume ratio free-piston expander: Prototyping and experimental campaign. International Journal of Refrigeration 98, 70–79. https://doi.org/10.1016/j.ijrefrig.2018.10.004
[64] Park, B.-S., 2018. Review of Organic Rankine Cycle experimental data trends. Energy Conversion and Management 13.
[65] Landelle, A., Tauveron, N., Haberschill, P., Revellin, R., Colasson, S., 2017. Organic Rankine cycle design and performance comparison based on experimental database. Applied Energy 204, 1172–1187. https://doi.org/10.1016/j.apenergy.2017.04.012
[66] Dumont, O., Parthoens, A., Dickes, R., Lemort, V., 2018. Experimental investigation and optimal performance assessment of four volumetric expanders (scroll, screw, piston and roots) tested in a small-scale organic Rankine cycle system. Energy 165, 1119–1127. https://doi.org/10.1016/j.energy.2018.06.182
[67] Yang, S.-C., Hung, T.-C., Feng, Y.-Q., Wu, C.-J., Wong, K.-W., Huang, K.-C., 2017. Experimental investigation on a 3 kW organic Rankine cycle for low-grade waste heat under different operation parameters. Applied Thermal Engineering 113, 756–764. https://doi.org/10.1016/j.applthermaleng.2016.11.032
[68] Kosmadakis, G., Landelle, A., Lazova, M., Manolakos, D., Kaya, A., Huisseune, H., Karavas, C.-S., Tauveron, N., Revellin, R., Haberschill, P., De Paepe, M., Papadakis, G., 2016. Experimental testing of a low-temperature organic Rankine cycle (ORC) engine coupled with concentrating PV/thermal collectors: Laboratory and field tests. Energy 117, 222–236. https://doi.org/10.1016/j.energy.2016.10.047
[69] Collings, Mckeown, Wang, Yu, 2019. Experimental Investigation of a Small-Scale ORC Power Plant Using a Positive Displacement Expander with and without a Regenerator. Energies 12, 1452. https://doi.org/10.3390/en12081452
[70] Oudkerk, J.F., Dickes, R., Dumont, O., Lemort, V., 2015. Experimental performance of a piston expander in a small- scale organic Rankine cycle. IOP Conf. Ser.: Mater. Sci. Eng. 90, 012066. https://doi.org/10.1088/1757-899X/90/1/012066
[71] Wronski, J., Imran, M., Skovrup, M.J., Haglind, F., 2019. Experimental and numerical analysis of a reciprocating piston expander with variable valve timing for small-scale organic Rankine cycle power systems. Applied Energy 247, 403–416. https://doi.org/10.1016/j.apenergy.2019.04.028
[72] Hou, X., Zhang, H., Xu, Y., Yu, F., Zhao, T., Tian, Y., Yang, Y., Zhao, R., 2018. External load resistance effect on the free piston expander-linear generator for organic Rankine cycle waste heat recovery system. Applied Energy 212, 1252–1261. https://doi.org/10.1016/j.apenergy.2018.01.020
[73] Hou, X., 2017. Free piston expander-linear generator used for organic Rankine cycle waste heat recovery system. Applied Energy 11.
[74] Casella, F., 2017. Dynamic modeling and control of Organic Rankine Cycle plants, in: Organic Rankine Cycle (ORC) Power Systems. Elsevier, pp. 153–171. https://doi.org/10.1016/B978-0-08-100510-1.00006-5
[75] Bonilla, J., Dormido, S., Cellier, F.E., 2015. Switching moving boundary models for two-phase flow evaporators and condensers. Communications in Nonlinear Science and Numerical Simulation 20, 743–768. https://doi.org/10.1016/j.cnsns.2014.06.035
[76] Desideri, A., Dechesne, B., Wronski, J., van den Broek, M., Gusev, S., Lemort, V., Quoilin, S., 2016. Comparison of Moving Boundary and Finite-Volume Heat Exchanger Models in the Modelica Language. Energies 9, 339. https://doi.org/10.3390/en9050339

[77] Jiménez-Arreola, M., Pili, R., Wieland, C., Romagnoli, A., 2018. Analysis and comparison of dynamic behavior of heat exchangers for direct evaporation in ORC waste heat recovery applications from fluctuating sources. Applied Energy 216, 724–740. https://doi.org/10.1016/j.apenergy.2018.01.085
[78] Quoilin, S., Aumann, R., Grill, A., Schuster, A., Lemort, V., Spliethoff, H., 2011. Dynamic modeling and optimal control strategy of waste heat recovery Organic Rankine Cycles. Applied Energy 88, 2183–2190. https://doi.org/10.1016/j.apenergy.2011.01.015
[79] Wang, X., Shu, G., Tian, H., Liu, P., Jing, D., Li, X., 2018. The effects of design parameters on the dynamic behavior of organic ranking cycle for the engine waste heat recovery. Energy 147, 440–450. https://doi.org/10.1016/j.energy.2018.01.047
[80] Xu, B., Rathod, D., Kulkarni, S., Yebi, A., Filipi, Z., Onori, S., Hoffman, M., 2017. Transient dynamic modeling and validation of an organic Rankine cycle waste heat recovery system for heavy duty diesel engine applications. Applied Energy 205, 260–279. https://doi.org/10.1016/j.apenergy.2017.07.038
[81] Zampieri G. "CLOSED-CYCLE PLANT." U.S. Patent No. 20,160,032,786. 4 Feb. 2016.
[82] Declaye S., Quoilin S., Guillaume L., Lemort V. Experimental study on an open-drive scroll expander integrated into an ORC (Organic Rankine Cycle) system with R245fa as working fluid. Energy, vol. 55 (2013) 173-183. DOI: 10.1016/j.energy.2013.04.003.
[83] Liu, L., Zhu, T., Ma, J., 2017. Working fluid charge oriented off-design modeling of a small scale Organic Rankine Cycle system. Energy Conversion and Management 148, 944–953. https://doi.org/10.1016/j.enconman.2017.06.009
[84] Rice C. The effect of void fraction correlation and heat flux assumption on refrigerant charge inventory predictions. ASHRAE Trans 1987;93:341–67.
[85] Zivi, S.M., 1964. Estimation of Steady-State Steam Void-Fraction by Means of the Principle of Minimum Entropy Production. Journal of Heat Transfer 86, 247–251. https://doi.org/10.1115/1.3687113
[86] Premoli A, Francesco D, Prina A. A dimensional correlation for evaluating twophase mixture density. La Termotecnica 1971;25:17–26.
[87] Hughmark G. Holdup in gas liquid flow. Chem Eng Prog 1962;58(4):62–5
[88] Dickes, R., Dumont, O., Guillaume, L., Quoilin, S., Lemort, V., 2018. Charge-sensitive modelling of organic Rankine cycle power systems for off-design performance simulation. Applied Energy 212, 1262–1281. https://doi.org/10.1016/j.apenergy.2018.01.004
[89] Dickes, R., Dumont, O., Lemort, V., 2020. Experimental assessment of the fluid charge distribution in an organic Rankine cycle (ORC) power system. Applied Thermal Engineering 179, 115689. https://doi.org/10.1016/j.applthermaleng.2020.115689
[90] Patel, V.V., 2020. Ziegler-Nichols Tuning Method: Understanding the PID Controller. Reson 25, 1385–1397. https://doi.org/10.1007/s12045-020-1058-z
[91] Jiang T., Chen B., He X., Stuart P. Application of steady-state detection method based on wavelet transform. Computers & Chemical Engineering, vol. 27, issue 4 (2003) 569–578. DOI: 10.1016/S0098-1354(02)00235-1.
[92] Cao S., Rhinehart R.R. An efficient method for on-line identification of steady state. Journal of Process Control, 5(6):363–374, 1995. DOI: 10.1016/0959-1524(95)00009-F.
[93] Narasimhan S., Kao C. S., Mah R. S. H. Detecting changes of steady states using the mathematical theory of evidence. AIChE Journal, vol. 33, issue 11 (1987) 1930–1932. DOI: 10.1002/aic.690331125.
[94] Woodland B. J., Braun J. E., Groll E. A., Horton W. T. Experimental Testing of an Organic Rankine Cycle with Scroll-type Expander. In International Refrigeration and Air Conditioning Conference at Purdue, July 2012.
[95] Lecompte S. Performance Evaluation of Organic Rankine Cycle Architectures: Application to Waste Heat Valorisation. PhD. Thesis, 2016.
[96] Kim M., Ho Yoon S., Domanski P. A., Payne W. V. Design of a steadystate detector for fault detection and diagnosis of a residential air conditioner. International Journal of Refrigeration, vol. 31, issue 5 (2008) 790-799, DOI: 10.1016/j.ijrefrig.2007.11.008.
[97] Li X., Shu G., Tian H., Shi L., Huang G., Chen T., Liu P. Preliminary tests on dynamic characteristics of a CO2 transcritical power cycle using an expansion valve in engine waste heat recovery. Energy, vol. 140, Part 1 (2017) 696-707. DOI: 10.1016/j.energy.2017.09.022.

[98] Cao S., Rhinehart R. R. Critical values for a steady-state identifier. Journal of Process Control, vol. 7, issue 2 (1997) 149-152, DOI: 10.1016/S0959-1524(96)00026-1.
[99] Bianchi, M., Branchini, L., De Pascale, A., Orlandini, V., Ottaviano, S., Peretto, A., Melino, F., Pinelli, M., Spina, P.R., Suman, A., 2017. Experimental Investigation with Steady-State Detection in a Micro-ORC Test Bench. Energy Procedia 126, 469–476. https://doi.org/10.1016/j.egypro.2017.08.222.
[100] Bianchi, M., Branchini, L., Casari, N., Pascale, A.D., Fadiga, E., Melino, F., Ottaviano, S., Peretto, A., Pinelli, M., Spina, P.R., Suman, A., 2019. Uncertainty Quantification of Performance Parameters in a Small Scale ORC Test Rig. Proceedings of the 5th International Seminar on ORC Power Systems, September 9-11, 2019, Athens, Greece.
[101] Thorade M, Saadat A. Partial derivatives of thermodynamic state properties for dynamic simulation (2013) Environmental Earth Sciences, 70 (8), pp. 3497-3503. DOI: 10.1007/s12665-013-2394-z.
[102] Casari, N., Fadiga, E., Pinelli, M., Randi, S., Suman, A., 2019. Pressure Pulsation and Cavitation Phenomena in a Micro-ORC System. Energies 12, 2186. https://doi.org/10.3390/en12112186.
[103] D'Amico, F., Pallis, P., Leontaritis, A.D., Karellas, S., Kakalis, N.M., Rech, S., Lazzaretto, A., 2018. Semi-empirical model of a multi-diaphragm pump in an Organic Rankine Cycle (ORC) experimental unit. Energy 143, 1056–1071. https://doi.org/10.1016/j.energy.2017.10.127
[104] Kays, W., London, A.L. Compact Heat Exchangers. Ed. McGraw-Hill - Series in Mechanical Engineering, 1984.
[105] Gnielinski, V. New equations for heat and mass transfer in the turbulent pipe and channel flow. Int. Chem. Eng, 1975.
[106] Cavallini, Zecchin. A dimensionless correlation for heat transfer in forced convection condensation. 6th Int. Heat Transfer Conf. Tokyo, 1974, pp. 309-313.
[107] MathWorks, «Simscape, MATLAB Simulink documentation». 2019.
[108] Bianchi, M., Branchini, L., De Pascale, A., Melino, F., Ottaviano, S., Peretto, A., Torricelli, N., 2019. Application and comparison of semi-empirical models for performance prediction of a kW-size reciprocating piston expander. Applied Energy 249, 143–156. https://doi.org/10.1016/j.apenergy.2019.04.070